H Optimal Control for Linear Time Invariant and Parameter Dependent Conditions in Active Magnetic Bearing Systems

Wang, Muhao

Award date:
2016

Awarding institution:
University of Bath

H_∞ Optimal Control for Linear Time Invariant and Parameter Dependent Conditions in Active Magnetic Bearing Systems

Muhao Wang

A thesis submitted for the degree of Doctor of Philosophy

University of Bath
Department of Mechanical Engineering

April 2016

Table of Contents

List of Figures

List of Tables

Abstract

This thesis mainly focuses on the H_∞ optimal control for the mixed sensitivity problem in rotor/active magnetic bearing (AMB) systems by considering linear time invariant (LTI) and parameter dependent conditions. In order to attenuate vibrations when a rotor runs under contact-free conditions. Riccati based H_∞ optimization is introduced for a rotor/AMB system at particular rotational speeds. A H_∞ controller synthesized by the LMI based gain-scheduling technique was then designed to guarantee stability when the system operates with varying speed. Based on the LMI's framework, a gain-scheduling controller designed for contact-free recovery, is also presented. The controller's robust stability and contact-free recovery capability were verified through simulations and experiments.

Finite element modelling (FEM) is introduced into the description of a flexible rotor. The rotor/AMB model, including linearized AMB system actuation under PD control, is then used for robust H_∞ control design as a contact-free plant. In the LTI H_∞ optimization, singular value issues due to discrepancy number of system inputs and outputs is discussed. A solution to that problem is proposed, and examined numerically. In order to extend operating speeds, a switching control system including several LTI H_∞ controllers is introduced and tested in simulation.

Rotor/touchdown bearing contact dynamics are investigated numerically and experimentally. Based on the linearization method for rotor/touchdown bearing contact, a contact-dependent plant including the interaction of the rotor and a movable base was developed for contact-free recovery controller design. It relies on a feedforward contact estimation observer. The LMI based gain-scheduling control action enables the rotor to escape from trapped contact. Additionally, the potential limitation for the contact-recovery controllers is assessed experimentally under significant unbalance. Coast down tests were undertaken to verify contact-free recovery control action when the rotational speed varies in a transient manner.

Acknowledgements

This thesis presents the research I carried out at the Department of Mechanical Engineering, University of Bath. I would like to thank all who supported me during this project. In particular, I am grateful to my lead supervisor Patrick Keogh, for his patient guidance, supportive advice and encouragement. Also, I appreciate the one year supervision under Matthew Cole and the support from Necip Sahinkaya. I acknowledge the receipt of the scholarship from the University of Bath.

This thesis is dedicated to my parents, my family and the one who be with me.

Chapter 1 Introduction

Rotating machinery is used widely in industry, especially in power systems and transportation. Rotor systems differ in terms of rotor size, operating condition, power requirement, and complexity, serving in different industrial fields. Thus, a variety of bearings have been designed to support rotors in passive or active modes. The supported rotor may also interact with stationary components during operating. In order to isolate vibrations, rotating machinery may be mounted on foundations via isolators, or even operate with base motion such as in transport environments. The preliminary design procedures for rotating machines according to ISO [1] or API [2], require that a rotor system design has dynamic stability and the capability to verify system response to particular operating situations.

Due to economic growth, the demand for rotating machinery has increased, especially in incorporating safety, performance and operating precision. The potential for optimization lies with smart control. However, conventional passive rotating machinery has limitations for advanced control strategy implementation. Active mechatronic systems may satisfy the requirements, a successful example being active magnetic bearing (AMB) systems.

1.1 AMB Applications

Levitating a body without contact is not a new idea. The first successful implementation of a magnetic bearing was in the early 1970's for a satellite energy storage system, flywheels, and gyro stabilizers [3]. Since then, AMBs have been used in rotating machine applications as they provide advantages such as contact-free levitation, near frictionless operation, high rotational speeds, operation in extreme environments, and active vibration control capabilities [4]. Compared with conventional journal or ball bearings, the longer service life of an AMB system running with less maintenance and lower costs are distinctive. Furthermore, the energy consumption during normal rotor/AMB operation, is much less than other

equivalent passive systems. Thanks to these benefits, AMB systems have also been used in ventricular assist devices as reliable healthcare components. With AMBs, turbomachinery performance such as in turbocompressors, turbogenerators and turboexpanders, has improved. These machines have the capability to run through critical speeds, thus the operating speed range of the rotor is increased. Due to rotor harmonics, unbalance vibration may reveal quite large amplitudes in conventional passive rotating systems. However, AMBs can enable active control implementation, and reduce these vibrations significantly. Thus, safety and efficiency during operating are enhanced. Another successful application of AMB technology is in turbomolecular pumps, where higher rotational speeds enable higher vacuums. A turboexpender may be used in a nuclear power system to cool down the nuclear reactor. Due to high running speed operation, AMBs with appropriate control may also be used in milling and grinding spindle systems. Besides these main applications, AMBs may also be used in centrigufuges, X-ray devices, and gas turbines, potentially for transportation in aero engines as shown in the European research project [5]. However, disadvantages of AMB systems are also evident in industrial implementation as their relatively high complexity and high initial cost are notable.

1.2 Principle of AMBs

In 1842, Earnshaw demonstrated the unstable situation of a passive magnetic bearing system [6]. That occurs since the force generated by magnets or AMBs increases with decreasing gap between the electromagnets and core body. This may resemble the rotor being supported by a spring system having negative stiffness. Hence, appropriate control action is necessary. Position feedback control, which can overcome the negative stiffness effect, is commonly used to stabilize the system [7].

A typical single input and single output (SISO) control loop arrangement for a magnetic bearing system is shown in Figure 1.1. In order to levitate the rotor, a laminated core is usually mounted on the rotor as a ferromagnetic body. A displacement sensor measures the position and transmits a voltage signal. With the feedback, control integral action may be used to centralize the rotor position. Based

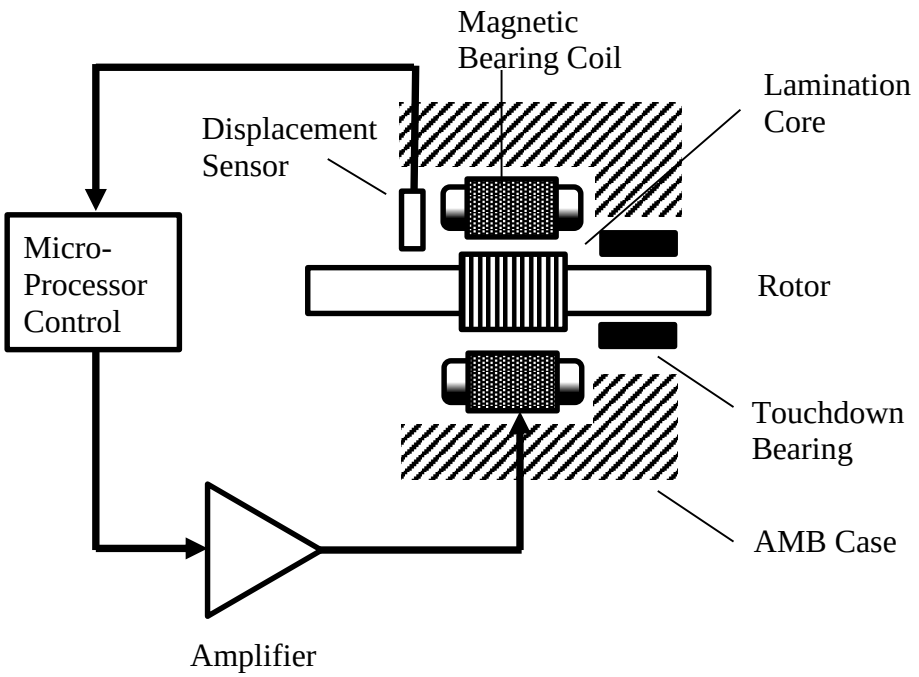

Figure 1.1 Schematic diagram of principle of an AMB under closed loop control

on a specific control strategy, other control action may be implemented to generate appropriate compensation forces. In order to drive the AMB system, the control signal is converted into current by an amplifier. In case of system power failure or temporary overload, the rotor could make contact with displacement sensors or AMB poles. This may induce severe damage to the machine. Thus, a touchdown bearing of appropriate clearance is usually included to constrain the rotor displacement.

1.3 Challenges for AMBs

Like other machinery, AMB systems may malfunction. Thus, how to identify system faults is essential for AMB development. Several methods have been developed by researchers. An open-loop adaptive control method to detect AMB system faults was published by Sahinkaya et al. [8] while Keogh et al. [9] specified rotor/AMB system faults in contact with a touchdown bearing (TDB) during operation. Schweitzer [10] discusses the safety and reliability issues of AMB applications. Rotor/AMB system malfunction may be induced by control action failure, due to hardware or unexpected

system dynamics. Rotor/stator contact may also induce control instability due to changes in the plant characteristics.

1.3.1 Hardware Failure

Actuation Faults: Control action in magnetic bearing systems is actuated by power amplifiers and magnetic coils. Either may fail and give rise to rotor/stator contact and uncontrolled vibration. AMB control force is generated by coil current from a power amplifier. Sudden amplifier failure may cause power current loss, and physical damage due to contact. Magnetic coil currents affect flux density in the magnetic gap during rotor/AMB operation. Electrical system faults such as a short circuit, may give rise to partial or total loss of actuation and ineffective control force due to insufficient windings during operation. Consequently, contact events could occur.

Displacement Measurement Faults: Rotor/AMB system operation relies on closed loop control. Displacement sensor measurements are essential for a control system to produce effective action in phase and magnitude. Depending on the situation, displacement sensor faults may give rise to system performance deterioration, rotor contact with a TDB or instability problem. Non-collocation of AMB and sensor planes, and signal distortion due to sensor surface damage may also degrade performance and/or stability.

1.3.2 Unexpected System Dynamics

Due to the complexity of rotor/AMB systems, dynamic underestimation of characteristics may lead to contact instability. These may include internal gyroscopic effects or external disturbances such as base motion, mass loss during operation, and rotor trapped in TDB contact events.

Speed Dependency: Gyroscopic coupling and aerodynamic influences have speed dependency, hence system dynamics may vary in the operating speed range. System identification techniques based on a ‘chirp’ test signal, or a multi harmonic signal

with phase angle adjustment developed by Schroeder [11], may not be able to estimate affine system dynamics sufficiently. Thus, the instability problem may arise from a rotor/AMB system controlled by a linear time invariant (LTI) controller.

Base Motion: A rotor/AMB system may be subject to various sources of vibrations, not only direct unbalance forcing, but transmitted through bearings owing to base motion [12]. Base motion may be significant and affect rotor dynamic behaviour, as measurement/AMB inertial actuation frames may vibrate. This may give rise to unexpected rotor motion in a rotating frame, and even contact with TDBs.

Mass Loss: Synchronous unbalance forcing applies directly to a spinning rotor, when rotor mass centre does not coincide with the geometric centre. During operation, a rotor may experience sudden mass loss, which may excite rotor higher harmonics, and local PD control action may not be able to attenuate the vibration globally.

Rotor/TDB Contact: Rotor/TDB interactions may lead to problematic rotor dynamic behaviour. Due to dynamic heat from rubbing component, instability may arise from thermal bends [13-15]. Normally, a linear dynamic model is derived from the Finite Element Method (FEM) to represent a levitated rotor without contact. However, under power failure (rotor sudden drop) [16, 17], overload or base motion, the rotor may come into contact with TDBs. That may give rise to dynamic plant changes [18, 19].

1.3.3 Contact Dynamics

Usually, initial conditions, operational conditions, and surface characteristics determine whether a rotor becomes trapped in a contact mode. Based on the experimental results [20], an analytical procedure was developed to present rotor/TDB contact dynamics including nonlinearities. Another possible method to describe rotor contact events, is to utilize wavelet analysis [21]. When contact events happen under PID control action, the rotor may have potentials to recover as a

contact-free state or continue persistent contact [22, 23]. Under appropriate unbalance forcing, rotor responses may be bi-stable [24].

If a rotor is subjected to synchronous unbalance forcing, the steady state responses under contact may be classified into three types: (a) limited vibration orbit due to steady rubbing; (b) periodic impacts with subharmonics; and (c) rotor whirl with asynchronous impacts. Research concerned with contact rubbing includes periodic impacts and subharmonics arising from a rotor having contact under base motion external load or TDB misalignment, were reported in last decades. In such periodic bouncing contact modes, the contact point locations are dispersed around the TDB with subharmonics of rotor rotational frequencies [12, 25-33]. In the asynchronous contact case, a TDB constrains rotor motion and suffers asynchronous impacts in a stationary (inertial) frame [34]. However, such contact behaviour is repetitive and rotor motion reveals forward or backward bouncing whirls [13, 35] if observed in a synchronous rotating frame. Eventually, that may give rise to continuous backward whirl, which must be avoided since very high contact forces apply.

1.4 Current Research for AMBs Optimal Control

In ideal operation, a rotor should be centralized under AMB actuation. In order to achieve better performance with lower initial cost, most research focuses on control algorithm implementation rather than hardware redesign. With appropriate control strategies, vibration orbits induced by unbalance force distributions can be attenuated effectively [36-39]. A rotor/AMB system offers a convenient environment for control implementation, either in active or passive strategy.

1.4.1 Classical Control

As the most common closed loop control strategy, PID feedback, can be implemented easily [40], however, rotor vibrations might be significant when passing resonance zones. Unbalance forcing excitation can be compensated by using synchronous forces applied AMBs [41]. The amplitude and phase of this correction force can be computed online based on dynamic modes. In addition to PID control,

μ-synthesis and Linear Quadratic Regulation (LQR) may be implemented in AMB systems as reported in [42, 43]. The implementation of fuzzy logic control strategies are demonstrated in [44-46]. For high speed machinery, rotor flexibility should be considered for the controller design, especially when flexible modes may be excited. Unlike Single Input and Single Output (SISO) control, Multiple Input and Multiple Output (MIMO) control can attenuate rotor vibration globally [37, 47]. Based on Fourier decomposition [48], an on-line computation controller having multi-entries enabled rotor steady amplitude and transient performance as an extended SISO control system. Nyquist-like techniques based on pole-placement are reported in [49] to solve multivariable control problems. The method cannot address robustness stability directly, but leaves a sufficient gain margin to allow closed loop stability.

1.4.2 Advanced Control

Modern multivariable control technique offers a powerful feedback design to guarantee robustness stability. The most successful implementation is the controller synthesis based on the H_∞ norm optimization. Depending on various approaches, this state-space formed control solution is embedded with a reduced order model and weightings for performance as can be found in [50]. H_∞ control optimization focuses on a mixed sensitivity problem, by a tradeoff minimize system output energy with unknown, but well-bounded input. That results in a system with high robustness. According to different control criteria, weighting matrix design methods for multivariable loop shaping are published in [51]. In the rotor vibration control field, a control engineer normally focuses on the system displacement response with less consideration on transients. Controllers synthesized by H_∞ optimization, to attenuate influence of synchronous/non-synchronous forcing disturbance in rotor/AMB system, and also demonstrating transient vibration attenuation are reported in [52]. In order to improve both steady and transient system response, a state-space solution for the H_2 mixed with H_∞ control optimization is developed in [53]. H_2 optimization, focuses mainly on the H_2 norm of system output energy, but may be weak in robustness and tracking performance. Mixing H_2 with H_∞ optimization enables the control system to be 'more damped', so that the closed loop controlled system has

the capability to improve system transients and handle Gaussian white noise. Implementations for such control strategy are published in [54, 55]. Another possible solution to improve transient performance, is a wavelet technique combined with H_∞ optimization [56]. By identifying localised time-frequency components under vibration effects and digital signal processing directly, [57-59] demonstrate the efficiency of wavelets in rotor transient control.

In general, rotor speed may cover a wide range, even though steady operating speed ranges may be narrow. Owing to this speed dependence, a single LTI H_∞ controller designed for a specific speed may not be able to stabilize the system over a complete operation range. Model uncertainties may arise from gyroscopic moments and other aerodynamic conditions that are speed dependent. In order to re-shape the frequency response over a large speed range, a switching signal driven control system contained a number of LTI H_∞ controllers may have potential [60].

As an enhancement to the most common H_∞ optimization, linear matrix inequality (LMI) approach [61] and its state-space formulation [62] has emerged as a powerful design tool in control engineering. Many control problems and design specifications have LMI formulations [63], and the controller can be synthesised via LMIs [64]. By comparing with the Riccati based control solution, the strength of an LMI formulation is the enabling of various constraints or objectives combined in a numerically tractable manner. Through efficient convex optimisation algorithms, LMIs can be formulated as constraints for LTI controller design [65]. They offer both robustness and stochastic benefits as for H_2 mixed with H_∞ [54]. Beyond the LTI control solution, the unique advantage of the LMI framework is the application of a gain-scheduling technique. In order to achieve a control system with more robustness, LMI gain-scheduling focuses mainly on optimization for a plant having parameter dependency. If system state-space matrices are functions of time-varying parameters, and such varying parameters can be measured, parameter dependency can normally be structured as a linear fractional transformation (LFT) with linear interpolation for trackable purposes [66]. The derivation of LMI controller synthesis algorithms

follows from polytopic models in classes of a vertex system, which can be gain-scheduled with linear parameter varying (LPV) feedback to coincide with varying system dynamics [67, 68]. Thus, the 'over conservative' solution in LTI H_∞ optimization, which treats the time-varying dynamics as additional plant multiplicative sensitivity, can be replaced by the LMI gain-scheduling approach. With these advantages, research has utilized LMI gain-scheduling to address the instability induced by gyroscopic effects [69, 70]. These papers included simulation studies of gain-scheduling control implementation on small rigid rotors supported by AMBs. Experimental results are achieved in [71, 72].

1.4.3 Contact Recovery

During rotor operation, vibration orbits may become significant under excitation and possibly lead to contact with TDBs. Optimal control for rotor contact recovery should be considered as essential field for safety and less maintenance. In [73] a modified controller is proposed to recover a rotor from contact. It demonstrates that contact induced nonlinear vibratory motion may arise from a linearly stable rotor orbit without contact. A synchronous controller may lose control due to phase errors. Based on an analytical method to describe contact dynamics [20], a robustness controller to enable a rotor to escape from contact based on a linear time-varying system model was designed in [74]. Feedforward control is also implemented in recovering rotor position from contact [75], which demonstrated a successful procedure by using active control based on contact observers.

1.5 Impacts of the Thesis

Based on the advanced control implementation stated in Section 1.4, this thesis aims to optimize rotor/AMB performance through H_∞ design for the closed loop mixed sensitivity problem. Low order weighting filters in [51-53], may be used to derive a state-space controller having fewer states for ease of implementation. However, the system response, especially around resonances, has the potential to be attenuated further by using high order weighting filters. LTI H_∞ control design has already been

demonstrated to obtain disturbance rejection for a rotor/AMB system [52]. However, the discrepancy between the number of sensors for feedback and the number of control axes would yield a sub-optimal synthesized solution. This may be overcome by scaling the output dimension. A LTI model may be insufficient to stabilize the rotor running over a wide speed range [60], hence switching action would be useful. A small H_∞ performance value would enable a relative large robustness margin for each LTI controller, to allow the controllers to work in tandem. This may solve the potential stability issue during switching action.

As an enhancement to LTI controller design, the LMI based gain-scheduling framework provides guaranteed robustness stability when a system has parameter dependency over a finite range. Several controllers have been implemented in rotor/AMB system to cope with the uncertainties induced by gyroscopic moments [69-72]. Beyond the implementations on small rigid rotors [69, 70], the LMI based gain-scheduling control technique may be considered to optimize a larger sized rotor/AMB system. Also, second order filter utilization for closed loop sensitivity may enhance the control performance reported in [71, 72].

In addition to gain-scheduling controllers to cope with rotor/AMB system speed dependency [69-72], LMI based-scheduling optimal control solution may be implemented to recover rotor position from rotor/TDB contact events. Feedforward control strategy has been demonstrated as an effective way to recover rotor from contact events [73, 75]. However, it has to rely on the active actuation explicitly. Gain-scheduling control may enable rotor contact-free recovery control under closed loop feedback.

1.6 Structure and Objectives of the Thesis

By considering the aims above, this thesis mainly focuses on the following objectives:

- Under contact-free operation, use Riccati based H_∞ control to facilitate vibration attenuation more effectively with high order weighting filters, considering a rotor/AMB system as a LTI plant;

- In order to extend the LTI control speed range, use switching control to enable several LTI controllers to work in tandem. The potential stability issue during switching action, should be overcome by each controller synthesized having a relative small H_∞ performance value;

- In order to guarantee robustness and stability over a wide running speed range, LMI based gain-scheduling control technique to be introduced to cope with rotor/AMB system speed dependency induced by gyroscopic moments;

- Complex rotor/TDB contact events to be linearized to enable LPVs. By using acceleration feedback, a feedforward observer to be created to estimate the 'effective stiffness' for the support base model. Contact condition to be estimated using LPV feedback;

- Based on the contact stiffness observer, a controller is to be synthesized by the LMI based gain-scheduling technique to enable rotor recovery from contact.

By starting from mathematical descriptions of a rotor/AMB system including rotor behaviour under rotor/TDB contact in inertial frames, the thesis introduces H_∞ optimization theory via Riccati/LMI based solutions. Several LTI controllers are designed by considering normal rotor/AMB system operation. A LMI based gain-scheduling technique is used to solve time varying uncertainties induced by rotor speed dependency. With appropriate modelling, the LPV control technique is also introduced into rotor/TDB contact-free recovery and verified experimentally.

As a basic plant for controller design, a mathematical model having sufficient accuracy to represent the physical machine is essential. Chapter 2 introduces the experimental equipment, and presents the free-free rotor modelling based on the Finite Element Method (FEM). A linear methodology for practical AMB forcing situation under PD control action is also presented. By considering inertial measurement/actuation frames in contact events, Chapter 2 also investigates interaction of the rotor/base through an estimated base rigid body modelling. It gives state-space formulation, which enables LMI based gain-scheduling control synthesis for rotor/TDB contact recovery.

Chapter 3 introduces H_∞ optimization theory and control solutions for a mixed sensitivity problem in the augmented plant. LTI H_∞ controllers, are synthesized for rotor/AMB system in specific speeds. However, singular value issues due to the unequal number of actuation and measurement, which may result in insufficient control performance due to a sub optimization procedure for a non-full rank plant. Thus, a 'non-conjugal' transposed plant is proposed to decompose singular values and derives a full column rank plant for controller design. Based on these techniques, several so called 'Square' LTI H_∞ controllers were designed for specific running speeds. A single LTI controller may not be able to stabilize system with parameter dependency. This thesis also proposes a control system with enabled switching action between LTI H_∞ controllers in Chapter 3.

A switching control system may attenuate rotor vibrations in wide speed range. However, the transients and potential instability due to switching cannot be neglected. The LMI based gain-scheduling technique may be an alternative powerful solution, especially in LPV control design. Chapter 4 introduces LMI formulations to optimize a speed dependent rotor/AMB system, by utilizing a gain-scheduling technique to enable a controller having LPV characteristics. Due to LMIs, system time varying uncertainties may be implemented in controller design. Gyroscopic effects may be

structured from a LFT. A speed dependent gain-scheduling H_∞ controller having two vertex systems, is proposed in this thesis.

Rotor/TDB contact-free recovery is a desire in rotor/AMB research. A classical closed loop control strategy may be insufficient to recover a rotor successfully due to contact event complexity. A linear modelling approach is proposed to estimate impact force amplitude; thus, the dynamics change induced by contact, could be predicted and formed as LPV in polytope. Based on LMI gain-scheduling, Chapter 5 introduces a robustness control design, which enables rotor recovery from contact with TDBs and having the capability to reject disturbances.

With different unbalance mass, Chapter 6 demonstrates the rotor/TDB contact response sensitivity to unbalance forces, and shows the bi-stable behaviour under rotor/TDB contact experimentally. Following the contact-free recovery controller design stated in Chapter 5, a controller to recover rotor from rotor/TDB contact is derived for real-time implementation by appropriate weightings. Chapter 6 verifies the closed loop stability and the controller's capability to reject disturbance under non-contact condition. Contact-free recovery were assessed experimentally in several speeds with different contact conditions (unbalances and non-driven end touchdown bushing misalignments). Also, Chapter 6 defines the potential limitations of the robustness controller experimentally. Besides of single speed, coast down test for contact-free recovery were also undertaken.

Chapter 2 Test Rig Modelling

Appropriate accuracy of a mathematical model representing a physical machine system is essential for controller design. As is well known, robust control strategies could stabilize a system and achieve disturbance rejection with a trade-off criterion. Sufficient modelling accuracy would constrain multiplicative model error to a low level, so that control performance may be improved under guaranteed stability.

This chapter presents a test rig with sensor/actuation planes for robust controller implementation. The Finite Element Method (FEM) is introduced for flexible free-free rotor modelling. In order to achieve a basic plant for controller design, the AMB PD control action is linearized and included in a state-space model. A rotor/AMB model is then developed, and also dynamic properties such as mode shapes under PD control, eigenvalues/vectors, and gyroscopic effects with speeds are presented. In rotor/TDB contact events, the interaction between rotor and base has to be considered. From physical parameter estimation, a rigid body base model having multi-inputs/outputs is developed and formed in state-space.

2.1 Rotor/AMB Modelling

2.1.1 Existing Test Rig

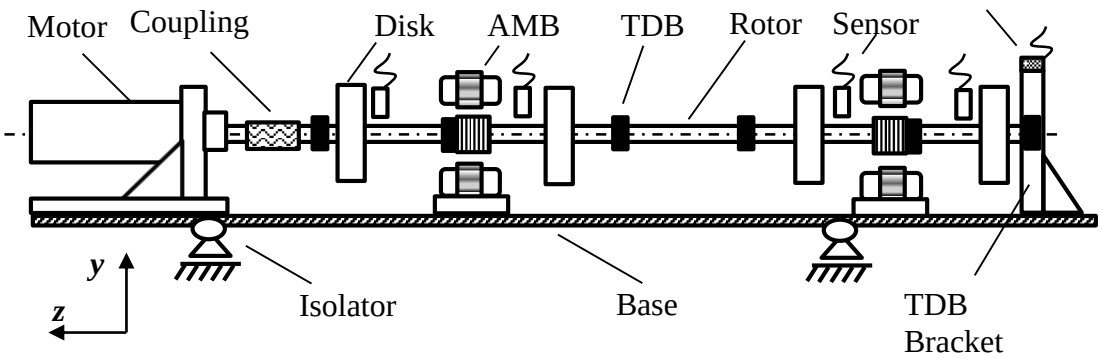

Figure 2.1 Schematic diagram of test rig

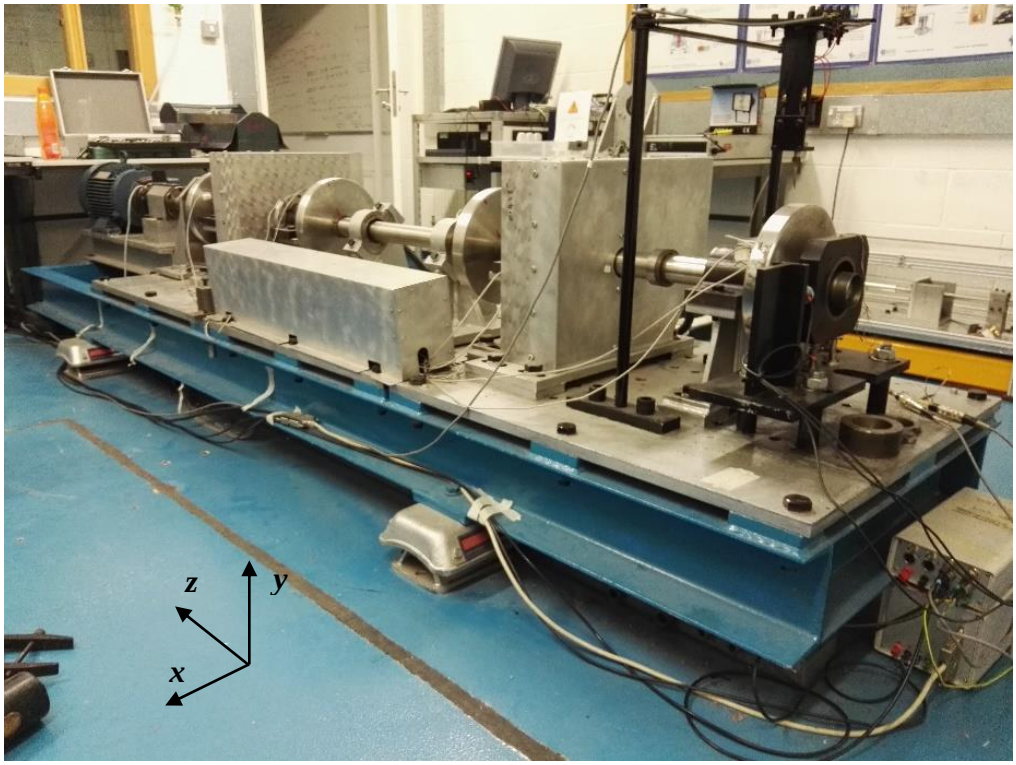

Figure 2.2 Photograph of the existing test rig

The existing test rig and corresponding schematic diagram are shown in Figures 2.1 and 2.2. There are two displacement sensors located adjacent to each AMB and two more at either end of the rotor. An accelerometer is located at the non-driven end bushing housing (stator side) to measure acceleration induced by base motion. A default PID controller uses only the local AMB sensors. Six touchdown bearings (TDBs) are presented, though for normal levitated operation. Two TDBs located adjacent to AMBs are used mainly to protect the AMBs when vibrations are significant. There are four disks and two lamination cores mounted on the shaft. An electric motor drives the shaft through a universal coupling. A base supported by four isolators is also presented in Figure 2.2. It is used to isolate the vibrations induced by rotor operation. The rig is capable of running up to 6000 rpm. Such an operation range covers four resonant frequencies, including the first two 'rigid body' modes (translational and rotational) and the first two flexible bending modes. The AMB's have an output limitation of 1500 N. This rig may be used to undertake vibration tests, even with operation under rotor/TDB contact.

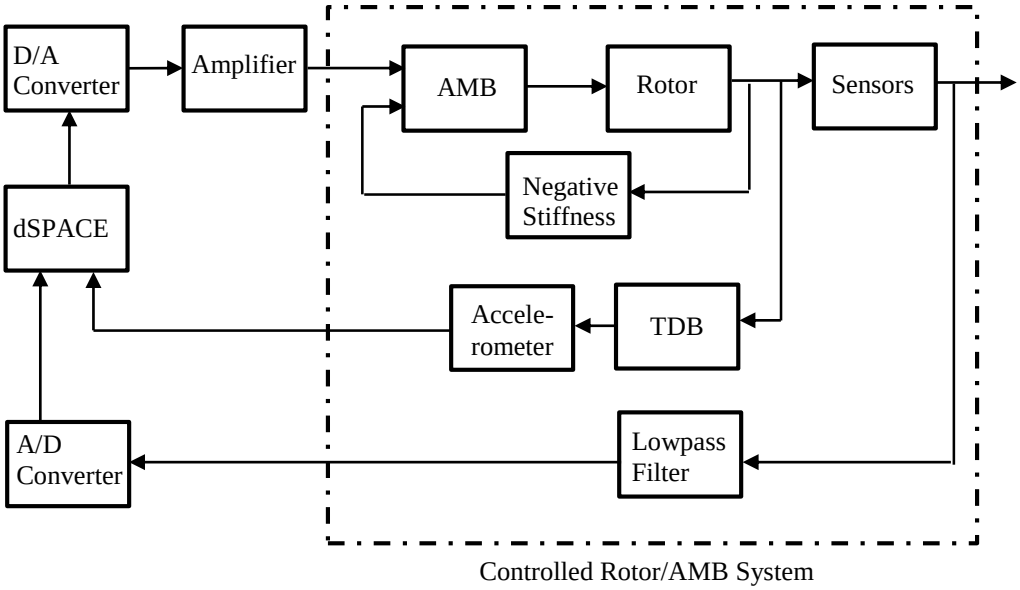

Figure 2.3 Active magnetic bearing system under closed loop control

Figure 2.3 shows the general control loop and associated hardware used in the test rig. Feedback control is essential to stabilize an AMB levitated rotor. dSPACE real-time hardware with 4000 Hz sampling frequency may be used enable controller implementation. By embedding Matlab/Simulink modelling, dSPACE processes signals (feedback and control input for AMB's actuation) in real-time, and the output drives the AMBs after amplification. A lowpass filter is used in the feedback loop to filter out noise at high frequencies. Accelerometer measurements feed into dSPACE directly.

Table 2.1 Physical parameter of AMB

Parameter	Value
Bias current	$i_B = 5$ A
Maximum current input	$i_m = 10$ A
Number of poles	$n_p = 8$
Angle between pole pairs	$\alpha_p = 45^{\circ}$
Coil turns per pole	$n_t = 316$
Pole cross-section area	$A_p = 13.99$ cm^2
Saturation force	$F_{AMB}^{S} = 1500$ N
Average radial gap	$s_a = 1.2$ mm
Levitation current	$i_l = 0.65$ A

2.1.2 Simplified Active Magnetic Bearing Model

AMBs are known to have nonlinear characteristics, including flux/force saturation action during overload. For the purpose of controller synthesis, it is common to linearize AMB characteristics. Under a non-leakage assumption, the magnetic flux may be described in high permeability materials with gaps. The AMB simplification may neglect the hysteresis and saturation effects, but the control input current must be designed to be less than the coil limits. Such a loss of detail in the model may induce some errors. However, the results are normally accepted with sufficient accuracy. Table 2.1 shows the physical parameters of an AMB system in the test rig.

AMB Simplification with Gravity Compensation

Figure 2.4 shows the internal structure of an AMB and a simplified AMB/rotor with a single pole. Based on the AMB system principle stated in [4], the energy generated by the single AMB pole in electric circuit is

$$E_{AMB} = \frac{1}{2}\int_0^{V_M} D_M P_M dV_M \tag{2.1}$$

where V_M is the air gap volume during AMB action. D_M is the magnetic flux density and P_M is the magnetic field strength, which may be obtained as

$$D_M = \sum_{i=1}^{n_t} \frac{i_{0i}}{\frac{l_f}{\mu_f}\frac{A_a}{A_p} + \frac{l_a}{\mu_a}}, \quad P_M = \sum_{i=1}^{n_t} \frac{i_{0i}}{\frac{\mu_a}{\mu_f}\frac{A_L}{A_p} l_f + l_a} \tag{2.2}$$

where l_f is the length of magnetic core, l_a is the effective length of magnetic core, μ_f is permeability of free space, μ_a is effective permeability of core, A_a is the effective cross-sectional area, A_p is the cross-sectional area, i_{0i} is the current for each core and n_t is the number of turns.

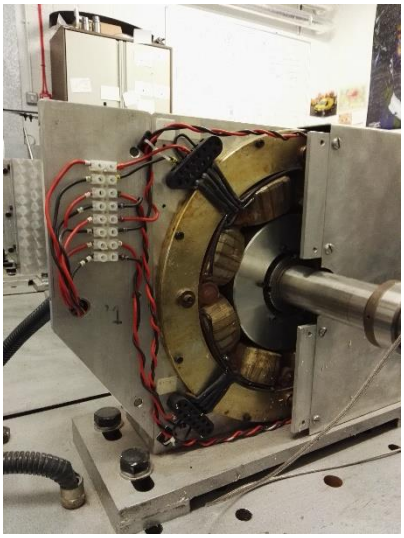

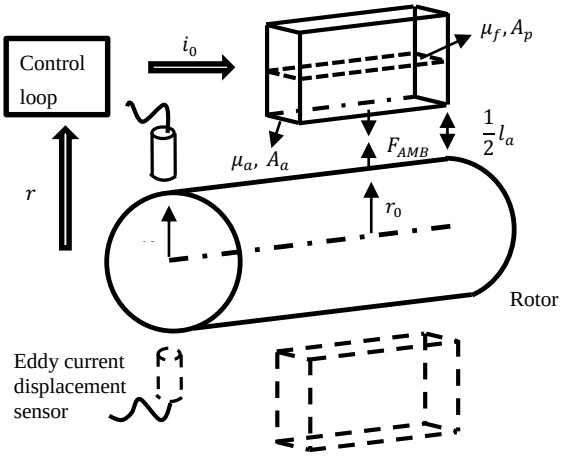

AMB internal structure Magnetic bearing pole

Figure 2.4 Photograph of an AMB and schematic diagram for a single magnetic actuator under feedback control

By setting $s_0 = \frac{1}{2}l_a$, the magnetic bearing force along with varying displacement may be obtained as

$$F_{AMB} = -\frac{\partial E_{AMB}}{\partial s_0} = \frac{\mu_0 A_a {n_t}^2}{4} \cdot \frac{(s_0 - \frac{l_f}{2\mu_r})i_0^2}{(s_0 + \frac{l_f}{2\mu_r})^3} \tag{2.3}$$

where $\mu_r = \frac{\mu_f}{\mu_0}$, where it is assumed that, $A_a = A_p$, and $\mu_a = \mu_0 = 4\pi \cdot 10^{-7}$ N/A. Neglecting $l_f/2\mu_r$ as being small compared with s_0, equation (2.3) simplifies to

$$F_{AMB} = \frac{\mu_0 A_a {n_t}^2}{4} \cdot \left(\frac{i_0}{s_0}\right)^2 \tag{2.4}$$

A magnetic bearing is commonly arranged as radial direction, two nearby magnetic poles may produce force [7] subject to

$$F_{AMB} = F_{AMB}^{+} - F_{AMB}^{-} = k_{AMB}\left(\left(\frac{i_0^{+}}{s_0 + r_0}\right)^2 - \left(\frac{i_0^{-}}{s_0 - r_0}\right)^2\right) \tag{2.5}$$

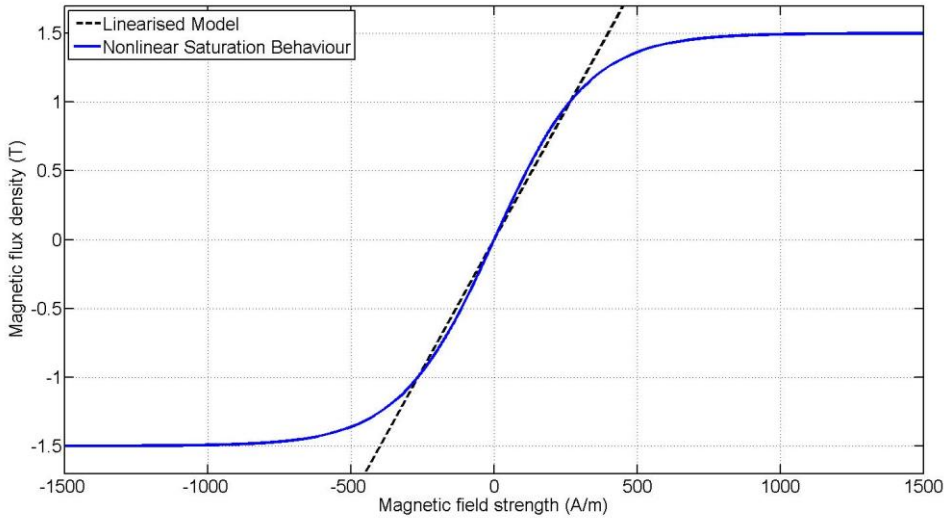

Figure 2.5 Nonlinear relation between magnetic field strength and flux density

where r_0 is the rotor displacement of magnetic force action point. The magnetic bearing constant k_{AMB} is

$$k_{AMB} = \frac{\mu_0 A_a {n_t}^2}{4} cos\, \beta_{AMB} \tag{2.6}$$

where β_{AMB} is the angle between acting pole and AMB system central line in *x*/*y* coordinates.

Figure 2.5 shows the nonlinear relationship between magnetic field strength and flux density and the linear region. A high bias current i_B adding to current i_c by control, introduces linearities to the reaction force F_{AMB} produced by active magnetic bearing. Integral action in PID control, levitates the rotor to a central position under gravity. With the levitation force compensated by the current i_l, the actuation current input may be given by

$$i_0^+ = i_B + i_l + i_c \text{ and } i_0^- = i_B - i_l - i_c \tag{2.7}$$

By inserting equation (2.7) into equation (2.5), F_{AMB} may be expressed as

$$F_{AMB} = k_{AMB}\left(\left(\frac{i_B + i_l + i_c}{s_0 + r_0}\right)^2 - \left(\frac{i_B - i_l - i_c}{s_0 - r_0}\right)^2\right) \tag{2.8}$$

The nonlinear magnetic bearing force may be linearized as

$$F_{l-AMB} = F_{AMB}|_P + \frac{\partial F_{AMB}}{\partial r_0}(r_0 - r_{0,P}) + \frac{\partial F_{AMB}}{\partial i_c}(i_c - i_{c,P}) \qquad (2.9)$$

Thus, linearized magnetic bearing model for control design may be obtained from i_c and r_0 as

$$F_{l-AMB} = k_i i_c - k_s r_0 \qquad (2.10)$$

where the current gain k_i and negative stiffness k_s may be defined according to magnetic bearing constant k_{AMB}

$$k_i = 4k_{AMB}\frac{i_B}{{s_0}^2}, \quad k_s = 4k_{AMB}\frac{{i_B}^2}{{s_0}^3} \qquad (2.11)$$

According to basic parameters shown in Table 2.1, current gain is calculated approximately as $k_i = 500\ \mathrm{N/A}$, and negative stiffness $k_s = 2 \cdot 10^6\ \mathrm{N/m}$.

2.1.3 Finite Element Method for Flexible Free-Free Rotor

The flexible rotor used in the test rig, includes a shaft with two lamination magnetic cores and four rigid discs mounted on it. Physical parameters of the rotor are shown in Table 2.2. In order to discretize and model as a linear axisymmetric rotor body, the FEM has advantages such as high accuracy and easy management of degrees of freedom. Nelson and McVaugh [76] introduce this technique into describe a flexible rotor under the actuation from bearing system. A flexible rotor global displacement could be obtained by various element solutions, typically known as Euler-Bernoulli and Timoshenko beam elements. Considering shear deformation, the Timoshenko beam element has higher modelling accuracy, and is more appropriate in modelling a thick shaft. The following assumptions apply:

- Rotor has small deformations axially
- Rotor operates without axial load and has no torsional deformation
- Besides small unbalance forcing, the shaft is axially symmetric
- The disks/cores are rigid, and thin enough to be added at an element node
- Bending stiffness is same as beam at a disk/core location

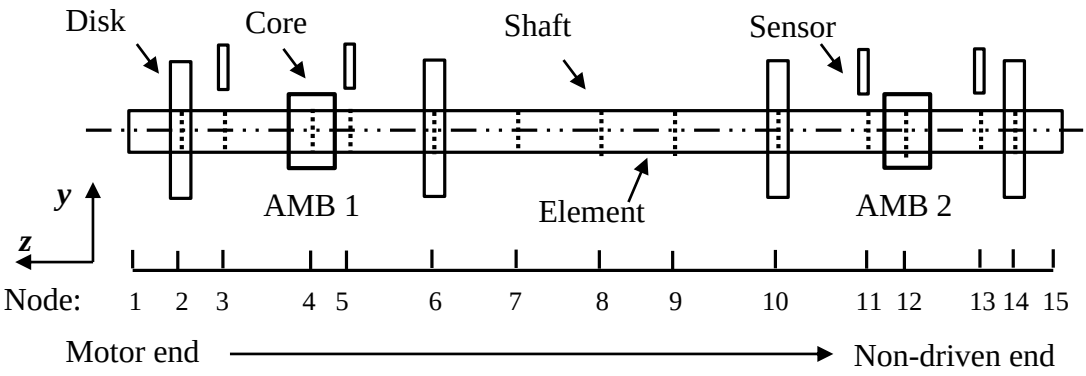

Figure 2.6 Rotor finite element model discretization

Figure 2.6 shows the beam element discretization with disks/cores assembled as a rotor finite element model. In this thesis, the shaft is divided into 14 Timoshenko elements, each having four degrees of freedom. Some nodes have to be defined based on disk locations and sensor/actuation planes in the test rig.

Table 2.2 Physical parameters of the shaft

Beam	Young's Modulus Length Diameter Mass Shear Modulus	$E_b = 206400\ \mathrm{N/mm^2}$ $L_b = 2.14\ \mathrm{m}$ $d_b = 50\ \mathrm{mm}$ $m_b = 32.98\ \mathrm{kg}$ $G = 80436\ \mathrm{N/mm^2}$
Disks	Mass Diameter Moment Inertia (Axial) Moment Inertia (Polar)	$m_d = 12.95\ \mathrm{kg}$ $d_d = 0.25\ \mathrm{m}$ $\Theta_d^a = 49.9\ \mathrm{g/m^2}$ $\Theta_d^p = 97.1\ \mathrm{g/m^2}$
Cores	Mass Diameter Moment Inertia (Axial) Moment Inertia (Polar)	$m_c = 7.99\ \mathrm{kg}$ $d_c = 0.175\ \mathrm{m}$ $\Theta_c^a = 28.2\ \mathrm{g/m^2}$ $\Theta_c^p = 16.5\ \mathrm{g/m^2}$

The flexible rotor motion can be described by ordinary differential equations and the order of system is determined by the number of discretized elements and degrees of freedom of each element node. The free-free rotor dynamics may be expressed as

$$\mathbf{M}_R\ddot{\mathbf{s}}_R + \mathbf{B}_R\dot{\mathbf{s}}_R + \mathbf{K}_R\mathbf{s}_R = \mathbf{f}_R \tag{2.12}$$

where $\mathbf{M}_R$ $\mathbf{B}_R$ and $\mathbf{K}_R$ are free-free flexible rotor system mass, damping and stiffness matrices of size 60×60. $\mathbf{s}_R = [\mathbf{s}_{R1}^T, \cdots \mathbf{s}_{R15}^T]^T$ is a 60×1 vector. Motion for each element node, $\mathbf{s}_{Ri} = \left[s_i^x, s_i^y, \varphi_i^x, \varphi_i^y\right]^T$, contains translational displacements $\left[s_i^x, s_i^y\right]^T$ and rotational angle $\left[\varphi_i^x, \varphi_i^y\right]^T$ in *x*/*y* coordinates. The generalized force vector $\mathbf{f}_R = [\mathbf{f}_{R1}^T, \cdots \mathbf{f}_{R15}^T]^T$ includes unbalance forces, AMB control forces and any contact forces. It could be separated as force components at each node, $\mathbf{f}_{Ri} = \left[f_i^x, f_i^y, t_i^x, t_i^y\right]^T$

Mass Matrix

With elements assembled and adding rigid body disks and cores, the flexible rotor system total mass matrix may be expressed as

$$\mathbf{M}_R = \mathbf{M}_B + \mathbf{M}_C + \mathbf{M}_D \tag{2.13}$$

where $\mathbf{M}_B$, $\mathbf{M}_C$, $\mathbf{M}_D$ are mass matrices of free-free beam, cores and disks; By using FEM matrices assembling techniques as stated in [76], $\mathbf{M}_B$ may obtained by superposing the translational element mass $\mathbf{M}_b^t$ and rotational $\mathbf{M}_b^r$.

Based on the Timenshenko element solution, the translational mass matrix is expressed as

$$\mathbf{M}_b^t = \mathbf{M}_{b0}^t + \emptyset\mathbf{M}_{b1}^t + \emptyset^2\mathbf{M}_{b2}^t \tag{2.14}$$

where $\emptyset = 12E_b\pi I_b/\kappa A_b G{L_b}^2$, A_b, L_b indicates the cross sectional area and length of each beam element. The second moment are$I_b = \pi R^4/4$, shear coefficient$\kappa = 6(1 + 2\mu + \mu^2)/(7 + 12\mu + 4\mu^2)$. Also, the rotational mass matrix $\mathbf{M}_b^r$ is given by

$$\mathbf{M}_b^r = \mathbf{M}_{b0}^r + \emptyset\mathbf{M}_{b1}^r + \emptyset^2\mathbf{M}_{b2}^r \tag{2.15}$$

where symmetric translational mass matrices $\mathbf{M}_{b0}^{t}$, $\mathbf{M}_{b1}^{t}$, $\mathbf{M}_{b2}^{t}$ and rotational mass matrices $\mathbf{M}_{b0}^{r}$, $\mathbf{M}_{b1}^{r}$, $\mathbf{M}_{b2}^{r}$ are stated in the Appendix C.

Core/disk mass matrices $\mathbf{M}_C$ and $\mathbf{M}_D$ have the same dimensions as $\mathbf{M}_B$, with a single element of core/disk added according to located node shown in Figure 2.6.

Single element motion mass matrices of cores, may be obtained:

$$\mathbf{M}_C^t = \begin{bmatrix} \mathbf{M}_c^t & \mathbf{0} \\ \mathbf{0} & \mathbf{0} \end{bmatrix}, \mathbf{M}_C^r = \begin{bmatrix} \mathbf{0} & \mathbf{0} \\ \mathbf{0} & \mathbf{M}_c^r \end{bmatrix} \tag{2.16}$$

where $\mathbf{M}_c^t = \begin{bmatrix} m_c & 0 \\ 0 & m_c \end{bmatrix}$ is the translational mass in *x*/*y* coordinates, $\mathbf{M}_c^r = \begin{bmatrix} I_c^a & 0 \\ 0 & I_c^a \end{bmatrix}$ is the rotational mass according to axis, and approximation $I_c^a \approx I_c^p/2$. $\mathbf{M}_D$ may be obtained with the same method by different element physical parameters.

Gyroscopic Matrix

The gyroscopic matrix for the complete rotor is expressed as

$$\mathbf{G}_R = \mathbf{G}_B + \mathbf{G}_C + \mathbf{G}_D \tag{2.17}$$

where $\mathbf{G}_B$, $\mathbf{G}_C$, $\mathbf{G}_D$ are gyroscopic matrices of free-free rotor cores and disks with superposing element solutions $\mathbf{G}_b$, $\mathbf{G}_c$ and $\mathbf{G}_d$.

The gyroscopic matrix for a single beam element with four degrees of freedom at each station is given by

$$\mathbf{G}_b = \mathbf{G}_{b0} + \emptyset\mathbf{G}_{b1} + \emptyset^2\mathbf{G}_{b2} \tag{2.18}$$

where $\mathbf{G}_{b0}$, $\mathbf{G}_{b1}$, $\mathbf{G}_{b2}$ are skew symmetric matrices as stated in the Appendix C.

And, gyroscopic element matrices $\mathbf{G}_c$ and $\mathbf{G}_d$ for cores and disks are given by

$$\mathbf{G}_c = \begin{bmatrix} 0 & -I_c^p \\ I_c^p & 0 \end{bmatrix}, \mathbf{G}_d = \begin{bmatrix} 0 & -I_d^p \\ I_d^p & 0 \end{bmatrix} \tag{2.19}$$

Stiffness Matrix

By assuming that cores/disks do not affect the shaft stiffness, the stiffness matrix $\mathbf{K}_R$ is obtained by superposing Timenshenko beam element $\mathbf{K}_b$ only. $\mathbf{K}_b$ is given by

$$\mathbf{K}_b = \mathbf{K}_{b0} + \emptyset\mathbf{K}_{b1} \tag{2.20}$$

where $\mathbf{K}_{b0}$, $\mathbf{K}_{b1}$ are symmetric matrices and shown in the Appendix C.

2.2 Rotor/AMB System

An AMB system is inherently unstable due to negative stiffness, if uncontrolled. Integral action can levitate a rotor, and compensate gravity. Closed loop PD control action is generally to stabilize a free-free rotor.

2.2.1 Rotor/AMB System State-Space Formulation

Rotor

Based on the FEM shown in equations (2.12)-(2.20), the dynamic motion of a free-free rotor may be formed in state-space as

$$\mathbf{P}_R: \begin{cases} \dot{\mathbf{q}}_R(t) = \mathbf{A}_R\mathbf{q}_R(t) + \mathbf{B}_R\mathbf{u}_R(t) \\ \mathbf{y}_R(t) = \mathbf{C}_R\mathbf{q}_R(t) + \mathbf{D}_R\mathbf{u}_R(t) \end{cases} \tag{2.21}$$

where $\mathbf{q}_R = \begin{bmatrix} \mathbf{s}_R \\ \dot{\mathbf{s}}_R \end{bmatrix}$ is state vector, $\mathbf{u}_R$, $\mathbf{y}_R$ are input and output states, respectively $\mathbf{C}_R = \mathbf{I}$ and $\mathbf{D}_R = \mathbf{0}$. Based on the dynamic equation

$$\ddot{\mathbf{s}}_R = \mathbf{M}_R^{-1}(\mathbf{f}_R - \mathbf{B}_R\dot{\mathbf{q}}_R - \mathbf{K}_R\mathbf{q}_R) \tag{2.22}$$

system matrices $\mathbf{A}_R$, $\mathbf{B}_R$ are obtained accordingly:

$$\begin{bmatrix} \dot{\mathbf{s}}_R \\ \ddot{\mathbf{s}}_R \end{bmatrix} = \begin{bmatrix} \mathbf{0} & \mathbf{I} \\ -\mathbf{M}_R^{-1}\mathbf{K}_R & -\mathbf{M}_R^{-1}\Omega\mathbf{G}_R \end{bmatrix} \begin{bmatrix} \mathbf{s}_R \\ \dot{\mathbf{s}}_R \end{bmatrix} + \begin{bmatrix} \mathbf{0} \\ \mathbf{M}_R^{-1} \end{bmatrix} \mathbf{f}_R \tag{2.23}$$

Hence a full order free-free rotor model is obtained. It has 120 states and each node has 8 states $\mathbf{q}_{Ri} = \begin{bmatrix} \mathbf{s}_{Ri} \\ \dot{\mathbf{s}}_{Ri} \end{bmatrix}$ over 15 nodes.

PD Control

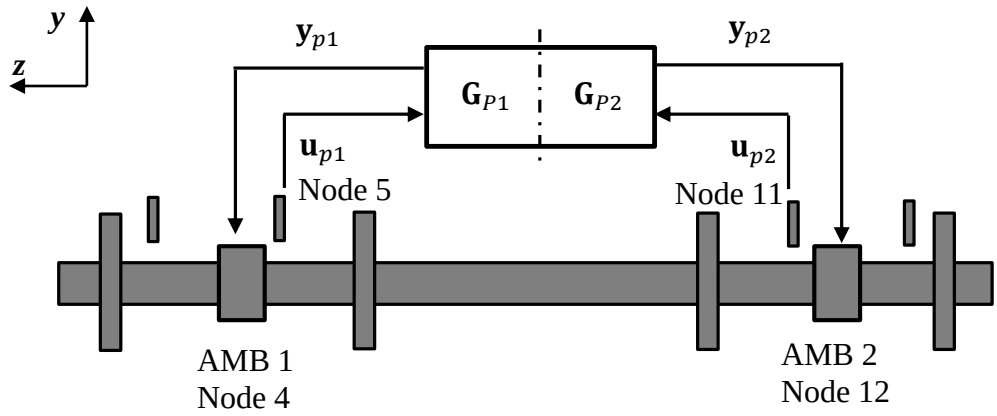

Figure 2.7 Sensor/actuation planes for PD control

As gravity acting on rotor may be compensated by integral action, only proportional derivative action is taken into account in the basic plant for controller design. Sensors/actuation planes are shown in Figure 2.7.

In the test rig, the rotor is controlled by two PID driven AMBs, each with the same PID parameter settings. Considering the simplified linear AMB model based on equation (2.11), for one control axis, the linearized force in *x*-direction at node 4 (AMB 1 location in FEM) is given by

$$f_{x4} = k_i i_{x4} + k_s s_4^x \tag{2.24}$$

The AMB 1 PD controlled current is

$$i_{x4} = -\left(k_P + k_D \frac{s}{1+\tau s}\right) s_5^x \tag{2.25}$$

where $1/\tau$ is the derivative cut-off frequency and s is Laplace transform variable. Hence, in the *x*-direction, PD control action is implemented as

$$f_{x4} = -k_i \left(k_P + k_D \frac{s}{1+\tau s}\right) s_5^x + k_s s_4^x \tag{2.26}$$

where s_4^x and s_5^x are the displacements of the rotor at nodes 4 and 5, respectively.

With a similar expression applied to the *y*-direction, it is appropriate to have the transfer function in MIMO (multi-input/output form) for PD controlled AMBs as

$$\begin{bmatrix}\mathbf{y}_{p1}\\ \mathbf{y}_{p2}\end{bmatrix} = \mathbf{G}_P(s)\begin{bmatrix}\mathbf{u}_{p1}\\ \mathbf{u}_{p2}\end{bmatrix} \tag{2.27}$$

where $\mathbf{u}_{p1} = [r_5^x \quad r_4^x]^T, \mathbf{u}_{p2} = [r_{11}^x \quad r_{12}^x]^T$, $\mathbf{y}_{p1} = [f_{x4} \quad f_{y4}]^T, \mathbf{y}_{p2} = [f_{x12} \quad f_{y12}]^T$ and $\mathbf{G}_P(s) = \begin{bmatrix}\mathbf{G}_{P1}(s) & \mathbf{0}\\ \mathbf{0} & \mathbf{G}_{P2}(s)\end{bmatrix}$ with

$$\mathbf{G}_{P1}(s) = \mathbf{G}_{P2}(s) = \begin{bmatrix} -k_i\left(k_P + k_D\frac{s}{1+\tau s}\right) & 0 & k_s & 0\\ 0 & -k_i\left(k_P + k_D\frac{s}{1+\tau s}\right) & 0 & k_s\end{bmatrix}$$

With control output $\mathbf{y}_p = \begin{bmatrix}\mathbf{y}_{p1}^T & \mathbf{y}_{p2}^T\end{bmatrix}^T$, input $\mathbf{u}_p = \begin{bmatrix}\mathbf{u}_{p1}^T & \mathbf{u}_{p2}^T\end{bmatrix}^T$, and MIMO transfer function $\mathbf{G}_P(s)$, the linear simplified AMBs under PD control may be formed in state-space as

$$\mathbf{P}_p: \begin{cases}\dot{\mathbf{q}}_p = \mathbf{A}_p\mathbf{q}_p + \mathbf{B}_p\mathbf{u}_p\\ \mathbf{y}_p = \mathbf{C}_p\mathbf{q}_p + \mathbf{D}_p\mathbf{u}_p\end{cases} \tag{2.28}$$

where $\mathbf{q}_p$ is a 4×1 vector contains four PD control states, $\mathbf{u}_p$ is a 8×1 vector including sensor feedback and displacement at AMB actuation node and $\mathbf{y}_p$ is a 4×1 control force output vector. $\mathbf{A}_p$ is a 4×4 system matrix. $\mathbf{B}_p$ is a 4×8 input matrix, $\mathbf{C}_p$ is a 4×4 matrix for output, and $\mathbf{D}_p = \mathbf{0}$.

Rotor under Actuation from PD controlled AMBs

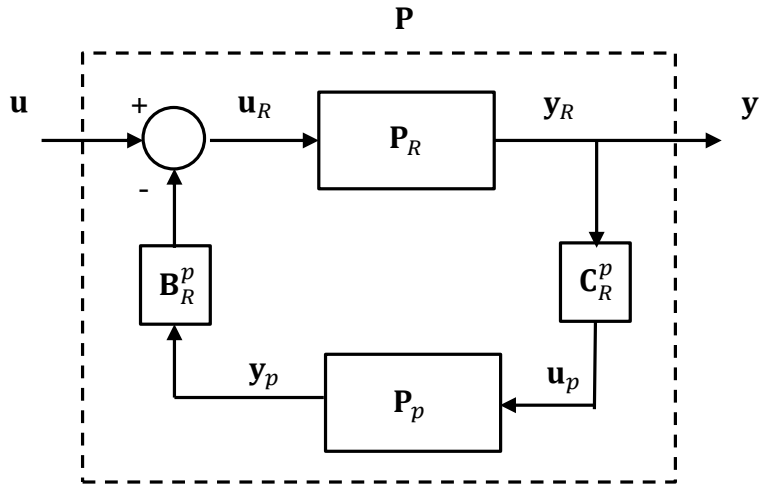

Figure 2.8 Block diagram for PD controlled rotor/AMB model

A Block diagram to stabilize a free-free rotor by PD controlled AMBs is shown in Figure 2.8. Based on the state-space forms, equation (2.21) and (2.28), dynamic motion of the free-free rotor under PD control is given by

$$\begin{aligned}\dot{\mathbf{q}}_R &= \mathbf{A}_R\mathbf{q}_R + \mathbf{B}_R\mathbf{u} - \mathbf{B}_R^p\mathbf{f}_p \\ \dot{\mathbf{q}}_p &= \mathbf{A}_p\mathbf{q}_p + \mathbf{B}_p\mathbf{C}_R^p\mathbf{q}_R\end{aligned} \tag{2.29}$$

where $\mathbf{f}_p = \mathbf{y}_p$ is the PD controlled AMB force, and $\mathbf{B}_R^p$ is a 120×4 matrix for specification of actuation locations, and $\mathbf{C}_R^p$ is a 8×120 matrix indicating the locations of sensor and AMB nodes. By inserting $\mathbf{y}_p = \mathbf{C}_p\mathbf{q}_p$, $\mathbf{y}_R^p = \mathbf{C}_R^p\mathbf{q}_R$

$$\begin{bmatrix}\dot{\mathbf{q}}_R \\ \dot{\mathbf{q}}_p\end{bmatrix} = \begin{bmatrix}\mathbf{A}_R & -\mathbf{B}_R^p\mathbf{C}_p \\ \mathbf{B}_p\mathbf{C}_R^p & \mathbf{A}_p\end{bmatrix}\begin{bmatrix}\mathbf{q}_R \\ \mathbf{q}_p\end{bmatrix} + \begin{bmatrix}\mathbf{B}_R \\ \mathbf{0}\end{bmatrix}\mathbf{u}_R \tag{2.30}$$

Therefore, rotor/AMB dynamics $\mathbf{P}(s)$ may be described as state-space form:

$$\mathbf{P}(s): \begin{cases}\dot{\mathbf{q}} = \mathbf{A}\mathbf{q} + \mathbf{B}\mathbf{u} \\ \mathbf{y} = \mathbf{C}\mathbf{q} + \mathbf{D}\mathbf{u}\end{cases} \tag{2.31}$$

where system states $\mathbf{q} = \begin{bmatrix}\mathbf{q}_R \\ \mathbf{q}_p\end{bmatrix}$, $\mathbf{u}$ is the external forcing. $\mathbf{A} = \begin{bmatrix}\mathbf{A}_R & -\mathbf{B}_R^p\mathbf{C}_p \\ \mathbf{B}_p\mathbf{C}_R^p & \mathbf{A}_p\end{bmatrix}$, $\mathbf{B} = \begin{bmatrix}\mathbf{B}_R \\ \mathbf{0}\end{bmatrix}$, $\mathbf{C}_{R,p}$ is the output matrix, and $\mathbf{D} = \mathbf{0}$.

2.2.2 Rotor/AMB System Forcing Response

In controlled rotor/AMB system operation, the external forcing components include unbalance, which is induced by an eccentric mass distribution. However, contact may occur between the rotor and TDB, if rotor motion orbits exceed the TDB clearance. In order to have well-controlled rotor motion, these two typical external forces are considered in the system modelling.

Unbalance Forcing

The unbalance force at a single node may be expressed as

$$F_{Bxi} + jF_{Byi} = m_e\Omega^2 e^{j\varphi_i} \tag{2.32}$$

where $m_e = m_d l_d$ is the mass eccentricity, Ω is the rotational speed, and $\varphi_i = \Omega t + \emptyset_i$ The unbalance forcing components in *x*/*y* coordinates may be expanded to

$$F_{Bxi} + jF_{Byi} = m_e\Omega^2(cos(\Omega t + \emptyset_i) + j\, sin(\Omega t + \emptyset_i)) \tag{2.33}$$

By assuming no torsional deformation stated in FEM, unbalance force vector produced by one disk is given by

$$\boldsymbol{f}_{Bi} = \begin{bmatrix} F_{Bxi} \\ F_{Byi} \\ 0 \\ 0 \end{bmatrix} = m_{ei}\Omega^2 \begin{bmatrix} cos(\Omega t + \emptyset_i) \\ sin(\Omega t + \emptyset_i) \\ 0 \\ 0 \end{bmatrix} \tag{2.34}$$

Rotor/TDB Contact Forcing

A rotor/AMB system and displacement sensors can be protected by TDBs, if the rotor experiences significant orbits. Also, TDBs can support a heavy rotor when power is switched off. TDBs may experience large contact forces, which may cause

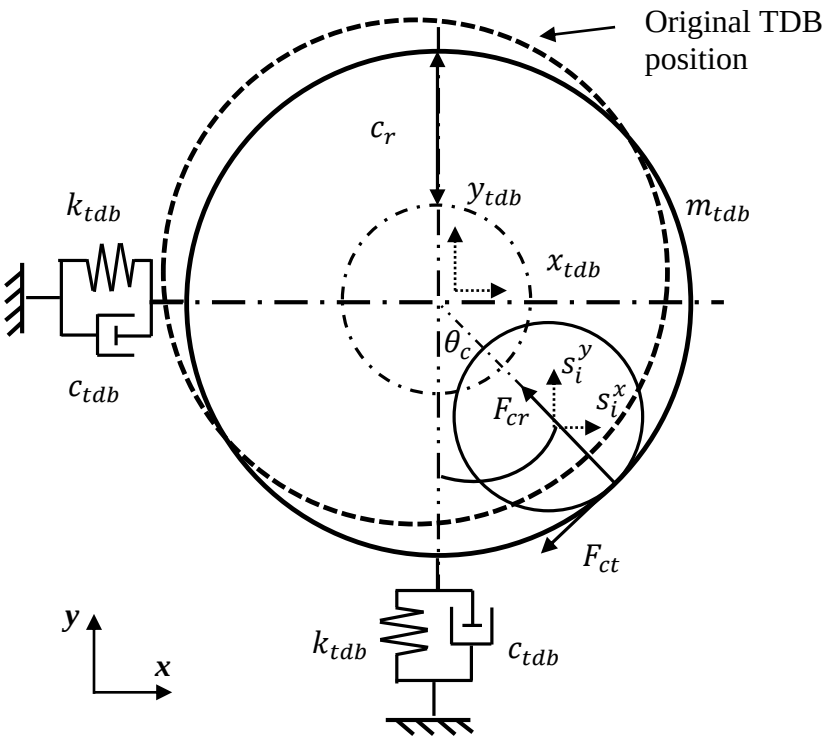

Figure 2.9 Schematic showing contact between a rotor and TDB

significant housing movement. In the first instance, contact dynamics are considered for a fixed housing. Figure 2.9 shows a contact event occurred between rotor and touchdown bearing in absolute coordinates.

Keogh and Cole [20] modelled rotor/TDB contact dynamics, with a resiliently amounted TDB and local distortion over a Hertzian contact zone with a flexible rotor. Contact happens, when the relative displacement reaches radial clearance c_r. Therefore, contact conditions apply whenever

$$s_d^c = \sqrt{(s_i^x - x_{tdb})^2 + (s_i^y - y_{tdb})^2} \geq c_r \tag{2.35}$$

for rotor displacement (s_i^x, s_i^y) at a TDB location. Generally, the amplitude of the radial contact force F_{cr} is determined by the penetration $\delta = s_d^c - c_r$ during contact. Under Hertzian contact stresses, δ is given by the implicit equation

$$\delta = \frac{2F_{cr}(1-\nu)}{\pi E_b l_{tdb}}\left(\frac{2}{3} + ln\frac{8E_b c_r l_{tdb}}{2.15^2 F_{cr}}\right) \tag{2.36}$$

where ν is the Poisson's ratio, and l_{tdb} is the circumferential length of contact zone on TDB.

The contact angle is defined by

$$\theta_c = \tan^{-1}((s_i^x - x_{tdb}), (s_i^y - y_{tdb})) \tag{2.37}$$

The relative velocity during contact is given by

$$v_c = R_s\Omega - (\dot{s}_i^x - \dot{x}_{tdb})\, sin\,\theta_c + (\dot{s}_i^y - \dot{y}_{tdb})\, cos\,\theta_c \tag{2.38}$$

With the assumption of dry friction, the tangential contact force is obtained as

$$F_{ct} = \mu F_{cr} sgn(v_c) \tag{2.39}$$

Hence the contact force vector at node *i* is given by

$$\mathbf{f}_{ci} = \begin{bmatrix} F_{cxi} \\ F_{cyi} \\ 0 \\ 0 \end{bmatrix} = \begin{bmatrix} \mathbf{G}_{\theta i} \\ \mathbf{0} \end{bmatrix} \begin{bmatrix} F_{cri} \\ F_{cti} \end{bmatrix} \tag{2.40}$$

where $\mathbf{G}_\theta = \begin{bmatrix} \cos\theta_{ci} & -\sin\theta_{ci} \\ \sin\theta_{ci} & \cos\theta_{ci} \end{bmatrix}$. If the contact forces acting on node positions as discretized in a FEM flexible rotor model, dynamics motion of an unbalanced rotor/AMB system under contact may be obtained as

$$\dot{\mathbf{q}} = \mathbf{A}\mathbf{q} + \mathbf{B}_u\mathbf{u}_u + \mathbf{B}_c\mathbf{u}_c \tag{2.41}$$

where $\mathbf{B}_u$ $\mathbf{B}_c$ are the location matrices for unbalance force and contact force; $\mathbf{u}_u = [\mathbf{f}_{B1}^T \quad ... \quad \mathbf{f}_{BM}^T]^T$ and $\mathbf{u}_c = [\mathbf{f}_{c1}^T, \quad ... \quad \mathbf{f}_{cN}^T]^T$.

2.2.3 Rotor/AMB System Frequency Response

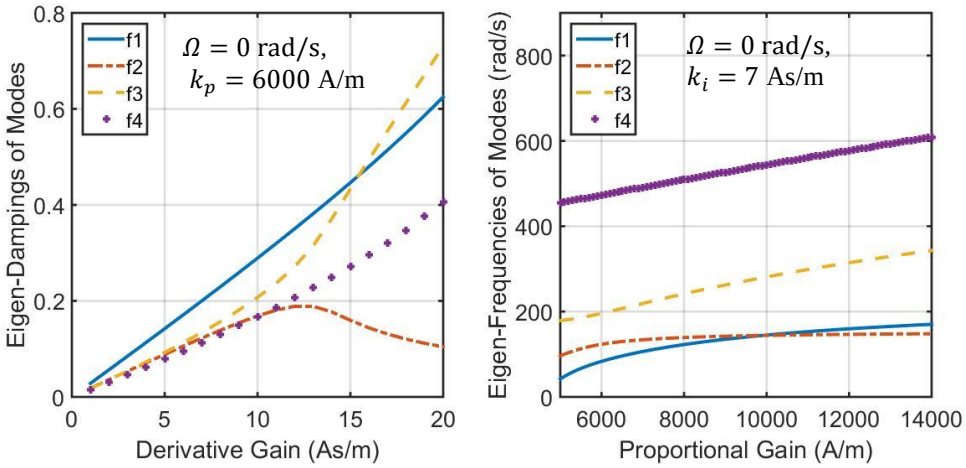

Figure 2.10 Rotor eigen-dampings/frequencies for a rotor/AMB system by PD control action

PD control can stabilize a rotor/AMB system, and also influence rotor eigen-dampings and modal frequencies. Figure 2.10 shows the relationship between rotor first four modes eigen-dampings/frequencies and PID gains for the test system. Without rotation, the derivative gain, k_D, may increase modal damping. As an external stiffness action, the proportional gain, k_p, can influence modal frequencies.

For H_∞ control optimization for dynamic system formed in state-space [50], maximum singular values of a plant may be usefully defined from frequency domain formulation, $\mathbf{P}(s)$. Under PD control, by inserting $s = j\omega$, the system H_∞ norm

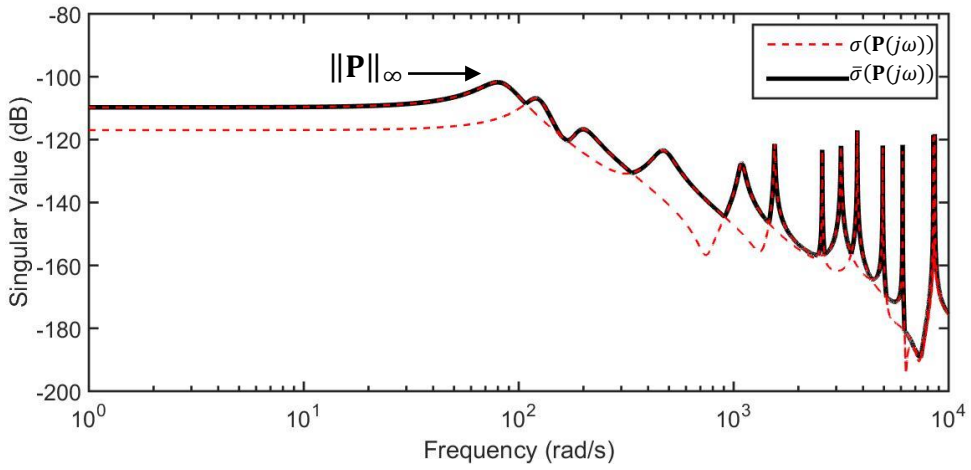

Figure 2.11 $\|\mathbf{P}\|_\infty$ and $\bar{\sigma}(\mathbf{P}(s))$

$\|\mathbf{P}\|_\infty$ may be obtained by the maximum amplitude response of a MIMO rotor/AMB system as following

$$\|\mathbf{P}\|_\infty = \sup_{-\infty<\omega<\infty} \bar{\sigma}(\mathbf{P}(j\omega)) \tag{2.42}$$

Figure 2.11 shows the $\|\mathbf{P}\|_\infty$ and the singular values of rotor/AMB system $\mathbf{P}(s)$. And Table 2.3 lists the eigen-dampings/frequencies the rotor controlled by PD action and the resonance frequency measured in an experiment. It demonstrated that, the mathematical rotor/AMB model in equation (2.31) having sufficient accuracy in operating range.

Table 2.3 Rotor eigen-dampings/frequencies in contrast to an experimental measurement

Modes		Eigen-Frequencies (rad/s)	Expermental Resonance (rad/s)	Eigen-Dampings
Cylindrical	f_1	83.3	87	$\xi_1 = 0.20$
Conical	f_2	123.4	135	$\xi_2 = 0.12$
Flexible 1_{st}	f_3	195.7	210	$\xi_3 = 0.13$
Flexible 2_{nd}	f_4	472.9	460	$\xi_4 = 0.11$

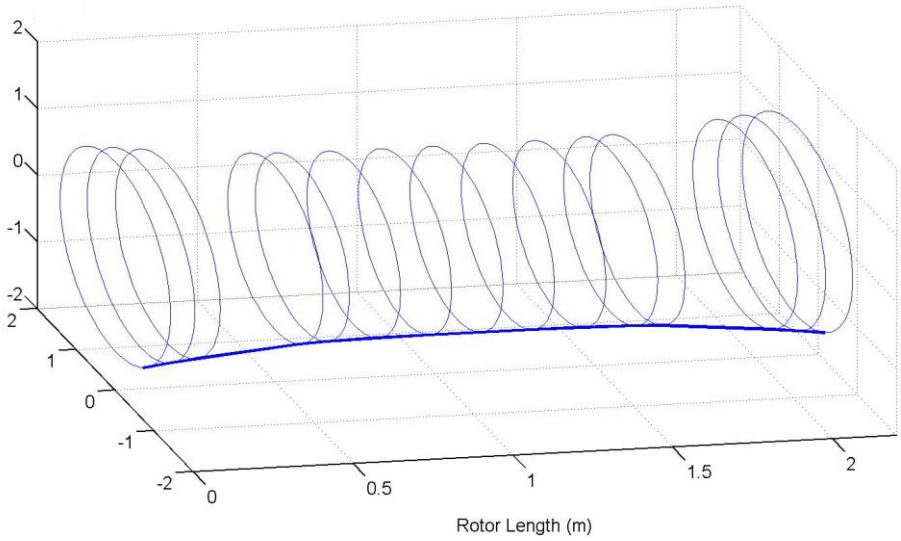

(a) Cylindrical

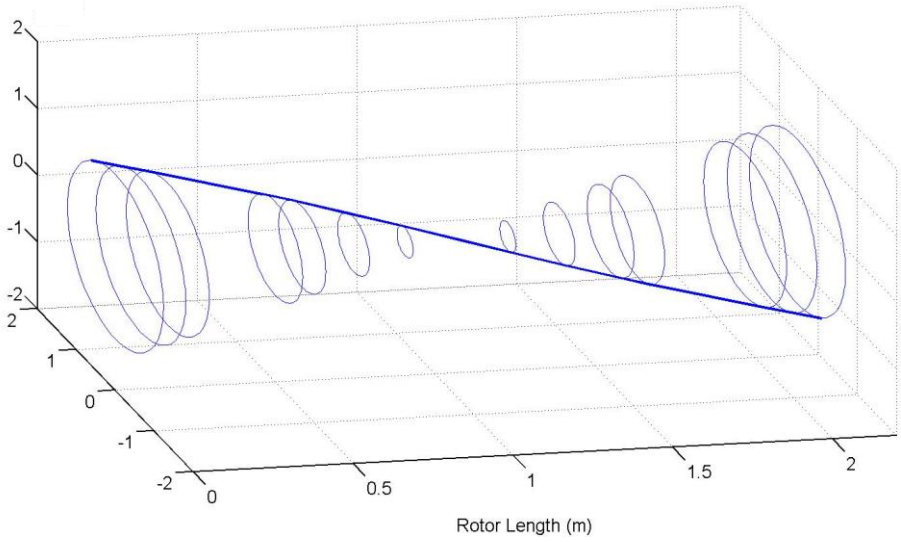

(b) Conical

Figure 2.12 Rotor modes under PD control dominated by rigid body motions

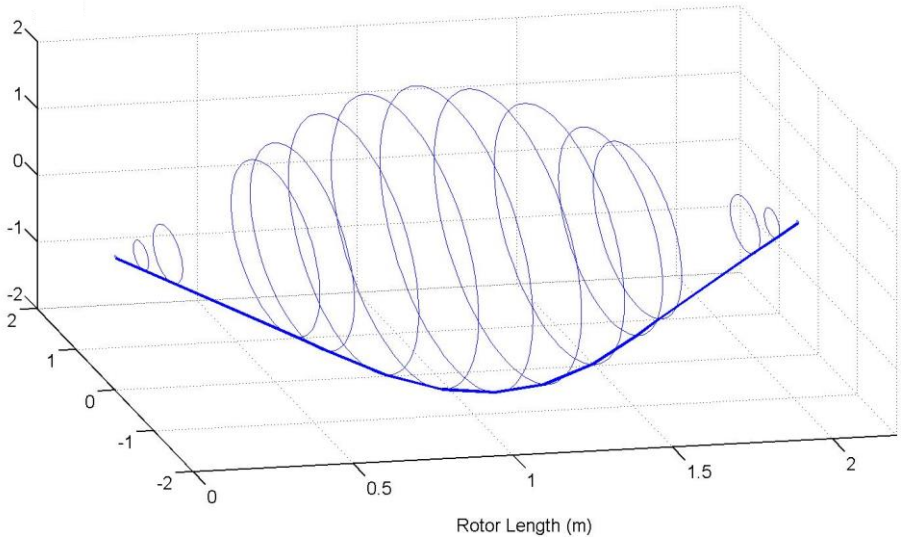

(a) Flexible 1_{st}

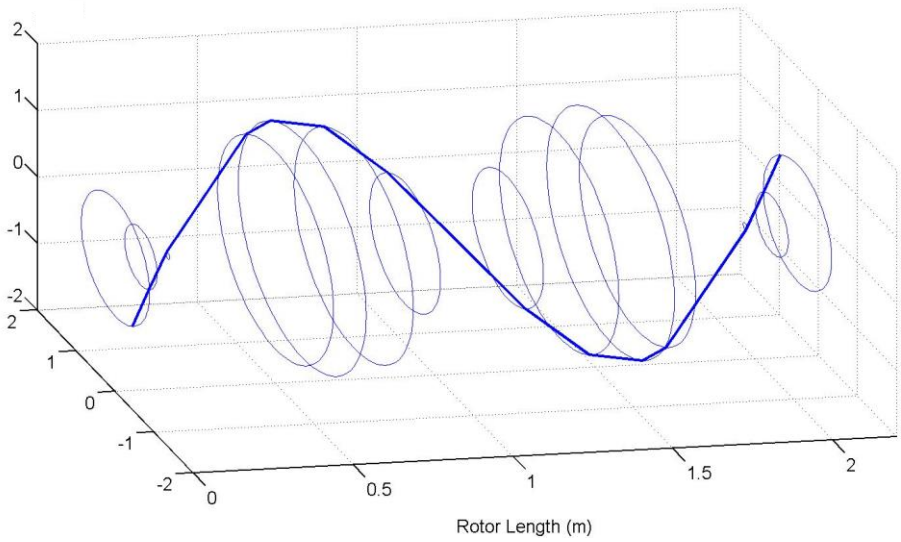

(b) Flexible 2_{nd}

Figure 2.13 Rotor modes under PD control dominated by first two bending motions

Gyroscopic effects

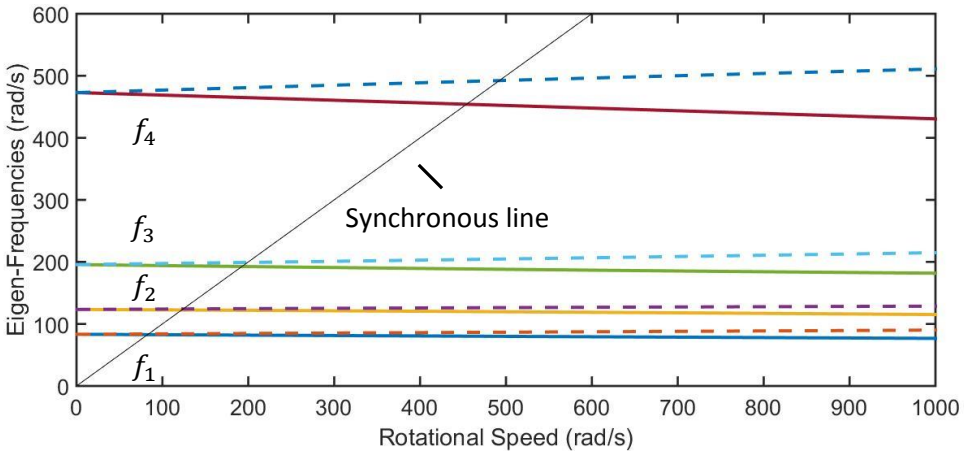

(a) Eigen-frequencies varied with the rotational speed

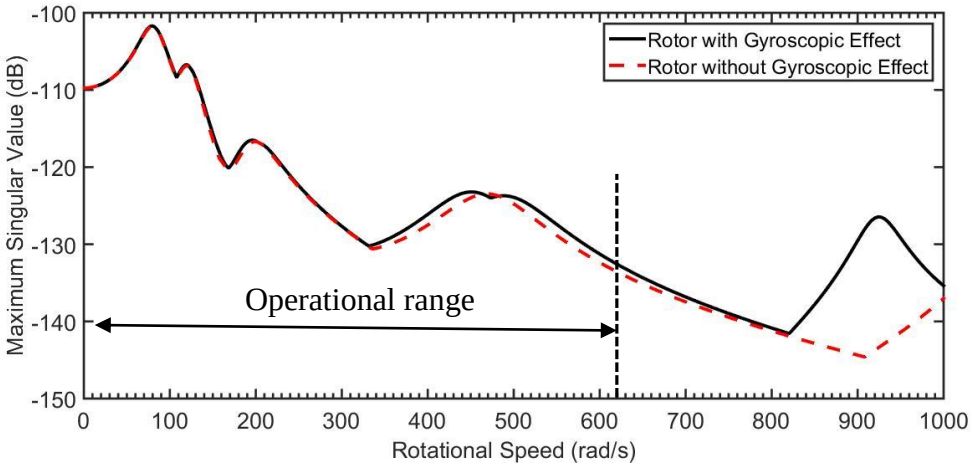

(b) Synchronous frequency response

Figure 2.14 Gyroscopic effects with rotational speed

Rotor eigen-frequencies split along with rotational speeds due to gyroscopic effects, as shown in Figure 2.14 (a). High order bending modes changes significantly with high running speed, as demonstrated in the synchronous frequency response of rotor modelled with/without gyroscopic effects in Figure 2.14 (b).

2.3 Base Modelling

When contact happens, contact forces will also react on a TDB, which could induce base motion of the rotor support structure. Such interaction between rotor and

moving base may effect sensors readings, AMB force, and AMB control. In order to expand the basic plant model, base motion is now considered.

2.3.1 Parameter Estimation

Base parameters need to be evaluated, such as base translational mass, and rotational inertias (yaw, pitch and roll). Those may be estimated by using Solid Edge according to rig drawings. Table 2.4 shows the details of each part. Assembling the all the parts with measured positions, Figure 2.15 shows base model in Solid Edge. A physical properties report issued by the Solid Edge analysis, was used for the base modelling. Table 2.5 shows the parameters for the estimated base model.

Table 2.4 Parts Parameters

Part	Mass (kg)	Quantity
AMB and Housing	75.39	2
Sensor Carrier	14.65	4
TDB Housing	12.97	2
Base Plate	97.95	3
Base Frame	177.90	1
Motor	95	1
Base Isolator	10	4
TDB Carrier (Motor end)	19.45	1

Table 2.5 Physical properties report from Solid Edge

Mass (kg)	867.09
Principal Moments of Inertia (kg· m^2)	
I_x	725.30
I_y	709.87
I_z	54.99
Radii of Gyration (m)	
K_x	0.91
K_y	0.90
K_z	0.25

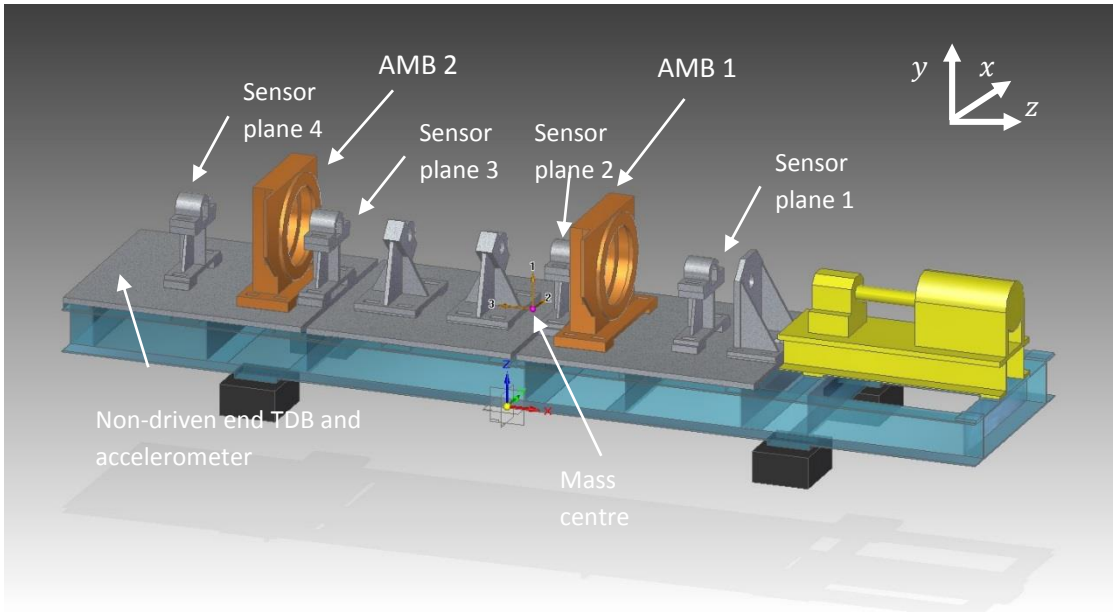

Figure 2.15 Solid Edge base model with all parts included

The distances of sensors, actuation and TDB planes from mass centre are shown in Table 2.6.

Table 2.6 Distance away from mass centre

Location	d_x (mm)	d_y(mm)
Accelerometer	1366.6	1366.6
AMB1	260.4	260.4
AMB2	874.6	874.6
TDB 1	141.6	141.6
TDB 2	472.6	472.6
Sensor plane 1	602.4	602.4
Sensor plane 2	123.4	123.4
Sensor plane 3	737.6	737.6
Sensor plane 4	1216.6	1216.6
Isolators Pair 1	850	850
Isolators Pair 2	1050	1050

2.3.2 Dynamic Rigid Body Base Motion

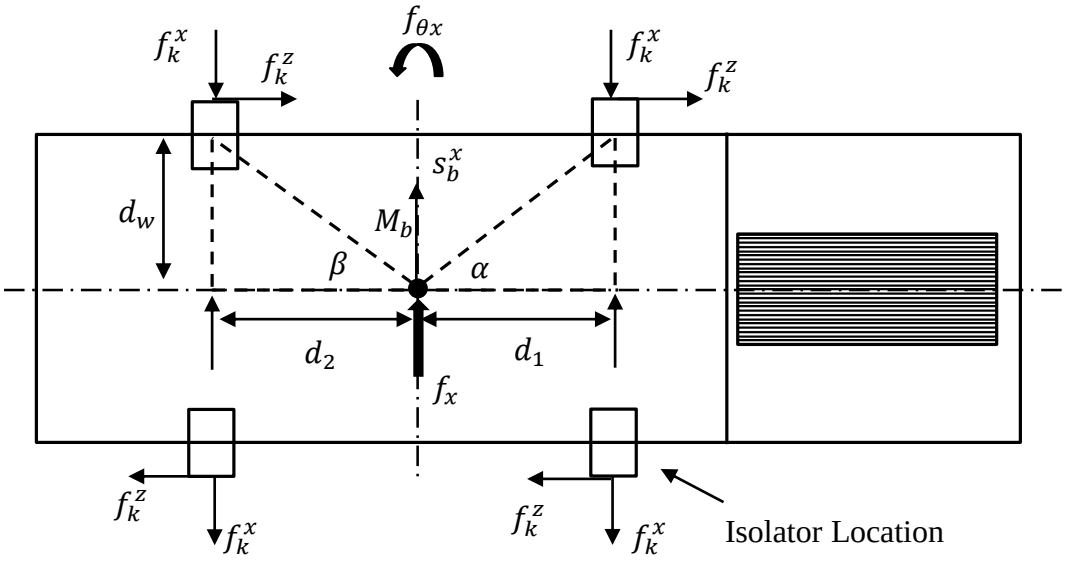

Figure 2.16 Rigid base motion in *x* axis/rotating frame yawing

Ignoring deformation of the base, a rigid body model was developed. As the test rig does not have axial motion when rotating, the rigid body base may be modelled as a 4 degree of freedom system with translational/rotational motion (yaw and pitch). Figure 2.16 shows the schematic figure representing base motion in one axis (s_b^x, θ_x) as an example.

The dynamic stiffnesses of the base isolators have the form:

$$\begin{aligned} k_x &= {\omega_{nx}}^2(M_b + M_r)/4 \\ k_y &= {\omega_{ny}}^2(M_b + M_r)/4 \end{aligned} \tag{2.43}$$

where $\omega_{nx} = 25\ \mathrm{rad/s}$ and $\omega_{ny} = 96\ \mathrm{rad/s}$ are the translational natural frequencies in *x*/*y* coordinates from an experimental measurement in [20]. Here base mass $M_b = 867\ \mathrm{kg}$, rotor mass $M_r = 100\ \mathrm{kg}$, $k_x = 1.5 \times 10^5$ N/m, and $k_y = 2.25 \times 10^5$ N/m. due to the isolating rubber aligned 45 deg to vertical, the stiffness k_y has sheer effect on rotational motion in *x* coordinates as $k_z = k_y$.

The equations for translational motion are

$$M_b\ddot{s}_b^x + 4c_b\dot{s}_b^x + 2c_b(d_2 - d_1)\dot{\theta}_x + 4k_x s_b^x + 2k_x(d_2 - d_1)\theta_x = f_x \tag{2.44}$$

where d_1, d_2 are the distances of isolator from base mass centre as shown in Table 2.6, damping $c_b = 5000$ Ns/m. According to equation (2.44), base translational motion in *y* coordinate may be expressed

$$M_b\ddot{s}_b^y + 4c_b\dot{s}_b^y + 2c_b(d_2 - d_1)\dot{\theta}_y + 4k_z s_b^y + 2k_y(d_2 - d_1)\theta_y = f_y \tag{2.45}$$

By including isolator stiffness, the equation for base yaw is

$$I_x\ddot{\theta}_x + 2c_b(d_2 - d_1)\dot{s}_b^x + 2c_b({d_1}^2 + {d_2}^2)\,\dot{\theta}_x + 2k_x(d_2 - d_1)s_b^x + (2k_x({d_1}^2 + {d_2}^2) + 4k_z{d_w}^2)\,\theta_x = f_{\theta x} \tag{2.46}$$

where $d_w = 0.34$ m is the distance from isolators to mass centre as shown in Figure 2.13. And equation for inertias in *y* coordinate may be expressed

$$I_y\ddot{\theta}_y + 2c_b(d_2 - d_1)\dot{s}_b^y + 2c_b({d_1}^2 + {d_2}^2)\,\dot{\theta}_y + 2k_y(d_2 - d_1)s_b^y + 2k_y({d_1}^2 + {d_2}^2)\theta_y = f_{\theta y} \tag{2.47}$$

Based on equations (2.44)-(2.47), the 4-degree of freedom base model may be expressed as state-space form as

$$\mathbf{P}_b: \begin{cases} \dot{\mathbf{q}}_b = \mathbf{A}_b\mathbf{q}_b + \mathbf{B}_b\mathbf{u}_b \\ \mathbf{y}_b = \mathbf{C}_b\mathbf{q}_b + \mathbf{D}_b\mathbf{u}_b \end{cases} \tag{2.48}$$

where, $\mathbf{s}_b = \left[s_b^x, s_b^y, \theta_x, \theta_y\right]^T$, $\mathbf{q}_b = \begin{bmatrix}\mathbf{s}_b \\ \dot{\mathbf{s}}_b\end{bmatrix}$, $\mathbf{u}_b = \left[f_x, f_y, f_{\theta x}, f_{\theta y}\right]^T$, $\mathbf{A}_b = \begin{bmatrix}\mathbf{0} & \mathbf{I} \\ -{\mathbf{M}_b}^{-1}\mathbf{K}_b & -{\mathbf{M}_b}^{-1}\mathbf{G}_b\end{bmatrix}$, $\mathbf{B}_b = \begin{bmatrix}\mathbf{0} \\ {\mathbf{M}_b}^{-1}\end{bmatrix}$, $\mathbf{C}_b = \mathbf{I}_{4\times4}$ and $\mathbf{D}_b = \mathbf{0}$. The base mass matrix $\mathbf{M}_b$, stiffness matrix $\mathbf{K}_b$ and damping matrix $\mathbf{G}_b$ are shown in Appendix. C.

Multi-Input/Output Transformation

Based on rigid body motion in equation (2.48), the displacement of each part mounted on the base can be obtained, through the transformation matrices shown in

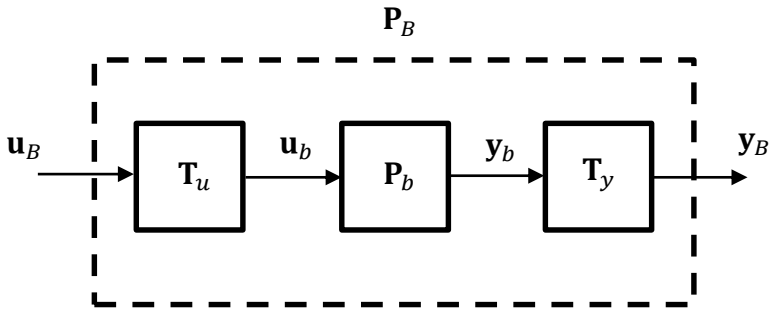

Figure 2.17 Block diagram for the base system

Figure 2.17. Here, $\mathbf{T}_u$ and $\mathbf{T}_y$ are the input/output transformation matrices specify the distance of parts away from base mass centre. A multi-input/output base model based on each sensors, actuations and contact plane may be written as

$$\mathbf{P}_B \coloneqq \begin{cases} \dot{\mathbf{q}}_B = \mathbf{A}_B\mathbf{q}_B + \mathbf{B}_B\mathbf{u}_B \\ \mathbf{y}_B = \mathbf{C}_B\mathbf{q}_B + \mathbf{D}_B\mathbf{u}_B \end{cases} \tag{2.49}$$

where $\mathbf{q}_B = \mathbf{q}_b$, $\mathbf{u}_B = \left[f_{accx}\,, f_{accy}\,, \dots\,, f_{tdb2x}\,, f_{tdb2y}\,\right]^T$ is the forcing vector, $\mathbf{y}_B = \left[s^x_{B,acc}\,, s^y_{B,acc}\,, \dots, s^x_{sen4,acc}\,, s^y_{sen4,acc}\right]^T$ is the displacement vector for each parts mounted on base, $\mathbf{A}_B = \mathbf{A}_b$, $\mathbf{B}_B = \mathbf{B}_b\mathbf{T}_u$, $\mathbf{C}_B = \mathbf{T}_y\mathbf{C}_b$ and $\mathbf{D}_B = \mathbf{T}_y\mathbf{D}_b\mathbf{T}_u = \mathbf{0}$. Based on data in Table 2.6, the input transformation matrix $\mathbf{T}_u$ is given by

$$\mathbf{T}_u = \begin{bmatrix} \mathbf{T}_{u,1} & \dots & \mathbf{T}_{u,n} \\ \mathbf{R}_{u,1} & \dots & \mathbf{R}_{u,n} \end{bmatrix} \tag{2.50}$$

where $\mathbf{T}_{u,i} = \begin{bmatrix} 1 & 0 \\ 0 & 1 \end{bmatrix}$, $\mathbf{R}_{u,i} = \begin{bmatrix} d_{xi} & 0 \\ 0 & d_{yi} \end{bmatrix}$.

The output transformation matrix $\mathbf{T}_y$ is may be obtained

$$\mathbf{T}_y = \begin{bmatrix} \mathbf{T}_{y-} \\ \mathbf{T}_{y+} \end{bmatrix} \tag{2.51}$$

where $\mathbf{T}_{y-} = \begin{bmatrix} \mathbf{T}_{y1} & -\mathbf{R}_{y1} \\ \vdots & \vdots \\ \mathbf{T}_{yn} & -\mathbf{R}_{yn} \end{bmatrix}$ and $\mathbf{T}_{y+} = \begin{bmatrix} \mathbf{T}_{y1} & \mathbf{R}_{y1} \\ \vdots & \vdots \\ \mathbf{T}_{yn} & \mathbf{R}_{yn} \end{bmatrix}$ $\mathbf{T}_{yi} = \begin{bmatrix} 1 & 0 \\ 0 & 1 \end{bmatrix}$,

$\mathbf{R}_{yi} = \begin{bmatrix} d_{xi} & 0 \\ 0 & d_{yi} \end{bmatrix}$.

Base Model Frequency Response

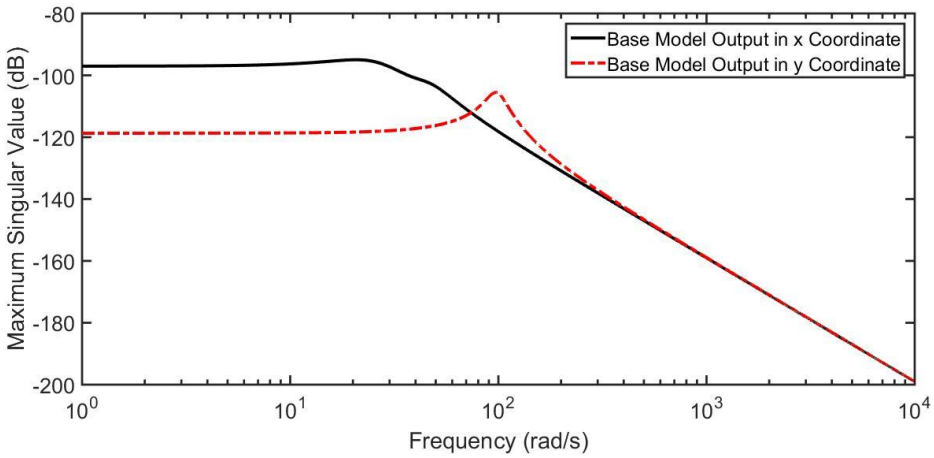

Figure 2.18 $\bar{\sigma}(\mathbf{P}_B(s))$ in *x*/*y* coordinates

Due to different dynamic stiffnesses in equation (2.43), frequency responses of base model $\mathbf{P}_B$ in *x*/*y* coordinates are different as shown in Figure 2.18. Base response in *x* direction is more sensitive at low frequencies compared to that in *y* direction. However, a significant vibration could be excited when frequency reaches the natural frequency $\omega_{ny} = 96\,\mathrm{rad/s}$. The natural frequencies of the base supported by isolators, are mainly determined by these dynamic stiffnesses. Table 2.7 shows dynamic parameters of base, and experimental measurement reported in [20]. This demonstrates the accuracy of base model.

Table 2.7 Damping ratios and natural frequency in base model and experimental measurements

Eigenvalue	Damping	Frequency (Simulation) rad/s	Frequency (Experimental) rad/s
$-1.14 \mp 26.1j$	0.0436	26.2	27
$-1.28 \mp 46.4j$	0.0276	46.4	50
$-1.08 \mp 98.4j$	0.0109	98.4	100
$-1.37 \mp 111j$	0.0123	111	125

Contact-Free Base/Rotor System

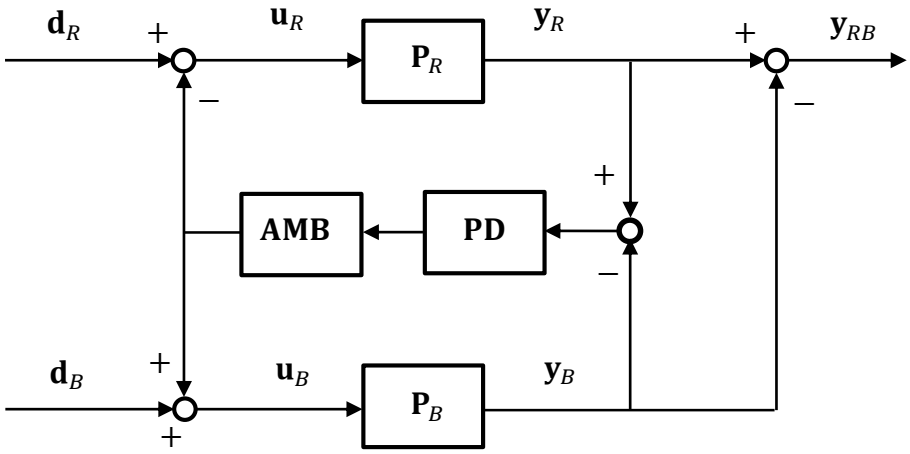

Figure 2.19 A block diagram of the rotor/base model interaction

Even without contact, the base motion will interact with the operating rotor. The control force reacting on the base will excite it to some vibration level. Figure 2.19 shows a block diagram of the interaction between the AMB controlled rotor and the rigid base model.

Based on the free-free rotor state-space form in equation (2.21), including the base model yields

$$\mathbf{P}_R: \begin{cases} \dot{\mathbf{q}}_R = \mathbf{A}_R\mathbf{q}_R - \mathbf{B}_R^p\mathbf{y}_p + \mathbf{B}_R^d\mathbf{d}_R \\ \mathbf{y}_R = \mathbf{C}_R\mathbf{q}_R + \mathbf{D}_R\mathbf{u}_R \end{cases} \tag{2.52}$$

where $\mathbf{B}_R^p$ and $\mathbf{B}_R^d$ define the locations of AMB control and unbalance forces. $\mathbf{u}_R$ is the external input force $\mathbf{u}_R = \mathbf{d}_R - \mathbf{y}_p$, when $\mathbf{d}_R$ and $\mathbf{y}_p$ are unbalance forcing and PD control input, respectively.

The base under interaction with rotor/AMB system has a state-space form

$$\mathbf{P}_B: \begin{cases} \dot{\mathbf{q}}_B = \mathbf{A}_B\mathbf{q}_B + \mathbf{B}_B^p\mathbf{u}_p + \mathbf{B}_B^d\mathbf{d}_B \\ \mathbf{y}_B = \mathbf{C}_B\mathbf{q}_B + \mathbf{D}_B\mathbf{u}_B \end{cases} \tag{2.53}$$

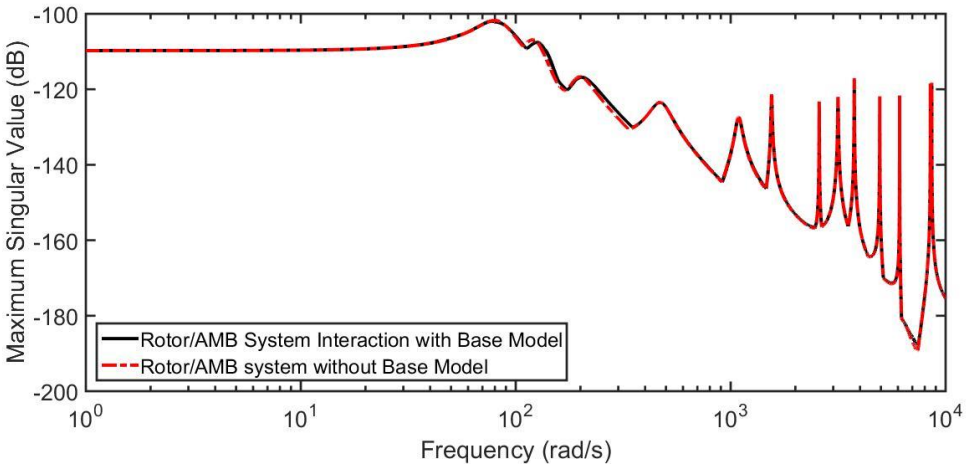

Figure 2.20 Maximum singular values of rotor-base model compared to that without base model

A linear AMB model under PD control may have a state-space form

$$\mathbf{P}_p: \begin{cases} \dot{\mathbf{q}}_p = \mathbf{A}_p\mathbf{q}_p + \mathbf{B}_p\mathbf{u}_p \\ \mathbf{y}_p = \mathbf{C}_p\mathbf{q}_p + \mathbf{D}_p\mathbf{u}_p \end{cases} \tag{2.54}$$

where $\mathbf{u}_p$ is the relative displacement, $\mathbf{u}_p = [\mathbf{y}_R - \mathbf{y}_B] = \mathbf{C}_R\mathbf{q}_R - \mathbf{C}_B\mathbf{q}_B$ with $\mathbf{D}_R = \mathbf{0}, \mathbf{D}_B = \mathbf{0}$.

The rotor/base model under PID control therefore has the state-space form

$$\mathbf{P}_{RB}: \begin{cases} \dot{\mathbf{q}}_{RB} = \mathbf{A}_{RB}\mathbf{q}_{RB} + \mathbf{B}_{RB}\mathbf{u}_{RB} \\ \mathbf{y}_{RB} = \mathbf{C}_{RB}\mathbf{q}_{RB} + \mathbf{D}_{RB}\mathbf{u}_{RB} \end{cases} \tag{2.55}$$

where $\mathbf{q}_{RB} = \begin{bmatrix} \mathbf{q}_R \\ \mathbf{q}_B \\ \mathbf{q}_p \end{bmatrix}$, $\mathbf{u}_{RB} = \begin{bmatrix} \mathbf{d}_R \\ \mathbf{d}_B \end{bmatrix}$,

$$\mathbf{A}_{RB} = \begin{bmatrix} \mathbf{A}_R - \mathbf{B}_R^p\mathbf{D}_p\mathbf{C}_R & \mathbf{B}_R^p\mathbf{D}_p\mathbf{C}_B & -\mathbf{B}_R^p\mathbf{C}_p \\ \mathbf{B}_B^p\mathbf{D}_p\mathbf{C}_R & \mathbf{A}_B - \mathbf{B}_b^p\mathbf{D}_p\mathbf{C}_B & \mathbf{B}_B^p\mathbf{C}_p \\ \mathbf{B}_p\mathbf{C}_R & -\mathbf{B}_p\mathbf{C}_B & \mathbf{A}_p \end{bmatrix},$$

$\mathbf{B}_{RB} = \begin{bmatrix} \mathbf{B}_R^d \\ \mathbf{B}_B^d \\ \mathbf{0} \end{bmatrix}$, $\mathbf{C}_{RB} = [\mathbf{C}_R \quad -\mathbf{C}_B \quad \mathbf{0}]$ and $\mathbf{D}_{RB} = \mathbf{0}$.

Based on the four sensors planes, maximum singular values of the rotor and base/rotor under PD control are shown in Figure 2.20. There are only slight differences between the models with and without the base model included. However, the differences may be large when contact happens. This is discussed further in Chapter 5.

2.4 Closure

This chapter starts from a short introduction for the test rig in aspects of hardware and software. Based on magnetic flux theory, it also shows the nonlinear magnetic bearing characteristics. Simplification for an AMB system controlled by PID feedback is presented, and incorporated with the rotor in a FEM framework. With a state-space description of the flexible rotor model, a rotor dynamics analysis is also given. As preparation for the rotor/TDB contact analysis in Chapter 5, a base parameter estimation and rigid body dynamic base model was derived. This is coupled to the rotor/AMB system.

Chapter 3 LTI Robust Control for Rotor/AMB Systems

PD control is commonly used for rotor/AMB systems. With tunable parameters, PD control offers useful performance. However, shaft orbits may become significant under excitation, leading to possible touchdown events. Unbalance forcing response may be attenuated through appropriate AMB control capability. H_∞ optimization may be introduced into the AMB control action, as it enables a control solution to the mixed sensitivity problem. The authors of [50, 51] consider solving the initial state uncertainty issue for the complementary sensitivity, and loop shaping procedures to achieve disturbance rejection. A combined PD/H_∞ control strategy is presented in this chapter, to penalize an external disturbance, especially since unbalance forcing is synchronized with rotational speed.

The number of inputs/outputs determines H_∞ controller order, and also the column rank of the basic plant. By using all sensors for feedback, a non-full column rank basic plant will be obtained in 'rectangular' (the number of actuation axes is not equal to that of feedback) state-space form. However, that may give rise to singular value issues, which influence the H_∞ optimization procedure for the mixed sensitivity problem. In this chapter, a 'square' basic plant (symmetric number of inputs/outputs) with full column rank is proposed. The problem induced by non-full column rank is therefore overcame in the H_∞ optimization procedure.

In general, shaft rotational speed may cover a wide range, even though operating speed ranges may be narrow. Owing to this speed dependence, a single LTI H_∞ controller designed for a specific speed range may not be able to facilitate disturbance rejection over other speed ranges, even result in instability issues. Model errors may arise from gyroscopic moments and other aerodynamic conditions that are speed dependent. In order to re-shape the frequency response over a large speed range, a switching signal driven control system containing a number of LTI H_∞ controllers may have potential. However, the transient motion induced by the switching action must be taken into account. Any overshoot caused by switching

could be significant and even unacceptable, leading to possible contact events. The design of the switching signal has an important influence in improving the transient rotor response.

3.1 Model Reduction Techniques for an LTI System

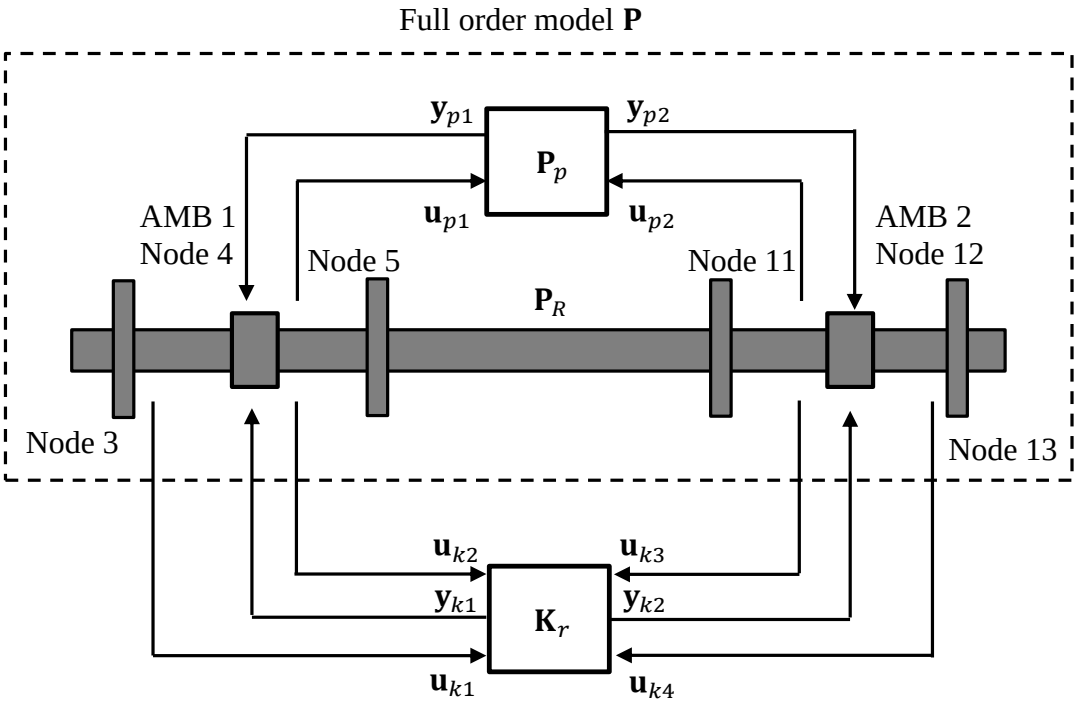

Figure 3.1 Sensor/actuation plane locations for control of the rotor

Figure 3.1 shows the sensor/actuator planes for the proposed LTI H_∞ control design. Eight displacement sensors are located at nodes 3, 5, 11 and 13 in orthogonal pairs at $\pm$ 45 degs to the vertical. The control action is applied through the AMBs at nodes 4 and 12 in pairs of orthogonal axes. As outlined in Chapter 2, default PD control uses only the local AMB sensors at nodes 5 and 11, though an LTI H_∞ controller may use all sensor signals for the rejection of external disturbances. With vibration signals provided by the two sensor pairs (nodes 3 and 13) located at both rotor ends, a model based controller can estimate flexible modes more comprehensively, and commence suitable control action.

3.1.1 High Frequency Response Truncation

Considering the implementation of model based control and simulation, model reduction is used to decrease high order dynamic models by truncating high frequency modes. The full order rotor/AMB model presented in Chapter 2, is given by

$$\begin{aligned} \dot{\mathbf{q}} &= \mathbf{A}\mathbf{q} + \mathbf{B}\mathbf{u} \\ \mathbf{y} &= \mathbf{C}\mathbf{q} + \mathbf{D}\mathbf{u} \end{aligned} \tag{3.1}$$

The eigenvalues and eigenvectors of $\mathbf{A}$ can be represented by the solution of

$$\mathbf{A}\mathbf{V} = \mathbf{V}\boldsymbol{\Lambda} \tag{3.2}$$

where $\mathbf{V}$ contains the eigenvectors as columns and $\boldsymbol{\Lambda}$ is a matrix with eigenvalues as diagonal elements.

Assume that the (complex) eigenvalues are in ascending order of modal frequency. A modal transformation is

$$\mathbf{q} = \mathbf{V}\mathbf{p} \tag{3.3}$$

Therefore, equation (3.1) may be transformed into

$$\begin{aligned} \dot{\mathbf{p}} &= \boldsymbol{\Lambda}\mathbf{p} + \mathbf{V}^{-1}\mathbf{B}\mathbf{u} \\ \mathbf{y} &= \mathbf{C}\mathbf{V}\mathbf{p} + \mathbf{D}\mathbf{u} \end{aligned} \tag{3.4}$$

Equation (3.4) may be partitioned into low and high (denoted as subscripts l, h) frequency modes as follows

$$\begin{gathered} \mathbf{p} = \begin{bmatrix} \mathbf{p}_l \\ \mathbf{p}_h \end{bmatrix}, \boldsymbol{\Lambda} = \begin{bmatrix} \boldsymbol{\Lambda}_l & \mathbf{0} \\ \mathbf{0} & \boldsymbol{\Lambda}_h \end{bmatrix} \mathbf{V}^{-1}\mathbf{B} = \begin{bmatrix} \breve{\mathbf{B}}_l \\ \breve{\mathbf{B}}_h \end{bmatrix}, \\ \mathbf{V} = [\mathbf{V}_l \quad \mathbf{V}_h], \mathbf{C}\mathbf{V} = [\mathbf{C}\mathbf{V}_l \quad \mathbf{C}\mathbf{V}_h] \end{gathered} \tag{3.5}$$

Thus, equation (3.4) may be decomposed into

$$\begin{aligned} \dot{\mathbf{p}}_l &= \boldsymbol{\Lambda}_l\mathbf{p}_l + \breve{\mathbf{B}}_l\mathbf{u} \\ \dot{\mathbf{p}}_h &= \boldsymbol{\Lambda}_h\mathbf{p}_h + \breve{\mathbf{B}}_h\mathbf{u} \end{aligned} \tag{3.6}$$

The output is given by

$$\mathbf{y} = \mathbf{C}\mathbf{V}_l\mathbf{p}_l + \mathbf{C}\mathbf{V}_h\mathbf{p}_h + \mathbf{D}\mathbf{u} \tag{3.7}$$

The nominal full order model is derived from a FEM model. Due to the limited element number, the lower frequency modes will be accurate, but the higher frequency modes may be inaccurate. The inaccuracy of the higher frequency modes will arise from erroneous natural frequencies and poorly defined mode shapes. Note also that the state-space model is necessarily finite, while a real system will have an infinite number of modes. Hence the full order system of equation (3.1) will have missing high frequency modes.

For model reduction and controller design purposes it is possible to ignore the contribution of the higher frequency modes. The deleted higher frequency contributions could then be treated as uncertainty (multiplicative model error) in the reduced order model. If the higher frequency modes are deleted, a reduced order model would be

$$\dot{\mathbf{p}}_l = \mathbf{\Lambda}_l\mathbf{p}_l + \breve{\mathbf{B}}_l\mathbf{u} \tag{3.8}$$

with the output state

$$\mathbf{y} = \mathbf{C}\mathbf{V}_l\mathbf{p}_l + \mathbf{D}\mathbf{u} \tag{3.9}$$

The remaining issue relates to steady state (low frequency) behaviour. Using equations (3.6) and (3.7) in steady state (time derivatives set to zero), the full order system gives rise to a steady state output

$$\mathbf{y} = -\mathbf{C}\mathbf{V}_l{\mathbf{\Lambda}_l}^{-1}\breve{\mathbf{B}}_l\mathbf{u} - \mathbf{C}\mathbf{V}_h{\mathbf{\Lambda}_h}^{-1}\breve{\mathbf{B}}_h\mathbf{u} + \mathbf{D}\mathbf{u} \tag{3.10}$$

However, the reduced order representation of equations (3.8) and (3.9) gives rise to a steady state output

$$\mathbf{y} = -\mathbf{C}\mathbf{V}_l{\mathbf{\Lambda}_l}^{-1}\breve{\mathbf{B}}_l\mathbf{u} + \mathbf{D}\mathbf{u} \tag{3.11}$$

A simple way to compensate for the discrepancy between equations (3.10) and (3.11) is to modify the output equation to give a reduced order model of

$$\begin{aligned}\dot{\mathbf{p}}_l &= \mathbf{\Lambda}_l \mathbf{p}_l + \breve{\mathbf{B}}_l \mathbf{u} \\ \mathbf{y} &= \mathbf{C}\mathbf{V}_l \mathbf{p}_l + \breve{\mathbf{D}}\mathbf{u}\end{aligned} \tag{3.12}$$

where $\breve{\mathbf{D}} = \mathbf{D} - \mathbf{C}\mathbf{V}_h {\mathbf{\Lambda}_h}^{-1} \breve{\mathbf{B}}_h$.

3.1.2 Real Forms for the Model Output

The use of the eigenvalue/vector transformation introduces complex numbers into equation (3.12) from an otherwise real-valued system of (3.1). For mechanical systems having positive definite and symmetric matrices, eigenvalues will occur in conjugate pairs. However, it is not necessary to assume this to be the case. Suppose that

$$\begin{aligned}\mathbf{p_l} &= [p_{R1} \pm j p_{I1}, p_{R2} \pm j p_{I2}, \cdots, p_{Rn} \pm j p_{In}]^T = \mathbf{p}_{Rl} \pm j \mathbf{p}_{Il} \\ \mathbf{\Lambda_l} &= diag(a_{R1} \pm j a_{I1}, a_{R2} \pm j a_{I2}, \cdots, a_{Rn} \pm j a_{In}) = \mathbf{\Lambda}_{Rl} \pm j \mathbf{\Lambda}_{Il} \\ \mathbf{V_l} &= [V_{R1} \pm j V_{I1}, V_{R2} \pm j V_{I2}, \cdots, V_{Rn} \pm j V_{In}] = \mathbf{V}_{Rl} \pm j \mathbf{V}_{Il}\end{aligned} \tag{3.13}$$

where p_{Ri}, p_{Ii} are the real and imaginary part of transformed system state, a_{Ri}, a_{Ii} and V_{R1}, V_{I1} are the real and imaginary part of eigenvalues/vectors at low frequencies.

Therefore, the reduced order system remained low frequencies dynamics and compensated high frequencies is given by

$$\mathbf{P}_r : \begin{cases}\dot{\mathbf{q}}_r = \mathbf{A}_r \mathbf{q}_r + \mathbf{B}_r \mathbf{u}_r \\ \mathbf{y}_r = \mathbf{C}_r \mathbf{q}_r + \mathbf{D}_r \mathbf{u}_r\end{cases} \tag{3.14}$$

where $\mathbf{q}_r = \begin{bmatrix}\mathbf{p}_{Rl} \\ \mathbf{p}_{Il}\end{bmatrix}$, $\mathbf{A}_r = \begin{bmatrix}\mathbf{\Lambda}_{Rl} & -\mathbf{\Lambda}_{Il} \\ \mathbf{\Lambda}_{Il} & \mathbf{\Lambda}_{Rl}\end{bmatrix}, \mathbf{B}_r = \begin{bmatrix}\breve{\mathbf{B}}_{Rl} \\ \breve{\mathbf{B}}_{Il}\end{bmatrix}$, and $\mathbf{y}_r$ and $\mathbf{u}_r$ indicates displacements sensor output and actuation input. For real valued outputs, any imaginary part of y must be zero. Hence the output matrices reduce to

$$\mathbf{C}_r = \mathbf{C}[\mathbf{V}_{Rl} - \mathbf{V}_{Il}], \mathbf{D}_r = (\mathbf{D} - \mathbf{C}\mathrm{Re}(\mathbf{V}_h {\mathbf{\Lambda}_h}^{-1} \breve{\mathbf{B}}_h)) \tag{3.15}$$

3.1.3 Multiplicative Model Error

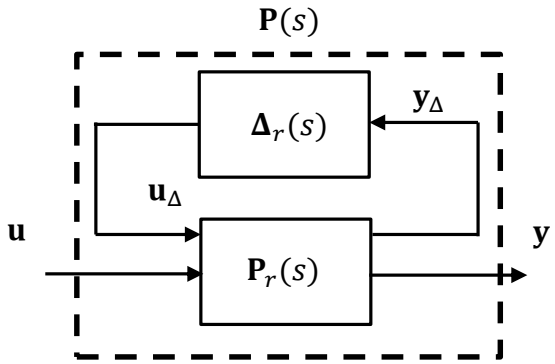

Figure 3.2 Block diagram for structured model uncertainty with robust control

Model reduction technique shown in equations (3.11)-(3.15) may produce a reduced order rotor/AMB model having insufficient high frequency response. That may give rise to large multiplicative model error, and lead to instability problem if not structured. To commence robust control design, system uncertainties must be estimated as shown in Figure 3.2.

In robust controller design, the model additive uncertainty may be described as

$$\mathbf{P}(s) = \mathbf{P}_r(s) + \mathbf{\Delta}_r(s) \tag{3.16}$$

where the uncertainty $\mathbf{\Delta}_r$ can be described as

$$\mathbf{\Delta}_r(s) = \begin{bmatrix} \Delta_{r1}(s) & \cdots & 0 \\ \vdots & \ddots & \vdots \\ 0 & \cdots & \Delta_{rn}(s) \end{bmatrix} \tag{3.17}$$

Therefore, the input multiplicative model error based on the model reduction technique may be obtained as

$$\mathbf{P}(s) = \mathbf{P}_r(s)(\mathbf{I} + \mathbf{\Delta}_m(s)) \tag{3.18}$$

where $\mathbf{\Delta}_m(s) = \mathbf{P}_r^{-1}(s)\mathbf{\Delta}_r(s)$, leading to

$$\mathbf{\Delta}_m(s) = \mathbf{P}_r^{-1}(s)(\mathbf{P}(s) - \mathbf{P}_r(s)) \tag{3.19}$$

By inserting $s = j\omega$ the maximum singular value of multiplicative model error is given by

$$\sup_{-\infty<\omega<\infty} \bar{\sigma}\big(\boldsymbol{\Delta}_m(j\omega)\big) = \|\mathbf{P}_r^{-1}(s)(\mathbf{P}(s) - \mathbf{P}_r(s))\|_\infty \tag{3.20}$$

3.1.4 D Matrix Compensation

Commonly, a reduced order model having a zero **D** matrix offers a simple way to synthesize a model based state-space controller. However, that may also enable multiplicative model error to be sensitive at high frequencies. In a rotor/AMB system, this may lead to instabilities during controller implementation. With frequency-independent compensation gain (**D** matrix) at high frequency shown in equation (3.15), $\boldsymbol{\Delta}_m(s)$ can remain at a relative low sensitivity. Figure 3.3 compares the full and reduced order model frequency responses with the zero/non-zero **D** matrix in reduced order model and the inherited multiplicative model errors induced by model reduction stated above. Table 3.1 shows the eigen-parameters for the reduced order model.

Table 3.1 Eigen-parameters for reduced order model

Eigenvalues	Eigen-Damping	Eigen-Frequency (rad/s)
$16.7 \pm 81.6j$	0.20	83.3
$15.1 \pm 122.3j$	0.12	123.3
$22.3 \pm 194.5j$	0.13	195.7
$53.3 \pm 47.0j$	0.11	472.9

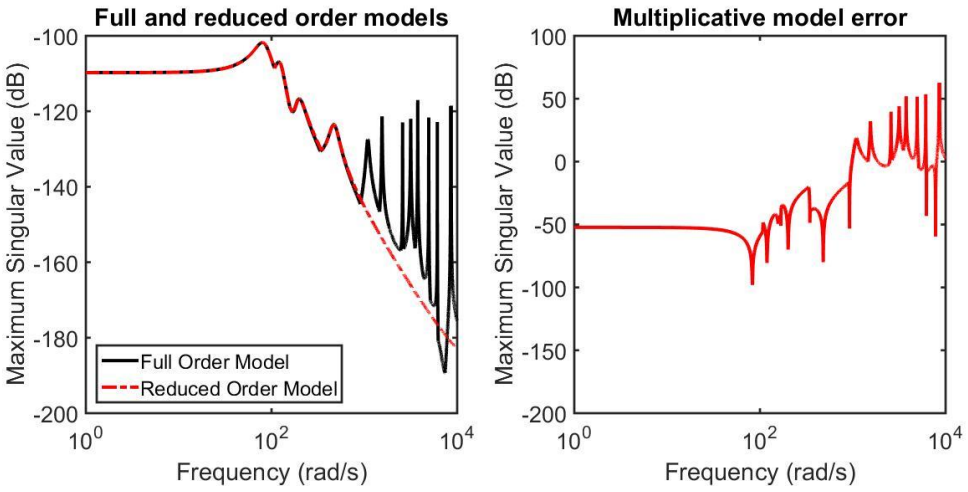

(a) $\bar{\sigma}(\mathbf{P}(s))$, $\bar{\sigma}(\mathbf{P}_r(s))$ and $\bar{\sigma}(\mathbf{\Delta}_m(s))$ when $\mathbf{D}_r = \mathbf{0}$

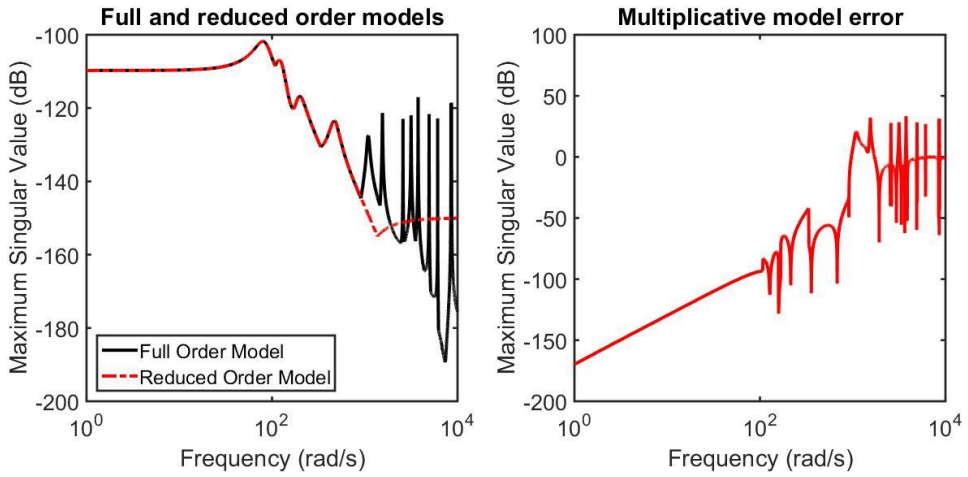

(b) $\bar{\sigma}(\mathbf{P}(s))$, $\bar{\sigma}(\mathbf{P}_r(s))$ and $\bar{\sigma}(\mathbf{\Delta}_m(s))$ when $\mathbf{D}_r = (\mathbf{D} - \mathbf{C}\mathrm{Re}(\mathbf{V}_h\mathbf{\Lambda}_h{}^{-1}\breve{\mathbf{B}}_h))$

Figure 3.3 Full/reduced order models and multiplicative model error obtained by different **D** matrix.

3.2 Riccati Based H_∞ Optimization for LTI Systems

Based on the H_∞ optimal control theory stated in [49, 50], this section provides several details to relate Riccati based H_∞ controller design for rotor/AMB test system stated in Chapter 2.

3.2.1 Sensitivity/Complementary Sensitivity in Feedback Control

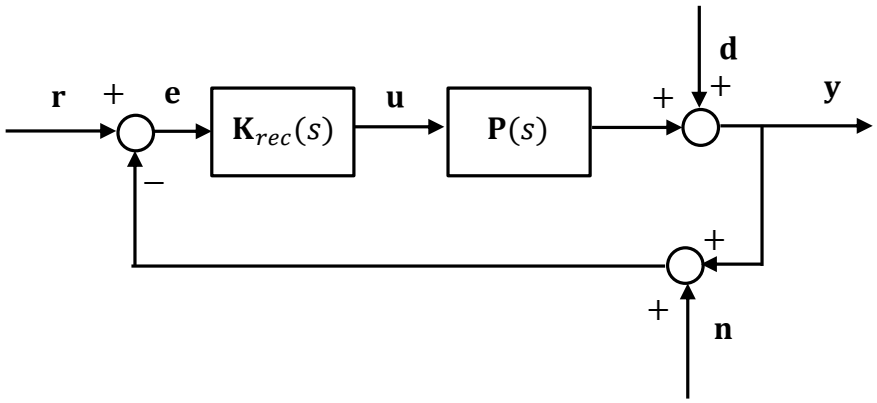

Figure 3.4 Block diagram for feedback loop

The classic feedback loop for controller design is shown in Figure 3.4. System external disturbance **d**, is defined as an external input adding to the plant output **y**. Displacement sensor noise is denoted by **n**.

The input/output of the plant under feedback robust control may be obtained as

$$\begin{aligned}\mathbf{u} &= \mathbf{K}_{rec}\mathbf{e} = \mathbf{K}_{rec}(\mathbf{r}-\mathbf{y}-\mathbf{n})\\ \mathbf{y} &= \mathbf{P}\mathbf{u}+\mathbf{d} = \mathbf{P}\mathbf{K}_{rec}(\mathbf{r}-\mathbf{y}-\mathbf{n})+\mathbf{d}\end{aligned} \tag{3.21}$$

The output **y** may be determined in the Laplace transform domain

$$\mathbf{y} = \mathbf{T}(s)\mathbf{r} - \mathbf{T}(s)\mathbf{n} + \mathbf{S}(s)\mathbf{d} \tag{3.22}$$

where the closed loop complementary sensitivity transfer function of the full order system $\mathbf{T}(s)$ is given by

$$\mathbf{T}(s) = \left(\mathbf{I} + \mathbf{P}(s)\mathbf{K}_{rec}(s)\right)^{-1}\mathbf{P}(s)\mathbf{K}_{rec}(s) \tag{3.23}$$

and the sensitivity transfer function $\mathbf{S}(s)$ is given by

$$\mathbf{S}(s) = \left(\mathbf{I} + \mathbf{P}(s)\mathbf{K}_{rec}(s)\right)^{-1} \tag{3.24}$$

It follows that

$$\mathbf{S}(s) + \mathbf{T}(s) = \mathbf{I} \tag{3.25}$$

3.2.2 Augmented Plant for Mixed Sensitivity Problem in Rotor/AMB System

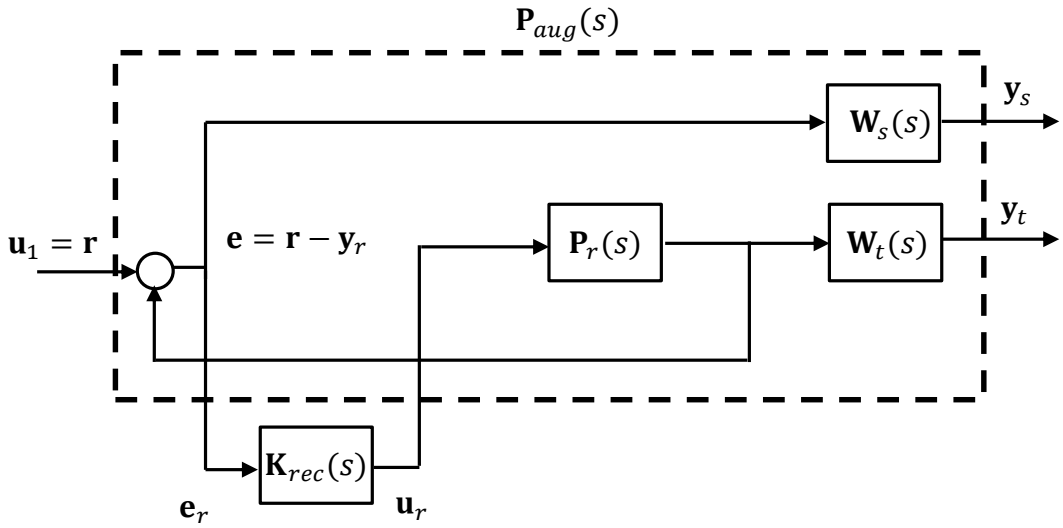

Figure 3.5 Plant augmentation for control design

An augmented plant for the rotor/AMB system may be created to modify the classic closed loop control system shown in Figure 3.4. A control structure for the solution to the mixed sensitivity problem is shown in Figure 3.5. In order to achieve stability, the system complementary sensitivity is weighted by $\mathbf{W}_t(s)$ based on multiplicative model error inherited from model reduction. The error signal $\mathbf{e}$ scaled by a suitable weightings $\mathbf{W}_s(s)$ to enables the control loop system to reject external disturbance.

The transfer function with weightings is denoted by $\mathbf{P}_{aug}(s)$. The scaled output is represented by $\mathbf{y}_{aug}$. This gives

$$\begin{bmatrix}\mathbf{y}_{aug}\\ \mathbf{e}_r\end{bmatrix} = \mathbf{P}_{aug}(s)\begin{bmatrix}\mathbf{u}_1\\ \mathbf{u}_r\end{bmatrix} \tag{3.26}$$

where $\mathbf{y}_{aug} = \begin{bmatrix}\mathbf{y}_s\\ \mathbf{y}_t\end{bmatrix}$.

Thus, the augmented plant $\mathbf{P}_{aug}(s)$ is partitioned by

$$\mathbf{P}_{aug}(s) = \begin{bmatrix} \mathbf{W}_s(s) & -\mathbf{W}_s(s)\mathbf{P}_r(s) \\ \mathbf{0} & \mathbf{W}_t(s)\mathbf{P}_r(s) \\ \mathbf{I} & -\mathbf{P}_r(s) \end{bmatrix} = \begin{bmatrix} \mathbf{P}_{11}(s) & \mathbf{P}_{12}(s) \\ \mathbf{P}_{21}(s) & \mathbf{P}_{22}(s) \end{bmatrix} \tag{3.27}$$

Hence

$$\begin{aligned} \mathbf{y}_{aug} &= \mathbf{P}_{11}(s)\mathbf{u}_1 + \mathbf{P}_{12}(s)\mathbf{u}_r \\ \mathbf{e}_r &= \mathbf{P}_{21}(s)\mathbf{u}_1 + \mathbf{P}_{22}(s)\mathbf{u}_r \end{aligned} \tag{3.28}$$

By inserting $\mathbf{u}_r = \mathbf{K}_{rec}(s)\mathbf{e}_r$, the closed loop transfer function is subject to

$$\mathbf{y}_{aug} = \mathbf{T}_{\mathbf{y}_{aug},\mathbf{u}_1}\mathbf{u}_1 \tag{3.29}$$

where $\mathbf{T}_{\mathbf{y}_{aug},\mathbf{u}_1} = \mathbf{P}_{11}(s) + \mathbf{P}_{12}(s)\mathbf{K}_{rec}(s)(\mathbf{I} - \mathbf{P}_{22}(s)\mathbf{K}_{rec}(s))^{-1}\mathbf{P}_{21}(s)$

This gives

$$\mathbf{T}_{\mathbf{y}_{aug},\mathbf{u}_1} = \begin{bmatrix} \mathbf{W}_s(s)\mathbf{S}_r \\ \mathbf{W}_t(s)\mathbf{T}_r \end{bmatrix} \tag{3.30}$$

Note that, $\mathbf{S}_r$ and $\mathbf{T}_r$ are sensitivity/complementary sensitivity transfer functions of the closed loop system with reduced order plant $\mathbf{P}_r$, which are used in the H_∞ optimization procedure. The robustness stability can be guaranteed, if model uncertainties due to model reduction are accounted for.

3.2.3 Riccati-Based H_∞ Optimization

Small Gain Theorem

This states that, if model uncertainties $\mathbf{\Delta}_m$ (multiplicative model error in this chapter) and closed loop transfer functions $\mathbf{T}_{\mathbf{y}_{aug},\mathbf{u}_1}$ are stable, the internal stability can be guaranteed when

$$\begin{aligned} \|\mathbf{\Delta}_m\|_\infty \le 1/\gamma \text{ if and only if } \left\|\mathbf{T}_{\mathbf{y}_{aug},\mathbf{u}_1}\right\|_\infty < \gamma \\ \|\mathbf{\Delta}_m\|_\infty < 1/\gamma \text{ if and only if } \left\|\mathbf{T}_{\mathbf{y}_{aug},\mathbf{u}_1}\right\|_\infty \le \gamma \end{aligned} \tag{3.31}$$

The H_∞ norm of the closed loop transfer function follows from

$$\left\|\mathbf{T}_{\mathbf{y}_{aug},\mathbf{u}_1}\right\|_\infty = \sqrt{\|\mathbf{W}_s\mathbf{S}_r\|_\infty^2 + \|\mathbf{W}_t\mathbf{T}_r\|_\infty^2} \le \gamma \tag{3.32}$$

Hence, if the maximum singular value of the closed loop transfer function is scaled by γ, then

$$\begin{aligned} \|\mathbf{W}_s\mathbf{S}_r\|_\infty &\leq \gamma \\ \|\mathbf{W}_t\mathbf{T}_r\|_\infty &\leq \gamma \end{aligned} \tag{3.33}$$

Mixed Sensitivity Problem

As a popular approach to achieve the two main objectives of good disturbance rejection and stability, a mixed sensitivity formulation is commonly used in H_∞ controller design. With direct loop shaping, the output sensitivity and complementary sensitivity function of the closed loop plant can be adjusted by the designed weightings. Thus, the optimization procedure is to find a controller $\mathbf{K}_{rec}(s)$ as a solution to mixed sensitivity problem, such that

$$\left\|\mathbf{F}_l\left(\mathbf{P}_{aug}, \mathbf{K}_{rec}\right)\right\|_\infty \leq \gamma \tag{3.34}$$

where, the lower linear fractional transformation (LFT) is

$$\mathbf{F}_l\left(\mathbf{P}_{aug}, \mathbf{K}_{rec}\right) = \mathbf{T}_{\mathbf{y}_{aug},\mathbf{u}_1} = \begin{bmatrix} \mathbf{W}_s(s)\mathbf{S}_r \\ \mathbf{W}_t(s)\mathbf{T}_r \end{bmatrix} \tag{3.35}$$

According to Nyquist analysis, the stability can be guaranteed if $\gamma \leq 1$, and

$$\bar{\sigma}(\boldsymbol{\Delta}_m((j\omega))) < \frac{1}{\bar{\sigma}\left(\mathbf{T}_r(j\omega)\right)} \tag{3.36}$$

Hence, weighting for complementary sensitivity may be designed based on

$$\bar{\sigma}\left(\boldsymbol{\Delta}_m(j\omega)\right) < \bar{\sigma}\left(\mathbf{W}_t(j\omega)\right) \tag{3.37}$$

Therefore, the complementary sensitivity is constrained by the weighting choice as

$$\bar{\sigma}\left(\mathbf{T}_r(j\omega)\right) \leq \bar{\sigma}(\mathbf{W}_t^{-1}(j\omega)\gamma) \tag{3.38}$$

and the closed loop sensitivity function is bounded by the weighting as

$$\bar{\sigma}\left(\mathbf{S}_r(j\omega)\right) \leq \bar{\sigma}(\mathbf{W}_s^{-1}(j\omega)\gamma) \tag{3.39}$$

However, both weightings cannot be ‘large’ together since

$$1 \le \bar{\sigma}\left(\mathbf{S}_r(j\omega)\right) + \bar{\sigma}\left(\mathbf{T}_r(j\omega)\right) \le \bar{\sigma}\left((\mathbf{W}_s)^{-1}(j\omega)\right) + \bar{\sigma}\left(\mathbf{W}_t^{-1}(j\omega)\right) \tag{3.40}$$

3.3 H_∞ Controller Synthesis

This section gives the detailed choice of weightings for controller design, and analyses control performance based on the theory stated in Section 3.2. Also, it presents the semi-optimal H_∞ control solution induced by the non-full rank plant.

3.3.1 Weighting Choice

Figure 3.6 shows the maximum singular value of the weighting choice for the closed loop system complementary sensitivity based on statement shown in equation (3.37). Given eight sensor signals, weighting $\mathbf{W}_t(s)$ for complementary sensitivity may be expressed as

$$\mathbf{W}_t(s) = \mathbf{I}_{8\times 8} w_t(s) \tag{3.41}$$

where

$$w_t(s) = \left(\frac{s+a}{s+b}\right)\left(\frac{s^2 + 2\xi_1 w_{n1} s + {w_{n1}}^2}{s^2 + 2\xi_2 w_{n2} s + {w_{n2}}^2}\right)\left(\frac{b{w_{n2}}^2}{a{w_{n1}}^2}\right) \tag{3.42}$$

with $a = 0, b = 3000,$ $\xi_1 = 0.1\,, \xi_2 = 0.2, w_{n1} = 83$ rad/s, and $w_{n2} = 1200$ rad/s.

For disturbance rejection, the transfer function of the weighting for the closed loop sensitivity was selected as second order filter to obtain sufficient control performance over a designed frequency range around the natural frequency of the filter. $\mathbf{W}_s(s)$ is given by

$$\mathbf{W}_s(s) = \mathbf{I}_{8\times 8} w_s(s) \tag{3.43}$$

where

$$w_s(s) = \varepsilon_i \left(\frac{{w_{nsi}}^2}{s^2 + 2\xi_{si} w_{nsi} s + {w_{nsi}}^2}\right) \tag{3.44}$$

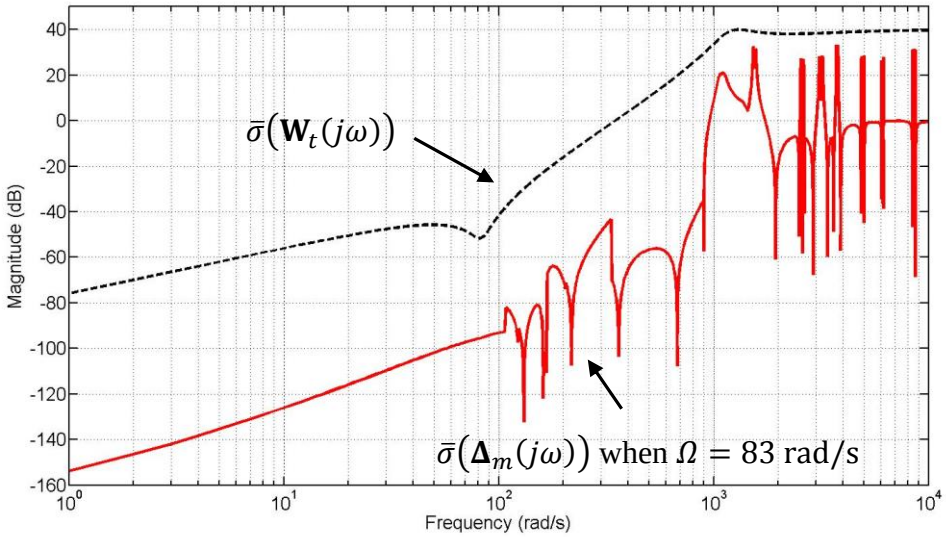

Figure 3.6 $\bar{\sigma}(\mathbf{W}_t(j\omega))$ and $\bar{\sigma}(\mathbf{\Delta}_m(j\omega))$

where ε_i is the static gain, w_{nsi} is the natural frequency and ξ_{si} is the damping ratio. With $\varepsilon_i = 0.02$, $w_{nsi} = 83$ rad/s and $\xi_{si} = 0.1$, a model based H_∞ controller $\mathbf{K}_{rec}$ may be derived from the H_∞ optimization shown in equations (3.34)-(3.35). The H_∞ cost, $\gamma = 0.1$, is found by iteration to satisfy the robustness and stability condition stated in equation (3.35). The controller has a state-space form as

$$\mathbf{K}_{rec}: \begin{cases} \dot{\mathbf{q}}_{rec}^K = \mathbf{A}_{rec}^K \mathbf{q}_{rec}^K + \mathbf{B}_{rec}^K \mathbf{u}_{rec}^K \\ \mathbf{y}_{rec}^K = \mathbf{C}_{rec}^K \mathbf{q}_{rec}^K + \mathbf{D}_{rec}^K \mathbf{u}_{rec}^K \end{cases} \tag{3.45}$$

where the controller output $\mathbf{y}_{rec}^K = \mathbf{u}_r$ and controller input $\mathbf{u}_{rec}^K = \mathbf{e}_r$. As a model based controller synthesis procedure, the controller $\mathbf{K}_{rec}$ input and output are determined by the reduced order plant $\mathbf{P}_r$ as shown in the rotor/AMB schematic of Figure 3.1.

3.3.2 Non-Full Column Feedforward Loop Term

Based on the controller $\mathbf{K}_{rec}$ derived from augmented plant shown in Figure 3.5, the rank of the open-loop term $\mathbf{Q}_{rec,m\times m} = \mathbf{P}_{r,m\times n}\mathbf{K}_{rec,n\times m}$ may be obtained by

$$\begin{aligned}\operatorname{rank}(\mathbf{P}_{r,m\times n}) + \operatorname{rank}(\mathbf{K}_{rec,n\times m}) - n \leq \operatorname{rank}(\mathbf{Q}_{rec,m\times m}) \\ \leq \min(\operatorname{rank}(\mathbf{P}_{r,m\times n}), \operatorname{rank}(\mathbf{K}_{rec,n\times m}))\end{aligned} \tag{3.46}$$

where $m = 8$ is the number of sensors and $n = 4$ is the number of control axes. This gives

$$\begin{aligned}\operatorname{rank}(\mathbf{P}_{r,m\times n}) = 4 \\ \operatorname{rank}(\mathbf{K}_{rec,m\times n}) = 4\end{aligned} \tag{3.47}$$

The singular value decomposition of $\mathbf{Q}_{rec}$ is given by

$$\mathbf{Q}_{rec}\,(j\omega) \;=\; \mathbf{U}\,\mathbf{\Sigma}_{rec}(j\omega)\,\mathbf{V}^T \tag{3.48}$$

where $\mathbf{U}$ has dimensions $m \times m$ and $\mathbf{V}$ is $n \times n$. and

$$\mathbf{\Sigma}_{rec}(j\omega) = \begin{bmatrix} \Sigma_{rec,1}(j\omega) & \cdots & 0 \\ \vdots & \ddots & \vdots \\ 0 & \cdots & \Sigma_{rec,m}(j\omega) \end{bmatrix} \tag{3.49}$$

where $\Sigma_{rec,i}(j\omega) = \sigma_i(\mathbf{Q}_{rec}\,(j\omega))$ subject to

$$\Sigma_{rec,1} \geq \cdots \geq \Sigma_{rec,m} > 0 \tag{3.50}$$

If $i > \operatorname{rank}(\mathbf{Q}_{rec})$, that gives singular values $\Sigma_{rec,i} = 0$ in the feedforward term $\mathbf{Q}_{rec}$ due to $\operatorname{rank}(\mathbf{Q}_{rec}) = 4$. Figure 3.7 shows the non-zero singular values for i = 1,2,3,4. The singular values for i = 5,6,7,8 are to be regarded as zero within the numerical precision of the evaluation process.

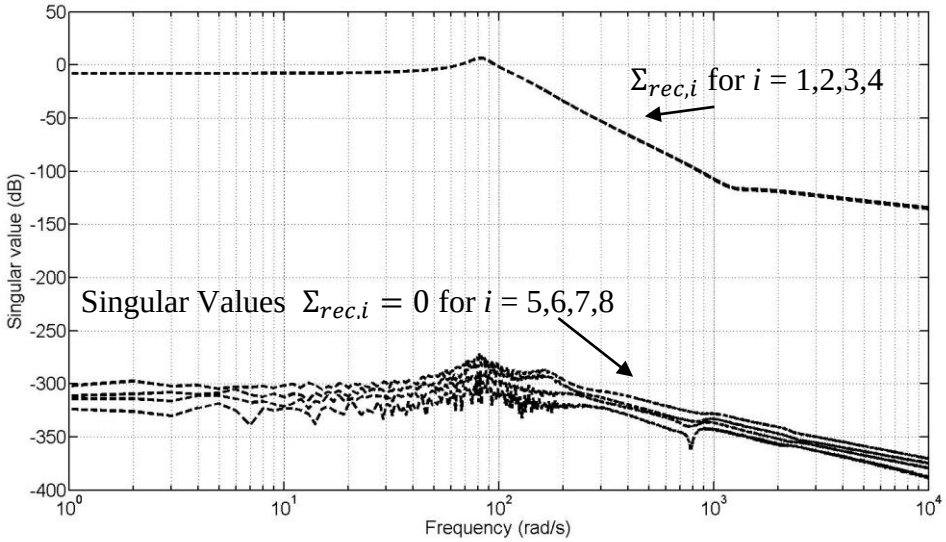

Figure 3.7 Singular values of the non-full rank feedforward loop term $\mathbf{Q}_{rec}(j\omega)$

3.3.3 Singular Values Issues in Mixed Sensitivity

The rotor/AMB system with sensor/actuation planes shown in Figure 3.1, may have singular values issues in a mixed sensitivity problem optimization. Through singular value decomposition in equation (3.48), singular values of the closed sensitivity transfer function are given by

$$\sigma\big(\mathbf{S}_r(j\omega)\big) = \begin{bmatrix} \Sigma^s_{rec,1}(j\omega) & \cdots & 0 \\ \vdots & \ddots & \vdots \\ 0 & \cdots & \Sigma^s_{rec,m}(j\omega) \end{bmatrix} \tag{3.51}$$

Based on equation (3.24), the singular values of the closed loop transfer function shown in equation (3.51) satisfy

$$\Sigma^s_{rec,1} \geq \cdots \geq \Sigma^s_{rec,m} > 0 \tag{3.52}$$

If $i >$ rank($\mathbf{Q}_{rec}$), singular values $\Sigma^s_{rec,i} = \sigma_i\big(\mathbf{S}_r(j\omega)\big) = 1$.

With regard to the complementary sensitivity, it has singular values in the diagonal matrix

$$\sigma\left(\mathbf{T}_r(j\omega)\right) = \begin{bmatrix} \Sigma_{rec,1}^T(j\omega) & \cdots & 0 \\ \vdots & \ddots & \vdots \\ 0 & \cdots & \Sigma_{rec,m}^T(j\omega) \end{bmatrix} \tag{3.53}$$

Each singular value $\Sigma_{rec,i}^T$ of $\mathbf{T}_r$ may subject to

$$\Sigma_{rec,1}^T \geq \cdots \geq \Sigma_{rec,m}^T > 0 \tag{3.54}$$

if $i >$ rank($\mathbf{Q}_{rec}$), singular values $\Sigma_{rec,i}^T = \sigma_i\left(\mathbf{T}_r(j\omega)\right) = 0$.

3.3.4 Semi-Optimization Induced by Singular Value Issue

As shown in equations (3.51)-(3.54), singular values $\Sigma_{rec,i}^S = 1$ and $\Sigma_{rec,i}^T = 0$ (for *i*=5,6,7,8) effect the control solution procedure. The optimal iteration procedure cannot commence further, as H_∞ optimization has to satisfy the maximum singular value inequality stated in equations (3.38) and (3.39). This give rise to a semi-optimization control solution. Figure 3.8 shows that the largest singular value of $\mathbf{S}_r(j\omega)$ cannot be bounded less than unity. As a result of semi-optimization, the H_∞ cost, γ, cannot obtain well-bound for the $\left\|\mathbf{F}_l\left(\mathbf{P}_{aug}, \mathbf{K}_{rec}\right)\right\|_\infty$ as stated in equations (3.34) and (3.35) (Figure 3.9).

Due to singular value issues stated in this section, the controller $\mathbf{K}_{rec}$ designed based on the plant having 8 outputs and 4 inputs, may not be optimized fully. Although robust stability can be guaranteed by H_∞ optimization, the capability to achieve disturbance rejection is limited. In order to obtain better control performance form a Riccati based H_∞ solution, these singular values issues need to be overcome.

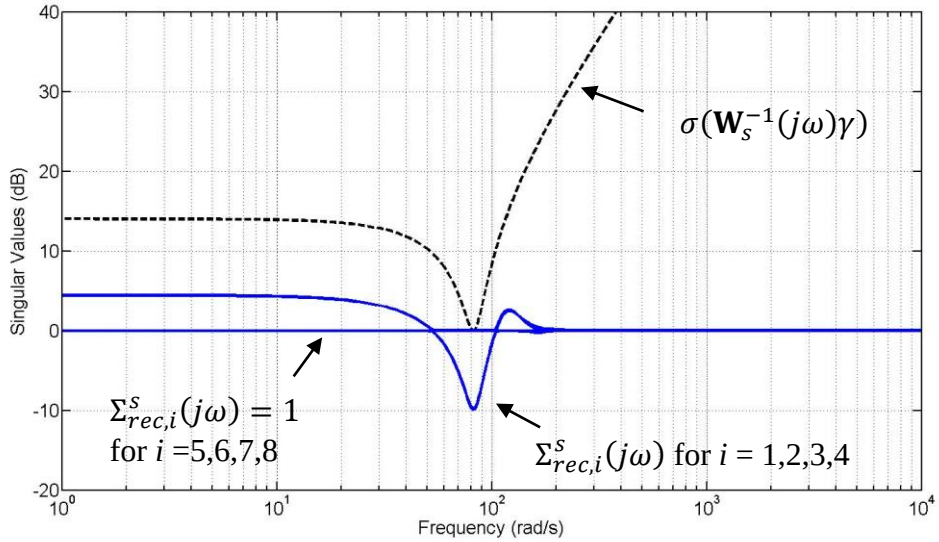

(a) Semi-Optimized $\sigma(\mathbf{S}_r(j\omega))$ and $\sigma(\mathbf{W}_s^{-1}(j\omega)\gamma)$

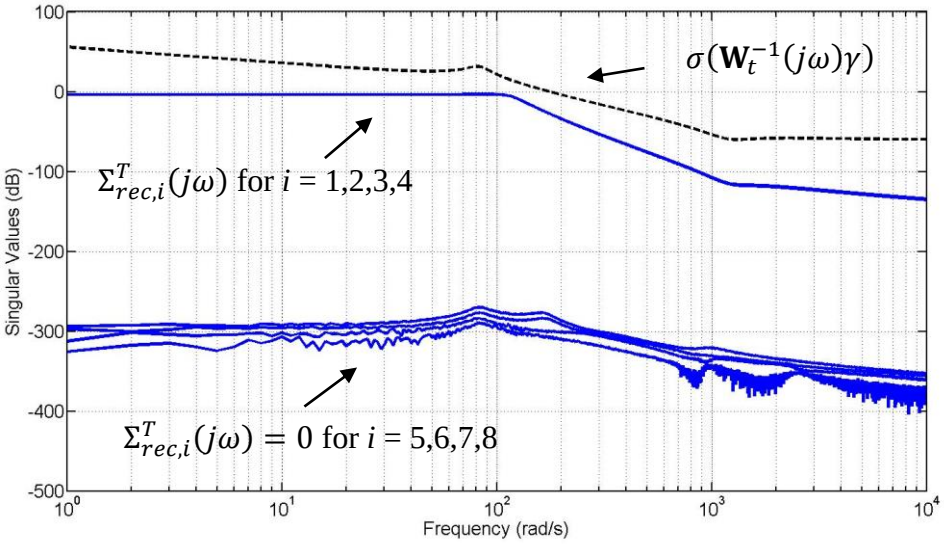

(b) Semi-Optimized $\sigma(\mathbf{T}_r(j\omega))$ and $\sigma(\mathbf{W}_t^{-1}(j\omega)\gamma_s)$

Figure 3.8 Semi-Optimized closed loop sensitivity/complementary sensitivity

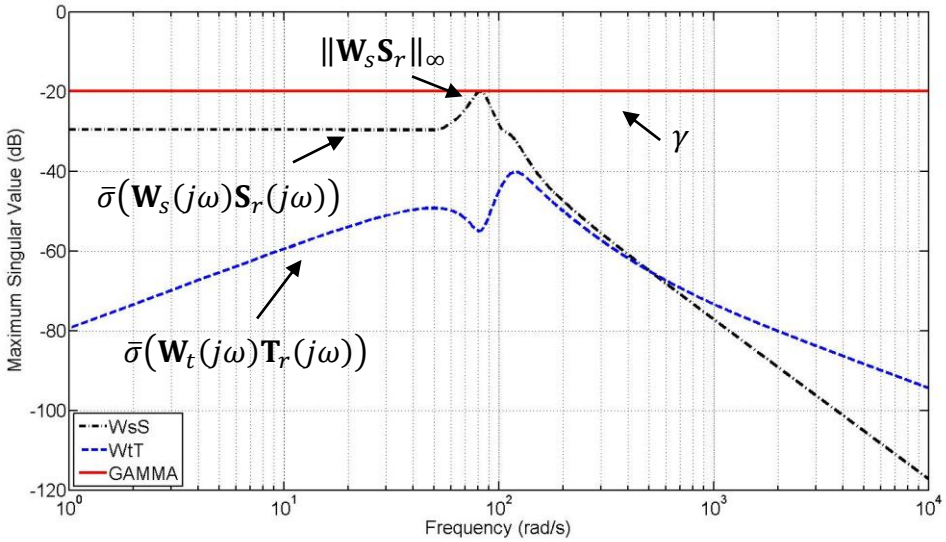

Figure 3.9 Semi-Optimization procedure

3.4 'Square' Plant Based Controller Design

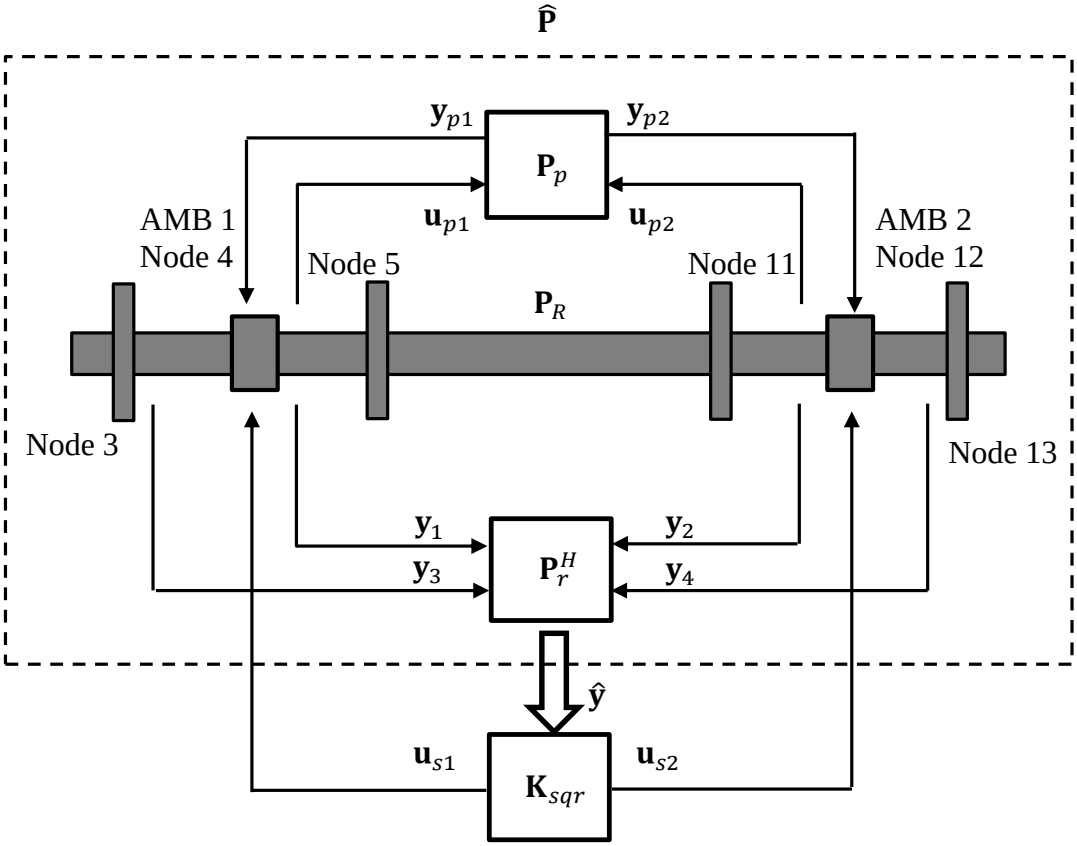

Figure 3.10 Output scaled model for controller design

In order to obtain full H_∞ optimization, a solution for the singular value issues is proposed in this section. A dynamic weighting $\mathbf{P}_r^H$ (Hermitian of the basic plant $\mathbf{P}_r$) is used to scale the plant output size to be the same as the actuation input dimension. Hence, a 'square' plant (same number of inputs and outputs) having full column rank is obtained for the H_∞ optimization procedure. The sensor/actuation planes are shown in Figure 3.10.

3.4.1 'Square' Closed Loop Control Structure

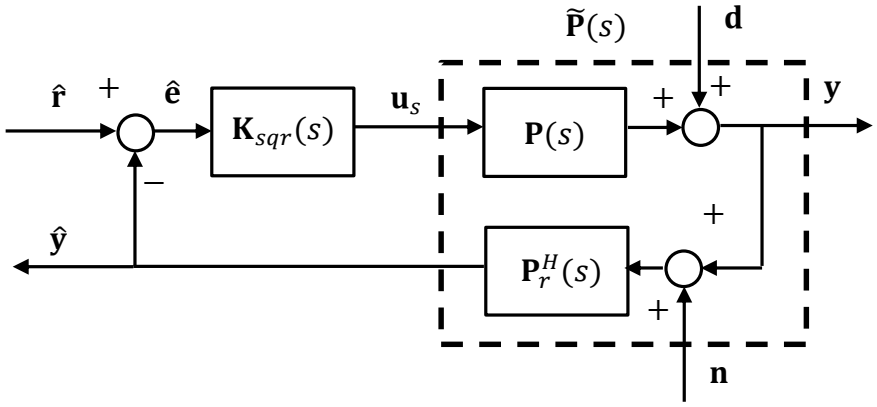

Figure 3.11 Configuration of closed loop system with output size scaling

Figure 3.11 shows a block diagram of the closed loop system for the 'square' plant, the system feedback vector $\mathbf{y}_{8\times1}$ is scaled by $\mathbf{P}_{r,4\times8}^H$ internally, and fed in the controller $\mathbf{K}_{sqr}$ as the error $\hat{\mathbf{e}}_{4\times1}$. Thus, the rotor/AMB system $\widetilde{\mathbf{P}}$ with output disturbance and sensor noise, may be partitioned as

$$\begin{bmatrix}\mathbf{y}\\ \hat{\mathbf{y}}\end{bmatrix} = \begin{bmatrix}\mathbf{P} & \mathbf{I} & \mathbf{0}\\ \hat{\mathbf{P}} & \mathbf{P}_r^H & \mathbf{P}_r^H\end{bmatrix}\begin{bmatrix}\mathbf{u}_s\\ \mathbf{d}\\ \mathbf{n}\end{bmatrix} \tag{3.55}$$

where the 'rectangular' full order system is scaled as 'square' $\hat{\mathbf{P}}_{4\times4} = \mathbf{P}_r^H\mathbf{P}$, That gives

$$\begin{aligned}\mathbf{u}_s &= \mathbf{K}_{sqr}\hat{\mathbf{e}} = \mathbf{K}_{sqr}(\hat{\mathbf{r}} - \hat{\mathbf{y}} - \hat{\mathbf{n}})\\ \hat{\mathbf{y}} &= \hat{\mathbf{P}}\mathbf{u}_s + \hat{\mathbf{d}} = \hat{\mathbf{P}}\mathbf{K}_{sqr}(\hat{\mathbf{r}} - \hat{\mathbf{y}}) + \hat{\mathbf{d}}\end{aligned} \tag{3.56}$$

where $\mathbf{u}_s$ is the control input, the scaled displacement sensor noise $\hat{\mathbf{n}} = \mathbf{P}_r^H\mathbf{n}$, and output disturbance $\hat{\mathbf{d}} = \mathbf{P}_r^H\mathbf{d}$. Thus, the output $\hat{\mathbf{y}}$ may be determined by

$$\hat{\mathbf{y}} = \hat{\mathbf{T}}(s)\hat{\mathbf{r}} - \hat{\mathbf{T}}(s)\hat{\mathbf{n}} + \hat{\mathbf{S}}(s)\hat{\mathbf{d}} \tag{3.57}$$

Based equations (3.23) and (3.24), the closed loop sensitivity for the 'square' plant $\hat{\mathbf{S}}$ tracking from $\hat{\mathbf{d}}$ to $\hat{\mathbf{y}}$ is given by

$$\hat{\mathbf{S}} = \left(\mathbf{I} + \hat{\mathbf{P}}\mathbf{K}_{sqr}\right)^{-1} \tag{3.58}$$

The complementary sensitivity function $\widehat{\mathbf{T}}$ tracking from $\hat{\mathbf{r}}$ to $\hat{\mathbf{y}}$ is obtained as

$$\widehat{\mathbf{T}} = \left(\mathbf{I} + \widehat{\mathbf{P}}\mathbf{K}_{sqr}\right)^{-1}\widehat{\mathbf{P}}\mathbf{K}_{sqr} \tag{3.59}$$

3.4.2 H_∞ Controller Synthesis for 'Square' Plant

An augmented plant for the reduced order 'square' plant $\widehat{\mathbf{P}}_r$ is shown in Figure 3.12. The weighting for complementary sensitivity may be formed as

$$\widehat{\mathbf{W}}_t(s) = \mathbf{I}_{4\times4} w_t(s) \tag{3.60}$$

where the transfer function w_t is same as shown in equation (3.42). The multiplicative model error in 'square' plant follows

$$\widehat{\boldsymbol{\Delta}}_m(s) = \boldsymbol{\Delta}_m(s) \tag{3.61}$$

Equation (3.61) can be verified mathematically in equation (3.18) by multiplying by $\mathbf{P}_r^H$. Also, $\mathbf{P}_r^H$ introduces no additional model uncertainties into system.

The weighting for sensitivity based on augmented plant shown in Figure 3.12 is given by

$$\widehat{\mathbf{W}}_s(s) = \mathbf{I}_{4\times4} w_s \tag{3.62}$$

where the transfer function follows the second order filter form shown in equation (3.44) with parameter $\varepsilon_i = 0.1$ $w_{nsi} = 83$ rad/s and $\xi_{si} = 0.1$.

Based on equation (3.34), a Riccati based H_∞ optimal control solution can be synthesized subject to

$$\left\|\mathbf{F}_l\left(\widehat{\mathbf{P}}_{aug}, \mathbf{K}_{sqr}\right)\right\|_\infty \leq \hat{\gamma} \tag{3.63}$$

that gives

$$\left\|\begin{matrix}\widehat{\mathbf{W}}_s(s)\hat{\mathbf{S}}_r \\ \widehat{\mathbf{W}}_t(s)\widehat{\mathbf{T}}_r\end{matrix}\right\|_\infty \leq \hat{\gamma} \tag{3.64}$$

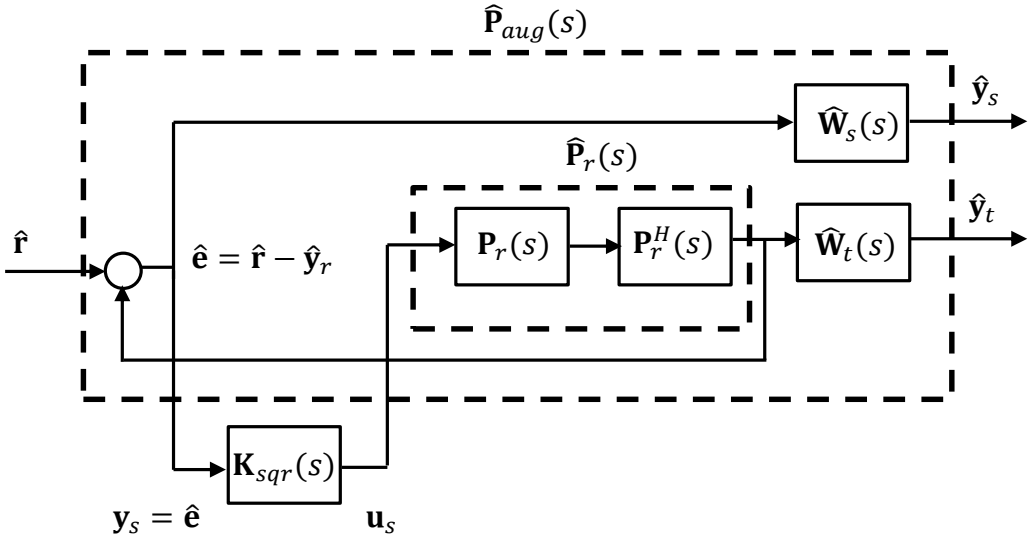

Figure 3.12 Augmentation for 'square' plant

Thus, with $\hat{\gamma} = 0.1 < 1$, a H_∞ controller based on 'square' plant is synthesized and may have the following state-space form

$$\mathbf{K}_{sqr}: \begin{cases} \dot{\mathbf{q}}_{sqr}^K = \mathbf{A}_{sqr}^K \mathbf{q}_{sqr}^K + \mathbf{B}_{sqr}^K \mathbf{u}_{sqr}^K \\ \mathbf{y}_{sqr}^K = \mathbf{C}_{sqr}^K \mathbf{q}_{sqr}^K + \mathbf{D}_{sqr}^K \mathbf{u}_{sqr}^K \end{cases} \tag{3.65}$$

where the controller input $\mathbf{u}_{sqr}^K = \hat{\mathbf{e}}_{4\times 1}$ and controller output $\mathbf{y}_{sqr}^K = \mathbf{u}_{s,4\times 1}$.

3.4.3 Full Column Rank Feedforward Term

In the 'square' plant, the feedforward term is given by

$$\mathbf{Q}_{sqr,m\times m} = \widehat{\mathbf{P}}_{r,n\times m} \mathbf{K}_{sqr,n\times m} \tag{3.66}$$

where $m = n = 4$. The rank of $\mathbf{Q}_{sqr}$ may be obtained by equation (3.46) as

$$\text{rank}(\mathbf{Q}_{sqr}) = \text{rank}(\widehat{\mathbf{P}}_\text{r}) = \text{rank}(\mathbf{K}_{sqr}) = 4 \tag{3.67}$$

Hence, based on singular value decomposition of equations (3.48) and (3.49), the singular values of $\mathbf{Q}_{sqr}$ follows

$$\sigma\left(\mathbf{Q}_{sqr}\ (j\omega)\right) = \Sigma_{sqr}(j\omega) = \begin{bmatrix} \Sigma_{sqr,1}(j\omega) & \cdots & 0 \\ \vdots & \ddots & \vdots \\ 0 & \cdots & \Sigma_{sqr,m}(j\omega) \end{bmatrix} \tag{3.68}$$

where the $\Sigma_{sqr,i}(j\omega)$ satisfy

$$\Sigma_{sqr,1} \geq \cdots \geq \Sigma_{sqr,m} > 0, m = \text{rank}\left(\mathbf{Q}_{sqr}\right) \tag{3.69}$$

Therefore, due to the full column rank feedforward term $\mathbf{Q}_{sqr}$, the singular value issues stated in equations (3.49) and (3.50) are now overcome.

3.4.4 Comprehensive H_∞ Optimization

Due to the full column rank of the feedforward term $\mathbf{Q}_{sqr}$ in the 'square' plant as stated in equations (3.66)-(3.69), comprehensive H_∞ optimization is now possible. Figure 3.13 shows the fully bounded closed loop sensitivity/complementary sensitivity functions obtained by the solution to singular value issue stated before. By comparing with those shown in Figure 3.8, singular values for the 'rectangular' plant are eliminated by the 'square' plant design. $\hat{\mathbf{S}}_r$ and $\hat{\mathbf{T}}_r$ now are well bounded by $\widehat{\mathbf{W}}_s^{-1}\hat{\gamma}$ and $\widehat{\mathbf{W}}_t^{-1}\hat{\gamma}$ following the H_∞ optimization. Therefore, the solution to the mixed sensitivity problem is now able to find a 'tight' bound for the H_∞ cost, $\hat{\gamma}$, as shown in Figure 3.14. This is in contrast to the 'loose' bound in the semi-optimization procedure shown in Figure 3.9.

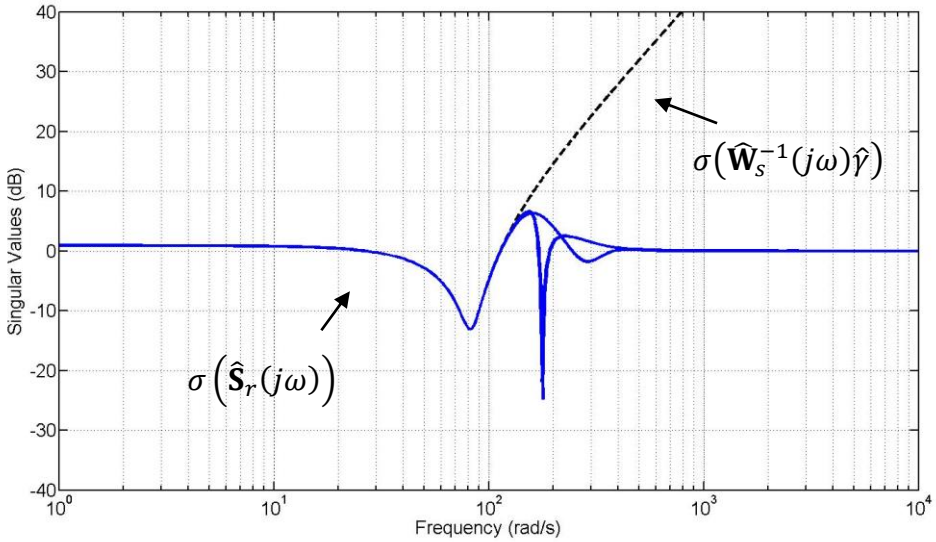

(a) Optimized $\sigma\left(\hat{\mathbf{S}}_r(j\omega)\right)$ and $\sigma\left(\hat{\mathbf{W}}_s^{-1}(j\omega)\hat{\gamma}\right)$

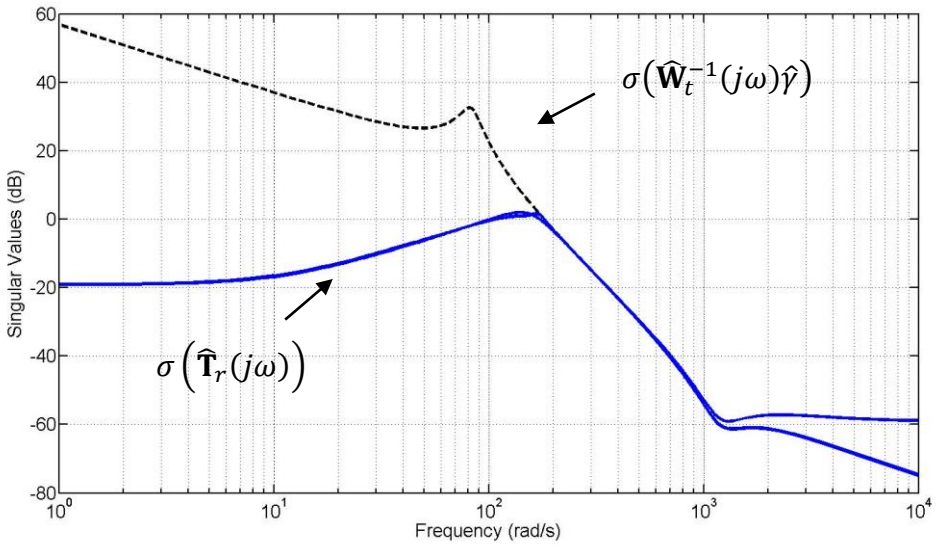

(b) Optimized $\sigma\left(\hat{\mathbf{T}}_r(j\omega)\right)$ and $\sigma\left(\hat{\mathbf{W}}_t^{-1}(j\omega)\hat{\gamma}\right)$

Figure 3.13 Optimized closed loop sensitivity/complementary sensitivity for 'square' plant design

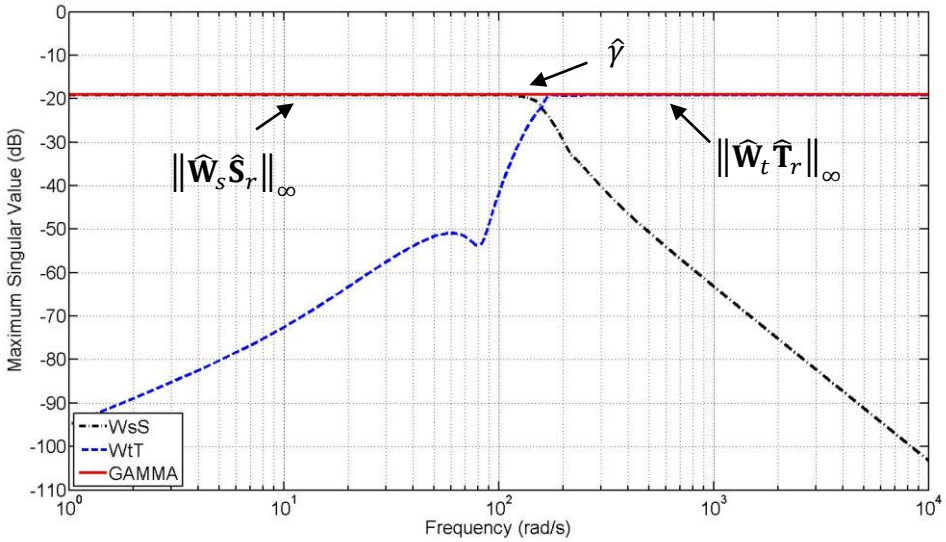

Figure 3.14 Comprehensive optimization procedure

3.5 'Rectangular'/'Square' Based Control Performance

This section presents the control performance from 'rectangular' and 'square' based H_∞ controllers designed in Sections 3.3 and 3.4. With regard to unbalance forcing response and simulated results, both control design methods are compared with different sensitivity weightings. The LTI controllers focus mainly on the rotor vibration attenuation under contact-free operation, especially around the rotor/AMB system first two resonance zones (83 rad/s and 125 rad/s) as stated in Section 2.2. The sensitivity design parameters are given in Table 3.2.

Table 3.2 'Rectangular'/'Square' design criteria

		H_∞ Cost	ε_i	w_{nsi} (rad/s)	ξ_{si}
'Rectangular'	$\mathbf{K}_{rec,1}$	$\gamma_1 = 0.1$	0.02	83	0.1
	$\mathbf{K}_{rec,2}$	$\gamma_2 = 0.105$	0.02	125	0.1
'Square'	$\mathbf{K}_{sqr,1}$	$\hat{\gamma}_1 = 0.11$	0.1	83	0.1
	$\mathbf{K}_{sqr,2}$	$\hat{\gamma}_2 = 0.109$	0.06	125	0.1

3.5.1 Unbalance Forcing Response

Rotor unbalance forcing response is important for safe machine operation. As a global view of vibrations at all sensors locations, RMS based unbalance forcing response is used:

$$v = \frac{1}{N}\sqrt{\sum_{i=1}^{N} s_{ix}^2} \tag{3.70}$$

where $N = 4$ is the number of observed nodes (3, 5, 11 and 13), and s_{ix}^2 is the squared displacement of node i in x direction. An eccentricity $m_e = 200\ \text{g} \cdot \text{cm}$ is considered on the disk at the non-driven end (node 14).

The unbalance forcing responses under PD only and Riccati based H_∞ controllers are shown in Figure 3.15. The rotor unbalance forcing response under 'square' control loop with $\mathbf{K}_{sqr,i}$ is attenuated more and over a wide rotational speed range compared with the 'rectangular' controller $\mathbf{K}_{rec,i}$.

In Figure 3.15(a), the closed loop system $\mathbf{F}_{cl}\left(\mathbf{P}(\Omega), \mathbf{K}_{rec,1}\right)$ becomes more sensitivity to unbalance forcing around 107 rad/s and then gets worse above that speed. However, $\mathbf{F}_{cl}\left(\widehat{\mathbf{P}}(\Omega), \mathbf{K}_{sqr,1}\right)$ still has the capability to reject disturbance at that speed, and can achieve vibration attenuation up to 120 rad/s, as can also be verified by $\hat{\mathbf{S}}_r$ shown in Figure 3.13 (a). Note that, due to the damped filter embedded in sensitivity weightings, control performance cannot be achieved when the rotor runs out of the design range.

The situations in Figure 3.15(b) are similar. The closed loop transfer function $\mathbf{F}_{cl}\left(\widehat{\mathbf{P}}(\Omega), \mathbf{K}_{sqr,2}\right)$ achieves better control perfomance by comparing with $\mathbf{F}_{cl}\left(\mathbf{P}(\Omega), \mathbf{K}_{rec,2}\right)$ in the design range. However, $\left(\widehat{\mathbf{P}}(\Omega), \mathbf{K}_{sqr,2}\right)$ is more sensitive to unbalance out of the design range when compared with $\mathbf{F}_{cl}\left(\mathbf{P}(\Omega), \mathbf{K}_{rec,2}\right)$.

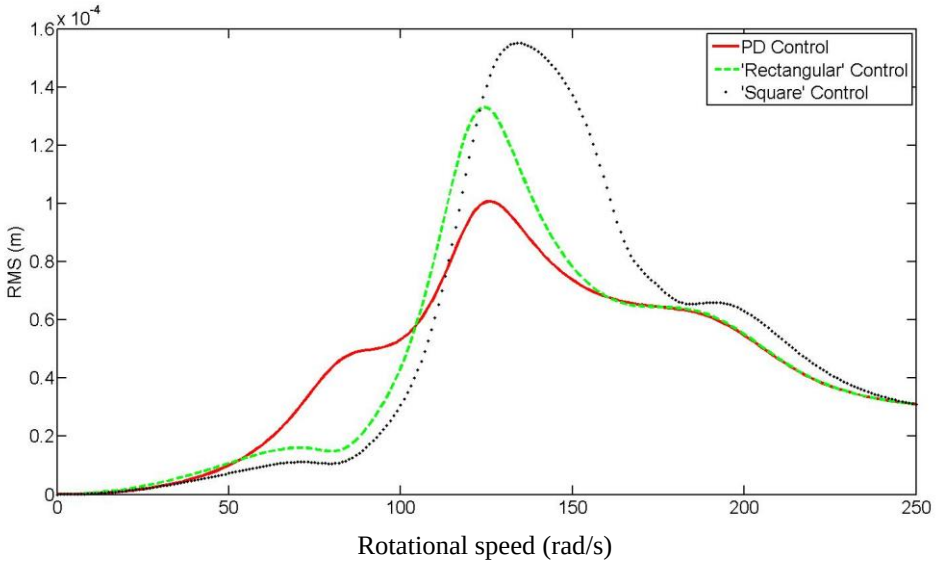

(a) Rotor/AMB system under controlled by ‘Rectangular’/‘Square’ controllers designed for 83 rad/s

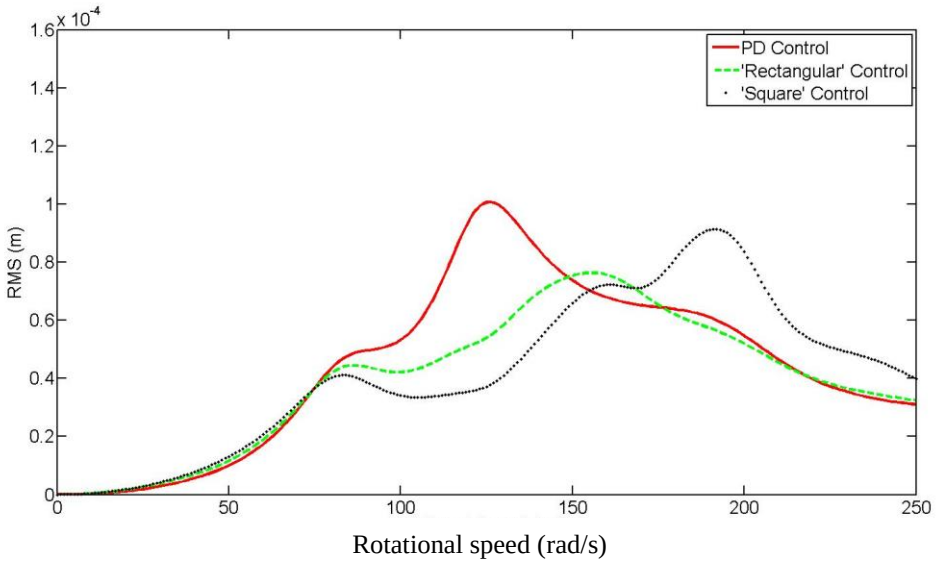

(b) Rotor/AMB system under controlled by ‘Rectangular’/‘Square’ controllers designed for 125 rad/s

Figure 3.15 Unbalance forcing response (RMS) variation with rotational speed, PD control only is shown in red, rotor under controlled by ‘rectangular’ is shown in green dashed line and ‘square’ is shown in black

3.5.2 Simulated results

Simulated Results of Controllers $\mathbf{K}_{rec,1}$ and $\mathbf{K}_{sqr,1}$

Simulation results of rotor/AMB system under controlled by $\mathbf{K}_{rec,1}$ and $\mathbf{K}_{sqr,1}$ are presented at two typical running speeds. The speed 83 rad/s is the design operating speed for both controllers. Also, the rotor is considered to run at 110 rad/s to examine the control performance when the rotational speed is out of the design range. These two specific speeds may indicate the benefits from 'square' control action, which could also be demonstrated in Figure 3.15.

Running at 83 rad/s: Rotor displacement in the *x*-coordinate of two sensor planes nearby the rotor non-driven end and AMB 2 (nodes 13 and 11) are shown in Figures 3.16 and 3.17. Both control actions activate at 1s, the vibrations due to unbalancing forcing are attenuated significantly under control. By comparing the results of 'rectangular' control, the benefits of 'square' control synthesis are not obvious due to rotor behaving as a rigid body mode at that speed. The stability/disturbance rejection from both controllers are thus good when rotor running at 83 rad/s. The rotor displacements of the other two sensor planes are similar and shown in Figures 1 and 2 in the Appendix A.

When rotating at 83 rad/s, control forces from the two controllers in time domain reveal almost the same amplitude, as shown in Figures 3 and 4 in Appendix A. Figure 3.18 shows the error signal $\hat{\mathbf{e}}(t) = -\hat{\mathbf{y}}(t)$ in time domain, fed into the controller $\mathbf{K}_{sqr,1}$.

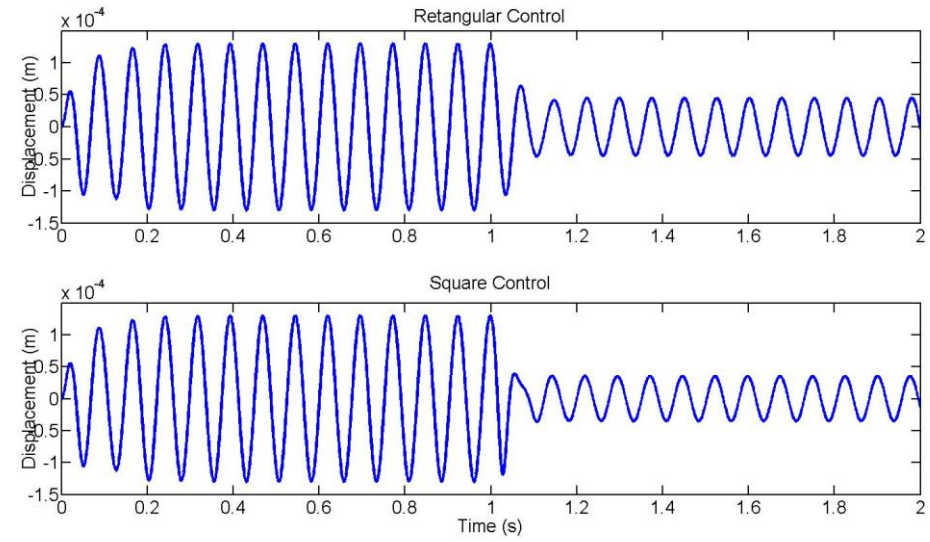

Figure 3.16 Rotor displacement in *x*-direction at sensor plane close to the rotor non-driven end (node 13) when $\Omega = 83$ rad/s, control action is activated at 1s

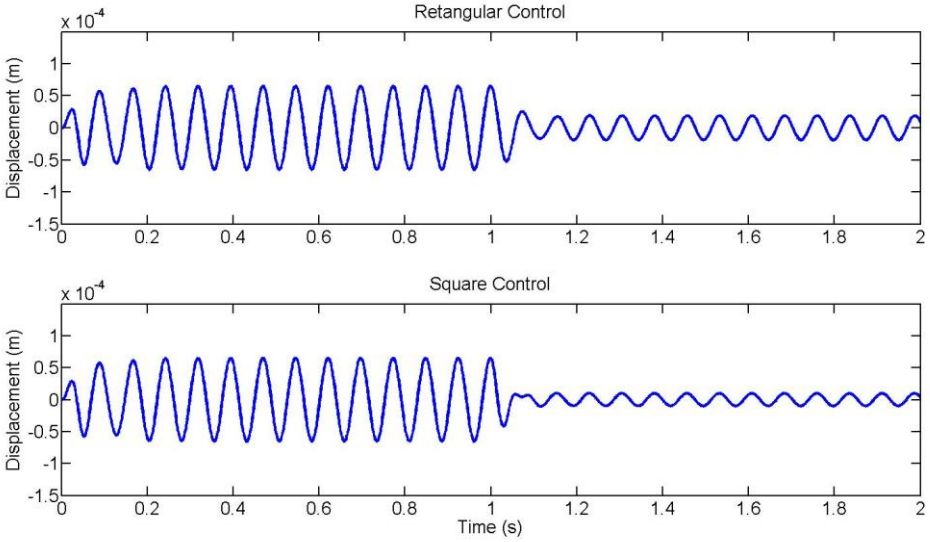

Figure 3.17 Rotor displacement in *x*-direction at sensor plane close to AMB 2 (node 11) when $\Omega = 83$ rad/s, control action is activated at 1s

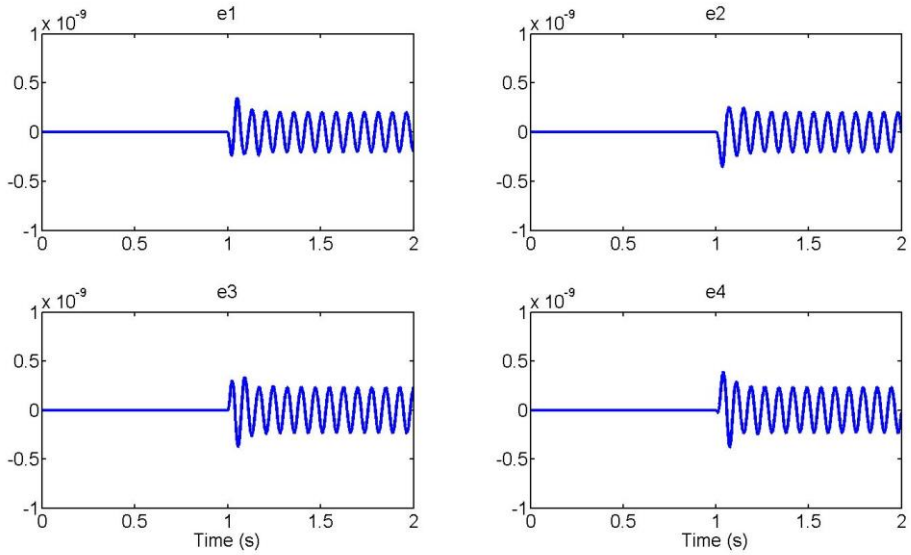

Figure 3.18 The dimension scaled error fed-in 'square' controller $\mathbf{K}_{sqr,1}$ when running at 83 rad/s

Running at 110 rad/s: Rotor displacement in *x*-coordinate of two sensor planes nearby the rotor non-driven end and AMB 2 (node 13 and 11) are shown in Figures 3.19 and 3.20. At such running speed, the 'rectangular' control action cannot attenuate rotor vibrations, and even makes worse. In contrast to that, the 'square' control action can still impose disturbance rejection. The rotor displacements of the other two sensor planes are similar and shown in Figures 5 and 6 in Appendix A.

With better disturbance rejection from controller $\mathbf{K}_{sqr,1}$, control forces from $\mathbf{K}_{sqr,1}$ has larger amplitude than that of $\mathbf{K}_{rec,1}$ when settling down. The corresponding control forces from the both control actions are shown in Figures 7 and 8 in the Appendix A. Figure 3.21 shows the error signal $\hat{\mathbf{e}}(t) = -\hat{\mathbf{y}}(t)$ when rotor runs at 110 rad/s.

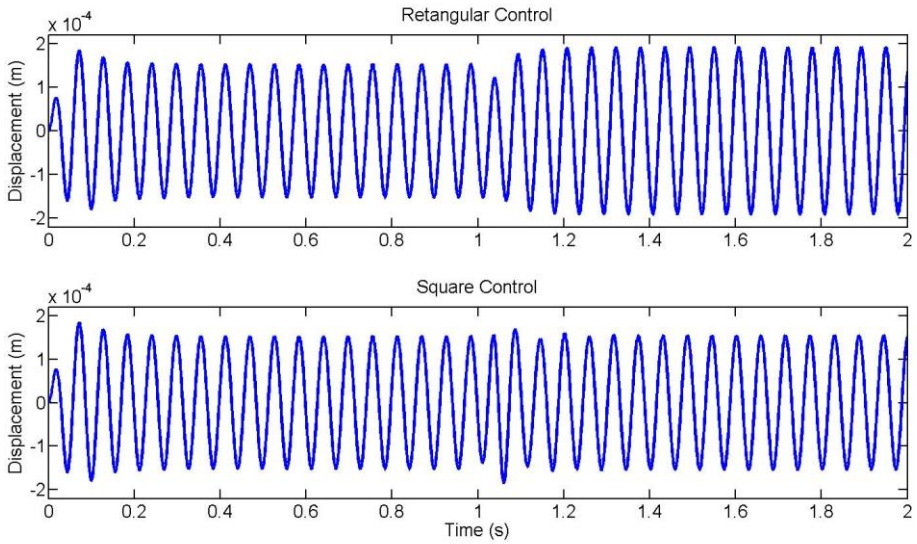

Figure 3.19 Rotor displacement in *x*-direction at sensor plane close to the rotor non-driven end (node 13) when $\Omega = 110$ rad/s, control action is activated at 1s

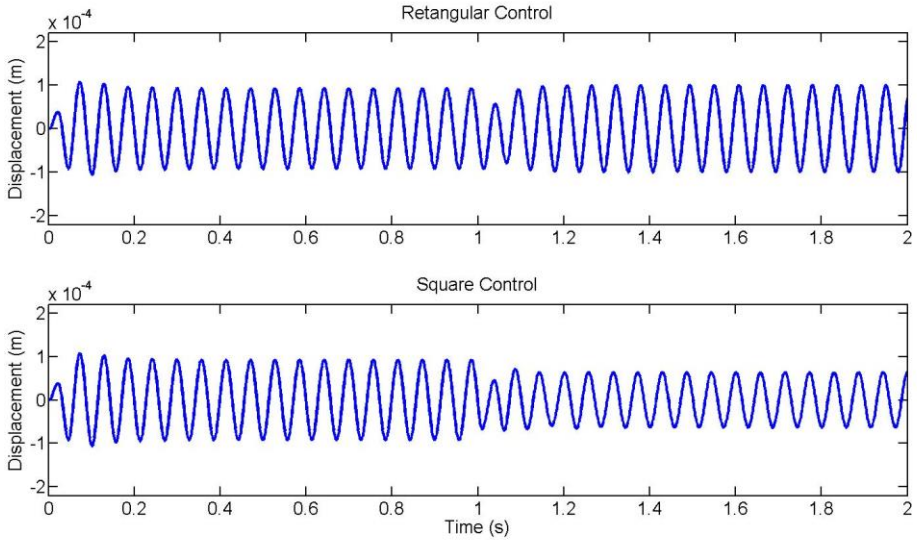

Figure 3.20 Rotor displacement in *x*-direction at sensor plane close to AMB 2 (node 11) when $\Omega = 110$ rad/s, control action is activated at 1s

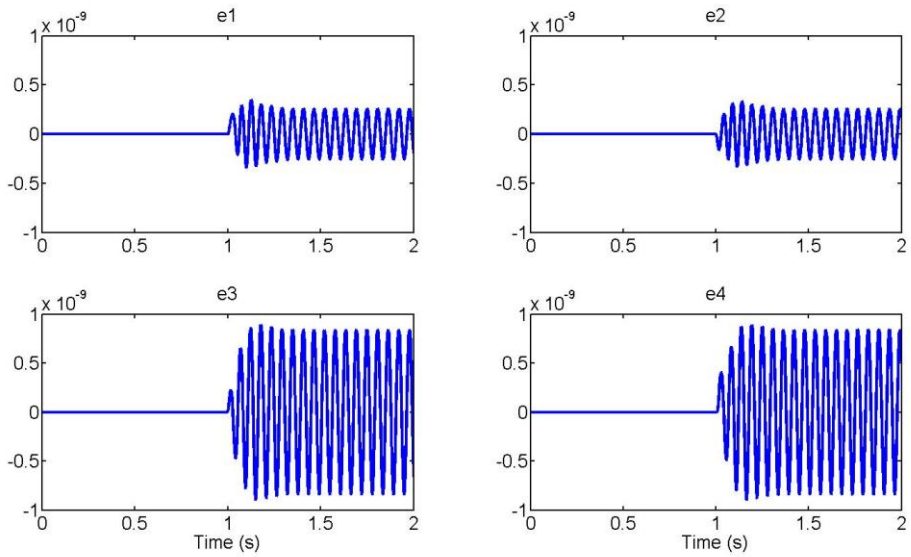

Figure 3.21 The dimension scaled error fed-in 'square' controller $\mathbf{K}_{sqr,1}$ when running at 110 rad/s

Simulated Results of Controllers $\mathbf{K}_{rec,2}$ and $\mathbf{K}_{sqr,2}$

Simulation results of rotor/AMB system under controlled by $\mathbf{K}_{rec,2}$ and $\mathbf{K}_{sqr,2}$ are presented, by two typical running speeds (125 rad/s and 140 rad/s). The two controllers are examined numerically, when rotor was running at the designed rotational speed (125 rad/s) and a speed out of design range (140 rad/s).

Running at 125 rad/s: Rotor displacement in *x*-coordinate of two sensor planes nearby non-driven end and AMB 2 are shown in Figures 3.22 and 3.23. Both controllers ($\mathbf{K}_{rec,2}, \mathbf{K}_{sqr,2}$) activate at 1s, the rotor vibrations due to unbalancing forcing are attenuated significantly. At such speed, 'square' control reveals slight better control performance. The rotor displacements of the other two sensor planes are similar and shown in Figures 9 and 10 in the Appendix A. The control forces are shown in Figures 11 and 12 in the Appendix.

Running at 140 rad/s: Rotor displacement in *x*-coordinate of two sensor planes nearby non-driven end and AMB 2 are shown in Figures 3.24 and 3.25. The rotor

behaves conical body motion when runs at 140 rad/s. The rotor vibrations at both ends are significant, especially at non-driven end nearby the unbalance forcing disk.

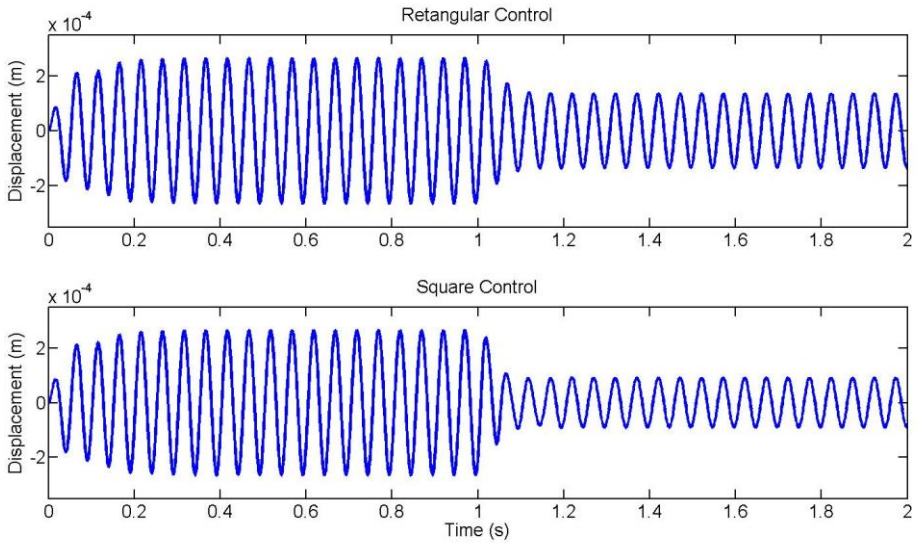

Figure 3.22 Rotor displacement in *x*-direction at sensor plane close to the rotor non-driven end (node 13) when $\Omega = 125$ rad/s, control action is activated at 1s

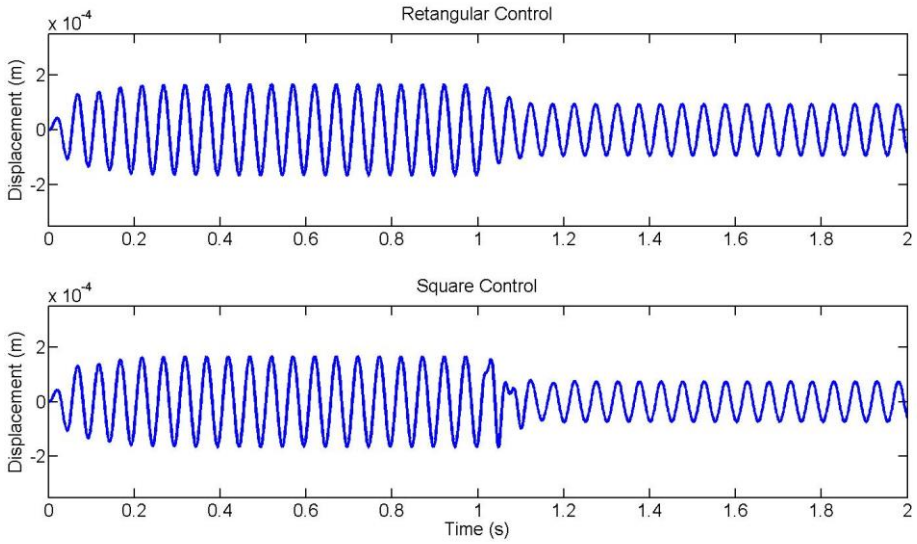

Figure 3.23 Rotor displacement in *x*-direction at sensor plane close to AMB 2 (node 11) when $\Omega = 125$ rad/s, control action is activated at 1s

Vibration attenuation by controllers are obvious; And the 'square' controller $\mathbf{K}_{sqr,2}$ achieves better performance than the 'rectangular' controller $\mathbf{K}_{rec,2}$. The rotor

displacements of the other two sensor planes are similar and shown in Figures 13 and 14, the control forces are shown in Figures 15 and 16 in the Appendix A. Figures 3.26 and 3.27 show the corresponding $\hat{\mathbf{e}}(t)$ fed in the 'square' controller $\mathbf{K}_{sqr,2}$.

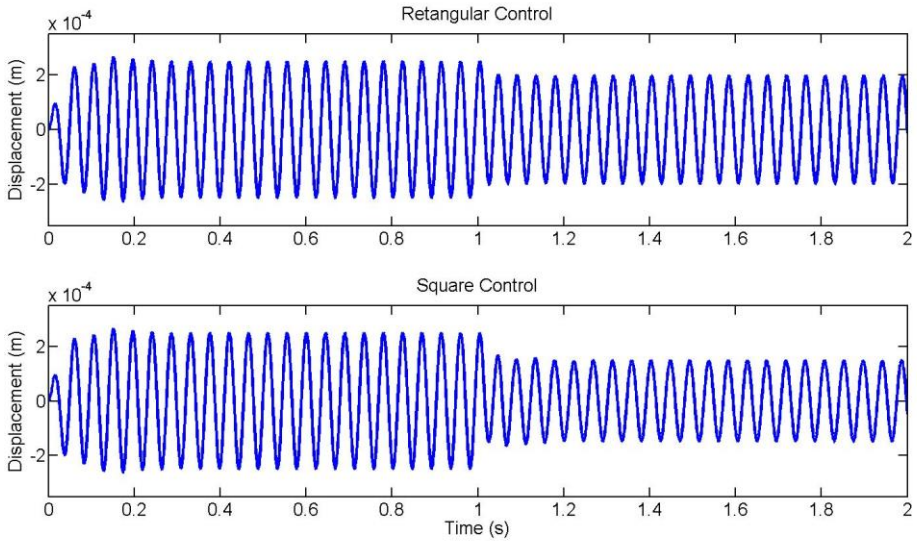

Figure 3.24 Rotor displacement in *x*-direction at sensor plane close to the rotor non-driven end (node 13) when $\Omega = 140$ rad/s, control action is activated at 1s

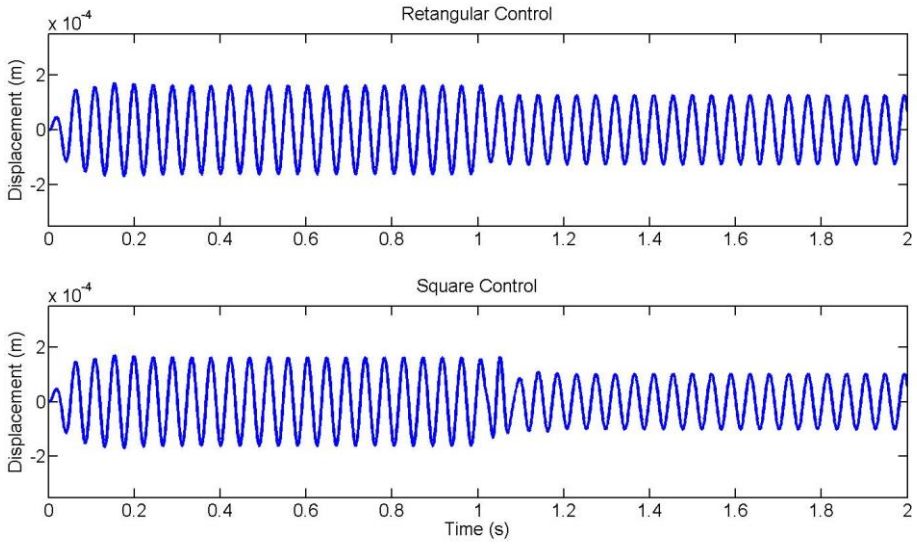

Figure 3.25 Rotor displacement in *x*-direction at sensor plane close to AMB 2 (node 11) when $\Omega = 140$ rad/s, control action is activated at 1s

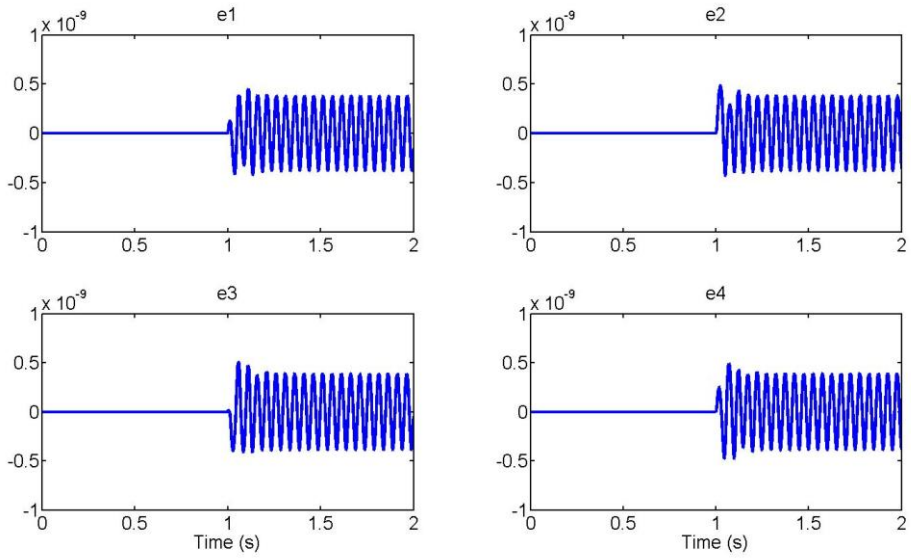

Figure 3.26 The dimension scaled error fed-in 'square' controller $\mathbf{K}_{sqr,2}$ when running at 125 rad/s

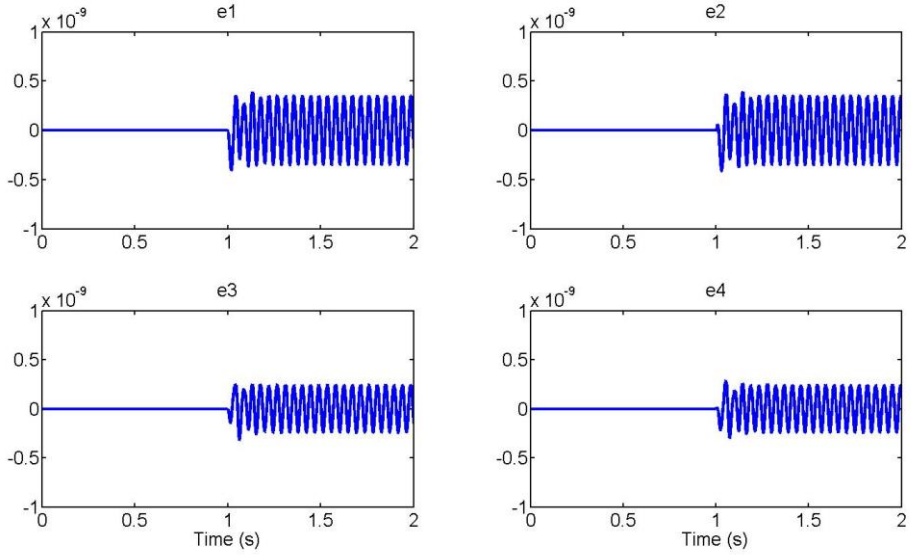

Figure 3.27 The dimension scaled error fed-in 'square' controller $\mathbf{K}_{sqr,2}$ when running at 140 rad/s

3.6 LTI Controller Switching Action

The benefits of the 'square' plant based H_∞ optimized control performance design is presented in Section 3.5. Over a large operating speed range, it may not be possible stabilize a rotor by using only one linear time invariant (LTI) H_∞ controller that has speed independent characteristics. This section addresses that problem by introducing a switching control system. The system contains two 'square' H_∞ controllers ($\mathbf{K}_{sqr,1}, \mathbf{K}_{sqr,2}$), designed to cover different speed ranges, together with an external signal to drive the switching action. When speed dependent unbalance forcing acts, each of the controllers is able to attenuate vibration of the rotor over the specific speed ranges. The controller switching points are selected according to a metric that takes account of measured rotor lateral vibration. However, a sudden switching action may induce significant transient disturbance and give rise to rotor vibration overshoot, possibly to the extent of causing rotor/TDB contact event. To alleviate this problem, a ramp switching signal was introduced such that two controllers may be switched smoothly over a given time period. The stability when two LTI controller working in tandem during ramp switching action was also examined numerically.

3.6.1 Switching Control Formulation

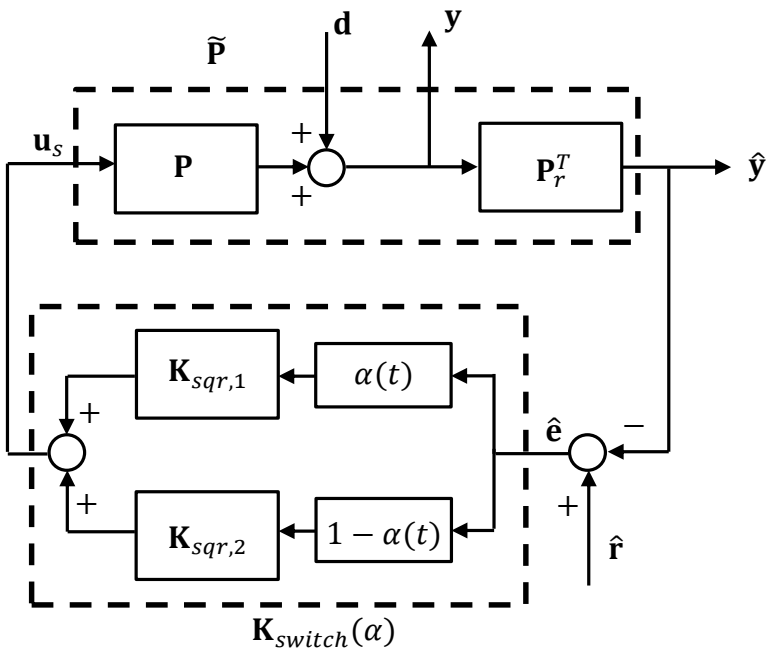

Figure 3.28 Configuration of switching control system implementation

Figure 3.28 shows the closed loop system for switching control system. When switching action activates, the input/output signal for each 'square' controller having state-space form according to equation (3.65) may be obtained as

$$\mathbf{y}_t^K = [\mathbf{I} \quad \mathbf{I}] \begin{bmatrix} \mathbf{y}_{sqr,1}^K \\ \mathbf{y}_{sqr,2}^K \end{bmatrix} \tag{3.71}$$

and

$$\begin{bmatrix} \mathbf{u}_{sqr,1}^K \\ \mathbf{u}_{sqr,2}^K \end{bmatrix} = \begin{bmatrix} \alpha(t) \\ 1-\alpha(t) \end{bmatrix} \hat{\mathbf{e}} \tag{3.72}$$

Thus, the switching control system, which is dependent on switching signal $\alpha(t)$, may be formed in time domain as

$$\mathbf{y}_t^K = \mathbf{K}_{switch}(\alpha)\hat{\mathbf{e}} \tag{3.72}$$

where $\mathbf{K}_{switch}(\alpha) = \begin{bmatrix} \mathbf{K}_{sqr,1} & \mathbf{0} \\ \mathbf{0} & \mathbf{K}_{sqr,2} \end{bmatrix} \begin{bmatrix} \alpha(t) \\ 1-\alpha(t) \end{bmatrix}$. Based on equations (3.71) and (3.72), two separately designed LTI model based controllers may have to be

implemented online cooperatively at same time period. Normally, that induces robustness stability issues, since each controller is designed without taking the other control action into account.

During switching, complementary sensitivity functions in control loop for each controller may be obtained as

$$\begin{aligned}\widehat{\mathbf{T}}_{switch,1} &= \left(\mathbf{I}+\mathbf{F}_{cl}\left(\widehat{\mathbf{P}},\mathbf{K}_{sqr,2}\right)\mathbf{K}_{sqr,1}\right)^{-1}\mathbf{F}_{cl}\left(\widehat{\mathbf{P}},\mathbf{K}_{sqr,2}\right)\mathbf{K}_{sqr,1}\\ \widehat{\mathbf{T}}_{switch,2} &= \left(\mathbf{I}+\mathbf{F}_{cl}\left(\widehat{\mathbf{P}},\mathbf{K}_{sqr,1}\right)\mathbf{K}_{sqr,2}\right)^{-1}\mathbf{F}_{cl}\left(\widehat{\mathbf{P}},\mathbf{K}_{sqr,1}\right)\mathbf{K}_{sqr,2}\end{aligned} \tag{3.73}$$

The sensitivity functions can be expressed as:

$$\begin{aligned}\hat{\mathbf{S}}_{switch,1} &= \left(\mathbf{I}+\mathbf{F}_{cl}\left(\widehat{\mathbf{P}},\mathbf{K}_{sqr,2}\right)\mathbf{K}_{sqr,1}\right)^{-1}\\ \hat{\mathbf{S}}_{switch,2} &= \left(\mathbf{I}+\mathbf{F}_{cl}\left(\widehat{\mathbf{P}},\mathbf{K}_{sqr,1}\right)\mathbf{K}_{sqr,2}\right)^{-1}\end{aligned} \tag{3.74}$$

It is possible to design controllers with complementary sensitivity functions based on equations (3.73) and (3.74) including observer based switching scheme, but this would increase the order of the controller, making it difficult to implement in real-time.

3.6.2 Switching Arrangement

The switching point is selected based on unbalance forcing RMS responses shown in Figure 3.29. RMS response estimated by equation (3.70), can show the global vibration situation under unbalance forcing. The selected switching point, from $\mathbf{K}_{sqr,1}$ to $\mathbf{K}_{sqr,2}$ (102 rad/s) as summarized in Table 3.2, can benefit all sensor vibration signals during switching action. Under designed switching, the first two resonant modes vibration are attenuated significantly. Furthermore, control action may be switched back to PD control only when running above160 rad/s.

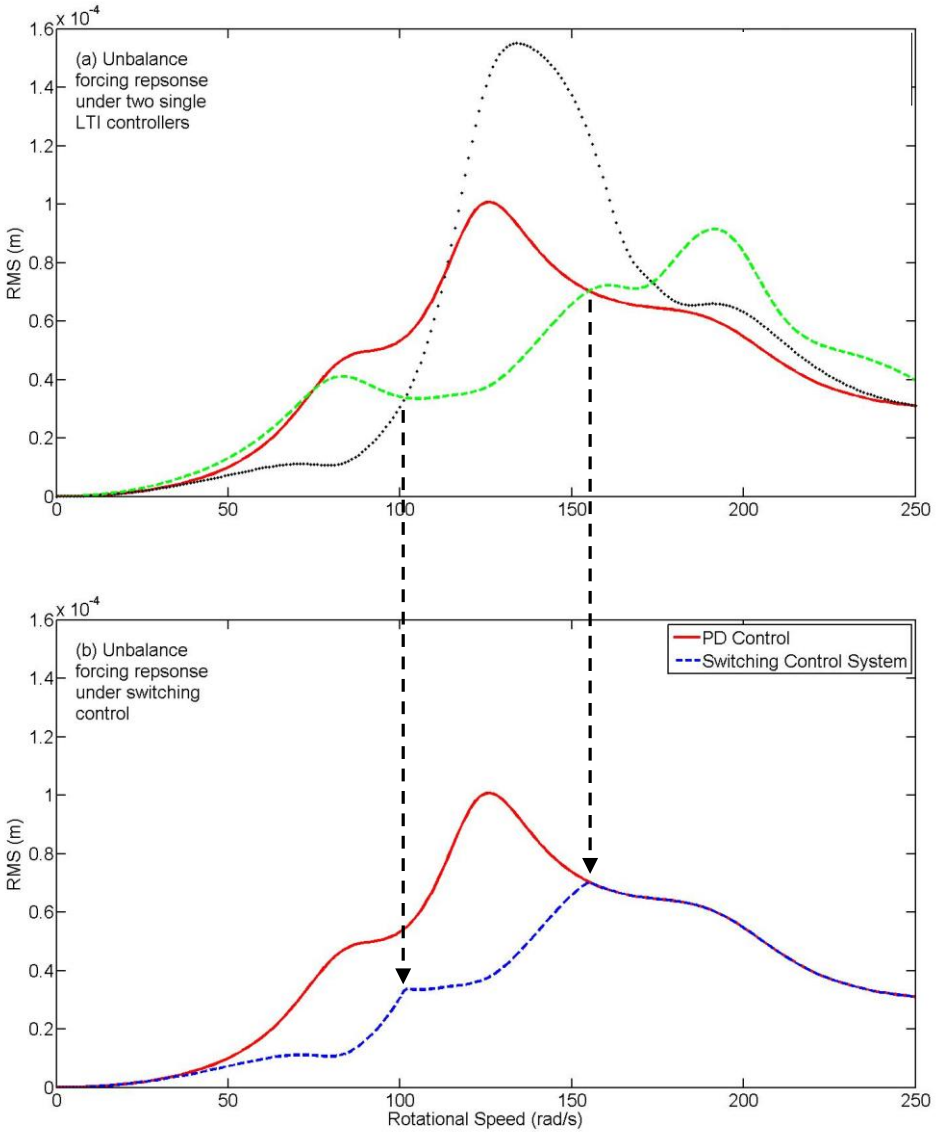

Figure 3.29 Unbalance forcing RMS response variation with rotational speed, rotor/AMB system controlled by $\mathbf{K}_{sqr,1}$ is shown in black, and $\mathbf{K}_{sqr,2}$ is shown in green dashed line

Switching Signal

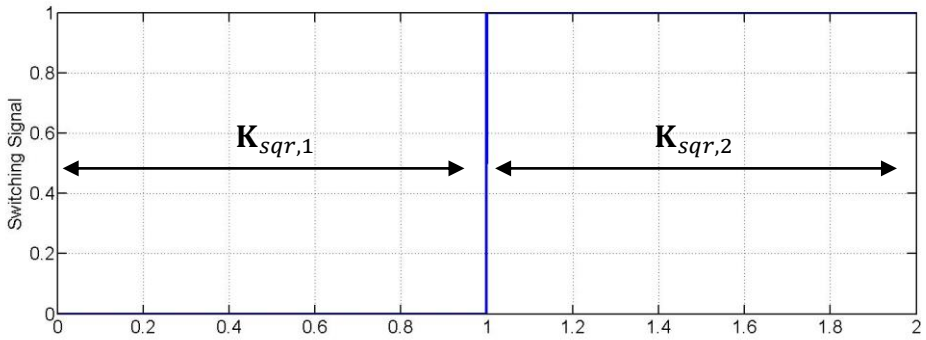

(a) Step switching signal

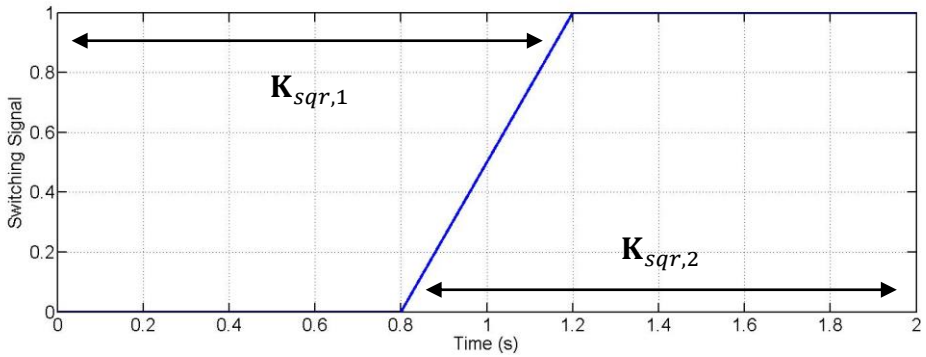

(b) Ramp switching signal

Figure 3.30 Switching signals

Figure 3.30 shows the switching signals. In this section, two switching signals (step/ramp) are considered. The step signal may be able to avoid the situation that, two controllers are working in the same time period. However, the sudden switching action may cause significant overshoot and have potential to excite system high frequency modes, those may lead to an instability issue. The ramp signal would smooth out transients.

3.6.3 Simulated Switching Action

Figures 3.31-3.34 shows the rotor displacements at sensor planes when controllers commence switching action at 102 rad/s. The step switching action as shown in Figure 3.31-3.34 excites system high frequency response after 1s. The time domain response of the rotor/AMB system controlled by $\mathbf{K}_{sqr,2}$ reveal stability issues with the rotor displacement including obvious high frequency from 1s to 2s. In contrast to those happened during step switching, ramp switching action revealed better transients with evident less overshoot. When switching action finished, rotor vibration revealed stable response as shown in Figures 3.31-3.34. Stability issue induced by controllers working in tandem, was not detected during ramp switching action. That may be explained that, the two controllers ($\mathbf{K}_{sqr,1}$ and $\mathbf{K}_{sqr,2}$) obtained less H_∞ cost $\hat{\gamma}_1 = 0.11$ and $\hat{\gamma}_2 = 0.109$, which are far from the critical robust stability guaranteed value 1. Thus, the both controllers are enabled more robustness.

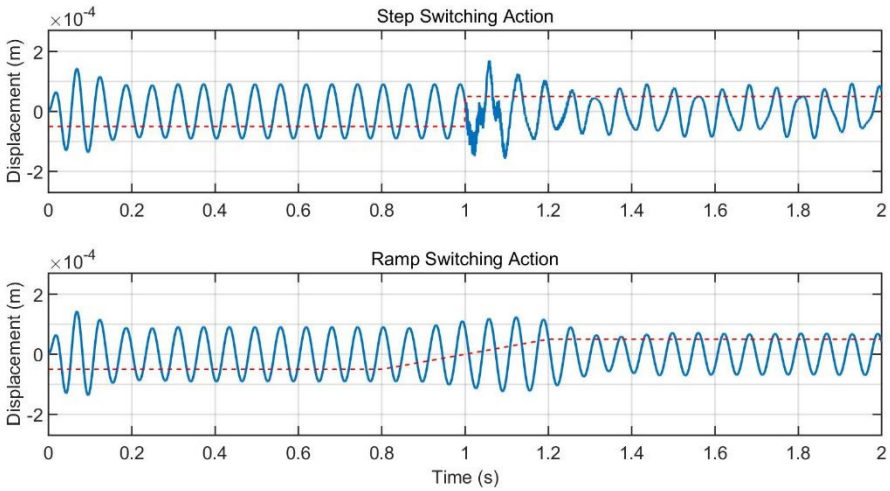

Figure 3.31 Rotor displacement in *x*-direction at sensor plane close to the rotor non-driven end (node 13) during step/ramp switching action when $\Omega = 102\ \mathrm{rad/s}$, red dashed line indicates the switching signal

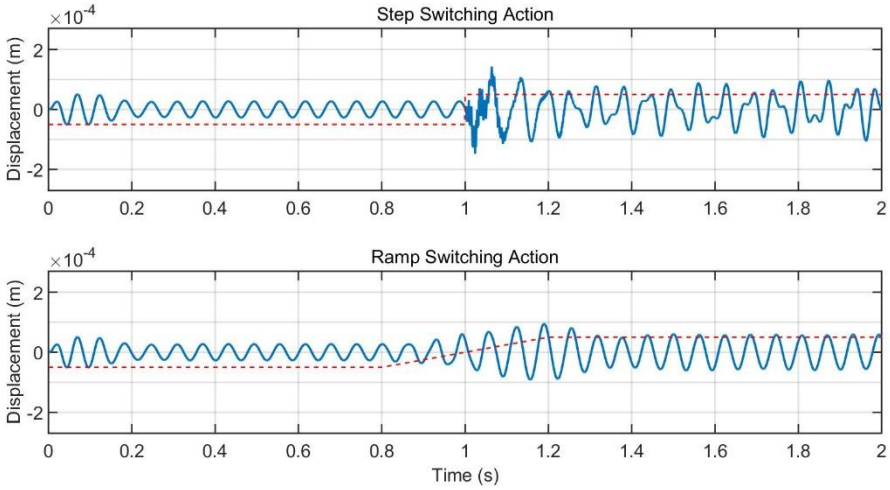

Figure 3.32 Rotor displacement in *x*-direction at sensor plane close to AMB 2 (node 11) during step/ramp switching action when $\Omega = 102\ \mathrm{rad/s}$, red dashed line indicates the switching signal

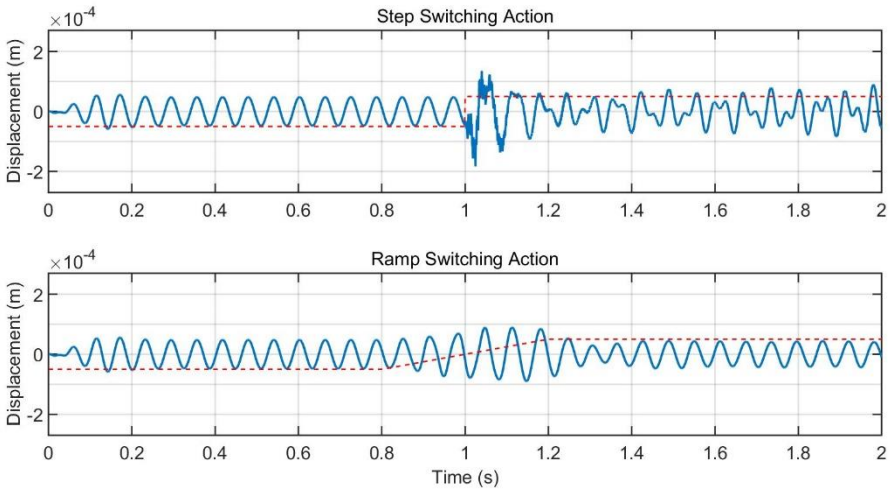

Figure 3.33 Rotor displacement in *x*-direction at sensor plane close to AMB 1 (node 5) during step/ramp switching action when $\Omega = 102$ rad/s, red dashed line indicates the switching signal

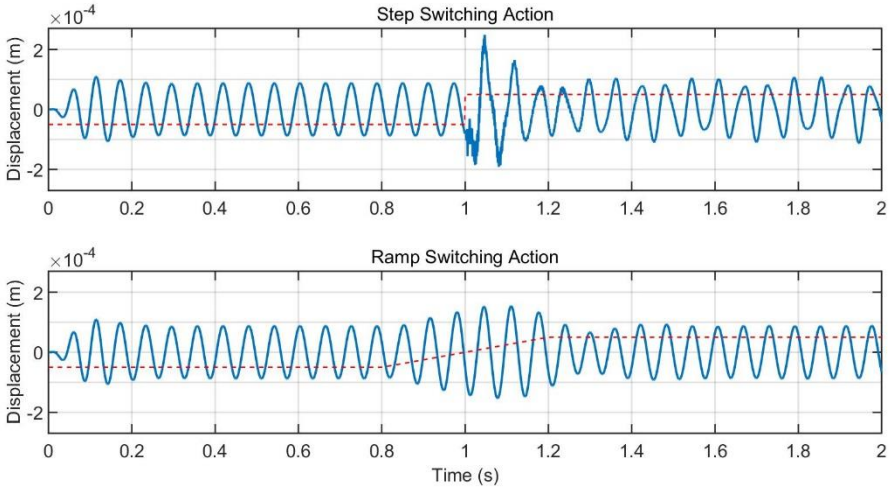

Figure 3.34 Rotor displacement in *x*-direction at sensor plane close to the motor end (node 3) during step/ramp switching action when $\Omega = 102$ rad/s, red dashed line indicates the switching signal

3.7 Closure

This chapter introduces a model reduction technique for the LTI system, and shows how the '**D**' matrix in a reduced order model effects system multiplicative model error. Based on the LTI reduced order system, Section 3.2 presents a Riccati based H_∞ optimization procedure and also the solution to the mixed sensitivity problem. Then, a Riccati based H_∞ controller is synthesized in Section 3.3. However, due to the discrepancy between the number of system inputs and outputs a so called 'rectangular' plant, with a non-full column rank feedforward term would be derived. That may give rise to singular values issues and result in a semi-optimized control solution. In order to consider H_∞ optimization fully, Section 3.4 proposes a 'square' plant to cope with the singular values issues as stated in Section 3.3. By using simulation results, Section 3.5 compares the both LTI control design in class of controllers, and discusses the advantages of 'square' controller.

To extend the LTI H_∞ controller operation range, Section 3.6 proposes a switching control system to enable a number of H_∞ controllers working in tandem. Step and ramp switching action is presented in the simulation results. It can be concluded that, ramp switching signal offers better control performance with better transients and less sensitivity to high frequency response. However, the stability during ramp switching should be considered as the controllers synthesized with low H_∞ cost value.

Chapter 4 LMI Robust Control for Speed Dependent Rotor/AMB System

Due to gyroscopic moments, rotor dynamics will vary with rotational speed during rotor/AMB system operation. Flexible rotor responses split into separate backward/forward modes when running at high speed. As augmented, plant parameter independency usually applies. Riccati based H_∞ controller optimization at a single speed may not be able to stabilize a system over all speeds although disturbance rejection may be achieved over a narrow range. Chapter 3 introduced a switching control system with two LTI controllers, which attenuates vibrations over a wider speed range. However, transients during switching are evitable. Also, sudden switching may excite high order modes. There is therefore a need to employ speed as a controller parameter. If established, this would be a new approach to speed dependent vibration control of rotor/AMB systems.

Linear Matrix Inequalities (LMIs) enable a framework for a design tool to solve the mixed sensitivity problem in H_∞ control optimization, and enable gain-scheduling. A controller may use real-time measurements to guarantee robust stability when the controlled system has parameter dependency. For speed-dependent control, rotational speed measured from an encoder can be used as linear parameter varying (LPV) input to adjust a LMI controller. Accordingly, a speed dependent rotor/AMB system may be modelled as a polytopic form with two vertex systems representing min/max rotational speed.

4.1 LPV System Description

If system dynamic depends on a variable parameter, a linear time invariant (LTI) state-space model may be insufficient for controller design purposes. Generally, the parameter dependent plants can be formed as

$$\mathbf{P}(\theta(t)): \begin{cases} \dot{\mathbf{q}}(t) = \mathbf{A}(\theta(t))\mathbf{q}(t) + \mathbf{B}(\theta(t))\mathbf{u}(t) \\ \mathbf{y}(t) = \mathbf{C}(\theta(t))\mathbf{q}(t) + \mathbf{D}(\theta(t))\mathbf{u}(t) \end{cases} \tag{4.1}$$

where the time varying parameter dependency induced by $\theta(t)$ can be treated as structured uncertainty. It is used in feedback to adapt a gain-scheduled controller to satisfy the varying plant dynamics [67]. Practically, $\theta(t)$ would have to be measured.

However, the equation (4.1) shows parameter dependency in all system matrices **A**, **B**, **C**, **D**, which may induce unnecessary issues during controller design. It is possible to restrict system parameter dependency to be in one of state-space matrices only, such as **A**:

$$\mathbf{P}\big(\theta(t)\big) = \begin{bmatrix} \mathbf{A}(\theta(t)) & \mathbf{B} \\ \mathbf{C} & \mathbf{D} \end{bmatrix} \tag{4.2}$$

4.1.1 LFT Formulation for LPV System

Equation (4.2) shows a very general description for a parameter dependent system having parameter dependency in the **A** matrix. It is possible to explain the nature of a parameter dependent system in particular circumstances. However, an insufficient description on how a varying parameter represents the system dynamics may induce difficulties for LMI based gain-scheduling control optimization. A linear fractional transformation LFT may be able to solve such problems, with the assumption that the system matrix $\mathbf{A}(\theta(t))$ is a linear fractional function of the varying parameter $\theta(t)$ and the plant $\mathbf{P}\big(\theta(t)\big)$ dynamics may depend affinely on the time-varying parameter $\theta(t)$. Thus, $\mathbf{A}(\theta(t))$ may be expressed as

$$\mathbf{A}\big(\theta(t)\big) = \mathbf{A}_0 + \theta(t)\mathbf{A}_\theta \tag{4.3}$$

where $\mathbf{A}_0$ is independent of system dynamics and $\mathbf{A}_\theta$ is a matrix coefficient of the dynamic term having parameter dependency.

Based on equations (4.2) and (4.3), the LPV plant may be expressed as

$$\mathbf{P}\big(\theta(t)\big) = \mathbf{P}_0 + \theta(t)\mathbf{P}_\theta \tag{4.4}$$

where $\mathbf{P}_0 = \begin{bmatrix} \mathbf{A}_0 & \mathbf{B} \\ \mathbf{C} & \mathbf{D} \end{bmatrix}$ and $\mathbf{P}_\theta = \begin{bmatrix} \mathbf{A}_\theta & \mathbf{0} \\ \mathbf{0} & \mathbf{0} \end{bmatrix}$.

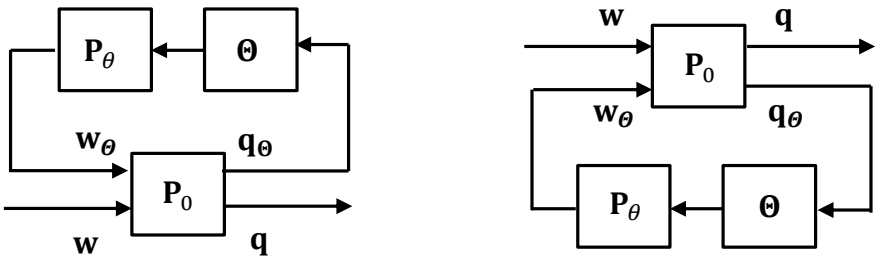

Figure 4.1 Block diagram of LFT

The upper/lower linear fractional transformations of a parameter dependent plant with interaction of linear varying parameter can be expressed as

$$\mathbf{y} = \mathbf{F}_{\boldsymbol{u}}(\mathbf{P}_0, \mathbf{P}_\theta \mathbf{\Theta})\mathbf{u}, \mathbf{y} = \mathbf{F}_{\boldsymbol{l}}(\mathbf{P}_0, \mathbf{P}_\theta \mathbf{\Theta})\mathbf{u} \tag{4.5}$$

where $\mathbf{\Theta}$ is the time varying parameter polytope, which specifies how $\theta(t)$ enters the system dynamics. The corresponding block diagrams are shown in Figure 4.1.

In the real-time implementation, $\theta(t)$ may be measured in discrete time, in which case

$$\mathbf{\Theta} = \text{diag}(\theta_1 \mathbf{I}_1, \theta_2 \mathbf{I}_2, \dots, \theta_k \mathbf{I}_k) \tag{4.6}$$

where θ_i specifies how the continuous time variable $\theta(t)$ enters into the system.

4.1.2 Polytope LPV System

For computational reasons, it is convenient to form the parameter dependent plant as a polytope to enable gain-scheduling for a controller. The real-time measured varying parameter $\theta(t)$ normally is restricted to varying in a specified 'parameter box' as

$$\theta(t) \in \mathbf{\Theta} := \mathbf{Co}\{\theta_1, \theta_2, \dots, \theta_n)\} \tag{4.7}$$

where

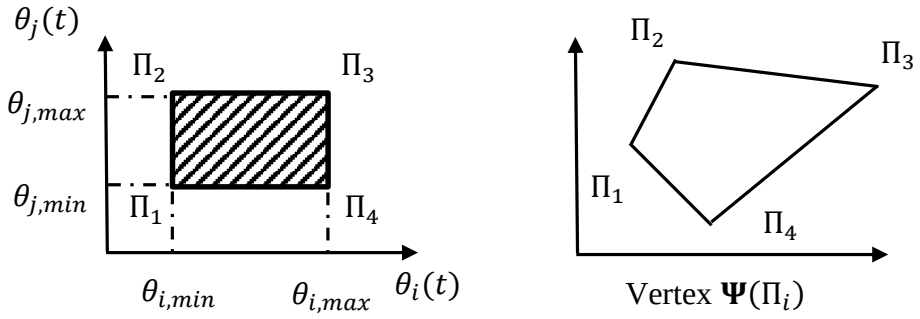

Figure 4.2 Polytope state-space matrices defined by a 'parameter box'

$$\mathbf{Co}\{\theta_1, \theta_2, \dots, \theta_n)\} = \left\{ \sum_{i=1}^{n} a_i \theta_i : \; a_i \geq 0, \sum_{i=1}^{n} a_i = 1 \right\} \tag{4.8}$$

where a_i is the polytopic coordinate.

Hence, from equations (4.7) and (4.8), the varying parameter can be defined as ranging in a polytopic space $\boldsymbol{\mathcal{R}}^n$ as

$$\theta(t) \in \; \boldsymbol{\Theta} := \mathbf{Co}\{\Pi_1, \Pi_2, \dots, \Pi_n)\} \tag{4.9}$$

where Π_i is a 'corner' vertex, characterizing the polytope. It can be mapped in the 'parameter box' by the lower and upper bounds of each θ_i.

Based on the polytopic variation of the system stated in equation (4.9), a LPV system in polytope is given by

$$\mathbf{P}\big(\theta(t)\big) := \mathbf{Co}\{\boldsymbol{\Psi}(\Pi_i)\} = \sum_{i=1}^{n} a_i \boldsymbol{\Psi}(\Pi_i) \tag{4.10}$$

where $\boldsymbol{\Psi}(\Pi_i) = \begin{bmatrix} \mathbf{A}_0 + \Pi_i \mathbf{A}_\theta & \mathbf{B} \\ \mathbf{C} & \mathbf{D} \end{bmatrix}$ is the vertex plant 'frozen' at a polytope corner. Figure 4.2 shows the case when $n = 4$, under the mapped $\boldsymbol{\Psi}(\Pi_i)$, if the polytope parameter box is defined by the vertices Π_i.

4.2 LPV Model Reduction

Model reduction for a LPV system may be proposed as stated in Section 3.1. By deleting full order model high frequencies modes, a reduced order model retains low frequency response with sufficient accuracy. Following the solution to equation (3.2), the system parameter independent term may be defined:

$$\mathbf{A}_0\mathbf{V}_0 = \mathbf{V}_0\mathbf{\Lambda}_0 \tag{4.11}$$

where $\mathbf{V}_0$ and $\mathbf{\Lambda}_0$ are eigen-vectors/values of $\mathbf{A}_0$, that enable system states as

$$\mathbf{q} = \mathbf{V}_0\mathbf{p}_0 \tag{4.12}$$

it follows that

$$\begin{gathered}\dot{\mathbf{p}}_0 = \mathbf{\Lambda}_0\mathbf{p}_0 + \theta\mathbf{Q}\mathbf{p}_0 + \mathbf{V}_0^{-1}\mathbf{B}\mathbf{u} \\ \mathbf{y} = \mathbf{C}\mathbf{V}_0\mathbf{p}_0 + \mathbf{D}\mathbf{u}\end{gathered} \tag{4.13}$$

where $\mathbf{Q} = \mathbf{V}_0^{-1}\mathbf{A}_\theta\mathbf{V}_0$ is a non-diagonal matrix having parameter dependency, and can be partitioned as $\mathbf{Q} = \begin{bmatrix}\mathbf{Q}_{ll} & \mathbf{Q}_{lh} \\ \mathbf{Q}_{hl} & \mathbf{Q}_{hh}\end{bmatrix}$ by low 'l' and high 'h' frequencies, $\mathbf{p}_0 = \begin{bmatrix}\mathbf{p}_{0l} \\ \mathbf{p}_{0h}\end{bmatrix}$ Therefore,

$$\begin{bmatrix}\dot{\mathbf{p}}_{0l} \\ \dot{\mathbf{p}}_{0h}\end{bmatrix} = \begin{bmatrix}\mathbf{\Lambda}_{0l} & \mathbf{0} \\ \mathbf{0} & \mathbf{\Lambda}_{0h}\end{bmatrix}\begin{bmatrix}\mathbf{p}_{0l} \\ \mathbf{p}_{0h}\end{bmatrix} + \theta\begin{bmatrix}\mathbf{Q}_{ll} & \mathbf{Q}_{lh} \\ \mathbf{Q}_{hl} & \mathbf{Q}_{hh}\end{bmatrix}\begin{bmatrix}\mathbf{p}_{0l} \\ \mathbf{p}_{0h}\end{bmatrix} + \begin{bmatrix}\breve{\mathbf{B}}_l \\ \breve{\mathbf{B}}_h\end{bmatrix}\mathbf{u}_c \tag{4.14}$$

Retaining low frequency states only,

$$\dot{\mathbf{p}}_{0l} = \mathbf{\Lambda}_{0l}\mathbf{p}_{0l} + \theta\mathbf{Q}_{ll}\mathbf{p}_{0l} + \breve{\mathbf{B}}_l\mathbf{u}_c \tag{4.15}$$

then following equations (3.12) and (3.13), the LPV reduced order model may be expressed as

$$\mathbf{P}_r\big(\theta(t)\big) = \begin{bmatrix}\mathbf{A}_r^0 & \mathbf{B}_r \\ \mathbf{C}_r & \mathbf{D}_r\end{bmatrix} + \theta(t)\begin{bmatrix}\mathbf{A}_r^\theta & \mathbf{0} \\ \mathbf{0} & \mathbf{0}\end{bmatrix} \tag{4.16}$$

where $\mathbf{A}_r^0 = \begin{bmatrix}\mathrm{Re}(\mathbf{\Lambda}_{0l}) & -\mathrm{Im}(\mathbf{\Lambda}_{0l}) \\ \mathrm{Im}(\mathbf{\Lambda}_{0l}) & \mathrm{Re}(\mathbf{\Lambda}_{0l})\end{bmatrix}$, $\mathbf{A}_r^\theta = \begin{bmatrix}\mathrm{Re}(\mathbf{Q}_{ll}) & -\mathrm{Im}(\mathbf{Q}_{ll}) \\ \mathrm{Im}(\mathbf{Q}_{ll}) & \mathrm{Re}(\mathbf{Q}_{ll})\end{bmatrix}$, $\mathbf{B}_r = \begin{bmatrix}\mathrm{Re}(\breve{\mathbf{B}}_l) \\ \mathrm{Im}(\breve{\mathbf{B}}_l)\end{bmatrix}$,

$\mathbf{C}_r = \mathbf{C}[\mathrm{Re}(\mathbf{V}_{0l}) - \mathrm{Im}(\mathbf{V}_{0l})]$ and $\mathbf{D}_r = (\mathbf{D} - \mathbf{C}\mathrm{Re}(\mathbf{V}_{0h}{\mathbf{\Lambda}_{0h}}^{-1}\breve{\mathbf{B}}_h))$.

Based on equations (4.9) and (4.10), a reduced order plant with linear interpolation may be specified as polytope:

$$\mathbf{P}_r\big(\theta(t)\big) := \sum_{i=1}^{n} a_i \boldsymbol{\Psi}_r(\Pi_i) \tag{4.17}$$

where $\boldsymbol{\Psi}_r(\Pi_i) = \begin{bmatrix} \mathbf{A}_r^0 + \Pi_i \mathbf{A}_r^\theta & \mathbf{B}_r \\ \mathbf{C}_r & \mathbf{D}_r \end{bmatrix}$.

4.3 LMI Based Gain-Scheduling Control

Rather than seeking a single robust LTI controller, the LMI based gain-scheduling control technique enable a control solution to incorporate a varying parameter from real-time measurement to adjust itself to dynamic operating conditions. Such a controller can achieve higher control performance, especially when the controlled system operates over larger parameter variations.

Depending on the plant form, a gain-scheduling controller can be synthesized with parameter dependency. A controller in polytopic mode is commonly used, as it is practical for real-time implementation.

4.3.1 LPV Control Structure

Apkarian et al. [68] introduce a gain-scheduling H_∞ optimal controller computation method based on the LMI approach, when a parameter dependent plant can be formed as a polytope with varying parameter $\boldsymbol{\Theta}$. That allows each single LMI based gain-scheduling H_∞ controller, as an optimal control solution to mixed sensitivity problem at the vertex Π_i, to work as a convex combination through gain-scheduling technique. The asymptotic stability for controllers working online can be guaranteed by using a single Lyapunov function. Therefore, the computed controller may naturally have a polytopic expression

$$\mathbf{K}(\theta) = \sum_{i=1}^{n} a_i \mathbf{K}_i \tag{4.18}$$

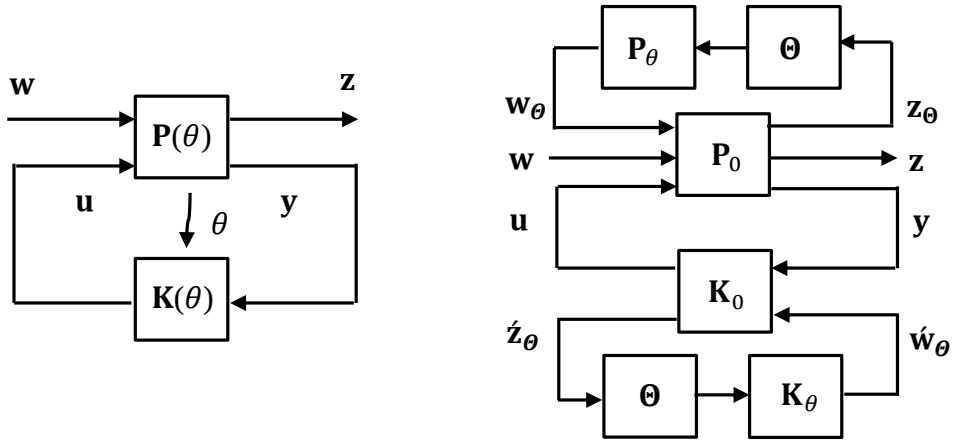

Figure 4.3 LPV control structure and linear fractional transformation

where $\mathbf{K}_i$ is vertex of state-space controller form. Following the H_∞ optimization stated in equations (3.34) and (3.35), $\mathbf{K}_i$is computed based on each vertex Π_i in the varying parameter polytope corresponding to each corner value in the parameter box. Considering the plant described in equation (4.17), the controller in vertex is expressed as

$$\mathbf{K}_i = \begin{bmatrix} \mathbf{A}_K(\Pi_i) & \mathbf{B}_K \\ \mathbf{C}_K & \mathbf{D}_K \end{bmatrix} \tag{4.19}$$

Thus, by a LFT, a gain-scheduling controller $\mathbf{K}(\theta)$ may be expressed as

$$\mathbf{K}(\theta) = \mathbf{K}_0 + \theta\mathbf{K}_\theta \tag{4.20}$$

Figure 4.3 shows the general LPV control structure and system parameter dependency transformed by the LFT. In the control loop, the upper LFT parameter dependent plant may be expressed as

$$\begin{bmatrix} \mathbf{z} \\ \mathbf{y} \end{bmatrix} = \mathbf{F}_u(\mathbf{P}_0, \mathbf{P}_\theta\boldsymbol{\Theta}) \begin{bmatrix} \mathbf{w} \\ \mathbf{u} \end{bmatrix} \tag{4.21}$$

and if there exists a gain-scheduling controller, the parameter dependency may be obtained as a lower LFT:

$$\begin{bmatrix} \mathbf{u} \\ \grave{\mathbf{z}}_{\boldsymbol{\theta}} \end{bmatrix} = \mathbf{F}_l(\mathbf{K}_0, \mathbf{K}_\theta\boldsymbol{\Theta}) \begin{bmatrix} \mathbf{y} \\ \grave{\mathbf{w}}_{\boldsymbol{\theta}} \end{bmatrix} \tag{4.22}$$

Thus, the closed loop transfer function mapping from $\mathbf{w}$ to $\mathbf{q}$ may be expressed as

$$\mathbf{z} = \mathbf{T}_{\mathbf{q},\mathbf{w}}((\mathbf{P}_0, \mathbf{P}_\theta), (\mathbf{K}_0, \mathbf{K}_\theta), \boldsymbol{\Theta})\mathbf{w} \tag{4.23}$$

where $\mathbf{T}_{\mathbf{q},\mathbf{w}}((\mathbf{P}_0, \mathbf{P}_\theta), (\mathbf{K}_0, \mathbf{K}_\theta), \boldsymbol{\Theta}) = \mathbf{F}_l(\mathbf{F}_u(\mathbf{P}_0, \mathbf{P}_\theta\boldsymbol{\Theta}), \mathbf{F}_l(\mathbf{K}_0, \mathbf{K}_\theta\boldsymbol{\Theta}))$.

4.3.2 Gain-Scheduling Control Solution

The description for $\mathbf{P}(\theta)$ may be partitioned as

$$\begin{bmatrix} \dot{\mathbf{q}} \\ \mathbf{z} \\ \mathbf{y} \end{bmatrix} = \begin{bmatrix} \mathbf{A}(\theta) & \mathbf{B}_1 & \mathbf{B}_2 \\ \mathbf{C}_1 & \mathbf{D}_{11} & \mathbf{D}_{12} \\ \mathbf{C}_2 & \mathbf{D}_{21} & \mathbf{D}_{22} \end{bmatrix} \begin{bmatrix} \mathbf{q} \\ \mathbf{w} \\ \mathbf{u} \end{bmatrix} \tag{4.24}$$

In order to derive a gain-scheduling controller, three classical assumptions [67] must be made in normal circumstances (system matrices $\mathbf{B}$, $\mathbf{C}$, $\mathbf{D}$ are parameter dependent):

1. In a parameter affine plant, $\mathbf{D}_{22}(\theta) = 0$, or equivalently in the polytopic model, $\mathbf{D}_{22i} = 0$ for $i = 1,2, \dots, r$;

2. $\mathbf{B}_2(\theta)$, $\mathbf{C}_2(\theta), \mathbf{D}_{12}(\theta), \mathbf{D}_{21}(\theta)$ are parameter-independent, or equivalently, in polytopic model
   $\mathbf{B}_{2i} = \mathbf{B}_2, \mathbf{C}_{2i} = \mathbf{C}_2, \mathbf{D}_{12i} = \mathbf{D}_{12}, \mathbf{D}_{21i} = \mathbf{D}_{21}$;

3. The pairs $(\mathbf{A}(\theta) \quad \mathbf{B}_2)$ and $(\mathbf{A}(\theta) \quad \mathbf{C}_2)$ are quadratically stable and quadratically detectable over $\boldsymbol{\Theta}$.

If the reduced order plant follows the model reduction stated in Section 4.1, the second and third assumptions can be satisfied. However, a parameter independent non-zero $\mathbf{D}$ matrix compensating steady output, may be derived by the LPV system model reduction techniques equation (4.16). That issue can be solved by feeding $\bar{\mathbf{y}} = \mathbf{y} - \mathbf{D}_{22}\mathbf{u}$ to eliminate the non-zero $\mathbf{D}_{22}$ effects.

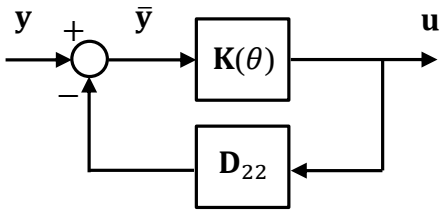

Figure 4.4 Block diagram for controller with non-zero **D** matrix correction

Figure 4.4 shows the block diagram for such correction, and the gain-scheduling controller each vertex is obtained as

$$\bar{\mathbf{K}}(\theta) = \sum_{i=1}^{n} a_i \bar{\mathbf{K}}_i = \sum_{i=1}^{n} a_i \begin{bmatrix} \bar{\mathbf{A}}_K(\Pi_i) & \bar{\mathbf{B}}_K \\ \bar{\mathbf{C}}_K & \bar{\mathbf{D}}_K \end{bmatrix} \tag{4.25}$$

where $\bar{\mathbf{A}}_K(\Pi_i) = \mathbf{A}_K(\Pi_i) - \mathbf{B}_K\mathbf{D}_{22}(\mathbf{I} + \mathbf{D}_{22}\mathbf{D}_K)^{-1}\mathbf{C}_K$, $\bar{\mathbf{B}}_K = \mathbf{B}_K(\mathbf{I} - \mathbf{D}_{22}(\mathbf{I} + \mathbf{D}_{22}\mathbf{D}_K)^{-1}\mathbf{D}_K)$, $\bar{\mathbf{C}}_K = (\mathbf{I} + \mathbf{D}_{22}\mathbf{D}_K)^{-1}\mathbf{C}_K$ and $\bar{\mathbf{D}}_K = (\mathbf{I} + \mathbf{D}_{22}\mathbf{D}_K)^{-1}\mathbf{D}_K$.

The closed loop system at each vertex in polytope $\boldsymbol{\Theta}$, may be expressed as

$$\begin{bmatrix} \dot{\mathbf{q}}_{cl} \\ \mathbf{z} \end{bmatrix} = \begin{bmatrix} \mathbf{A}_{cl}(\Pi_i) & \mathbf{B}_{cl} \\ \mathbf{C}_{cl} & \mathbf{D}_{cl} \end{bmatrix} \begin{bmatrix} \mathbf{q}_{cl} \\ \mathbf{w} \end{bmatrix} \tag{4.26}$$

where

$$\begin{bmatrix} \mathbf{A}_{cl}(\Pi_i) & \mathbf{B}_{cl} \\ \mathbf{C}_{cl} & \mathbf{D}_{cl} \end{bmatrix} = \begin{bmatrix} \widetilde{\mathbf{A}}(\Pi_i) - \mathbf{B}_c\bar{\mathbf{K}}_i\mathbf{C}_c & \widetilde{\mathbf{B}} - \mathbf{B}_c\bar{\mathbf{K}}_i\widetilde{\mathbf{D}}_{21} \\ \tilde{\mathbf{C}} - \widetilde{\mathbf{D}}_{21}\bar{\mathbf{K}}_i\mathbf{C}_c & \mathbf{D}_{11} - \widetilde{\mathbf{D}}_{12}\bar{\mathbf{K}}_i\widetilde{\mathbf{D}}_{21} \end{bmatrix} \tag{4.27}$$

and

$$\begin{bmatrix} \widetilde{\mathbf{A}}(\Pi_i) & \widetilde{\mathbf{B}} & \mathbf{B}_c \\ \tilde{\mathbf{C}} & \mathbf{D}_{11} & \widetilde{\mathbf{D}}_{12} \\ \mathbf{C}_c & \widetilde{\mathbf{D}}_{21} & \bar{\mathbf{K}}_i \end{bmatrix} = \begin{bmatrix} \mathbf{A}(\Pi_i) & \mathbf{0} & \mathbf{B}_1 & \mathbf{0} & \mathbf{B}_2 \\ \mathbf{0} & \mathbf{0} & \mathbf{0} & \mathbf{I} & \mathbf{0} \\ \mathbf{C}_1 & \mathbf{0} & \mathbf{D}_{11} & \mathbf{0} & \mathbf{D}_{12} \\ \mathbf{0} & \mathbf{I} & \mathbf{0} & \bar{\mathbf{A}}_K(\Pi_i) & \bar{\mathbf{B}}_K \\ \mathbf{C}_2 & \mathbf{0} & \mathbf{D}_{12} & \bar{\mathbf{C}}_K & \bar{\mathbf{D}}_K \end{bmatrix} \tag{4.28}$$

Gahinet and Apkarian [68] indicate that the LMI based H_∞ optimal control problem for a single vertex system is equivalent to the existence of a positive definite solution $\mathbf{X} > 0$, subject to the inequality

$$\begin{bmatrix} \mathbf{A}_{cl}{}^{T}\mathbf{X} + \mathbf{X}\mathbf{A}_{cl} & \mathbf{X}\mathbf{B}_{cl} & \mathbf{C}_{cl}{}^{T} \\ \mathbf{B}_{cl}{}^{T}\mathbf{X} & -\gamma\mathbf{I} & \mathbf{D}_{cl}{}^{T} \\ \mathbf{C}_{cl} & \mathbf{D}_{cl} & -\gamma\mathbf{I} \end{bmatrix} < 0 \tag{4.29}$$

According to the LMI based gain-scheduling H_∞ control technique stated in [69], the control problem can be solved for LPV system in equation (4.24), by reformulating as if there exist two symmetric matrices $\mathbf{R}, \mathbf{S} \in \mathbb{R}^{n^P \times n^K}$ satisfying the system of $2n + 1$ LMIs as

$$\begin{bmatrix} \boldsymbol{N}_R & \mathbf{0} \\ \mathbf{0} & \mathbf{I} \end{bmatrix}^T \begin{bmatrix} \mathbf{A}(\Pi_i)\mathbf{R} + \mathbf{R}\mathbf{A}^T(\Pi_i) & \mathbf{R}\mathbf{C}_1^T & \mathbf{B}_1 \\ \mathbf{C}_1\mathbf{R} & -\gamma\mathbf{I} & \mathbf{D}_{11} \\ \mathbf{B}_1^T & \mathbf{D}_{11}^T & -\gamma\mathbf{I} \end{bmatrix} \begin{bmatrix} \boldsymbol{N}_R & \mathbf{0} \\ \mathbf{0} & \mathbf{I} \end{bmatrix} < 0 \tag{4.30}$$

$$\begin{bmatrix} \boldsymbol{N}_S & \mathbf{0} \\ \mathbf{0} & \mathbf{I} \end{bmatrix}^T \begin{bmatrix} \mathbf{A}^T(\Pi_i)\mathbf{S} + \mathbf{S}\mathbf{A}(\Pi_i) & \mathbf{S}\mathbf{B}_1 & \mathbf{C}_1^T \\ \mathbf{B}_1^T\mathbf{S} & -\gamma\mathbf{I} & \mathbf{D}_{11}^T \\ \mathbf{C}_1 & \mathbf{D}_{11} & -\gamma\mathbf{I} \end{bmatrix} \begin{bmatrix} \boldsymbol{N}_S & \mathbf{0} \\ \mathbf{0} & \mathbf{I} \end{bmatrix} < 0 \tag{4.31}$$

$$\begin{bmatrix} \mathbf{R} & \mathbf{I} \\ \mathbf{I} & \mathbf{S} \end{bmatrix} \geq 0 \tag{4.32}$$

where $i = 1, \ldots, n$, are the defined vertices in the polytope parameter box; and $\boldsymbol{N}_R$, $\boldsymbol{N}_S$ represent the orthonormal bases of the null spaces of $[\mathbf{B}_2^T \mathbf{D}_{12}^T]$ and $[\mathbf{C}_2 \mathbf{D}_{21}]$. If $\text{rank}(\mathbf{I} - \mathbf{RS}) = n^K \leq n^P$, the reduced order controllers exist with rank $n^K < n^P$.

In order to obtain a unique solution $\mathbf{X}$ using the LMI approach, two matrices $\mathbf{M}, \mathbf{N} \in \mathbb{R}^{n^P \times n^K}$ with full column rank may be defined as

$$\mathbf{M}\mathbf{N}^T = \mathbf{I} - \mathbf{R}\mathbf{S} \tag{4.33}$$

Then, $\mathbf{X}$ can be obtained uniquely from the solution of

$$\begin{bmatrix} \mathbf{S} & \mathbf{I} \\ \mathbf{N}^T & \mathbf{0} \end{bmatrix} = \mathbf{X} \begin{bmatrix} \mathbf{I} & \mathbf{R} \\ \mathbf{0} & \mathbf{M}^T \end{bmatrix} \tag{4.34}$$

The gain-scheduling controller state-space matrices can be solved by the LMI approach by substituting equation (4.24) into equation (4.29). The asymptotic stability over the whole parameter varying range defined by the polytope $\boldsymbol{\Theta}$, can be guaranteed by the following single Lyapunov function

$$V(\mathbf{x}) = \mathbf{x}^T \mathbf{X} \mathbf{x} \tag{4.35}$$

with **x** subject to

$$\begin{gathered} V(\mathbf{x}) > \mathbf{0} \quad \forall \mathbf{x} \neq \mathbf{0} \\ \mathcal{H}V(\mathbf{x}) < \mathbf{0} \end{gathered} \tag{4.36}$$

where $\mathcal{H}V(\mathbf{x})$ represents the negative definite Hessian of $V(\mathbf{x})$ as

$$\mathcal{H}V(x_1, \ldots, x_n) = \begin{bmatrix} \dfrac{\partial^2 V}{\partial x_1^2} & \cdots & \dfrac{\partial^2 V}{\partial x_1 \partial x_n} \\ \vdots & \ddots & \vdots \\ \dfrac{\partial^2 V}{\partial x_n \partial x_1} & \cdots & \dfrac{\partial^2 V}{\partial x_n^2} \end{bmatrix} \tag{4.37}$$

In contrast with the Riccati solution, the LMI approach also bounds the transient performance gain in term of 2-norm between input and output by using the H_∞ cost γ:

$$\|\mathbf{z}\|_2 < \gamma \|\mathbf{w}\|_2 \tag{4.38}$$

4.3.3 Gain-Scheduling Control Real-Time Implementation

Figure 4.5 shows the real-time implementation of a gain-scheduling controller $\overline{\mathbf{K}}(\theta) = \sum_{i=1}^{2} a_k \overline{\mathbf{K}}_i$, if the varying parameter polytope $\boldsymbol{\Theta} := \mathbf{Co}\{\Pi_1, \Pi_2\}$ has one dimension, namely, one parameter varying over a defined range. The controller at each vertex can be expressed as

$$\overline{\mathbf{K}}_i := \begin{cases} \dot{\mathbf{q}}_c^K = \overline{\mathbf{A}}_K(\Pi_i)\mathbf{q}_c^K + \overline{\mathbf{B}}_K \mathbf{u}_c^K \\ \mathbf{y}_c^K = \overline{\mathbf{C}}_K \mathbf{q}_c^K + \overline{\mathbf{D}}_K \mathbf{u}_c^K \end{cases} \tag{4.39}$$

With the lower LFT, the parameter dependent term may be obtained as

$$\overline{\mathbf{K}}_\theta = \begin{bmatrix} \overline{\mathbf{A}}_K^\theta & \mathbf{0} \\ \mathbf{0} & \mathbf{0} \end{bmatrix} \tag{4.40}$$

where $\overline{\mathbf{A}}_K^\theta = \overline{\mathbf{A}}_K(\Pi_2) - \overline{\mathbf{A}}_K(\Pi_1)$.

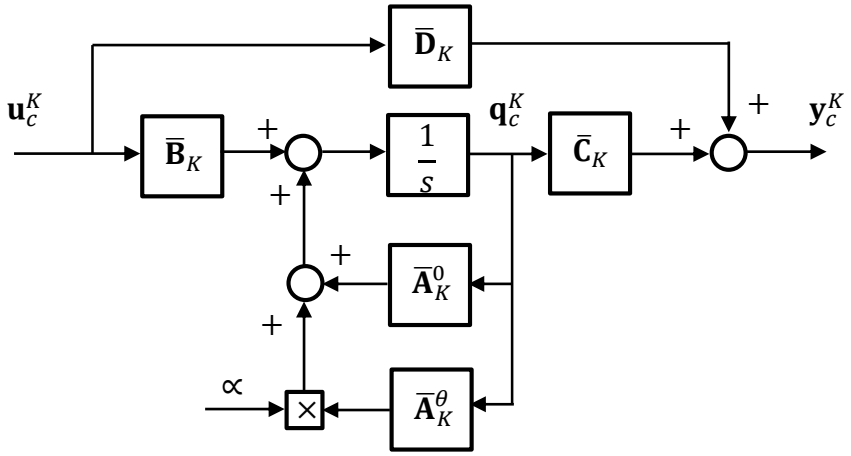

Figure 4.5 Block diagram of controller $\bar{\mathbf{K}}(\theta)$ implementation

Thus, the controller parameter dependency may be obtained with linear interpolation as

$$\bar{\mathbf{K}}(\theta) = \bar{\mathbf{K}}_0 + \propto \bar{\mathbf{K}}_\theta = \begin{bmatrix} \bar{\mathbf{A}}_K(\Pi_1) + \propto \bar{\mathbf{A}}_K^\theta & \bar{\mathbf{B}}_K \\ \bar{\mathbf{C}}_K & \bar{\mathbf{D}}_K \end{bmatrix} \tag{4.41}$$

where the scheduling gain subject to $\propto = \boldsymbol{\Theta}/(\Pi_2 - \Pi_1)$ should vary in range

$$0 \leq \propto \leq 1 \tag{4.42}$$

4.4 Speed-Dependent Rotor/AMB System Control

Due to gyroscopic moments, a rotor/AMB system has speed dependency. Linear Time Invariant (LTI) system modelling, having specific dynamics at a single rotational speed, may not be sufficient to derive a LPV controller. Thus, a LPV rotor/AMB plant varying in defined speed polytope is necessary.

Figure 4.6 shows the sensor feedbacks and controlled actuation nodes for LMI based H_∞ controller design. The control loop may use only four sensors located at both ends as feedback to actuate AMBs. PD control action may mainly attenuate vibrations at two AMB sensors planes (four sensors).

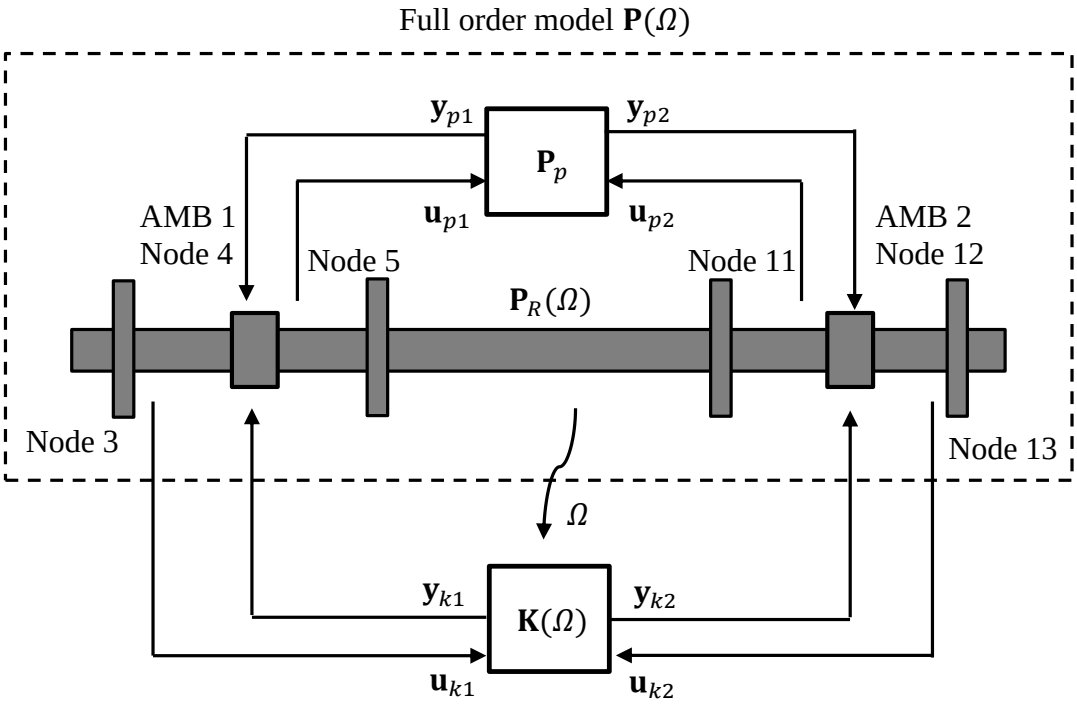

Figure 4.6 Sensors planes for gain-scheduling controller design

With a lower feedback dimension, the controller order can be limited and implemented. The model based control system may be able to attenuate vibrations effectively within running speed below the third bending mode. However, such effective control performance range is sufficient to cover the normal test rig running speed.

4.4.1 Speed-Dependent Plant

Based on equation (4.2), the speed dependent rotor/AMB LPV system under PD control may be expressed as an affine system having speed dependency as parameter variation

$$\mathbf{P}(\Omega(t)) = \begin{bmatrix} \mathbf{A}(\Omega(t)) & \mathbf{B} \\ \mathbf{C} & \mathbf{D} \end{bmatrix} \tag{4.43}$$

where Ω is rotational speed, and can be measured in real-time.

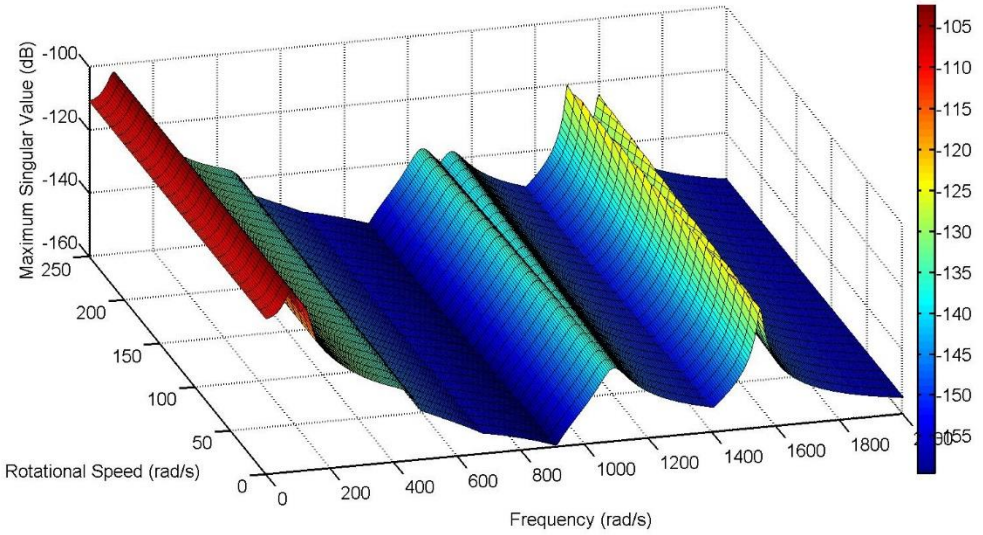

Figure 4.7 $\bar{\sigma}(\mathbf{P}(s,\Omega))$

According to equation (4.3), the system $\mathbf{A}$ having speed dependency on Ω can be reformed as

$$\mathbf{A}(\Omega(t)) = \mathbf{A}_0 + \Omega(t)\mathbf{A}_G \tag{4.44}$$

where the PD controlled rotor/AMB system matrix without the gyroscopic effect is $\mathbf{A}_0 = \begin{bmatrix} \mathbf{A}_{R,0} & -\mathbf{B}_R^p\mathbf{C}_p \\ \mathbf{B}_p\mathbf{C}_R^p & \mathbf{A}_p \end{bmatrix}$, and gyroscopic effect for LPV modelling is $\mathbf{A}_G = \begin{bmatrix} \mathbf{A}_{R,G} & \mathbf{0} \\ \mathbf{0} & \mathbf{0} \end{bmatrix}$ according to equation (2.31). $\mathbf{A}_{R,0}$ and $\mathbf{A}_{R,G}$ may be derived from equation (2.23) as

$$\mathbf{A}_{R,0} = \begin{bmatrix} \mathbf{0} & \mathbf{I} \\ -\mathbf{M}_R^{-1}\mathbf{K}_R & \mathbf{0} \end{bmatrix}, \mathbf{A}_{R,G} = \begin{bmatrix} \mathbf{0} & \mathbf{0} \\ \mathbf{0} & -\mathbf{M}_R^{-1}\mathbf{G}_R \end{bmatrix} \tag{4.45}$$

Time varying rotational speed $\Omega(t)$ is scaled between non-rotating $\Omega_0 = 0$ and the maximum speed $\Omega_{max} = 250$ rad/s. A single time varying parameter may produce two corners in the parameter box. The parameter polytope may have two dimensions in space, which can be defined as

$$\Omega(t) \in \boldsymbol{\Theta} := \mathbf{Co}\{\Pi_1, \Pi_2\} \tag{4.46}$$

where $\Pi_1 = \Omega_0$ and $\Pi_2 = \Omega_{max}$.

Therefore, based on equation (4.10), the speed-dependent plant $\mathbf{P}(\Omega)$ can be described in polytopic form by referencing $\boldsymbol{\Theta}$ as

$$\mathbf{P}(\Omega) := \mathbf{Co}\{\boldsymbol{\Psi}(\Pi_1), \boldsymbol{\Psi}(\Pi_2)\} \tag{4.47}$$

where $\boldsymbol{\Psi}(\Pi_i)=\begin{bmatrix}\mathbf{A}_0 + \Pi_i\mathbf{A}_G & \mathbf{B}\\ \mathbf{C} & \mathbf{D}\end{bmatrix}$.

Figure 4.7 shows the synchronous frequency response of the full order speed-dependent plant $\mathbf{P}(\Omega)$ in maximum singular value as H_∞ norm defined in Chapter 2.

Then, by following LPV system model reduction, $\mathbf{P}(\Omega)$ may have a reduced order model as

$$\mathbf{P}_r(\Omega) := \mathbf{Co}\{\boldsymbol{\Psi}_r(\Pi_1), \boldsymbol{\Psi}_r(\Pi_2)\} \tag{4.48}$$

where $\boldsymbol{\Psi}_r(\Pi_i) = \begin{bmatrix}\mathbf{A}_r^0 + \Pi_i\mathbf{J}_r & \mathbf{B}_r\\ \mathbf{C}_r & \mathbf{D}_r\end{bmatrix}$. By defining $\mathbf{J} = \mathbf{V}_0^{-1}\mathbf{A}_G\mathbf{V}_0$ in equation (4.13), the reduced order plant matrices may be obtained as

$$\mathbf{A}_r^0 = \begin{bmatrix}\mathrm{Re}(\boldsymbol{\Lambda}_{0l}) & -\mathrm{Im}(\boldsymbol{\Lambda}_{0l})\\ \mathrm{Im}(\boldsymbol{\Lambda}_{0l}) & \mathrm{Re}(\boldsymbol{\Lambda}_{0l})\end{bmatrix}, \mathbf{J}_r = \begin{bmatrix}\mathrm{Re}(\mathbf{J}_{ll}) & -\mathrm{Im}(\mathbf{J}_{ll})\\ \mathrm{Im}(\mathbf{J}_{ll}) & \mathrm{Re}(\mathbf{J}_{ll})\end{bmatrix}, \mathbf{B}_r = \begin{bmatrix}\mathrm{Re}(\breve{\mathbf{B}}_l)\\ \mathrm{Im}(\breve{\mathbf{B}}_l)\end{bmatrix},$$

$\mathbf{C}_r = \mathbf{C}_c[\mathrm{Re}(\mathbf{V}_{0l}) - \mathrm{Im}(\mathbf{V}_{0l})]$ and $\mathbf{D}_r = (\mathbf{D}_c - \mathbf{C}_c\mathrm{Re}(\mathbf{V}_{0h}{\boldsymbol{\Lambda}_{0h}}^{-1}\breve{\mathbf{B}}_h))$.

Figure 4.8 shows the maximum singular values of two vertex of LPV plants $\mathbf{P}(\Omega)$ and $\mathbf{P}_r(\Omega)$. Such reduced order polytopic plant may be used to derive a gain-scheduling controller, with tractability for model varying dynamics. Now, $\mathbf{D}$ matrix compensates the steady output in the LPV reduced order model $\mathbf{P}_r(\Omega)$.

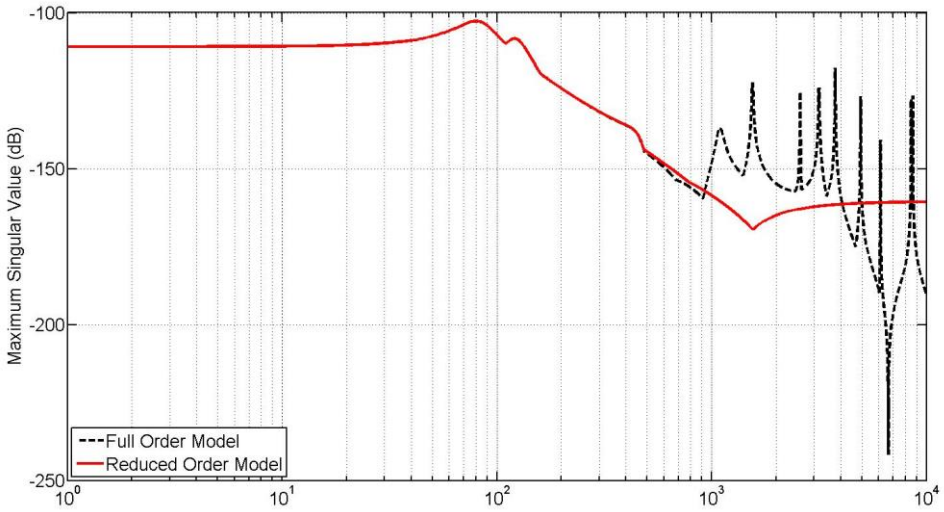

(a) when $\Omega = 0$ rad/s;

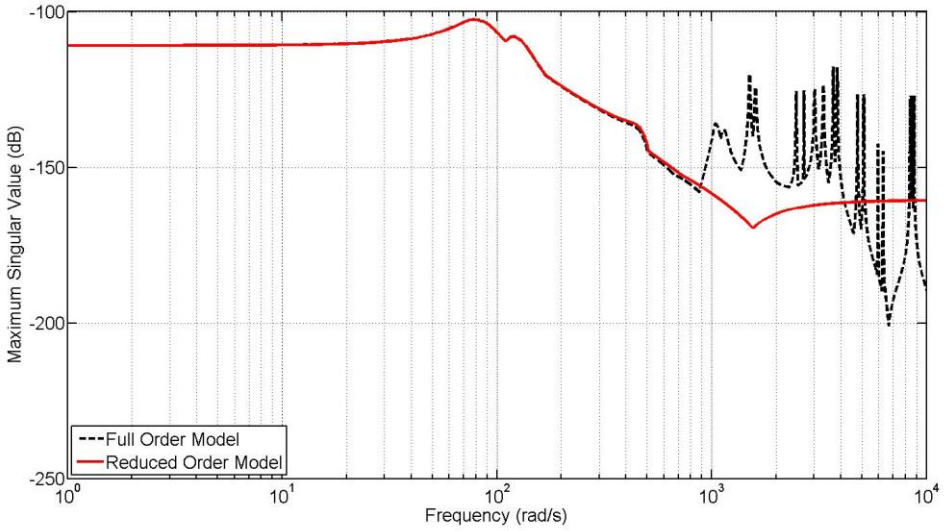

(b) when $\Omega = 250$ rad/s

Figure 4.8 $\bar{\sigma}(\mathbf{P}(s,\Omega))$ and $\bar{\sigma}(\mathbf{P}_r(s,\Omega))$

4.4.2 Speed-Dependent Model Uncertainties Estimation

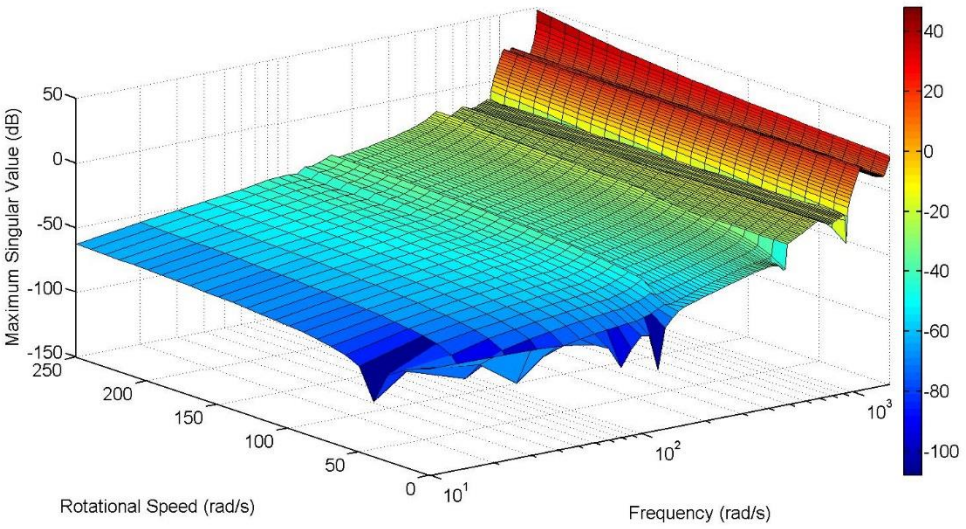

Figure 4.9 $\bar{\sigma}(\boldsymbol{\Delta}(s,\Omega))$

Unlike an LTI system, an LPV system model including multiplicative model error at each vertex defined by the parameter polytope $\boldsymbol{\Theta}$. Thus, may be expressed in speed dependent form as

$$\boldsymbol{\Delta}(s,\Omega) = \mathbf{Co}\{\boldsymbol{\Psi}_{\Delta}(s,\Pi_1), \boldsymbol{\Psi}_{\Delta}(s,\Pi_2)\} \tag{4.49}$$

Based on multiplicative model error estimation equations (3.18)-(3.20), the model error at each vertex system may be obtained as

$$\boldsymbol{\Psi}_{\Delta}(s,\Pi_i) = \boldsymbol{\Psi}_r^{-1}(s,\Pi_i)\big(\boldsymbol{\Psi}(s,\Pi_i) - \boldsymbol{\Psi}_r(s,\Pi_i)\big) \tag{4.50}$$

The estimated model error $\boldsymbol{\Psi}_{\Delta}(s,\Pi_i)$ may vary along with parameter polytope $\boldsymbol{\Theta}$ defined in equation (4.46). Over such a range, uncertainties induced by parameterization and multiplicative model error, remains at low level and can be accepted, as shown in Figure 4.9.

Sometimes, such parameterization of uncertainties could be significant and may reach high levels, especially when the parameter polytope range is wide, say if such a parameter represents effective stiffness for contact events. However, according to the small gain theorem stated in equation (3.31), the stability can be guaranteed if

multiplicative model error can be scaled. The parameterization uncertainties may not be necessary to be taken into account when design gain-scheduling control with large parameter varying range. This is discussed further in Chapter 5.

4.4.3 Speed-Dependent Gain-Scheduling Controller Synthesis

Weightings Choice for Mixed Sensitivity Problem

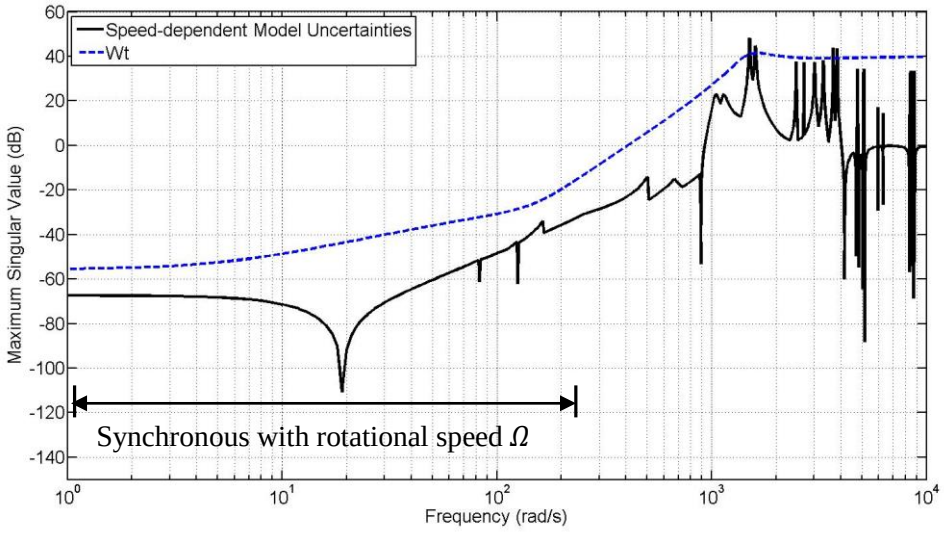

Figure 4.10 Speed-dependent model error and weighting for complementary sensitivity

As the rotational speed polytope $\boldsymbol{\Theta}$ defined is quite limited according to the test rig operating speed range, the model uncertainties estimated including dynamics vary based on the synchronous conditions, as shown in Figure 4.10. As real amplifiers have a cut-off frequency setting at 1500 rad/s, the rotor/AMB system test rig may not be as sensitive as the mathematical model at frequencies above that value. Thus, the weighting for complementary sensitivity choice does not have to leave a large margin at high frequencies; and can be imposed internally if high control performance is required.

For the speed-dependent rotor/AMB system, the weighting $\mathbf{W}_t^{\Omega}(s) = \mathbf{I}_{4\times4} w_t^{\Omega}(s)$, for complementary sensitivity may be obtained based on equation (3.42) as

$$w_t^{\Omega}(s) = \delta\left(\frac{s+a}{s+b}\right)\left(\frac{s^2 + 2\xi_1 w_{n1} s + {w_{n1}}^2}{s^2 + 2\xi_2 w_{n2} s + {w_{n2}}^2}\right)\left(\frac{b{w_{n2}}^2}{a{w_{n1}}^2}\right) \qquad (4.51)$$

where $\delta = 10^{-55/20}$ $a = 5, b = 3000,$ $\xi_1 = 0.5\,, \xi_2 = 0.2, w_{n1} = 150$ rad/s, and $w_{n2} = 1500$ rad/s,.

Based on the H_∞ sensitivity optimization of equation (3.44), the weighting for the sensitivity $\mathbf{W}_s^{\Omega}(s) = \mathbf{I}_{4\times4} w_s^{\Omega}(s)$ is designed as a low-pass filter, which can achieve disturbance rejection with a wide band-width

$$w_s^{\Omega}(s) = \left(\frac{{w_{ns}}^2}{s^2 + 2\xi_s w_{ns} s + {w_{ns}}^2}\right) \qquad (4.52)$$

where $w_{ns} = 100$ rad/s and $\xi_s = 0.5$.

Based on these weighting choices, the LMI based gain-scheduling H_∞ optimization solves the mixed sensitivity problem at each vertex according to equations (3.34)-(3.35) with a single H_∞ cost, γ_s, to guarantee the robustness stability when gain-scheduling, as

$$\left\| \begin{matrix} \varepsilon \mathbf{W}_s^{\Omega}(s)\mathbf{S}_r(s,\Pi_i) \\ \mathbf{W}_t^{\Omega}(s)\mathbf{T}_r(s,\Pi_i) \end{matrix} \right\|_\infty \leq \gamma_s \qquad (4.53)$$

Thus, at each defined vertex of polytope, the closed loop complementary sensitivity can be bounded according to equation (3.38) as

$$\bar{\sigma}(\mathbf{T}_r(s,\Pi_i)) \leq \bar{\sigma}\left(\mathbf{W}_t^{\Omega^{-1}}(s)\gamma_s\right) \qquad (4.54)$$

The sensitivity can be enveloped following equation (3.39) as

$$\bar{\sigma}\left(\mathbf{S}_r(s,\Pi_i)\right) \leq \bar{\sigma}\left(\varepsilon \mathbf{W}_s^{\Omega^{-1}}(j\omega)\gamma_s\right) \qquad (4.55)$$

Basic Plant Numerical Balancing

As the LMI based gain-scheduling approach may need much more iterations compared with the LTI Riccati solution, some numerical errors may arise during the

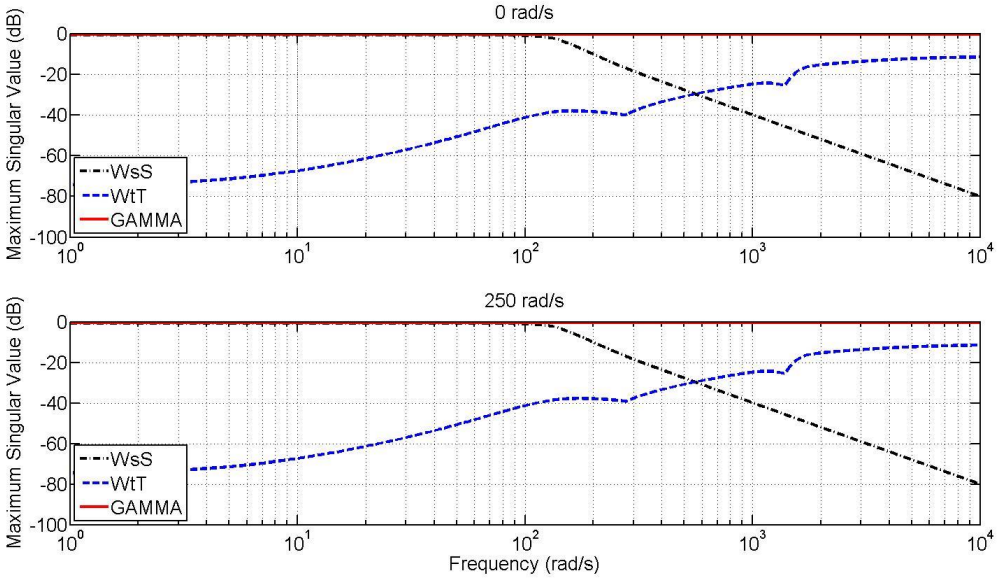

Figure 4.11 Mixed sensitivity problem solution with numerical unbalanced plant $\mathbf{P}_r(\Omega)$

optimization procedure with the original reduced order plant $\mathbf{P}_r(\Omega)$. Figure 4.10 shows the solution (H_∞ cost γ_s) to mixed sensitivity problem stated in equation (4.53) for original numerical unbalanced plant $\mathbf{P}_r(\Omega)$.

With $\varepsilon = 1$, the optimization procedure finds H_∞ cost $\gamma_s = 0.926$ as the solution for the numerical unbalanced LPV plant $\mathbf{P}_r(\Omega)$. However, as can be seen in Figure 4.11 the complementary sensitivity term $\mathbf{W}_t^{\Omega}(s)\mathbf{T}_r(s,\Pi_i)$ at each vertex is not bounded well by $\gamma_s = 0.926$. The closed loop complementary sensitivity function of each vertex $\mathbf{T}_r(s,\Pi_i)$ is 'small'; so that the sensitivity function $\mathbf{S}_r(s,\Pi_i)$ is too 'large' to be optimized as can be verified in the closed loop sensitivity stated in equation (3.25). Therefore, $\mathbf{S}_r(s,\Pi_i)$ can not be 'pushed down' by the closed loop sensitivity weighting $\varepsilon\mathbf{W}_s^{\Omega^{-1}}(j\omega)\gamma_s$ according to equation (4.55). Figure 4.12 shows the loop shaping issues for the numerical unbalanced plant $\mathbf{P}_r(\Omega)$.

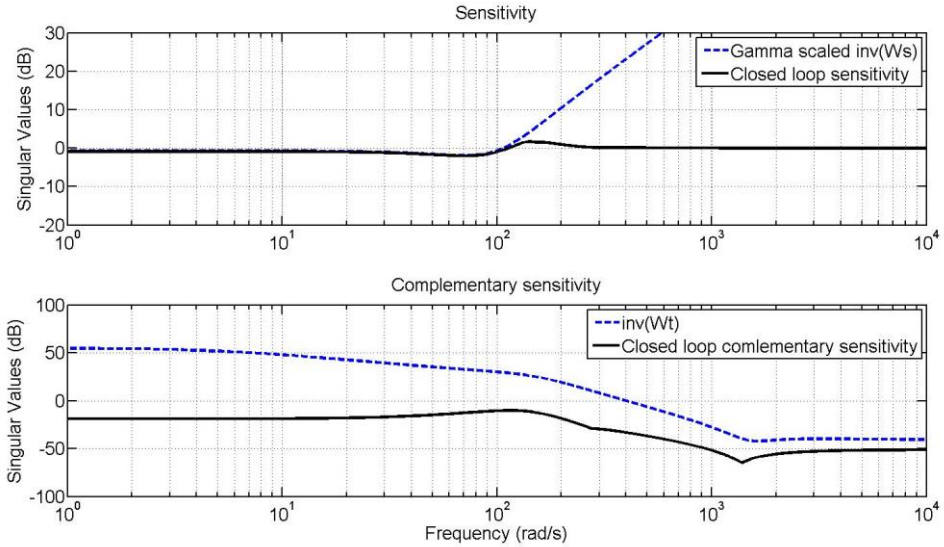

(a) $\Pi_1 = 0$ rad/s

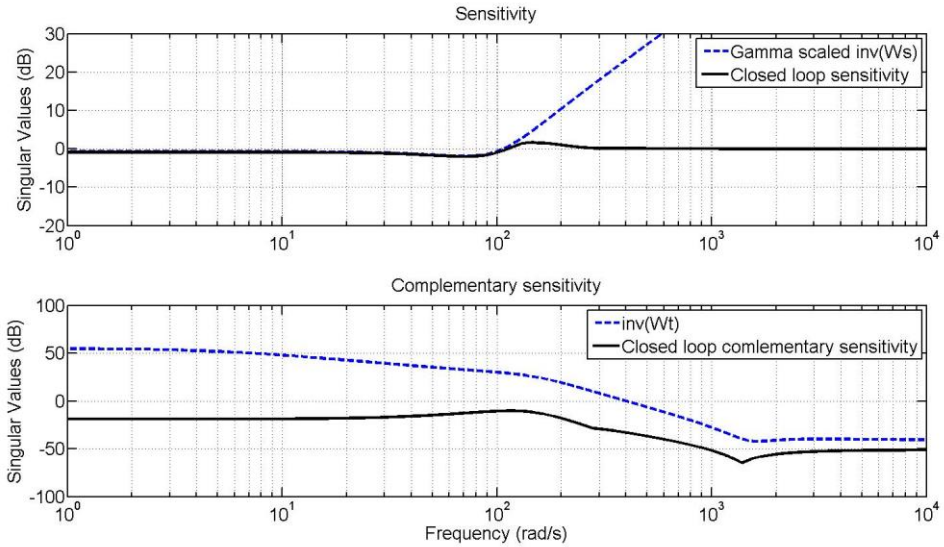

(b) $\Pi_2 = 250$ rad/s

Figure 4.12 $\bar{\sigma}(\mathbf{T}_r(s,\Pi_i))$ and $\bar{\sigma}(\mathbf{S}_r(s,\Pi_i))$ bounded by weightings

Such problems may be solved by scaling the outputs of reduced order plant by the radial sensor clearance as

$$\acute{\mathbf{P}}_r(\Omega) := \mathbf{Co}\left\{\begin{bmatrix}\mathbf{A}_r^0 + \Pi_1\mathbf{J}_r & \mathbf{B}_r \\ \varrho\mathbf{C}_r & \varrho\mathbf{D}_r\end{bmatrix}, \begin{bmatrix}\mathbf{A}_r^0 + \Pi_2\mathbf{J}_r & \mathbf{B}_r \\ \varrho\mathbf{C}_r & \varrho\mathbf{D}_r\end{bmatrix}\right\} \qquad (4.56)$$

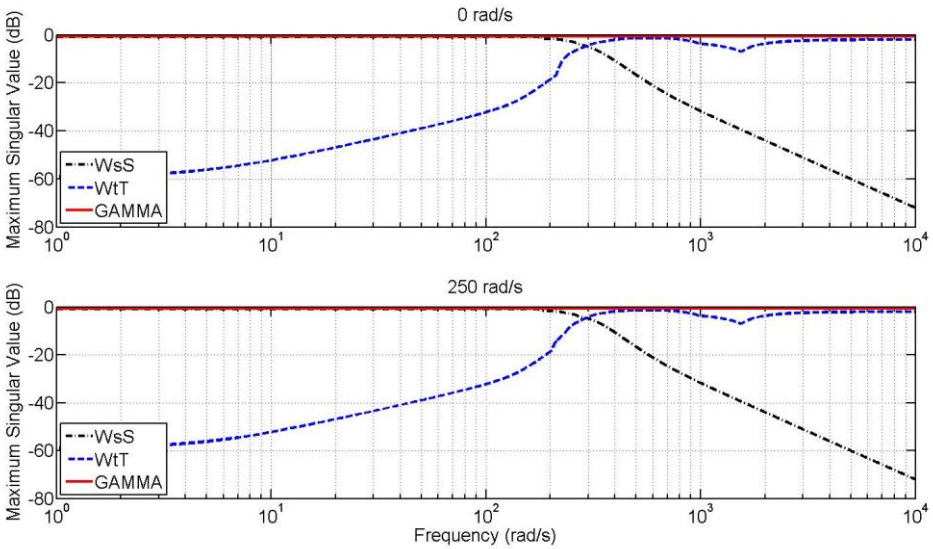

Figure 4.13 Mixed sensitivity problem solution with numerical balanced plant $\acute{\mathbf{P}}_r(\Omega)$

where $\varrho = 1/c_s$, and the sensor position clearance $c_s = 0.75 \times 10^{-3}$ m. With such scaling, the system $\acute{\mathbf{P}}_r(\Omega)$ may be balanced numerically and complementary sensitivity $\acute{\mathbf{T}}_r(s, \Pi_i)$ can be 'large' enough for control solution searching.

Figure 4.13 shows the mixed sensitivity problem bounded by $\gamma_s = 0.926$, with sensitivity weighting transfer function scaling $\varepsilon = 2.5$. In contrast of those in Figure 4.11, the controller design based on the numerical balanced reduced order plant $\acute{\mathbf{P}}_r(\Omega)$ shown in equation (4.56), achieves tight bounded solutions at each vertex , which ensures that good control performance may be obtained.

Figure 4.14 shows the optimal loop shaping in sensitivity/complementary sensitivity under control at each vertex. With such a numerically balanced plant, the two vertex systems having speed dependency are well controlled over the design frequency bandwidth and achieves better control performance compared to those in Figure 4.12.

However, the gain-scheduling control may still need to be verified when polytopic coordinates vary to adjust for dynamic situations with varying rotational speed Ω.

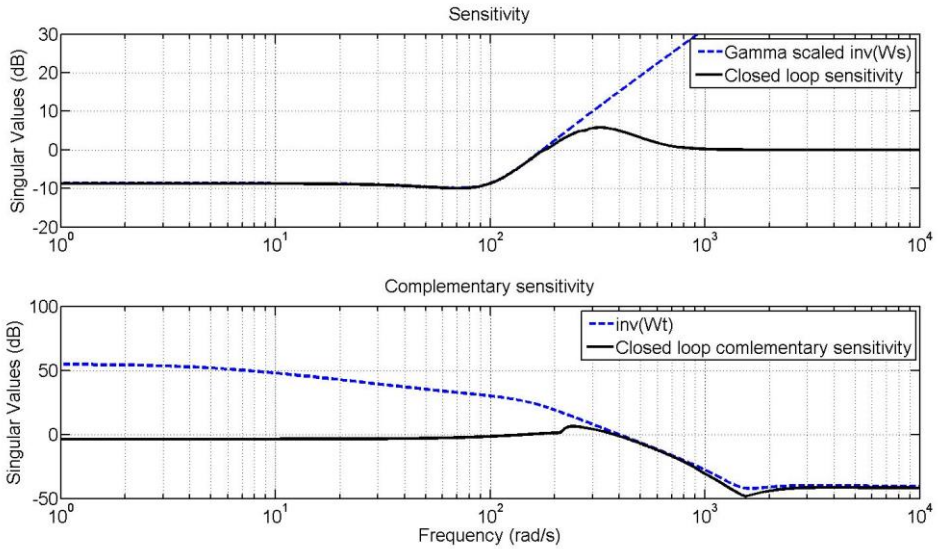

(a) $\Pi_1 = 0\, rad/s$

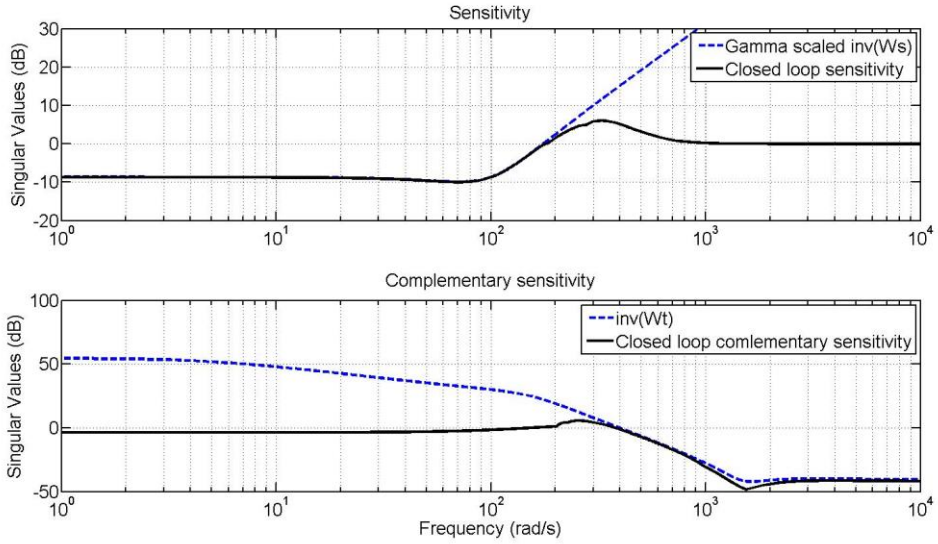

(b) $\Pi_2 = 250\, rad/s$

Figure 4.14 $\bar{\sigma}\left(\acute{\mathbf{T}}_r(s,\Pi_i)\right)$ and $\bar{\sigma}\left(\acute{\mathbf{S}}_r(s,\Pi_i)\right)$ bounded by weightings

Gain-Scheduling Control Performance Estimation

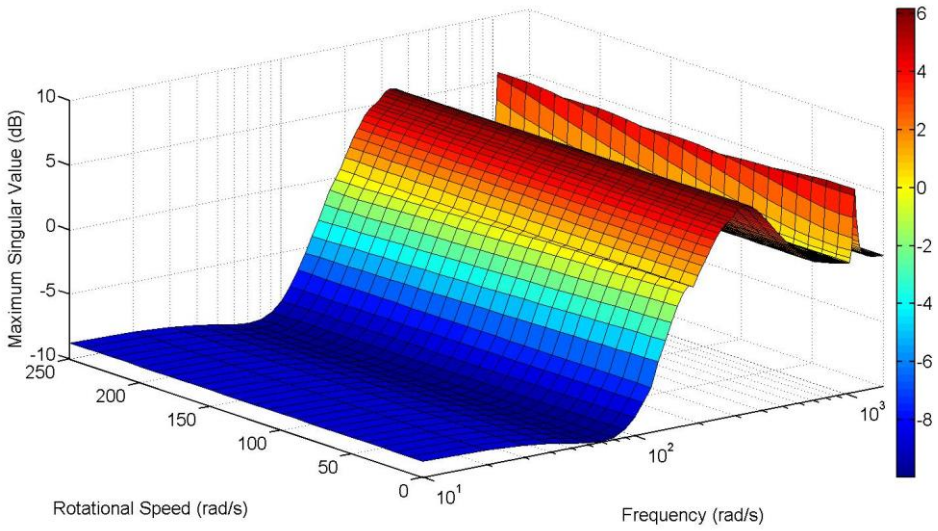

(a) $\bar{\sigma}\left(\acute{\mathbf{S}}(s,\Omega)\right)$

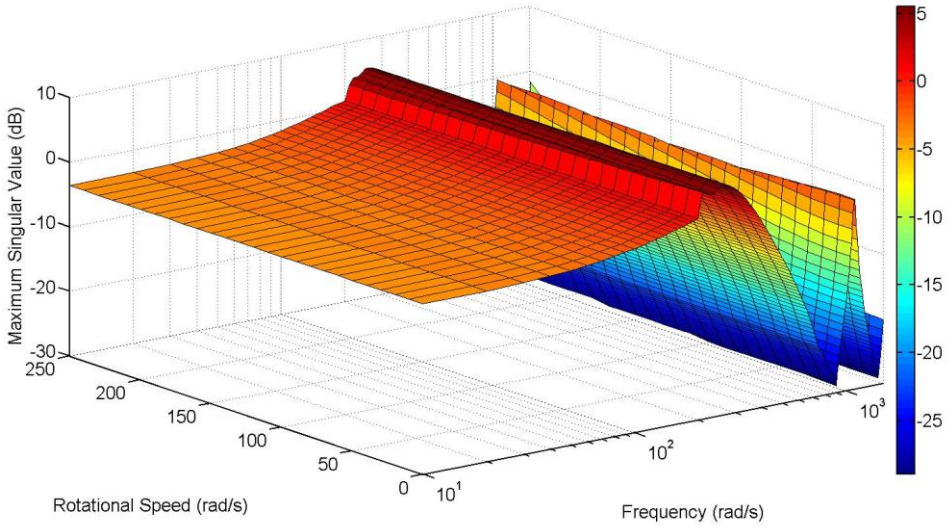

(b) $\bar{\sigma}\left(\acute{\mathbf{T}}(s,\Omega)\right)$

Figure 4.15 Gain-scheduling control performance estimation with full order LPV plant $\bar{\sigma}\left(\acute{\mathbf{S}}(s,\Omega)\right)$ and $\bar{\sigma}\left(\acute{\mathbf{T}}(s,\Omega)\right)$

Figure 4.15 shows the control performance of closed loop speed dependent rotor/AMB system $\acute{\mathbf{P}}_{cl}(\Omega)$ under the LMI based gain-scheduling control over the

frequency domain. The complementary sensitivity $\left(\acute{\mathbf{T}}(s,\Omega)\right)$ is well-bounded to guarantee stability and the sensitivity $\left(\acute{\mathbf{S}}(s,\Omega)\right)$ is reduced by gain-scheduling during rotational speed changes.

4.5 Speed-Dependent Control Simulated Results

In order to estimate time domain performance of a speed-dependent rotor/AMB system under LMI based gain-scheduling control, a simulated test is run under MATLAB SIMULINK. With a totally balanced rotor/AMB system in simulation, the offset mass $m_e = 200\ \mathrm{g \cdot cm}$ was located on disk at the non-driven end (node 14 in FEM) and control performance was tested at two resonances (84, 130 rad/s). Meanwhile, a varying speed test was also undertaken with rotational speed running from 0 rad/s up to 250 rad/s to assess the gain-scheduling controller design polytope range.

4.5.1Rotor Unbalance Forcing Response under LMI Speed-Dependent Control

Figure 4.16 shows the RMS unbalance forcing response in *x*-coordinate under control by PD action only and with the LMI/PD combination. The unbalance force is synchronous with rotational speed. The two sensor feedback planes in $\bar{\mathbf{K}}(\Omega)$ are well-controlled over the design frequency bandwidth compared with PD control action only. Two resonances around the first two modes are significantly attenuated under LMI based gain-scheduling control. Also, the two sensors planes for the PD controller achieve expected performance with rotational speed up to 150 rad/s. Then the vibration orbit becomes larger under LMI based gain-scheduling control, due to the synchronous unbalance forcing response approaching the first flexible mode around 197 rad/s (Figure 2.12 (a)). The controlled rotor can no longer be considered to be a rigid body. However, such a level of vibration at the sensors planes (node 5 and 11) can be acceptable, as it is still far from the TDB clearance ($c_{tdb,amb} = 0.7 \times 10^{-3}$ m) in the AMBs.

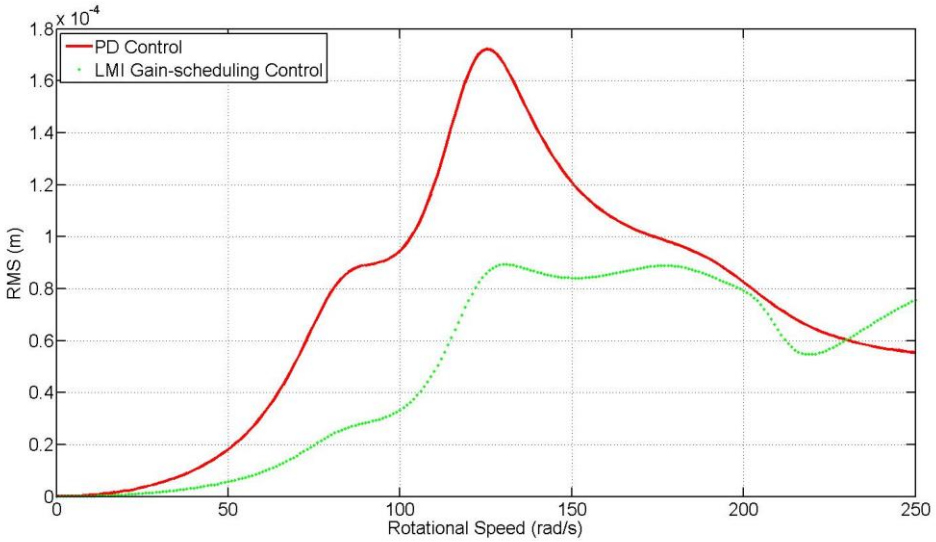

(a) $\bar{\mathbf{K}}(\Omega)$ controlled two sensors planes close to the rotor both ends (nodes 3 and 13)

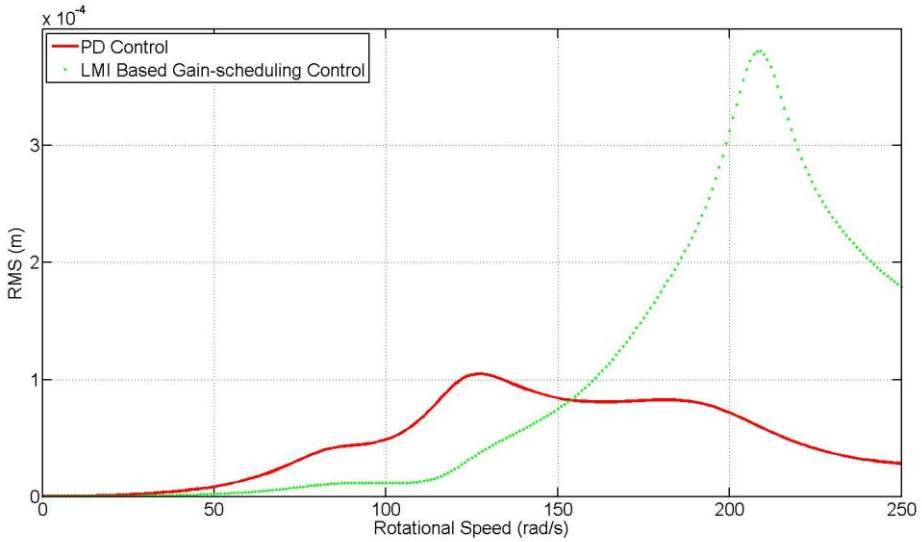

(b) PD controlled two sensors planes close to AMBs (nodes 5 and 11) in the closedloop system

Figure 4.16 RMS unbalance forcing response in *x*-coordinate under LPV control

4.5.2 Single Speed Simulation Test

Two typical rotational speeds around first two resonances, are selected to test control performance. The controller activates at 1 s, with the variation polytope $\boldsymbol{\Theta}$ frozen at a constant speed Ω. Thus, the sudden activiation of control action may induce transients and overshoot.

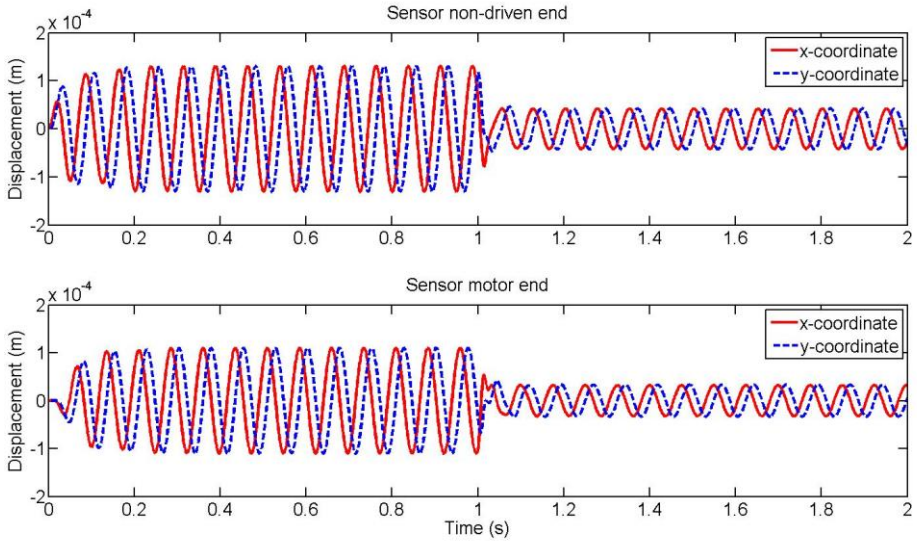

Figure 4.17 Rotor displacements at sensor planes close to the both ends (node 3 and 13) under LMI gain-scheduling control at 84 rad/s, controller was activated at 1s

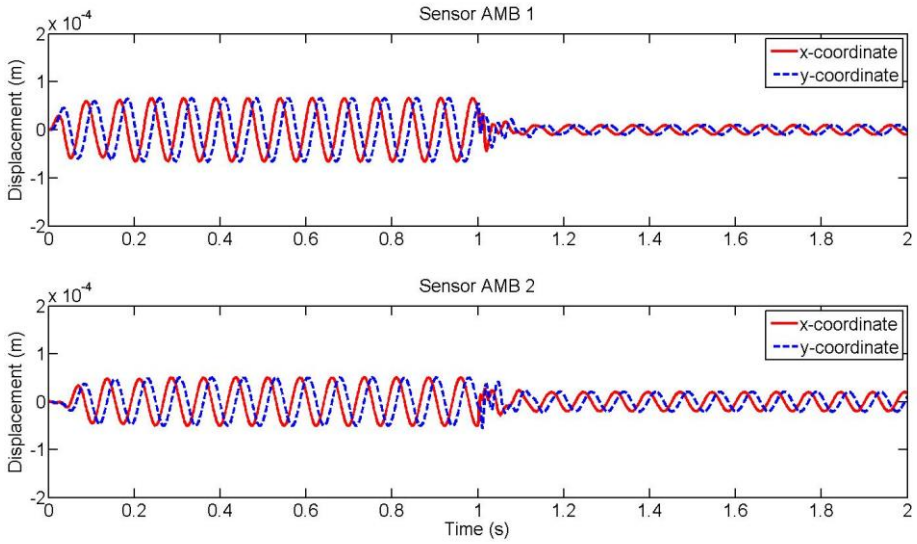

Figure 4.18 Rotor displacements at sensor planes close to the AMBs (node 5 and 11) under LMI gain-scheduling control at 84 rad/s, controller was activated at 1s

At 84 rad/s, for unbalance forcing, the rotor has a translational motion as rigid body. The four sensor planes are well-controlled with the scheduling gain $\propto = 0.336$ as shown in Figures 4.17 and 4.18. The transients of rotor response during sudden activation decay shortly.

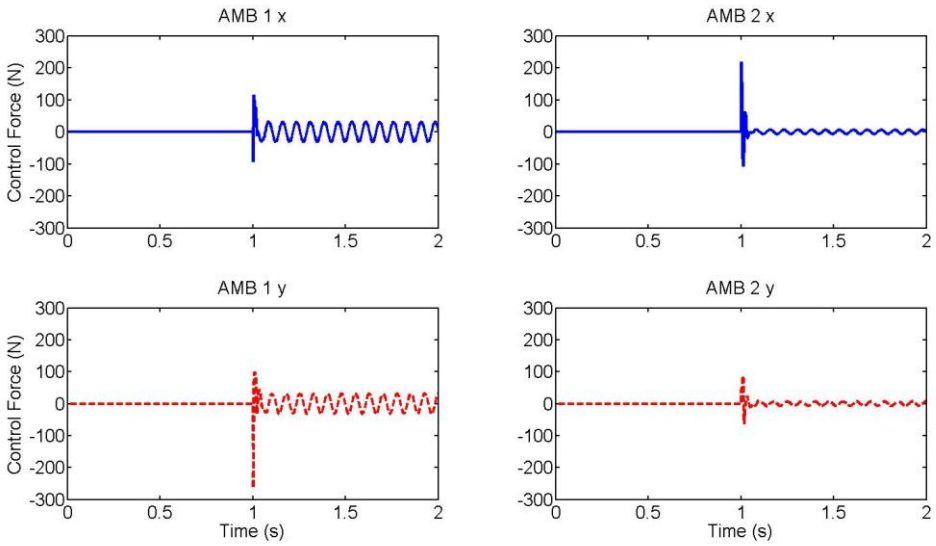

(a) Control forces by LMI gain-scheduling control

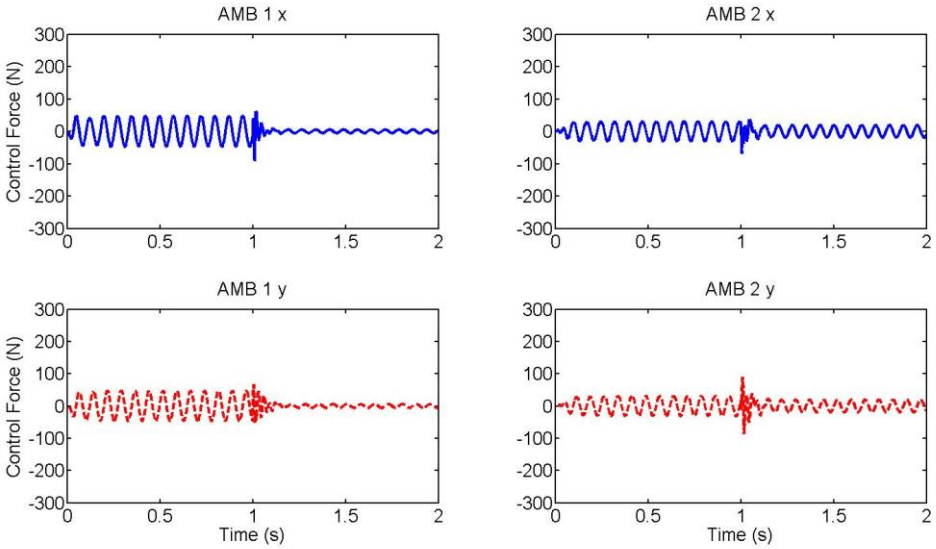

(b) Control forces by PD control

Figure 4.19 Control forces from AMBs

Figure 4.19 shows the controlled AMB force under PD action only and PD combined with LMI. As the gain-scheduling controller derived based on the plant under PD control, the two control strategies could cooperate well. The control force from gain-scheduling control has a significant peak due to the sudden feed-in of the displacement signal.

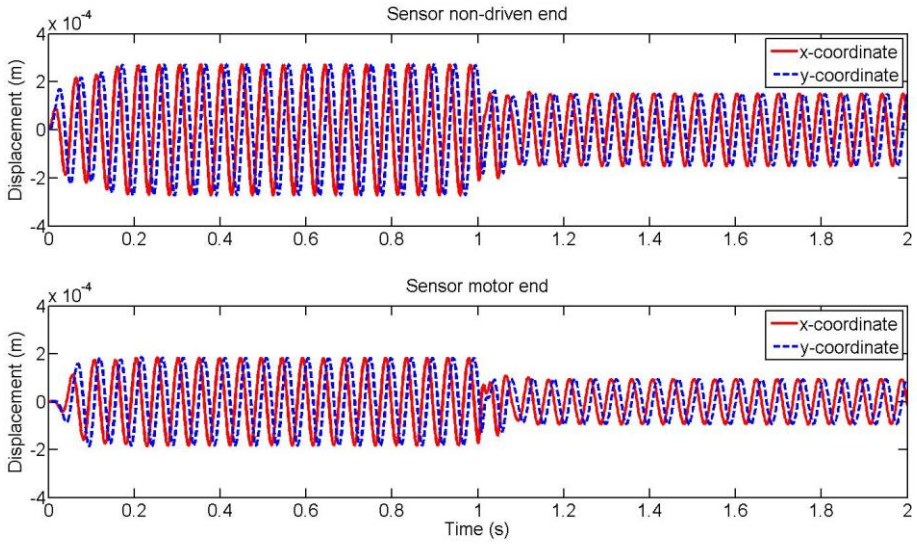

Figure 4.20 Rotor displacements at sensor planes close to the both ends (node 3 and 13) under LMI gain-scheduling control at 130 rad/s, controller was activated at 1s

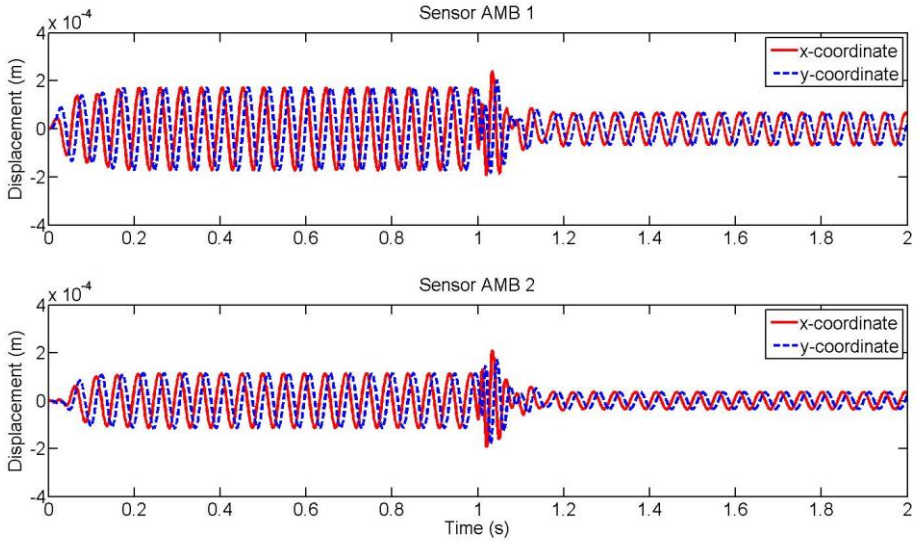

Figure 4.21 Rotor displacements at sensor planes close to the AMBs (node 5 and 11) under LMI gain-scheduling control at 130 rad/s, controller was activated at 1s

Figures 4.20 and 4.21 show the rotor displacement at sensor location during the LMI control action. When rotational speed was 130 rad/s, the vibration of rotor having second rigid body mode are reduced by gain-scheduling controller frozen at $\propto = 0.52$. Unlike low frequencies, the transients of sensors planes nearby AMBs has overshoot during sudden activation, but not significant. Figure 4.22 shows the corresponding control forces.

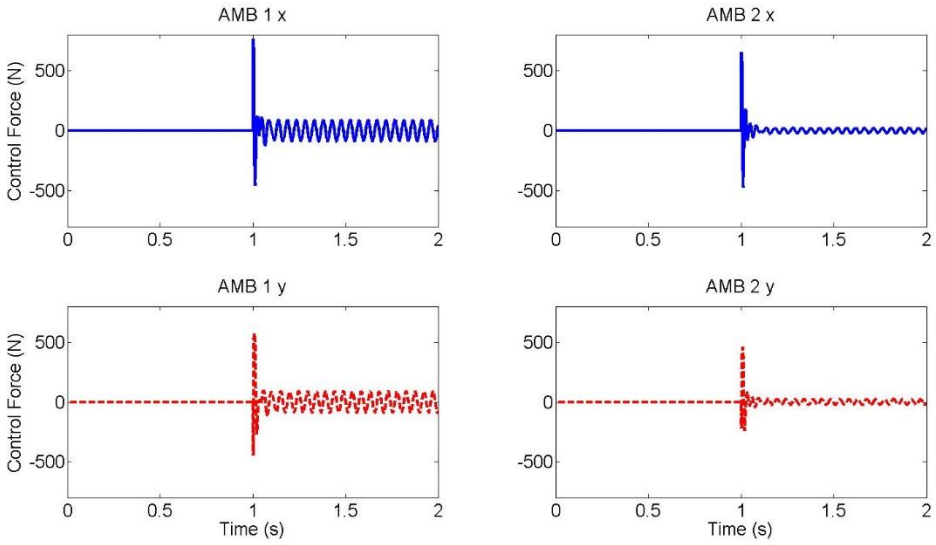

(a) Control forces by LMI gain-scheduling control

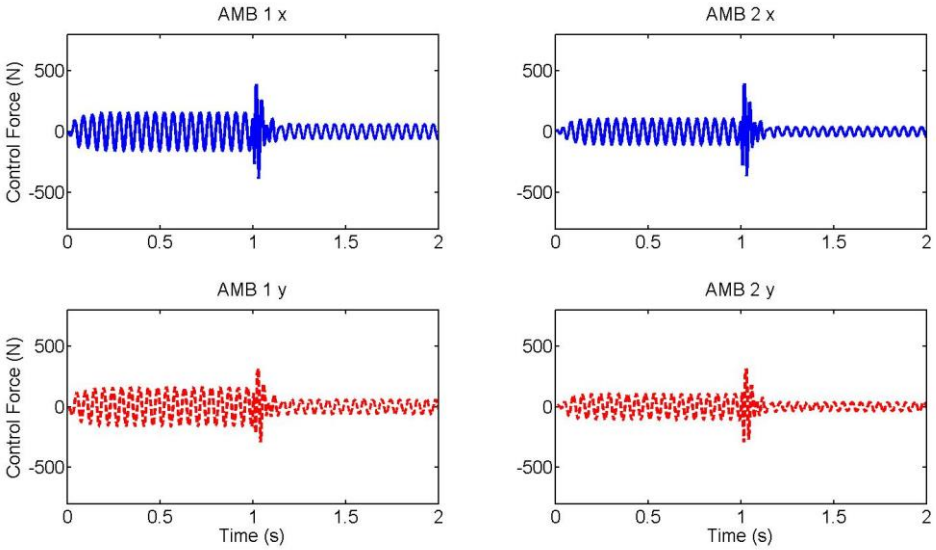

(b) Control forces by PD control

Figure 4.22 Control forces from AMBs

4.5.3 Varying Speed Test

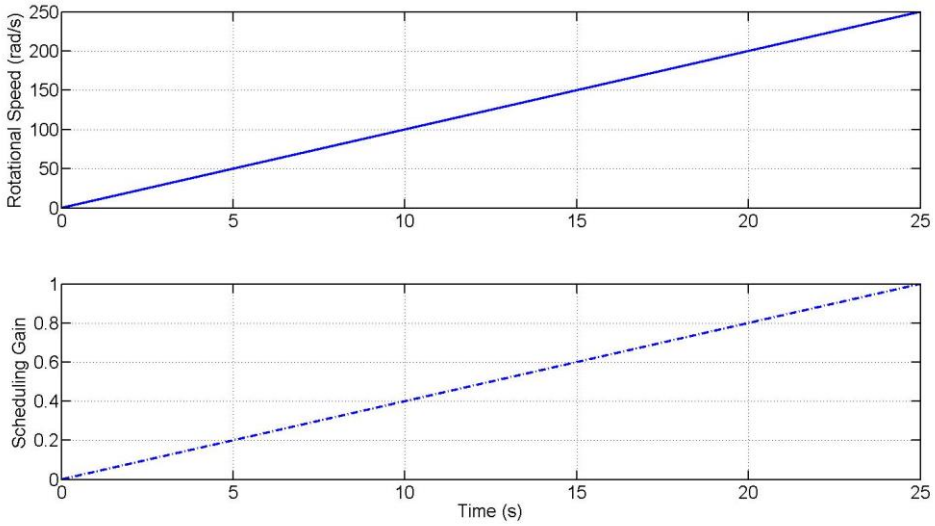

Figure 4.23 Varying rotational speed $\Omega(t)$ and scheduling gain $\propto (t)$ in run-up test

As a gain-scheduling control technique enables the controller to adapt itself online to satisfy the varying dynamics, varying speed was simulated test in time domain may be necessary to verify the capability of speed-dependent control. With an constant angular acceleration $\dot{\Omega} = 10\,\mathrm{rad/s^2}$, the rotational speed $\Omega(t)$ was run up to 250 rad/s as the maximum of the design speed range. Thus, the controller could stabilize a speed-dependent rotor/AMB system with scheduling gain $\propto (t)$ computed online. Figure 4.23 shows the varying speed $\Omega(t)$ and $\propto (t)$.

Figures 4.24 and 4.25 show the amplitude of the rotor vibration orbit at sensor planes (nodes 3, 5, 11 and 13). The time domain simulated results presented as similar as the unbalance forcing response estimation in Section 4.5.1. It also numerically demonstrates the stability offered by LMI based gain-scheduling speed-dependent control. Some oscillations can be seen when rotor is running above 180 rad/s (Figures 4.24 and 4.25). They may be induced by the numerical integral error in a long-time simulation procedure, but not by the control action. It could be demonstrated by the steady rotor response under control action when running at a typical speed in the oscillation range, say 220 rad/s (indicated in Figures 4.24 and 4.25). These

simulation results are shown in Figure 4.26 and 4.27. The control forces during the run-up test procedure are shown in Figure 4.28.

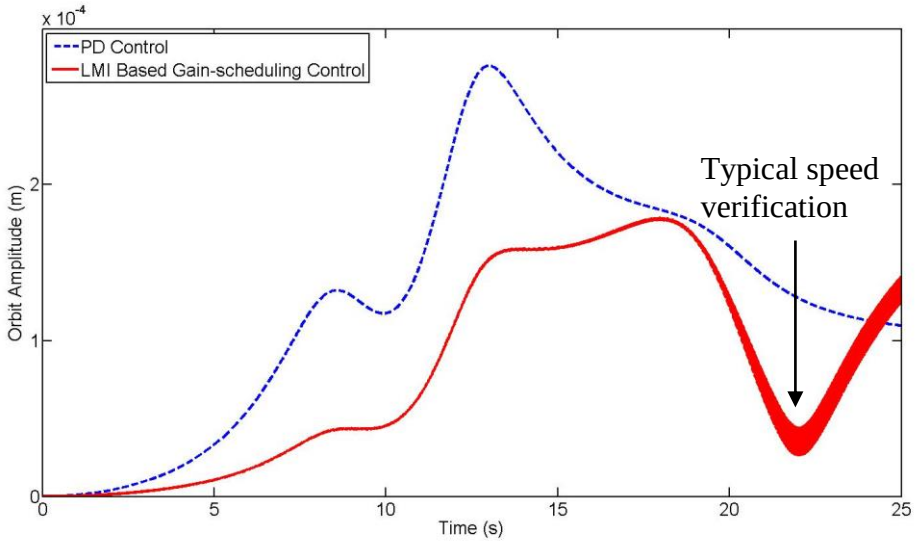

(a) Orbit amplitude at sensor plane close to the rotor non-driven end (node 13)

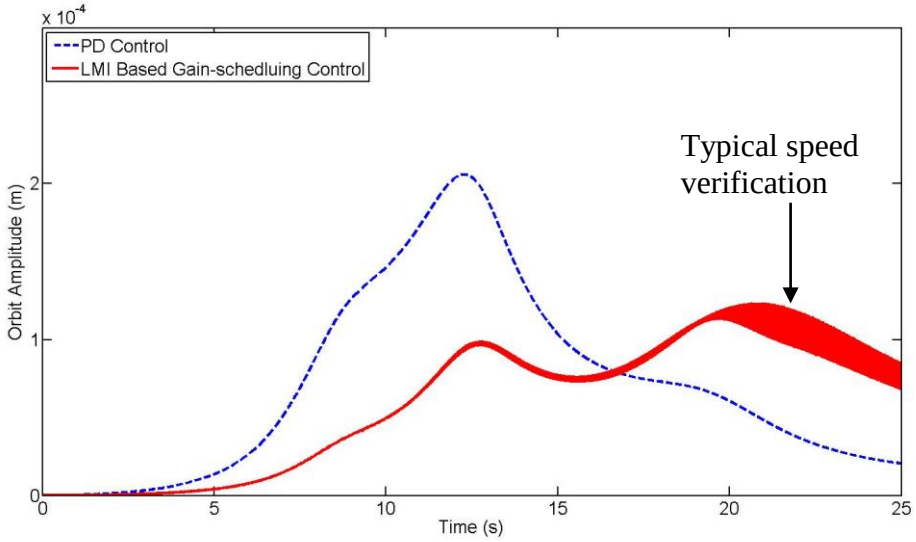

(b) Orbit amplitude at sensor plane close to the rotor motor end (node 3)

Figure 4.24 Orbit amplitudes of sensors planes at both ends under PD and PD/LMI based gain-scheduling control under run-up

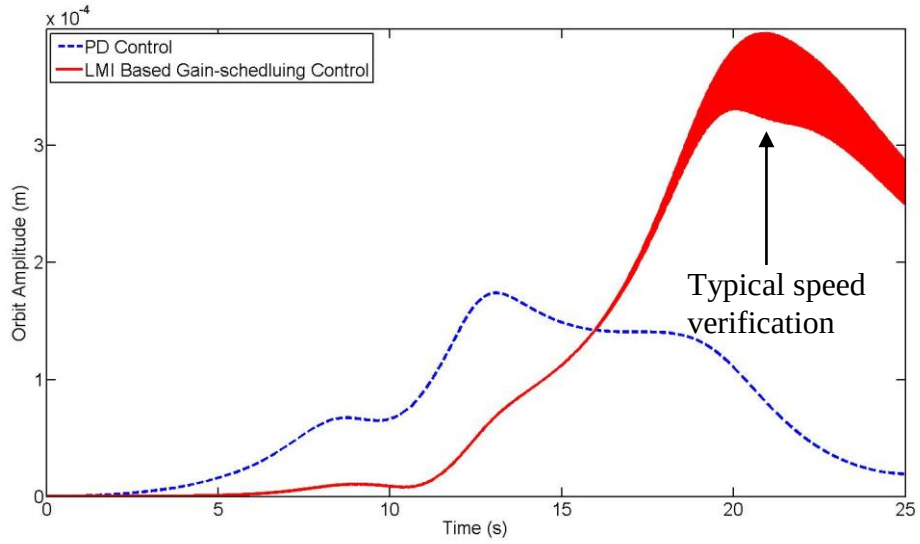

(a) Orbit amplitude at sensor plane close to the AMB 1 (node 5)

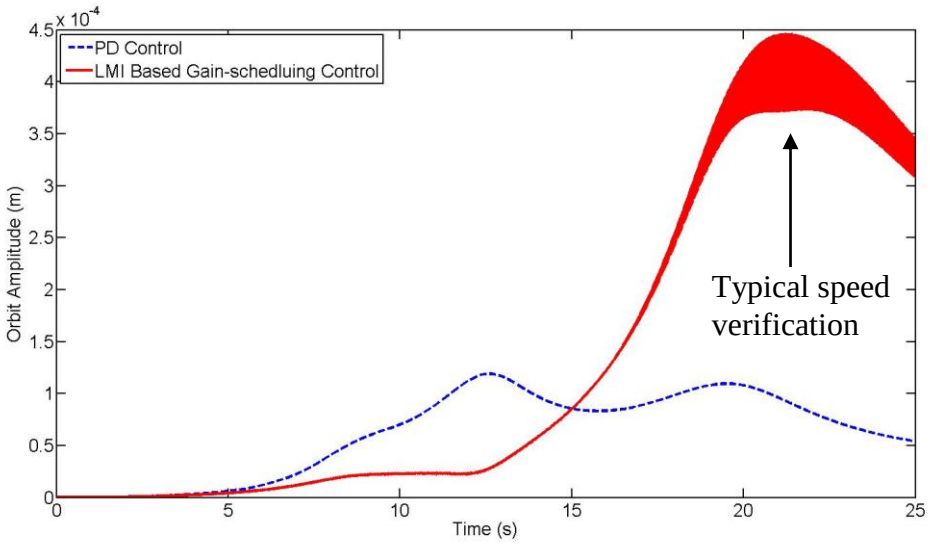

(b) Orbit amplitude at sensor plane close to the AMB 1 (node 11)

Figure 4.25 Orbit amplitudes of sensors planes nearby AMBs under PD and PD/LMI based gain-scheduling control under run-up

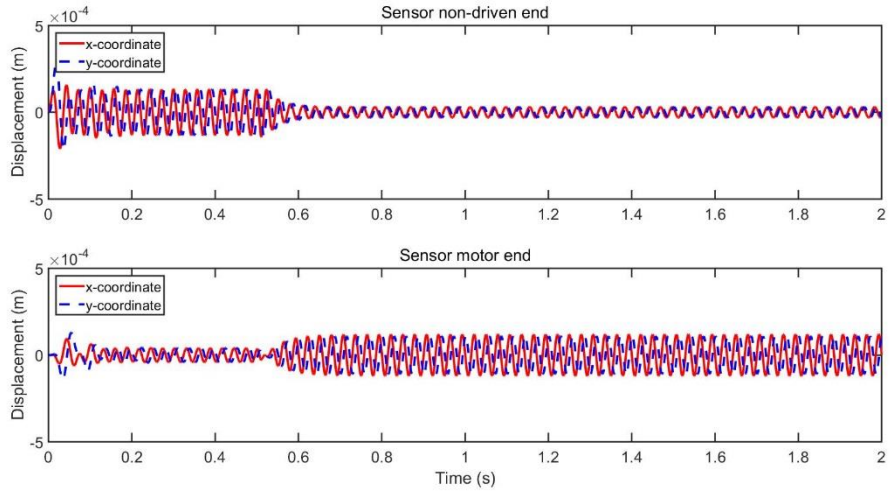

Figure 4.26 Rotor displacements at sensor planes close to the both ends (node 3 and 13) under LMI gain-scheduling control at 220 rad/s, controller was activated at 0.5 s

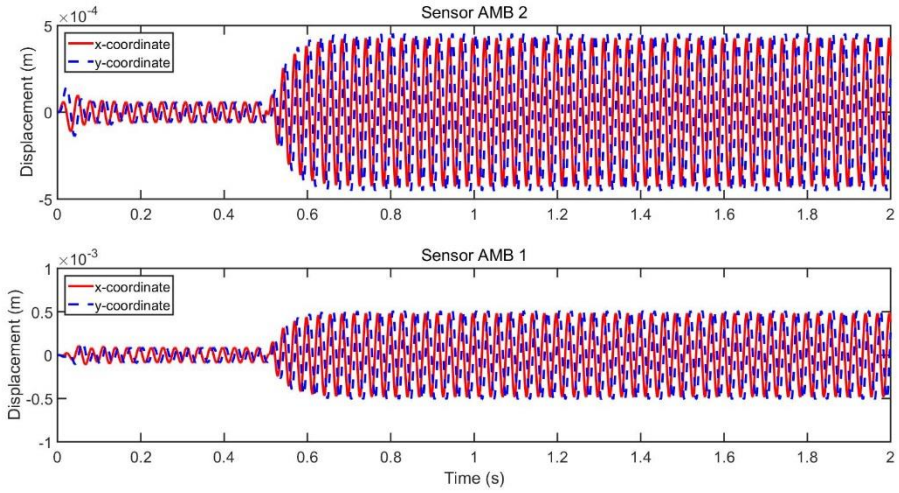

Figure 4.27 Rotor displacements at sensor planes close to the AMBs (node 5 and 11) under LMI gain-scheduling control at 220 rad/s, controller was activated at 0.5 s

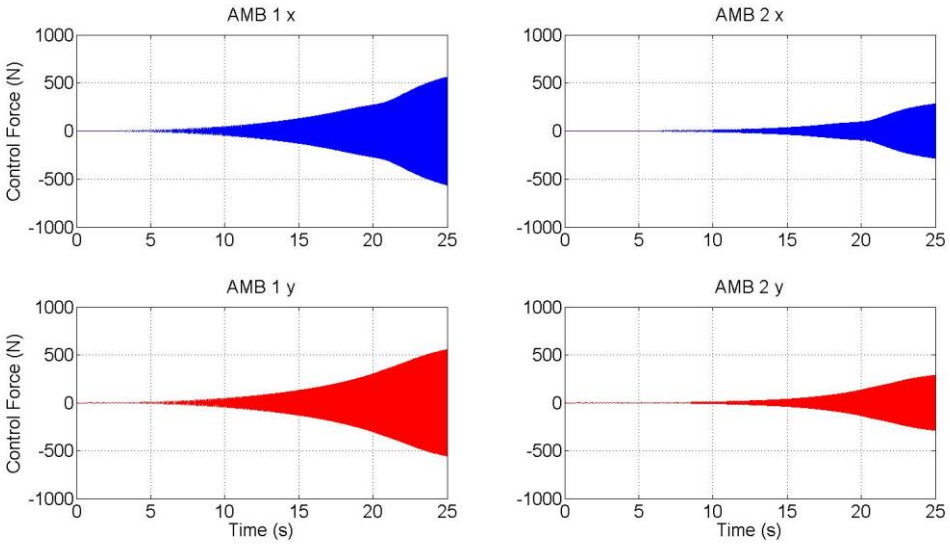

(a) Control forces by LMI gain-scheduling control

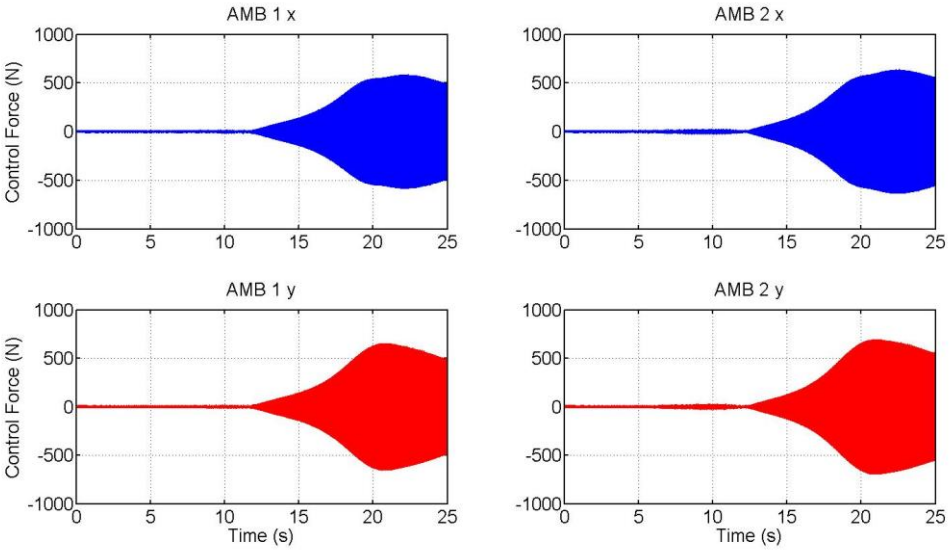

(b) Control forces by PD control

Figure 4.28 Control forces from AMBs during run-up simulated test

4.6 Closure

This chapter introduces a description for LPV system. Parameter-dependent system uncertainties can be defined through a polytope with tractability. The model reduction for the LPV system presented, enabling a reduced order model to obtain linear interpolation for LMI based gain-scheduling control design. Based on the LMI gain-scheduling technique, a controller for a speed-dependent rotor/AMB system was synthesized and improved by numerical balancing. Control performance was assessed in frequency/time domains. The simulated results showed the gain-scheduling controller could attenuate rotor vibration effectively over the designed speed range. Also, the stability of closed loop system was verified numerically when rotor runs in speed-up operation.

Chapter 5 LMI Based Gain-Scheduling H_∞ Control for Contact-free Recovery

Contact of a rotor with a touchdown bearing (TDB) during operation may be a problematic. A LTI H_∞ Riccati based controller may not be able to stabilize the system when the rotor is trapping in contact with a TDB, as system dynamics may change significantly during contact. Rotor orbits may have unpredictable behaviour depending on contact conditions and even become unstable, if a state-space controller does not include rotor contact dynamics. Nonlinear contact dynamics could be linearized and modelled as a basic plant for control design. However, a parameter independent LTI controller may not be able to adjust itself to linear parameter varying (LPV) feedback. Moreover, simply embedding contact dynamics in a rotor model may not be sufficient. In practice, large contact forces also react on the base supporting structure, hence sensor readings for closed loop control may be affected. Thus, a basic plant including a free-free rotor, linear AMB systems under PD control, contact dynamics and base structure dynamics would be useful.

In order to guarantee robust stability of a rotor/AMB system under contact, a LMI based gain-scheduling control technique is introduced in this chapter. Based on a parameter dependent augmented plant, the controller uses ‘effective stiffness’ to adjust itself to satisfy time varying dynamics during rotor/TDB events. For the linear varying feedback requirement, this chapter linearizes the contact according to TDB radial clearance, through ignoring penetration depth of contact. Observer include base and inverse base models to transform accelerometer direct feedback as a polytopic coordinate for LPV controller adjustment.

From a base/rotor interaction model incorporating an effective stiffness to represent contact, a LMI gain-scheduling H_∞ controller may be synthesized. Along with this time varying parameter, the controller is designed to bring the rotor out of contact and to reduce vibration.

5.1 Rotor/TDB Contact

During operation, rotor/TDB exhibits complex dynamic behaviour, which depends on conditions such as impact speed/angle, rotational speed, unbalance condition and material properties [13]. When impact occurs, a rotor under PD control may be able to be recovered to a contact-free state, or else remain trapped in contact. Contact induced rotor responses may involve in limit cycles (constant rubbing), or become chaotic with bouncing and sub-harmonics [19].

5.1.1 Contact Mode

In contact modelling, it is necessary to include the rotor/base interaction model shown in equation (2.55) as the motion of the base may have an effect on contact force estimation. The assumptions are [20]:

- The touchdown bearing remains rigid as a macro body
- Local distortion applies over a Hertzian contact patch with the rotor

Two typical non-linear contact modes are examined through simulation:

Type A: Rotor orbit under contact with constant rubbing
Type B: Rotor/TDB having periodic impact with sub-harmonics, and so-called bouncing

The simulation parameters are shown in Table 5.1, running speeds selected for the rubbing mode is 125 rad/s around the second rotor rigid body and 445 rad/s for bouncing around the second flexible mode. The rotor/auxiliary bearing clearance is $c_{rotor,tdb} = 0.4$ mm.

Table 5.1 Simulation parameters for contact

	m_e	Ω	Eccentric location	Contact
Type A	500 g · cm	125 rad/s	Disk 4 (node 14)	Non-driven (node 15)
Type B	400 g · cm	445 rad/s	Disk 4 (node 14)	Non-driven (node 15)

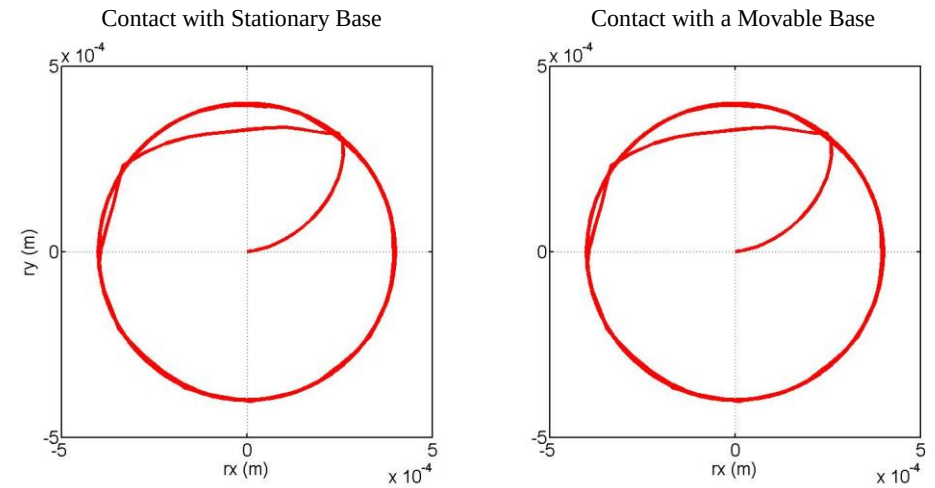

(a) Contact orbits

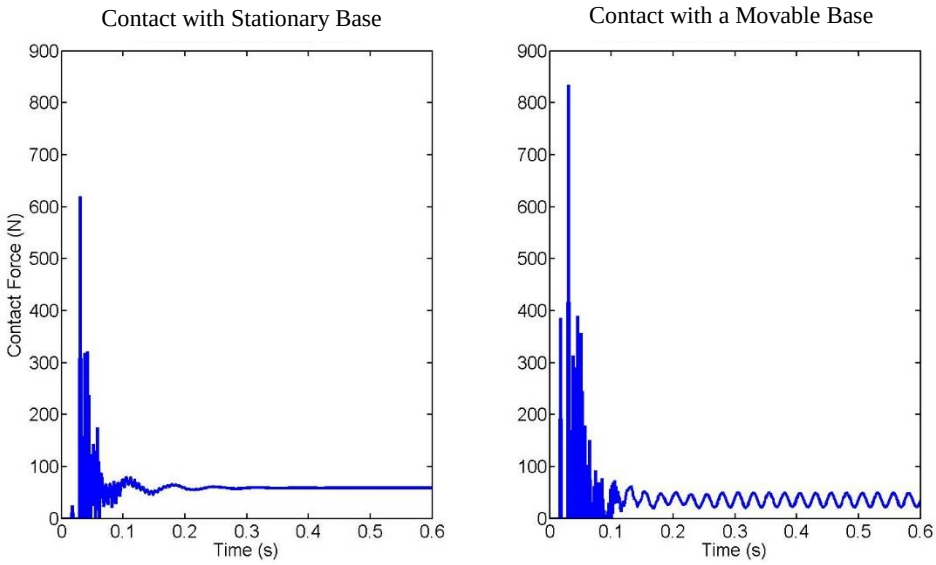

(b) Contact forces

Figure 5.1 Contact event in rubbing mode with different base models, Type A

Figure 5.1 shows the simulated rotor responses under contact in a rubbing mode. The rotor orbits are similar with stationary base and under interaction with a movable, and are limited by the rotor/TDB clearance $c_{rotor,tdb}$.

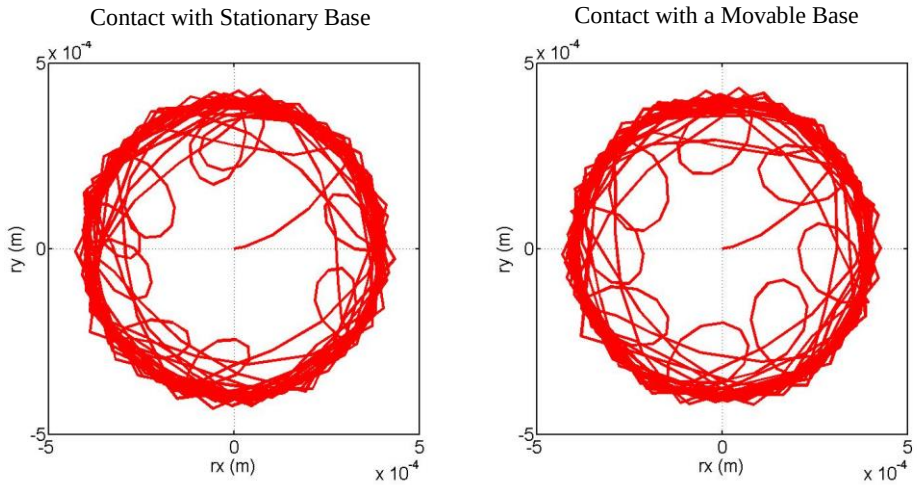

(a) Contact orbits

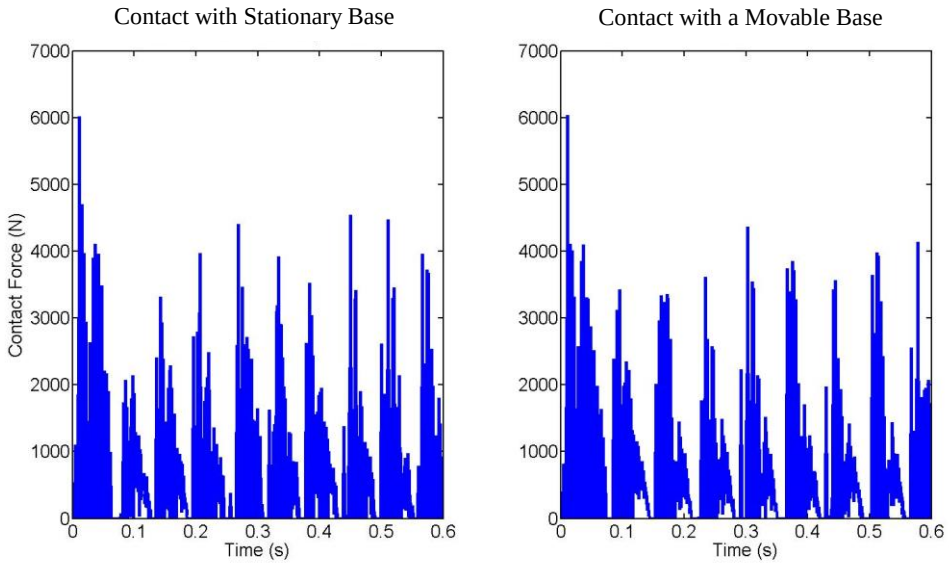

(b) Contact force

Figure 5.2 Contact events involving bouncing mode with different base models, Type B

Figure 5.2 shows the rotor responses under contact involving bouncing mode, with stationary and movable bases. The bouncing behaviour reveals sub-harmonics of the synchronous frequency, in each case.

5.1.2 Bi-stable Rotor Response

If the appropriate unbalance force amplitude remains constant and no other external disturbance occurs, a PD controlled rotor has same capability to recover from contact during run-up/down operation. The angular acceleration $\ddot{\varphi} = \dot{\Omega}$ and the unbalance forcing components have the following forms in a rotating frame:

$$\begin{aligned} F_B^u &= me_v\ddot{\varphi} + me_u\dot{\varphi}^2 \\ F_B^v &= -me_u\ddot{\varphi} + me_v\dot{\varphi}^2 \end{aligned} \tag{5.1}$$

Also, in a fixed frame of reference,

$$\begin{bmatrix} F_B^x \\ F_B^y \end{bmatrix} = \begin{bmatrix} \cos(\Omega t + \phi) & -\sin(\Omega t + \phi) \\ \sin(\Omega t + \phi) & \cos(\Omega t + \phi) \end{bmatrix} \begin{bmatrix} F_B^u \\ F_B^v \end{bmatrix} \tag{5.2}$$

Thus, PD controlled rotor responses may differ between run-up and run-down, exhibiting bi-stable characteristics.

The bi-stable behaviour can be shown in simulation. For mass eccentricity $me = 200\ \mathrm{g \cdot cm}$ mounted on Disk 4 (node 14) contact happens at the non-driven end (node 15) with rotor/TDB radical clearance same as $c_{rotor,tdb} = 0.4\ \mathrm{mm}$. The angular acceleration $\ddot{\varphi} = 5\ \mathrm{rad/s^2}$, and rotational speed Ω running up to 200 rad/s.

Figure 5.3 shows the simulated rotor responses with run-up and down operations. During run-up, the rotor hits the TDB at around 130 rad/s, after which bouncing contact occurs. With increasing speed, contact mode starts becomes rubbing from 145 rad/s to 170 rad/s, then contact ceases. The situation is quite different when run-down occurs. Contact in bouncing is reduced compared with run-up and contact ceases below 130 rad/s. Base supporting stiffness characteristics are also different in *x* and *y* directions, which is presented in the base modelling Section 2.3. These result in the responses in the base motions of Figure 5.4.

Figure 5.5 shows the contact forces during run-up and down, based on the contact forcing components shown in equations (2.35)-(2.40). The differences in each case are notable.

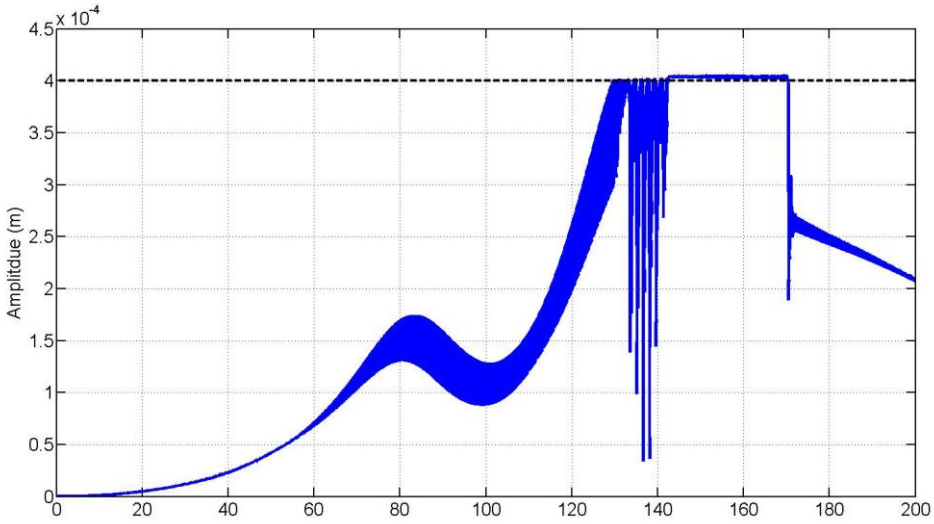

(a) Run-up operation

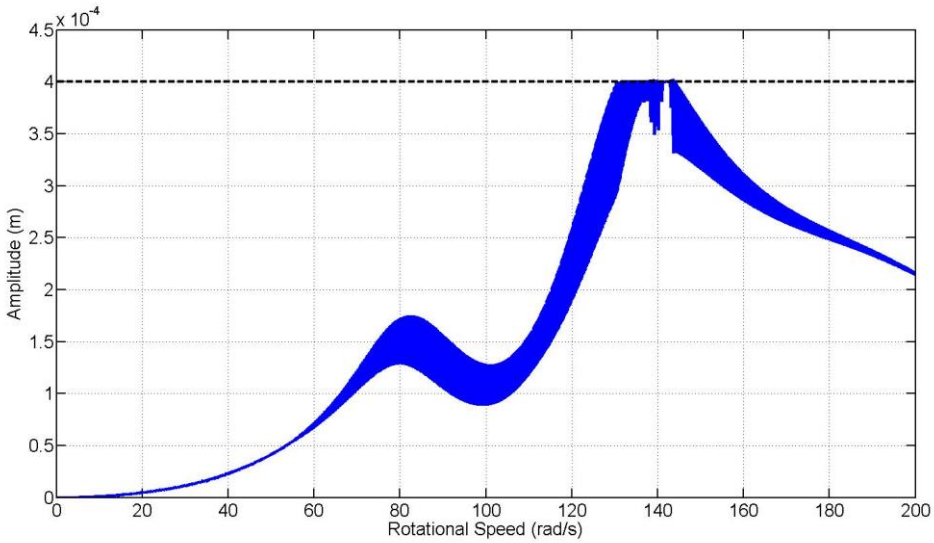

(b) Run-down operation

Figure 5.3 Simulated bi-stable rotor response at the non-driven end (node 15) with a movable base

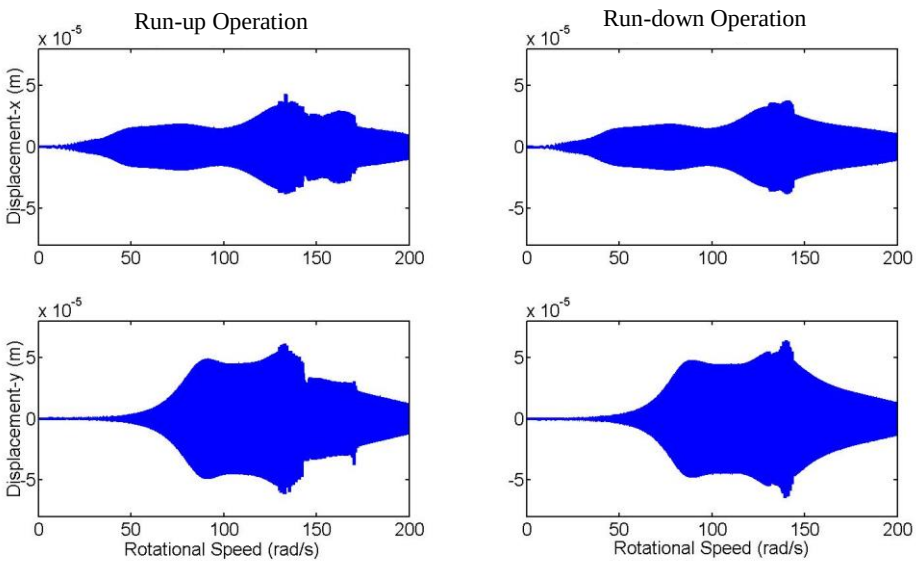

Figure 5.4 Base displacements during run-up and down

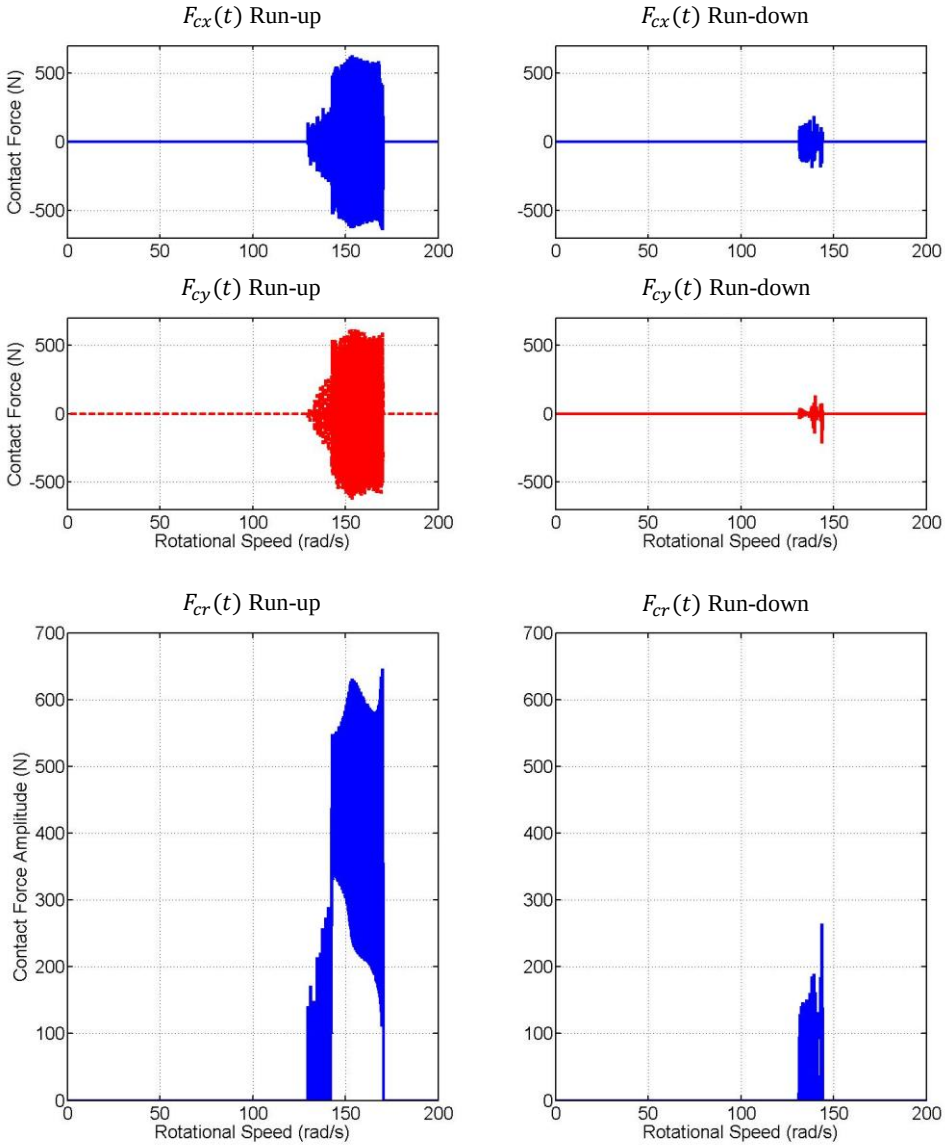

Figure 5.5 Contact forces during run-up and down

5.2 LPV Contact Feedback

Rotor/TDB contact force components have been discussed in Chapter 2. Such complex contact events may need simplification, linearization for dynamic tracking, based on the LMI based gain-scheduling technique stated in Chapter 4.

5.2.1 Effective Stiffness Estimation

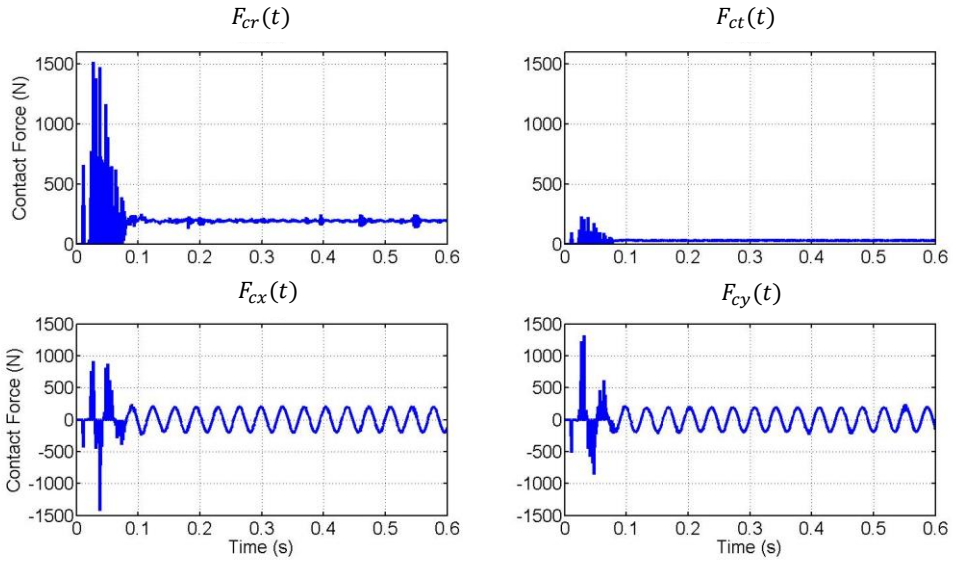

Figure 5.6 Simulated nonlinear contact force

Rotor/TDB contact normally has nonlinear behaviour. Contact forces may be determined from radial penetration and tangential friction as stated in equations (2.35)-(2.40). Practically, penetration is difficult to be measured. For LPV controller design, nonlinear contact may be linearized as a parameter embedded in the basic plant. The amplitude of contact force may be represented as clearance multiplied by an effective stiffness, which varies only when the rotor makes contact with a TDB.

Following equations (2.35)-(2.40), the radial contact force has components

$$\begin{aligned} F_{cx} &= F_c \cos\theta_c \\ F_{cy} &= F_c \sin\theta_c \end{aligned} \tag{5.3}$$

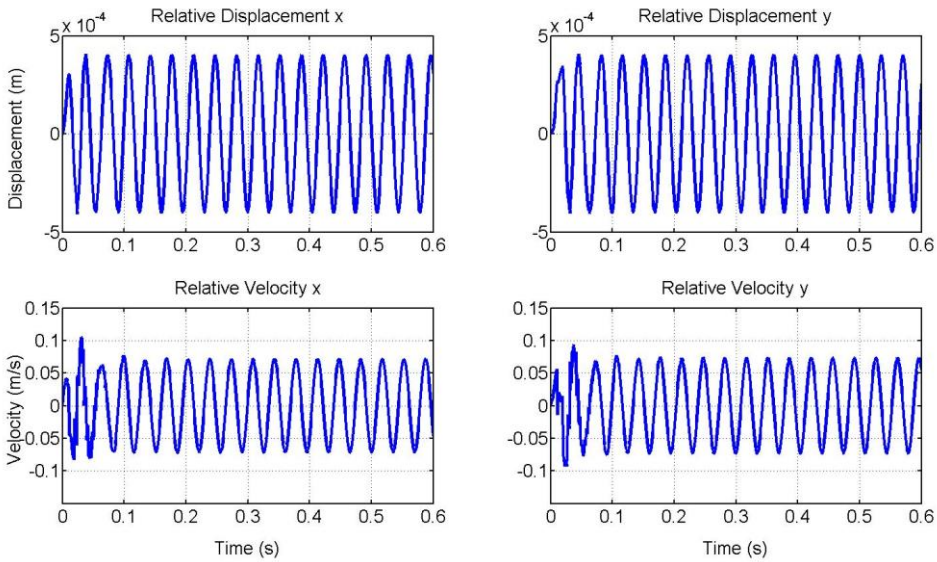

Figure 5.7 Relative displacement/velocity under contact

where the contact force amplitude $F_c = \sqrt{{F_{ct}}^2 + {F_{cr}}^2}$, and the impact angle θ_c. Here, F_{cr} is the normal component and F_{ct} is the tangential (friction) component. Figure 5.6 shows the contact force simulated rubbing like contact mode, with unbalance $me = 500$ g · cm running at 180 rad/s.

The relative rotor to TDB displacement at the contact end with small penetration $\delta(t)$ may be written as

$$\begin{aligned} s_{rel}^{x} &= (c_{rotor,tdb} + \delta(t))\cos\theta_c \\ s_{rel}^{y} &= (c_{rotor,tdb} + \delta(t))\sin\theta_c \end{aligned} \tag{5.4}$$

where the rotor/base relative displacement $s_{rel}^{x,y} = s_{non-driven}^{x,y} - s_{acc}^{x,y}$. According to equation (5.4), the rotor radial displacement under contact is given by

$$s_d^c(t) = c_{rotor,tdb} + \delta(t) \tag{5.5}$$

Figure 5.7 shows the relative displacement and velocity under contact at the non-driven end. Due to rubbing contact, the relative displacements $s_{rel}^{x}(t)$ and $s_{rel}^{y}(t)$ are constrained by the TDB radial clearance $c_{rotor,tdb}$.

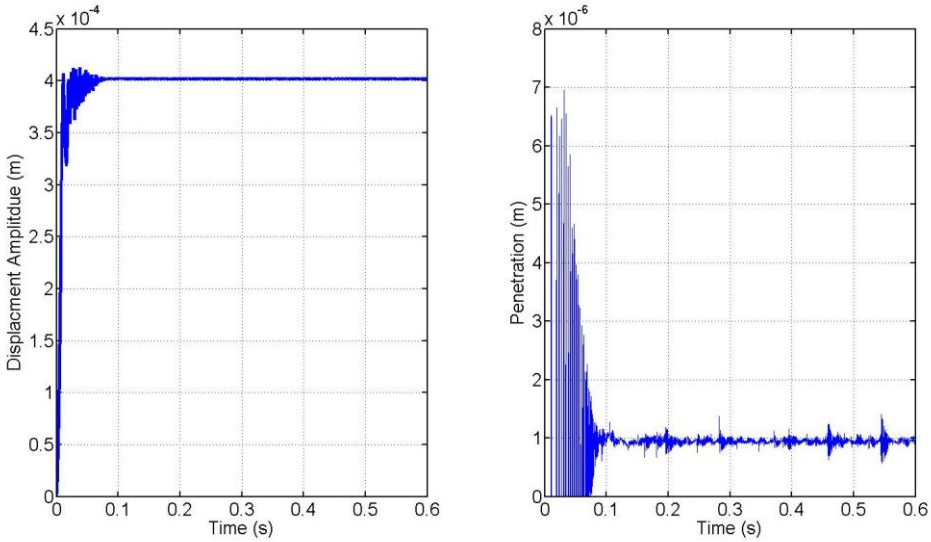

Figure 5.8 $s_d^c(t)$ and $\delta(t)$

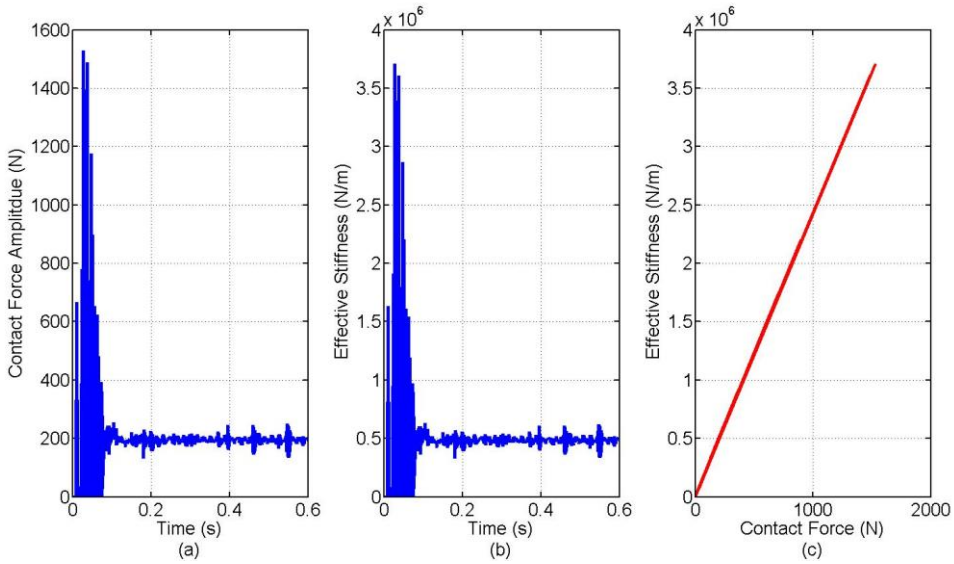

Figure 5.9 Effective stiffness estimation

By comparing the simulated results in Figure 5.8, the penetration may be ignored when estimating effective stiffness. Therefore, based on equations (5.4) the effective stiffness in *x*/*y* directions could be linearized as

$$k_e^x = \frac{F_{cx}}{s_{rel}^x} = \frac{F_c \cos\theta_c}{(c_{rotor,tdb} + \delta(t))\cos\theta_c} \approx \frac{F_c}{c_{rotor,tdb}}$$
$$k_e^y = \frac{F_{cy}}{s_{rel}^y} = \frac{F_c \sin\theta_c}{(c_{rotor,tdb} + \delta(t))\sin\theta_c} \approx \frac{F_c}{c_{rotor,tdb}} \quad (5.6)$$

Thus, the nonlinear contact force behaviour could be simplified as a linear effective stiffness for feedback purpose. The results are shown in Figure 5.9.

5.2.2 LPV Contact Feedback

Figure 5.10 shows the block diagram for the effective stiffness estimation observer. An accelerometer was used in the test rig to measure the base acceleration at the non-driven rotor end. Under acceleration feedback, it may be possible to estimate contact condition.

When rotor/TDB contact occurs, the base will be excited by the contact impact and also AMB actuation force. AMB force, which is dependent on input current, could be measured directly. A base model with acceleration output may be introduced to eliminate acceleration caused by the AMB force. Then, an inverse base model may be used to obtain contact force from acceleration.

For acceleration output, the base model $\mathbf{P}_B$ shown in equation (2.49) may be written as

$$\mathbf{P}_B^a : \begin{cases} \dot{\mathbf{q}}_B^a = \mathbf{A}_B^a \mathbf{q}_B^a + \mathbf{B}_B^a \mathbf{u}_B \\ \mathbf{y}_B^a = \mathbf{C}_B^a \mathbf{q}_B^a + \mathbf{D}_B^a \mathbf{u}_B \end{cases} \quad (5.7)$$

where $\mathbf{q}_B^a = \mathbf{q}_B$, $\mathbf{A}_B^a = \mathbf{A}_B$, $\mathbf{B}_B^a = \mathbf{B}_B$, $\mathbf{C}_B^a = [-\mathbf{M}_b^{-1}\mathbf{K}_b \quad -\mathbf{M}_b^{-1}\mathbf{G}_b]$ and $\mathbf{D}_B^a = \mathbf{M}_b^{-1}$.

Thus, the acceleration output signal may be obtained as

$$\mathbf{y}_{acc}^a = \mathbf{T}_{acc}(-\mathbf{M}_b^{-1}\mathbf{K}_b\mathbf{q}_B - \mathbf{M}_b^{-1}\mathbf{G}_b\dot{\mathbf{q}}_B + \mathbf{M}_b^{-1}\mathbf{u}_B) \quad (5.8)$$

where the acceleration output $\mathbf{y}_{acc}^a = \begin{bmatrix} y_{acc,x}^a \\ y_{acc,y}^a \end{bmatrix}$, the matrix $\mathbf{T}_{acc}$ specifies the accelerometer location in base modelling.

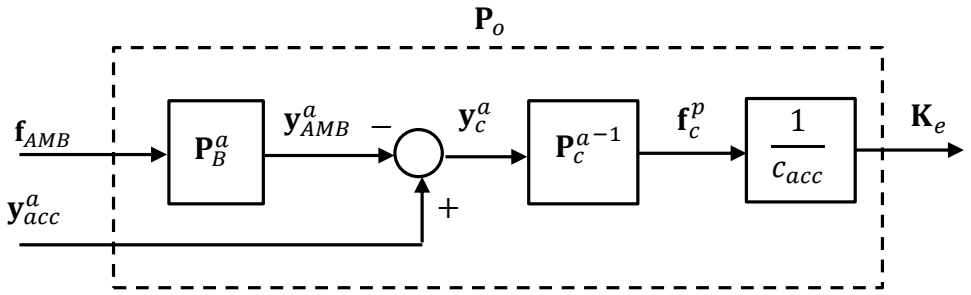

Figure 5.10 Block diagram of the observer for linear varying effective stiffness

Under contact, the acceleration may be expressed as

$$\begin{aligned}\mathbf{y}_{acc}^a &= \mathbf{y}_{AMB}^a + \mathbf{y}_c^a \\ \mathbf{y}_c^a &= \mathbf{y}_{acc}^a - \mathbf{y}_{AMB}^a\end{aligned} \tag{5.9}$$

where $\mathbf{y}_c^a = \begin{bmatrix} y_{c,x}^a \\ y_{c,y}^a \end{bmatrix}$ and $\mathbf{y}_{AMB}^a = \mathbf{P}_B^a \mathbf{f}_{AMB}$ the acceleration caused by AMB control force, and $\mathbf{f}_{AMB}$ is known. Thus, the acceleration by the contact force only may be obtained.

Now write

$$\mathbf{y}_c^a = \mathbf{P}_c^a \mathbf{f}_c^p \tag{5.10}$$

where $\mathbf{f}_c^p = \begin{bmatrix} F_{cx}^p \\ F_{cy}^p \end{bmatrix}$ is a vector of contact force components, and the base model with contact force input and acceleration output may be obtained as

$$\mathbf{P}_c^a = \begin{bmatrix} \mathbf{A}_c^a & \mathbf{B}_c^a \\ \mathbf{C}_c^a & \mathbf{D}_c^a \end{bmatrix} \tag{5.11}$$

where $\mathbf{A}_c^a = \mathbf{A}_B^a$, $\mathbf{B}_c^a = \mathbf{B}_B^a \mathbf{T}_c$, $\mathbf{C}_c^a = \mathbf{T}_{acc} \mathbf{C}_B^a$, $\mathbf{D}_c^a = \mathbf{T}_{acc} \mathbf{D}_B^a$ and $\mathbf{T}_c$ determines the location of the contact events.

Therefore, with the invertible $\mathbf{D}_c^a$ matrix in equation (5.11), an inverse base model may be obtained as follows:

$$\mathbf{f}_c^p = \mathbf{P}_c^{a-1} \mathbf{y}_c^a \tag{5.12}$$

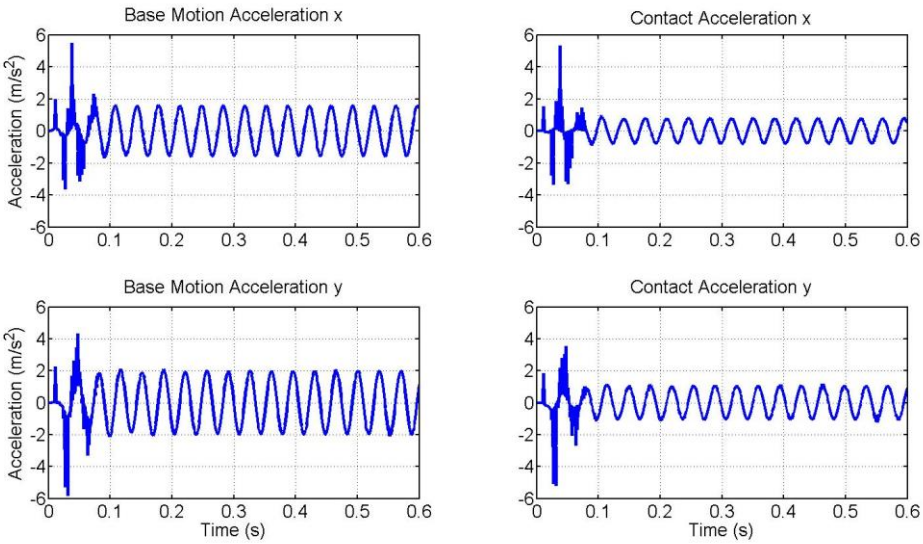

Figure 5.11 Simulated results for $\mathbf{y}_{acc}^{a}(t)$ and $\mathbf{y}_{c}^{a}(t)$

where $\mathbf{P}_c^{a-1} = \begin{bmatrix} \mathbf{A}_c^a - \mathbf{B}_c^a \mathbf{D}_c^{a-1} \mathbf{C}_c^a & \mathbf{B}_c^a \mathbf{D}_c^{a-1} \\ -\mathbf{D}_c^{a-1} \mathbf{C}_c^a & \mathbf{D}_c^{a-1} \end{bmatrix}$. Thus, the disturbance observer to estimate effective stiffness may be obtained as

$$\mathbf{f}_c^p = \mathbf{P}_o \begin{bmatrix} \mathbf{f}_{AMB} \\ \mathbf{y}_{acc}^a \end{bmatrix} \tag{5.13}$$

where $\mathbf{P}_o = \begin{bmatrix} -\mathbf{P}_c^{a-1} \mathbf{P}_B^a & \mathbf{P}_c^{a-1} \end{bmatrix}$.

Thus, effect stiffness could be estimated from equation (5.6).

The observer for contact prediction was examined in simulation, with same parameter as unbalance $m_e = 500\ \text{g} \cdot \text{cm}$ running at 180 rad/s. Figure 5.11 shows the acceleration of the base motion and the sub-acceleration caused only be contact. The corresponding base motion and inferred acceleration are shown in Figure 5.12. In the aspect of numerical study, it also gives the contact force and the prediction by the observer as shown in Figure 5.13.

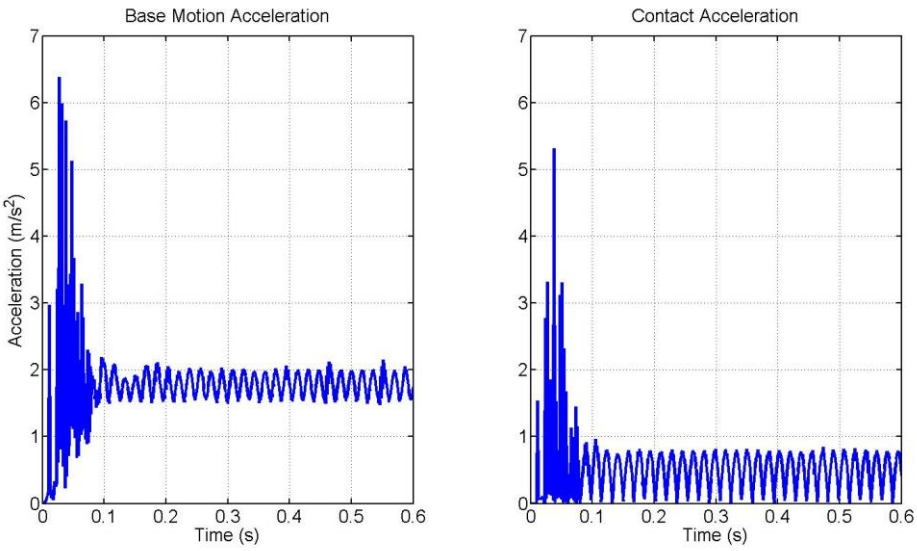

Figure 5.12 Simulated base motion acceleration and inferred acceleration caused only by contact

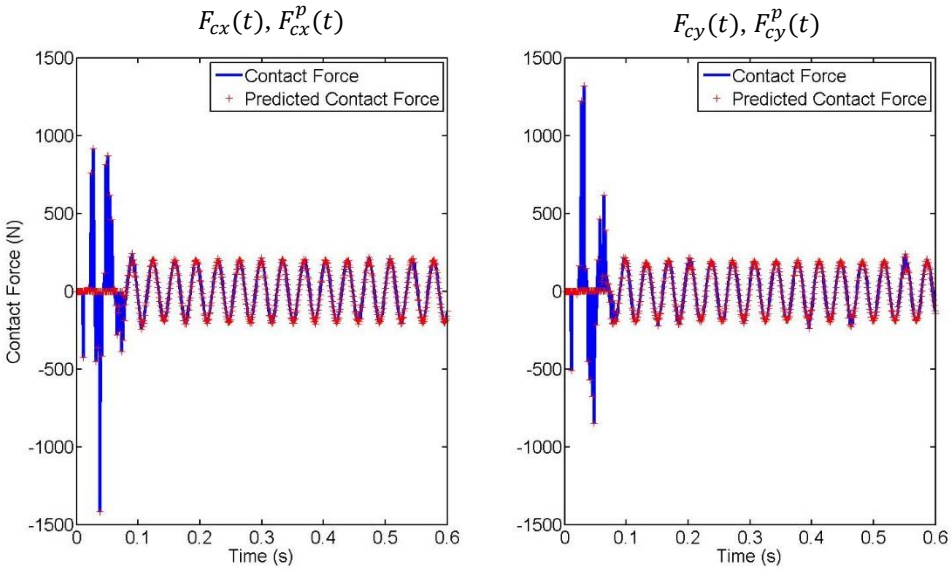

Figure 5.13 Simulated contact forces $F_{cx}(t)$ and $F_{cy}(t)$, and predicted contact force $F_{cx}^{p}(t)$ and $F_{cy}^{p}(t)$

From the simulated results shown in Figures 5.11-5.13, the contact estimation observer $\mathbf{P}_o(s)$ is able to predict the contact force with acceleration feedback. By introducing $\mathbf{P}_B^a$, acceleration caused by AMB force was able to be eliminated.

Acceleration from contact is thus extracted from direct acceleration feedback, and estimated as contact force through $\mathbf{P}_c^{a-1}$.

5.3 Contact-Dependent Rotor/Base System

Contact-dependent rotor/base system may be formed as LPVs, if effective stiffness can be estimated based on an accelerometer feedback signal through the observer presented in Section 5.2. Thus, rotor/AMB system dynamic uncertainties induced by contact events can be structured tractably. Then, the linear interpolation in the LPV system may be obtained allowing LMI based gain-scheduling control optimization to be implemented.

5.3.1 Rotor/Base Contact LPV Modelling

In order to guarantee stability during contact, contact dynamics needs to be evolved in a basic plant for controller design. In addition to a rotor under linear AMB PD control, the base model and effective stiffness represented by contact dynamics are also essential. A block diagram of the basic plant is shown in Figure 5.14. The system input is control force, while outputs are sensor node displacements in relative coordinates. A PD controlled AMB force acts on the free-free rotor and the base, in an equal opposite manner. Base model outputs (displacements of sensor brackets) feed into the PD controller. The effective stiffness block, including *x*/*y* coordinates, is embedded with rotor and base models.

Effective Stiffness Dependent Plant State-Space Form

Under varying contact force, a free-free rotor may be considered as a stiffness-dependent system. Based on the free-free rotor model shown in equation (2.21), it may be written as

$$\mathbf{P}_R(k_e): \begin{cases} \dot{\mathbf{q}}_R = \mathbf{A}_R\mathbf{q}_R + \mathbf{B}_R\mathbf{u}_e - \mathbf{B}_R^p\mathbf{u}_p + \mathbf{B}_R^c\mathbf{f}_c(k_e) \\ \mathbf{y}_R = \mathbf{C}_R\mathbf{q}_R + \mathbf{D}_R\mathbf{u}_R \end{cases} \tag{5.14}$$

where $\mathbf{B}_R^p$ and $\mathbf{B}_R^c$ are the location matrices definning AMB's control and contact event nodes.

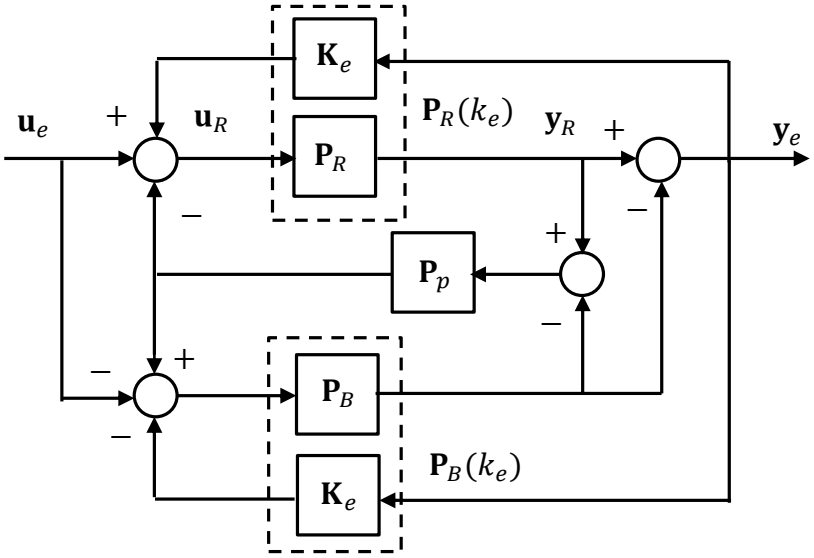

Figure 5.14 Block diagram of the effective stiffness dependent plant including rotor, base and PD control action

Further, $\mathbf{u}_R = \mathbf{u}_e - \mathbf{u}_p + \mathbf{f}_c(k_e)$, $\mathbf{u}_e, \mathbf{u}_p$ and $\mathbf{f}_c(k_e)$ are the LMI based gain-scheduling control input, PD control input and contact force. In this linear model,

$$\mathbf{f}_c(k_e) = \mathbf{K}_e[\mathbf{s}_R^{acc} - \mathbf{s}_B^{acc}] \tag{5.15}$$

where, $\mathbf{s}_R^{acc} = \mathbf{T}_R^{acc}\mathbf{y}_R = \begin{bmatrix} s_{R,acc}^x \\ s_{R,acc}^y \end{bmatrix}$ and $\mathbf{s}_B^{acc} = \mathbf{T}_B^{acc}\mathbf{y}_B = \begin{bmatrix} s_{B,acc}^x \\ s_{B,acc}^y \end{bmatrix}$ are displacements of the rotor non-driven end (node 15) and any accelerometer mounted on the base. Also, $\mathbf{K}_e = \begin{bmatrix} k_e & 0 \\ 0 & k_e \end{bmatrix}$ is the effective stiffness matrix.

Based on the MIMO base model shown in equation (2.49), the rigid body base under contact and control has a state-space form

$$\mathbf{P}_B(k_e): \begin{cases} \dot{\mathbf{q}}_B = \mathbf{A}_B\mathbf{q}_B - \mathbf{B}_B\mathbf{u}_e + \mathbf{B}_B^p\mathbf{u}_p - \mathbf{B}_B^c\mathbf{f}_c(k_e) \\ \mathbf{y}_B = \mathbf{C}_B\mathbf{q}_B + \mathbf{D}_B\mathbf{u}_B \end{cases} \tag{5.16}$$

Also, a linear AMB model under PD control shown in equation (2.28), can be written as

$$\mathbf{P}_p: \begin{cases} \dot{\mathbf{q}}_p = \mathbf{A}_p\mathbf{q}_p + \mathbf{B}_p\mathbf{u}_p \\ \mathbf{y}_p = \mathbf{C}_p\mathbf{q}_p + \mathbf{D}_p\mathbf{u}_p \end{cases} \tag{5.17}$$

where $\mathbf{u}_p = [\mathbf{s}_R^{AMB} - \mathbf{s}_B^{AMB}] = \mathbf{T}_R^{AMB}\mathbf{y}_R - \mathbf{T}_B^{AMB}\mathbf{y}_B$.

Therefore, the effective stiffness dependent rotor/base model under PD control action is formed in LPVs

$$\mathbf{P}_e(k_e): \begin{cases} \dot{\mathbf{q}}_e = \mathbf{A}_e(k_e)\mathbf{q}_e + \mathbf{B}_e\mathbf{u}_e \\ \mathbf{y}_e = \mathbf{C}_e\mathbf{q}_e + \mathbf{D}_e\mathbf{u}_e \end{cases} \tag{5.18}$$

where

$$\mathbf{A}_e(k_e) = \begin{bmatrix} \mathbf{A}_R - \mathbf{B}_R^p\mathbf{D}_p\mathbf{C}_R + \mathbf{B}_R^c\mathbf{K}_e\mathbf{C}_R & \mathbf{B}_R^p\mathbf{D}_p\mathbf{C}_B - \mathbf{B}_R^c\mathbf{K}_e\mathbf{C}_B & -\mathbf{B}_R^p\mathbf{C}_p \\ \mathbf{B}_B^p\mathbf{D}_p\mathbf{C}_R - \mathbf{B}_B^c\mathbf{K}_e\mathbf{C}_R & \mathbf{A}_B - \mathbf{B}_b^p\mathbf{D}_p\mathbf{C}_B + \mathbf{B}_B^c\mathbf{K}_e\mathbf{C}_B & \mathbf{B}_B^p\mathbf{C}_p \\ \mathbf{B}_p\mathbf{C}_R & -\mathbf{B}_p\mathbf{C}_B & \mathbf{A}_p \end{bmatrix};$$

$\mathbf{B}_e = \begin{bmatrix} \mathbf{B}_R \\ -\mathbf{B}_B \\ \mathbf{0} \end{bmatrix}$, $\mathbf{C}_e = [\mathbf{C}_R \quad -\mathbf{C}_B \quad \mathbf{0}]$ and $\mathbf{D}_e = \mathbf{0}$. $\mathbf{q}_e = \begin{bmatrix} \mathbf{q}_R \\ \mathbf{q}_B \\ \mathbf{q}_p \end{bmatrix}$.

5.3.2 LPV Plant with Linear Interpolation

According to the LPV system expression stated in equations (4.3) and (4.4), the effective stiffness dependent rotor/base model shown in equation (5.18) may be expressed in parameter dependent/independent terms as

$$\mathbf{P}_e(k_e) = \mathbf{P}_{e,0} + k_e\mathbf{P}_{e,k} \tag{5.19}$$

where

$$\begin{aligned} \mathbf{P}_{e,0} &= \begin{bmatrix} \mathbf{A}_{e,0} & \mathbf{B}_e \\ \mathbf{C}_e & \mathbf{D}_e \end{bmatrix} \\ \mathbf{P}_{e,k} &= \begin{bmatrix} \mathbf{A}_{e,k} & \mathbf{0} \\ \mathbf{0} & \mathbf{0} \end{bmatrix} \end{aligned} \tag{5.20}$$

$$\mathbf{A}_{e,0} = \begin{bmatrix} \mathbf{A}_R - \mathbf{B}_R^p\mathbf{D}_p\mathbf{C}_R & \mathbf{B}_R^p\mathbf{D}_p\mathbf{C}_B & -\mathbf{B}_R^p\mathbf{C}_p \\ \mathbf{B}_B^p\mathbf{D}_p\mathbf{C}_R & \mathbf{A}_B - \mathbf{B}_b^p\mathbf{D}_p\mathbf{C}_B & \mathbf{B}_B^p\mathbf{C}_p \\ \mathbf{B}_p\mathbf{C}_R & -\mathbf{B}_p\mathbf{C}_B & \mathbf{A}_p \end{bmatrix},$$

and $\mathbf{A}_{e,k} = \begin{bmatrix} \mathbf{B}_R^c \mathbf{I}_e \mathbf{C}_R & -\mathbf{B}_R^c \mathbf{I}_e \mathbf{C}_B & \mathbf{0} \\ -\mathbf{B}_B^c \mathbf{I}_e \mathbf{C}_R & \mathbf{B}_B^c \mathbf{I}_e \mathbf{C}_B & \mathbf{0} \\ \mathbf{0} & \mathbf{0} & \mathbf{0} \end{bmatrix}$.

Effective Stiffness in a Polytope

The effective stiffness $k_e(t)$ has time-varying behaviour during contact. Thus, it is necessary to be formed in a polytope:

$$k_{e,min} \leq k_e(t) \leq k_{e,max} \tag{5.21}$$

where the minimum effective stiffness $k_{e,min} = 0$ N/m, for a non-contact situation and the maximum is dependent on polytope controller design vertex range. Therefore, $k_e(t)$ can be structured as a polytope having two corners in a parameter box based on equation (4.9)

$$k_e(t) \in \mathbf{\Theta}_e := \mathbf{Co}\{\Pi_{e,1}, \Pi_{e,2}\} \tag{5.22}$$

where $\Pi_{e,1} = k_{e,min}$ and $\Pi_{e,2} = k_{e,max}$.

By using the upper linear fractional transformations (LFTs) shown in equation (4.5) to structure the contact uncertainties, the contact-dependent full order model may be expressed as

$$\begin{bmatrix} \mathbf{z}_e \\ \mathbf{y}_e^k \end{bmatrix} = \mathbf{F_u}(\mathbf{P}_{e,0}, \mathbf{P}_{e,k}\mathbf{\Theta}_e) \begin{bmatrix} \mathbf{w}_e \\ \mathbf{u}_e^k \end{bmatrix} \tag{5.23}$$

In polytopic form,

$$\mathbf{P}_e(k_e) := \mathbf{Co}\{\mathbf{\Psi}_e(\Pi_{e,1}), \mathbf{\Psi}_e(\Pi_{e,2})\} \tag{5.24}$$

where $\mathbf{\Psi}_e(\Pi_{e,i}) = \begin{bmatrix} \mathbf{A}_{e,0} + \Pi_{e,i}\mathbf{A}_{e,k} & \mathbf{B}_e \\ \mathbf{C}_e & \mathbf{D}_e \end{bmatrix}$.

5.3.3 LPV Contact Model Varying Range

Contact force may be transient, and have potential to vary in large range depending on initial states. A LPV model $\mathbf{P}_e(k_e)$ depending on effective stiffness, may be able to represent the contact condition in the rotor/AMB system by dynamics varying within a finite parameter box. An appropriate varying range defined for effective stiffness is essential for model uncertainties estimation for controller design. Significant effective stiffness has the potential to effect the linear interpolation in the LPV model $\mathbf{P}_e(k_e)$.

Figure 5.15 shows the maximum singular values of LPV contact-dependent rotor/AMB stated in equation (5.24). With increasing effective stiffness, rotor resonances become shifted at low frequencies, but remained similar at high frequencies. Significant static gain is introduced when $k_e = 1.45 \times 10^5$ N/m. That may result in issues in the mixed sensitivity problem in the closed loop system, which will be discussed in the following sections. The effective stiffness varying range is selected as $k_{e,min} = 0$ N/m and $k_{e,max} = 1 \times 10^5$ N/m.

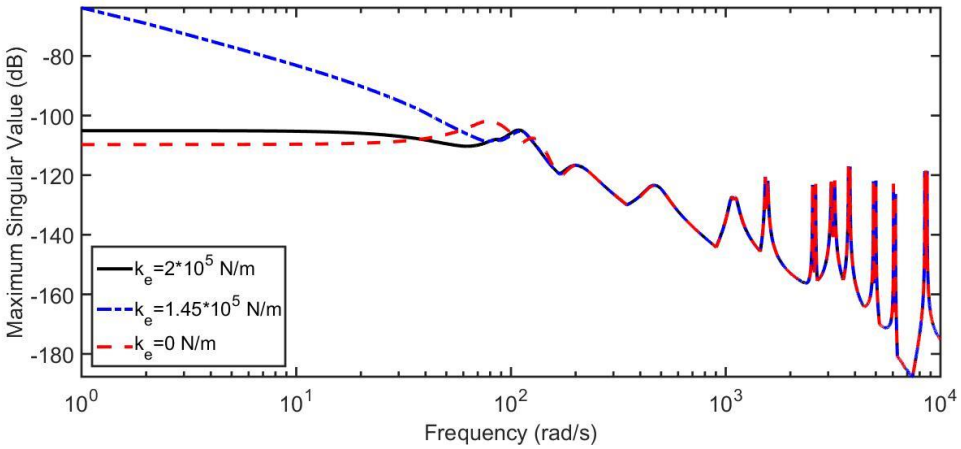

(a) $\bar{\sigma}(\mathbf{P}_e(s,k_e))$with different constant k_e values

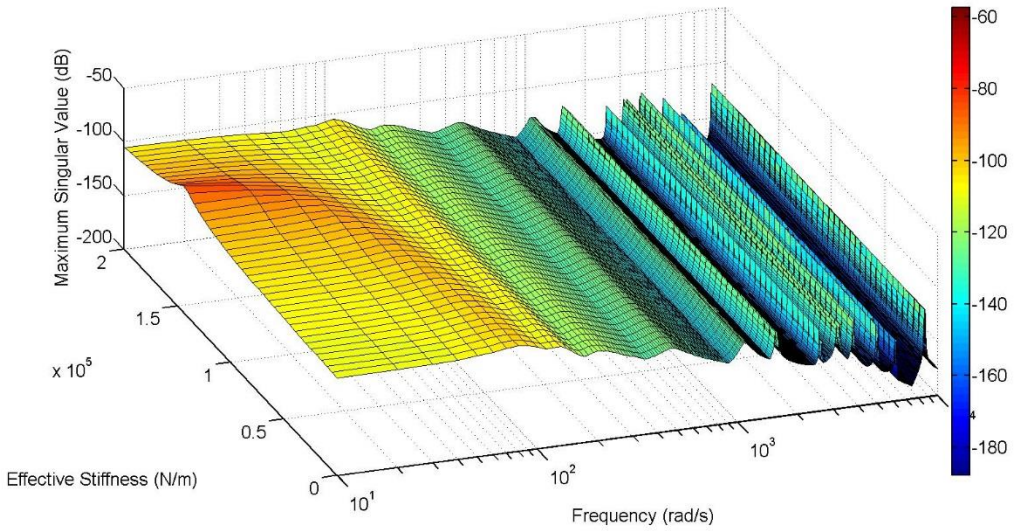

(b) $\bar{\sigma}(\mathbf{P}_e(s,k_e))$ with varying k_e

Figure 5.15 Maximum singular values of the LPV system, $\mathbf{P}_e(k_e)$, when $\Omega = 100$ rad/s

5.4 LMI Based Gain-Scheduling Control for Contact Escape

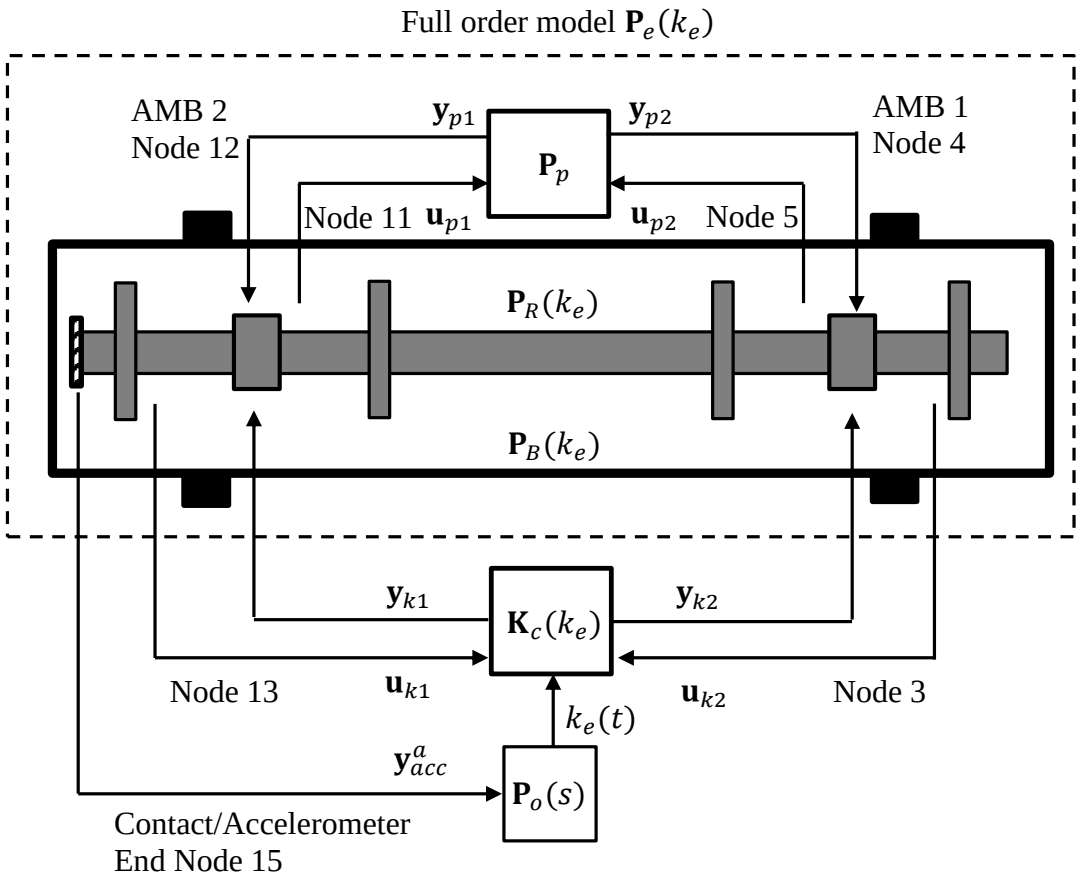

Figure 5.16 Sensor/actuation planes for gain-scheduling controller design to recover the rotor from contact

Figure 5.16 shows the sensor/actuator planes for controller design. The controller uses the sensors at two rotor ends as feedback to recover the rotor from contact. Acceleration measured online is transferred as effective stiffness through the feedforward observer. Estimated effective stiffness feeds into the controller to update the varying dynamics during contact.

5.4.1 Contact-Dependent Model Uncertainties

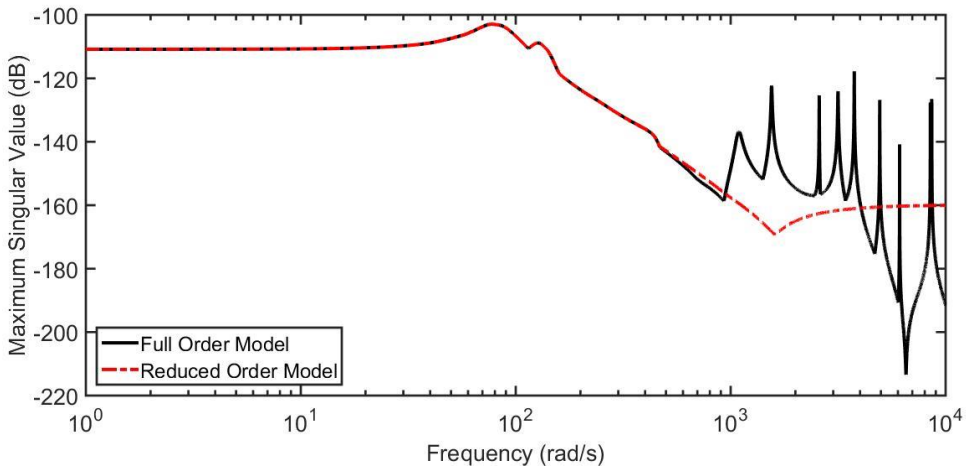

(a) $\bar{\sigma}(\boldsymbol{\Psi}_e(s, \Pi_{e,1}))$ and $\bar{\sigma}(\boldsymbol{\Psi}_r^e(s, \Pi_{e,1}))$, $\Pi_{e,1} = 0$ N/m

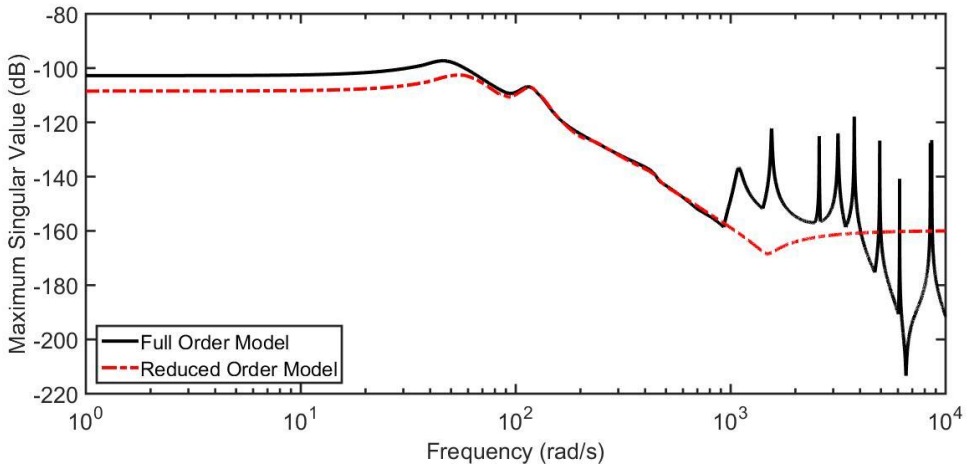

(b) $\bar{\sigma}(\boldsymbol{\Psi}_e(s, \Pi_{e,2}))$ and $\bar{\sigma}(\boldsymbol{\Psi}_r^e(s, \Pi_{e,2}))$, $\Pi_{e,2} = 1 \times 10^5$ N/m

Figure 5.17 Full and reduced order models in vertices $\bar{\sigma}(\boldsymbol{\Psi}_e(s, \Pi_{e,i}))$, $\bar{\sigma}(\boldsymbol{\Psi}_r^e(s, \Pi_{e,i}))$

Based on the LPV system, model reduction techniques are shown in equations (4.11)-(4.16). The full order polytopic plant in equation (5.24) may be reduced as

$$\mathbf{P}_r^e(k_e) := \mathbf{Co}\{\boldsymbol{\Psi}_r^e(\Pi_{e,1}), \boldsymbol{\Psi}_r^e(\Pi_{e,2})\} \tag{5.25}$$

where $\boldsymbol{\Psi}_r^e(\Pi_{e,i}) = \begin{bmatrix} \mathbf{A}_r^{e,0} + \Pi_{e,i}\mathbf{K}_r^v & \mathbf{B}_r^e \\ \mathbf{C}_r^e & \mathbf{D}_r^e \end{bmatrix}$.

The system matrices of the reduced order plant may be obtained by defining $\mathbf{K}_v = \mathbf{V}_{e,0}^{-1}\mathbf{A}_{e,k}\mathbf{V}_{e,0}$:

$$\mathbf{A}_r^{e,0} = \begin{bmatrix} \mathrm{Re}(\boldsymbol{\Lambda}_{0l}^{e,0}) & -\mathrm{Im}(\boldsymbol{\Lambda}_{0l}^{e,0}) \\ \mathrm{Im}(\boldsymbol{\Lambda}_{0l}^{e,0}) & \mathrm{Re}(\boldsymbol{\Lambda}_{0l}^{e,0}) \end{bmatrix}, \mathbf{K}_r^v = \begin{bmatrix} \mathrm{Re}(\mathbf{K}_{ll}^v) & -\mathrm{Im}(\mathbf{K}_{ll}^v) \\ \mathrm{Im}(\mathbf{K}_{ll}^v) & \mathrm{Re}(\mathbf{K}_{ll}^v) \end{bmatrix}, \mathbf{B}_r^e = \begin{bmatrix} \mathrm{Re}(\breve{\mathbf{B}}_l^e) \\ \mathrm{Im}(\breve{\mathbf{B}}_l^e) \end{bmatrix},$$

$\mathbf{C}_r^e = \mathbf{C}_c\left[\mathrm{Re}(\mathbf{V}_{0l}^{e,0}) - \mathrm{Im}(\mathbf{V}_{0l}^{e,0})\right]$ and $\mathbf{D}_r^e = (\mathbf{D}_c - \mathbf{C}_c\mathrm{Re}(\mathbf{V}_{0h}^{e,0}{\boldsymbol{\Lambda}_{0h}^{e,0}}^{-1}\breve{\mathbf{B}}_h^e)$.

Due to parameterization in the contact-dependent model, multiplicative model error between full and reduced order models become larger with higher effective stiffness. Figure 5.17 shows the full/reduced order models in the vertices defined by the parameter polytope $\boldsymbol{\Theta}_e$.

Figure 5.18 shows the behaviour of the reduced order model when k_e varies in $\boldsymbol{\Theta}_e$. And Figure 5.19 shows the model uncertainties including multiplicative model error and uncertainties induced by linear parameterization. Contact-dependent model uncertainties have significant dependency on $\boldsymbol{\Theta}_e$, as k_e may vary in a much larger parameter box. According to equations (4.49)-(4.50), the model uncertainties with contact dependency can be expressed as

$$\boldsymbol{\Delta}_e(k_e) = \mathbf{Co}\left\{\boldsymbol{\Psi}_\Delta^e(\Pi_{e,1}), \boldsymbol{\Psi}_\Delta^e(\Pi_{e,1})\right\} \tag{5.26}$$

Together with the varying parameter k_e, $\boldsymbol{\Delta}_e$ has significant gain at low frequencies as shown in Figure 5.19; However, this is not necessary to be taken into account when carrying out gain-scheduling controller design. The system multiplicative model error is considered to be estimated based on a static effective stiffness value.

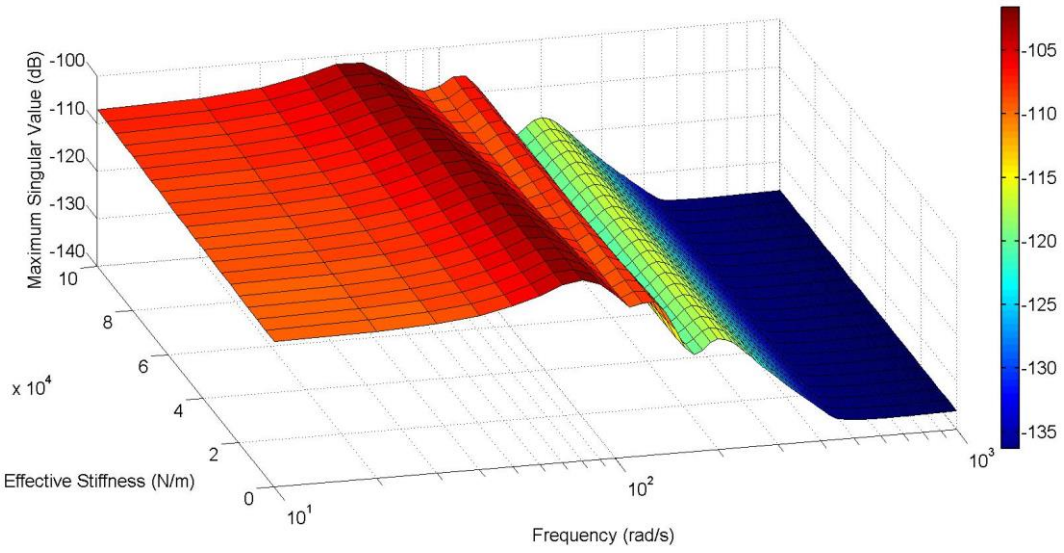

Figure 5.18 $\bar{\sigma}(\mathbf{P}_r^e(s, k_e))$ and $0 \leq k_e \leq 1 \times 10^5$ N/m

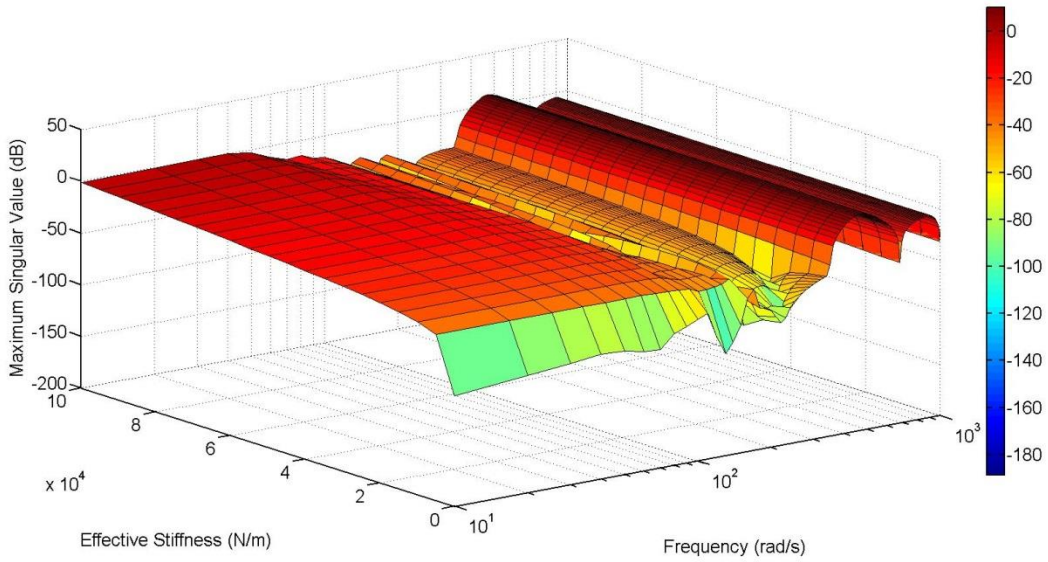

Figure 5.19 $\bar{\sigma}(\mathbf{\Delta}_e(s, k_e))$ and $0 \leq k_e \leq 1 \times 10^5$ N/m

5.4.2 Contact-Dependent Control Structure

In order to achieve LMI based H_∞ optimization, the output of the reduced order plant for controller synthesis may be scaled by sensor clearance as mentioned in Chapter 4:

$$\acute{\mathbf{P}}_r^e(k_e) = \mathbf{Co}\left\{\begin{bmatrix}\mathbf{A}_r^{e,0} + \Pi_{e,1}\mathbf{K}_r^e & \mathbf{B}_r^e \\ \varrho\mathbf{C}_r^e & \varrho\mathbf{D}_r^e\end{bmatrix}, \begin{bmatrix}\mathbf{A}_r^{e,0} + \Pi_{e,2}\mathbf{K}_r^e & \mathbf{B}_r^e \\ \varrho\mathbf{C}_r^e & \varrho\mathbf{D}_r^e\end{bmatrix}\right\} \quad (5.27)$$

Thus, the LMI based gain-scheduling control optimization may result in a controller in the polytopic model having internal lower LFT, and non-zero **D** matrix compensation based on equation (4.25)

$$\overline{\mathbf{K}}_c(k_e) = \sum_{i=1}^{2} a_i \overline{\mathbf{K}}_{c,i} \quad (5.28)$$

where each vertex of controller $\overline{\mathbf{K}}_{c,i} = \begin{bmatrix}\overline{\mathbf{A}}_K^c(\Pi_{e,i}) & \overline{\mathbf{B}}_K^c \\ \overline{\mathbf{C}}_K^c & \overline{\mathbf{D}}_K^c\end{bmatrix}$.

With output filtering through sensitivity/complementary sensitivity weightings, the augmented plant may be obtained based on equations (3.26)-(3.27)

$$\begin{bmatrix}\mathbf{y}_{aug}^e \\ \mathbf{e}_r^e\end{bmatrix} = \mathbf{P}_{aug}^e(k_e)\begin{bmatrix}\mathbf{u}_1^e \\ \mathbf{u}_r^e\end{bmatrix} \quad (5.29)$$

and formed with polytope $\boldsymbol{\Theta}_e$ as

$$\mathbf{P}_{aug}^e(k_e) = \sum_{i=1}^{2} a_i \boldsymbol{\Psi}_{aug}^e\left(\Pi_{e,i}\right) \quad (5.30)$$

where $\boldsymbol{\Psi}_{aug}^e\left(\Pi_{e,i}\right) = \begin{bmatrix}\mathbf{W}_s^e & -\mathbf{W}_s^e\boldsymbol{\Psi}_r^e\left(\Pi_{e,i}\right) \\ \mathbf{0} & \mathbf{W}_t^e\boldsymbol{\Psi}_r^e\left(\Pi_{e,i}\right) \\ \mathbf{I} & -\boldsymbol{\Psi}_r^e\left(\Pi_{e,i}\right)\end{bmatrix}$.

Thus, the closed loop transfer function given by LFT according to equation (4.23) at each vertex may be obtained as

$$\mathbf{T}_{\mathbf{y}_{aug}^{e},\mathbf{u}_1^{e}}(k_e) = \mathbf{F}_l\left(\mathbf{F}_u\left(\mathbf{P}_{e,0}, \mathbf{P}_{e,k}\boldsymbol{\Theta}_e\right), \mathbf{F}_l\left(\mathbf{K}_{e,0}, \mathbf{K}_{e,k}\boldsymbol{\Theta}_e\right)\right) = \sum_{i=1}^{2} a_i \boldsymbol{\Psi}_{\mathrm{T}}^{e}\left(\Pi_{e,i}\right) \tag{5.31}$$

where $\boldsymbol{\Psi}_{\mathrm{T}}^{e}\left(\Pi_{e,i}\right) = \begin{bmatrix}\mathbf{W}_s^e \mathbf{S}_r^e\left(\Pi_{e,i}\right) \\ \mathbf{W}_t^e \mathbf{T}_r^e\left(\Pi_{e,i}\right)\end{bmatrix}$.

Also, according to the LMI approach in equations (4.26)-(4.37), by using a single Lyapunov function to guarantee the robustness stability, the solution to the mixed sensitivity problem in the H_∞ optimization process can be found.

$$\left\| \begin{matrix}\mathbf{W}_s^e \mathbf{S}_r^e\left(\Pi_{e,i}\right) \\ \mathbf{W}_t^e \mathbf{T}_r^e\left(\Pi_{e,i}\right)\end{matrix} \right\|_\infty \leq \gamma_s^e \tag{5.32}$$

5.4.3 Contact-Dependent Controller Synthesis

For the complementary sensitivity problem in the H_∞ optimization of the contact-dependent plant, the model uncertainties $\boldsymbol{\Delta}_e(k_e)$ have significant dependency on the structured polytope $\boldsymbol{\Theta}_e$; and even reveals unacceptable DC static gain, if $k_e > 1 \times 10^4$ N/m. However, such uncertainty induced by parameterization is unnecessary according to the small gain theorem. Thus, the weighting $\mathbf{W}_t^e$ for complementary sensitivity may be designed to constrain $\boldsymbol{\Delta}_e(k_e)$ according to equation (3.37)

$$\bar{\sigma}\left(\boldsymbol{\Delta}_e(k_e^c)\right) < \bar{\sigma}(\mathbf{W}_t^e) \tag{5.33}$$

where $k_e^c = 1 \times 10^3$ N/m and weightings

$$\mathbf{W}_t^e(s) = \mathbf{I}_{4\times4} w_t^e(s) \tag{5.34}$$

where

$$w_t^e(s) = 10^{\frac{28}{20}}\left(\frac{s+a}{s+b}\right)^2\left(\frac{s^2 + 2\xi_1 w_{n1} s + {w_{n1}}^2}{s^2 + 2\xi_2 w_{n2} s + {w_{n2}}^2}\right)\left(\frac{b{w_{n2}}^2}{a{w_{n1}}^2}\right) \tag{5.35}$$

where $a = 150, b = 5000,\ \ \xi_1 = 0.2, \xi_2 = 0.2, w_{n1} = 250$ rad/s, and $w_{n2} = 1000$ rad/s.

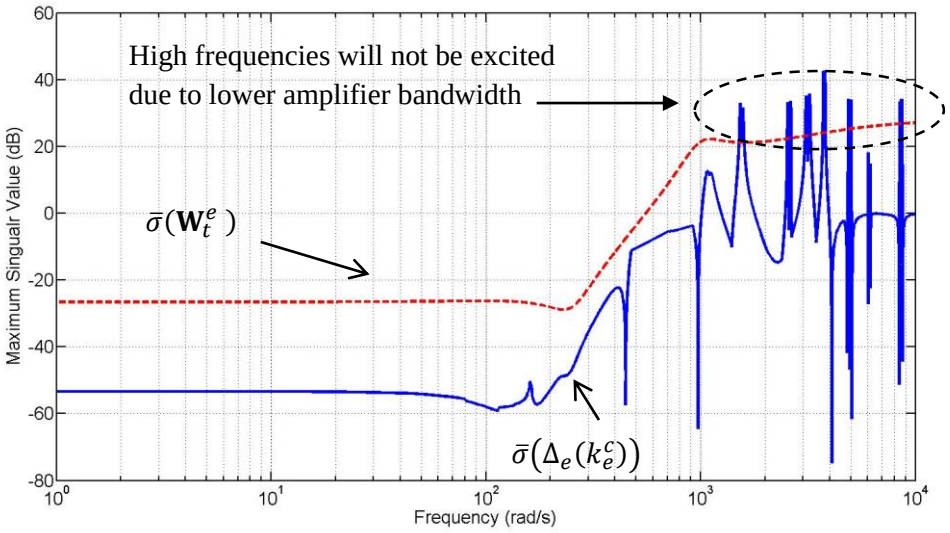

Figure 5.20 Multiplicative model error and weighting for complementary sensitivity when $k_e^c = 1 \times 10^3$ N/m at rotational speed $\Omega = 100$ rad/s

The transfer function for sensitivity has been designed as the form:

$$\mathbf{W}_s^e(s) = \mathbf{I}w_s^e(s) \tag{5.36}$$

where

$$w_s^e(s) = \alpha\left(\frac{{w_n}^2}{s^2 + 2\xi w_n s + {w_n}^2}\right) \tag{5.37}$$

where $w_n = 100$ rad/s, $\alpha = 1$ and $\xi = 0.5$.

Based on equation (5.32), the H_∞ cost, γ_s^e, was computed as 0.45 with a relative large margin to maintain robust stability when the $k_e(t)$ varying range is larger than the model uncertainties estimated. With a single γ_s^e solution for each vertex $\mathbf{W}_s^e\mathbf{S}_r^e(\Pi_{e,i})$, $\mathbf{W}_t^e\mathbf{T}_r^e(\Pi_{e,i})$, the contact dependent closed loop system $\mathbf{T}_{\mathbf{y}_{aug}^e,\mathbf{u}_1^e}(k_e)$ performance is scaled under LMI based gain-scheduling control. The results are shown in Figure 5.21.

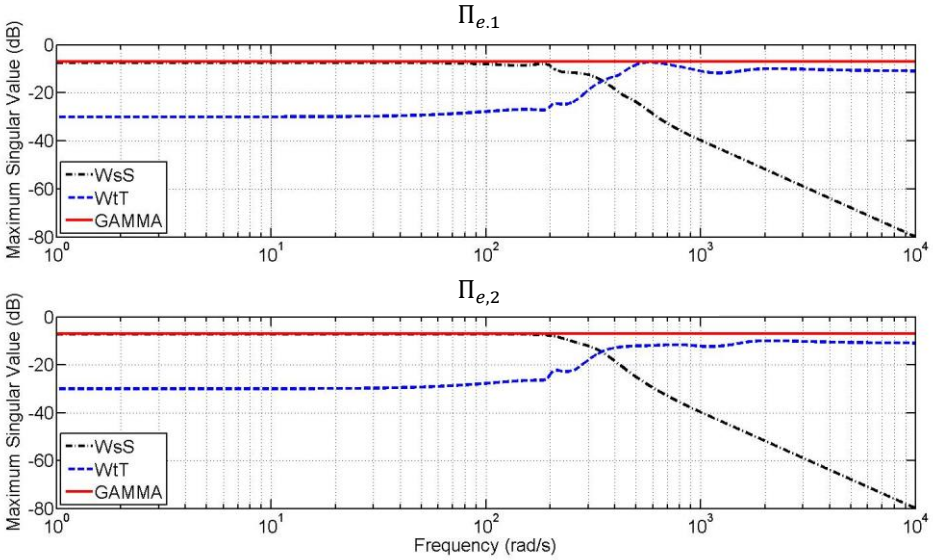

Figure 5.21 LMI based gain-scheduling mixed sensitivity problem solution for contact-dependent system $\mathbf{P}_r^e(k_e)$ at two vertex $\boldsymbol{\Psi}_r^e(\Pi_{e,i})$ $(i = 1,2)$

Figure 5.22 shows the closed loop sensitivity/complementary sensitivity scaled by the weightings choice shown in equations (5.34)-(5.37), with the effective contact stiffness value represented by the polytope corner $\Pi_{e,i}$. The disturbance rejection is achieved at both vertices over the design frequency range and the complementary sensitivity $\mathbf{T}_r^e(s, \Pi_{e,i})$ at the vertices are scaled by the designed weightings.

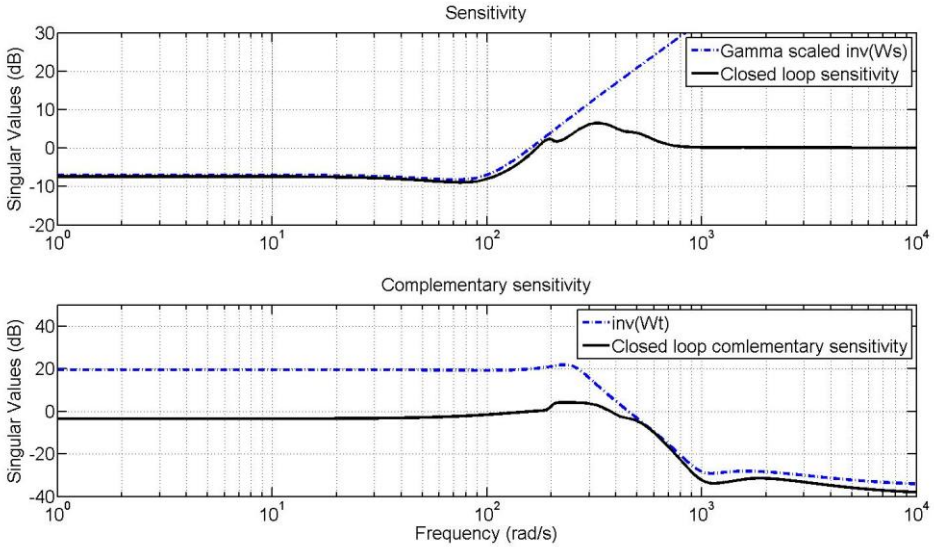

(a) $\Pi_{e,1} = 0$ N/m non-contact

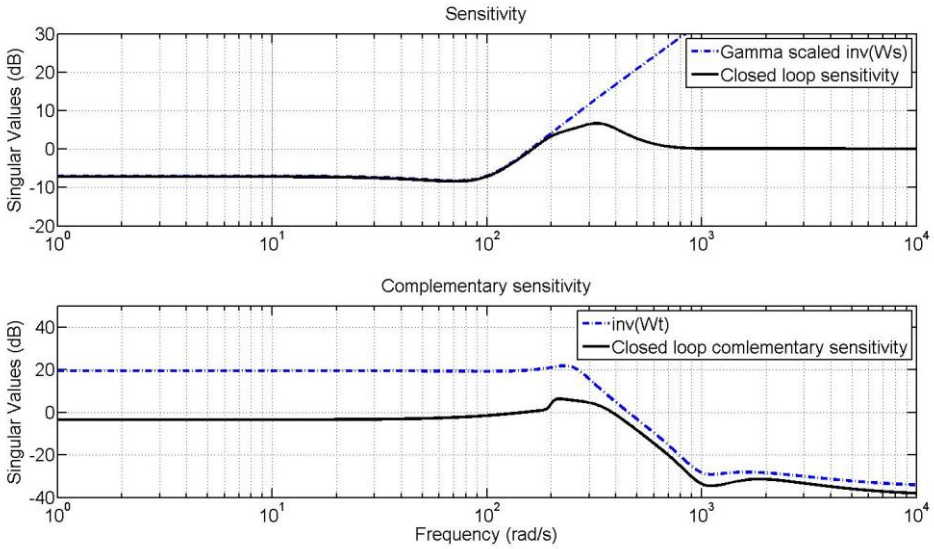

(b) $\Pi_{e,2} = 1 \times 10^5$ N/m

Figure 5.22 $\bar{\sigma}\left(\mathbf{T}_r^e(s, \Pi_{e,i})\right)$ and $\bar{\sigma}\left(\mathbf{S}_r^e(s, \Pi_{e,i})\right)$ bounded by weightings

5.4.4 Contact-dependent Control Performance Estimation in Frequency Domain

In this section, the control performance of the contact-dependent gain-scheduling controller $\bar{\mathbf{K}}_c(k_e)$ synthesized above, is estimated numerically in the frequency

domain, under cases of contact-free, effective stiffness varying in the design range, and contact condition out of design range:

- Under contact free assumption, controller $\bar{\mathbf{K}}_c(k_e)$ shown in equation (5.28) may be frozen at the non-contact polytopic corner, as $\Pi_{e,1}$ ($k_e = 0$ N/m), as in the LTI state-space form $\bar{\mathbf{K}}_{c,1}$.

- In the case of the effective stiffness varies in design parameter polytope shown in equation (5.22), the LPV controller $\bar{\mathbf{K}}_c(k_e)$ is tested in frequency domain, with $0 \leq k_e \leq 1 \times 10^5$ N/m.

- When the effective stiffness varies out of parameter polytope ($k_e > 1 \times 10^5$ N/m), the controller $\bar{\mathbf{K}}_c(k_e)$ may be considered to be saturated as a LTI form $\bar{\mathbf{K}}_{c,2}$ at $\Pi_{e,2}$ ($k_e = 1 \times 10^5$ N/m)

Contact-Free Unbalance Forcing Response

Figure 5.23 shows the unbalance forced response of the contact location (node 15) under control by $\bar{\mathbf{K}}_{c,1}$, with a contact-free assumption. The LMI based gain-scheduling controller $\bar{\mathbf{K}}_c(k_e)$ is able to achieve stability during contact, and enable the rotor to recover to a contact-free state. The control performance is estimated in the contact-free condition in order to assess how much the controlled rotor orbit response is less than the clearance. Figure 5.24 shows the RMS unbalance forced response at sensor planes under control by $\bar{\mathbf{K}}_{c,1}$, when rotor was running as contact-free assumption. In contrast to the experimental measurements shown in Figures 6.14 and 6.15, rotor unbalance forcing responses (under controlled by PID only/LMI based gain-scheduling) are similar. This also demonstrates that, the mathematical model for rotor/AMB system including movable base structure, has sufficient accuracy to undertake simulation test, and to be augmented for robust controller design purpose.

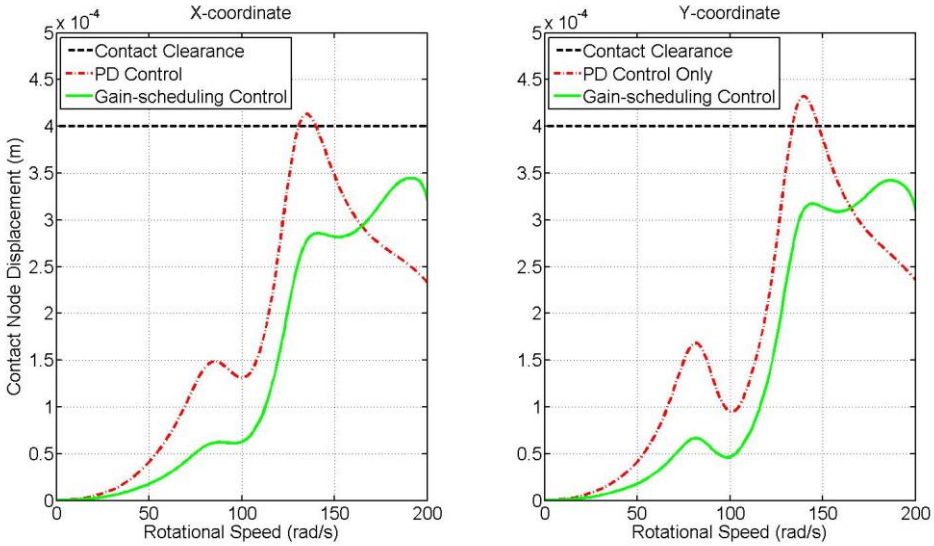

Figure 5.23 Unbalance forcing response of contact location (node 15) with eccentric mass $m_e = 200$ g · cm on disk 4 (node 14)

Due to base having different stiffness characteristics in *x*/*y* directions, the rotor orbits are elliptical, especially around natural frequencies of the base. The vertex controller $\bar{\mathbf{K}}_{c,1}$ would be able to reduce the rotor unbalance forcing responses from 0-170 rad/s as could be predicted by the closed loop sensitivity shown in Figure 5.22 (a). It means that the rotor controlled by $\bar{\mathbf{K}}_c(k_e)$**,** has the potential to recover from contact during running at such speeds. From Figure 5.23, contact may happen around 140 rad/s with the chosen unbalance of $m_e = 200$ g · cm.

The two sensors planes used for feedback in $\bar{\mathbf{K}}_{c,1}$are well-controlled over the design frequency bandwidth by compared with PD control only. When the rotor response shape becomes similar to the first flexible mode shape, the sensor planes close to the AMBs show larger vibration as sensors planes at two end are controlled by $\bar{\mathbf{K}}_{c,1}$. However, such level of vibrations closed to two AMBs may not be able to induce contact at AMBs inside, as it is still far from the AMB's touchdown bearing clearance $c_{tdb,amb} = 0.7 \times 10^{-3}$ m.

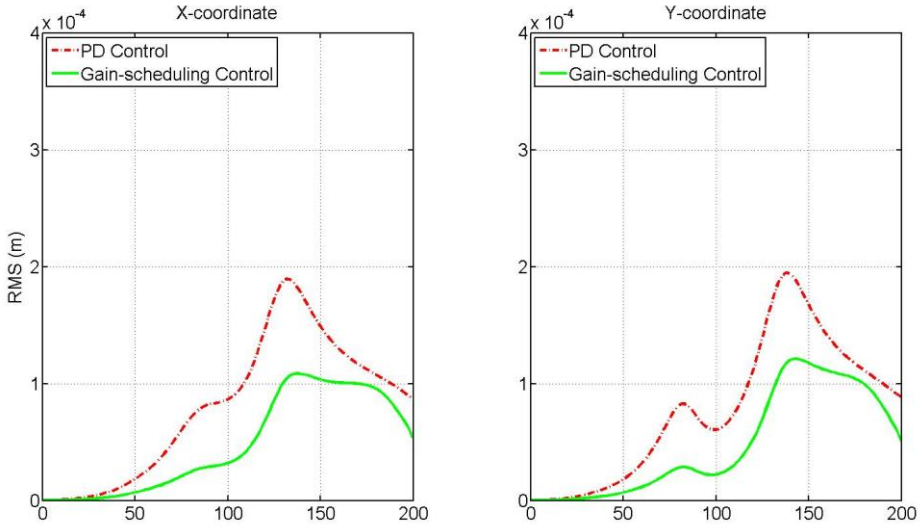

(a) $\overline{\mathbf{K}}_{c,1}$ controlled sensors planes close to the both rotor ends (nodes 3 and 13)

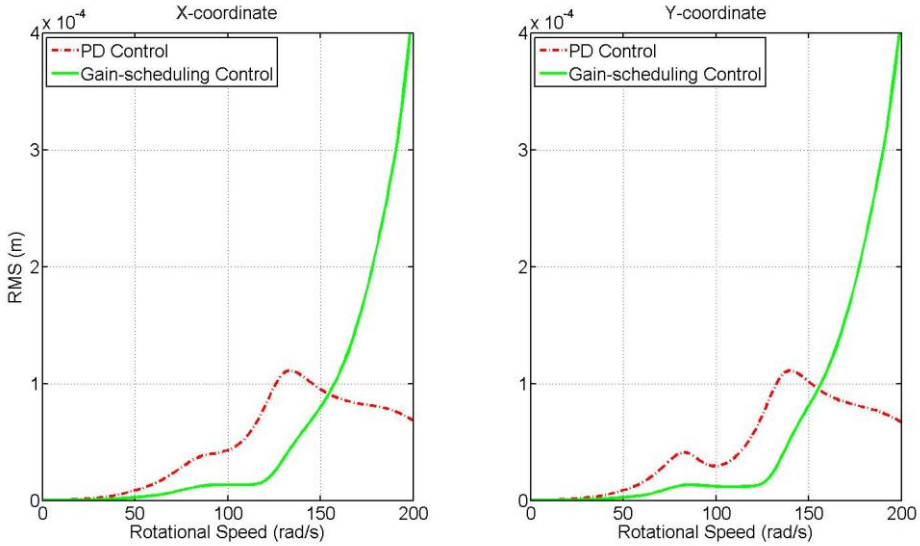

(b) PD controlled sensors planes close to two AMBs (nodes 5 and 11)

Figure 5.24 RMS unbalance forced response under control by $\overline{\mathbf{K}}_{c,1}$ under contact-free assumption, eccentric mass $m_e = 200$ g · cm on disk 4 (node 14)

Control Performance Estimation in Parameter Polytope Range

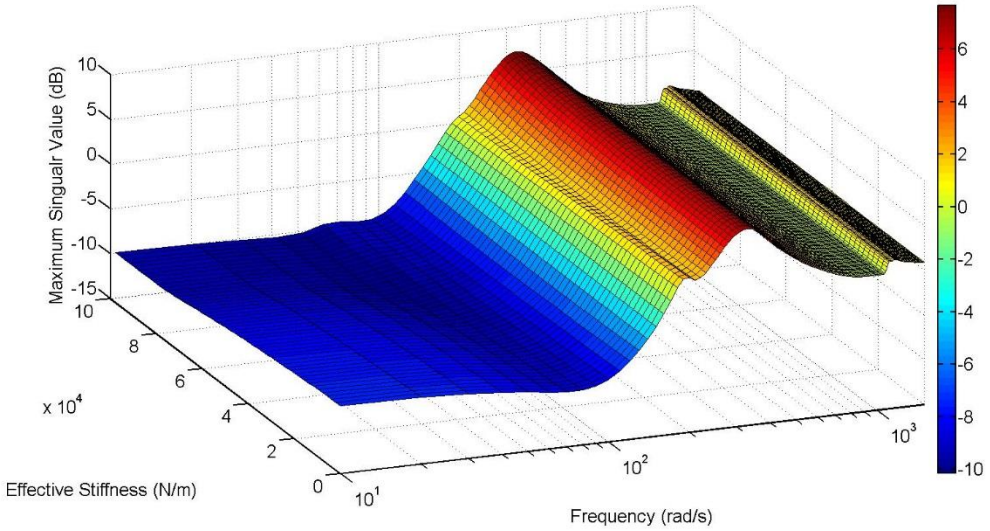

(a) Maximum singular value of closed loop sensitivity

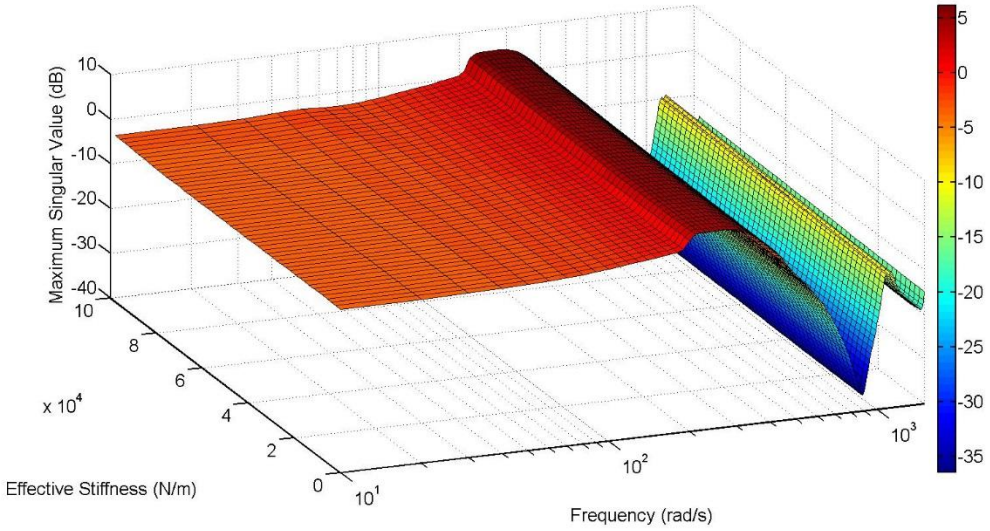

(b) Maximum singular value of closed loop complementary sensitivity

Figure 5.25 Gain-Scheduling control performance estimation with full order LPV plant $\bar{\sigma}\left(\acute{\mathbf{S}}_e(s,k_e)\right)$ and $\bar{\sigma}\left(\acute{\mathbf{T}}_e(s,k_e)\right)$ with effective stiffness in design range as $0 \leq k_e \leq 1\times10^5$ N/m

Figure 5.25 shows the frequency domain performance of the full order LPV plant $\mathbf{P}_e(k_e)$ controlled by $\overline{\mathbf{K}}_c(k_e)$. It is able to stabilize the plant $\mathbf{P}_e(k_e)$ over the designed effective stiffness range. The full order plant closed loop sensitivity $\acute{\mathbf{S}}_e(s, k_e)$ is reduced by the LPV controller $\overline{\mathbf{K}}_c(k_e)$.

Control Performance Estimation when k_e Varies Out of Parameter Polytope Range

The rotor/TDB contact condition could change in a transient manner, and may become chaotic. The effective stiffness inferred by contact force has the potential to exceed the polytope range as designed. It is necessary to estimate the control performance of the LPV controller $\overline{\mathbf{K}}_c(k_e)$, when k_e exceeds the designed range. The controller $\overline{\mathbf{K}}_c(k_e)$ has to be saturated as a LTI vertex system $\overline{\mathbf{K}}_{c,2}$, if k_e exceeds the parameter box corner, and varies in 1×10^5 N/m $\leq \vec{k}_e \leq 3 \times 10^5$ N/m. Thus, the closed loop system transfer function may be expressed as

$$\mathbf{T}_{\mathbf{y}^e_{aug},\mathbf{u}^e_1}(\vec{k}_e) = \mathbf{F}_{\boldsymbol{l}}\left(\mathbf{F}_{\boldsymbol{u}}\left(\mathbf{P}_{e,0}, \mathbf{P}_{e,k}\vec{\boldsymbol{\Theta}}_e\right), \overline{\mathbf{K}}_{c,2}\right) \tag{5.38}$$

The sensitivity and complementary sensitivity may be obtained as

$$\begin{aligned} \vec{\mathbf{S}}_e(\vec{k}_e) &= \left(\mathbf{I} + \mathbf{P}_e(\vec{k}_e)\,\overline{\mathbf{K}}_{c,2}\right)^{-1} \\ \vec{\mathbf{T}}_e(\vec{k}_e) &= \left(\mathbf{I} + \mathbf{P}_e(\vec{k}_e)\,\overline{\mathbf{K}}_{c,2}\right)^{-1}\mathbf{P}_e(\vec{k}_e)\,\overline{\mathbf{K}}_{c,2} \end{aligned} \tag{5.39}$$

Figure 5.26 shows maximum singular value of sensitivity/complementary sensitivity of the full order plant $\mathbf{P}_e(\vec{k}_e)$ under control by $\overline{\mathbf{K}}_{c,2}$. When $\vec{k}_e$ approaches around 2×10^5 N/m, the closed loop system reveals much more sensitivity to external disturbances at low frequency, but retains low sensitivity level at high frequencies. Such a situation also revealed in Figure 5.15. This can be explained by the effective stiffness introducing a low frequency mode when it is similar to the stiffness produced by the AMBs.

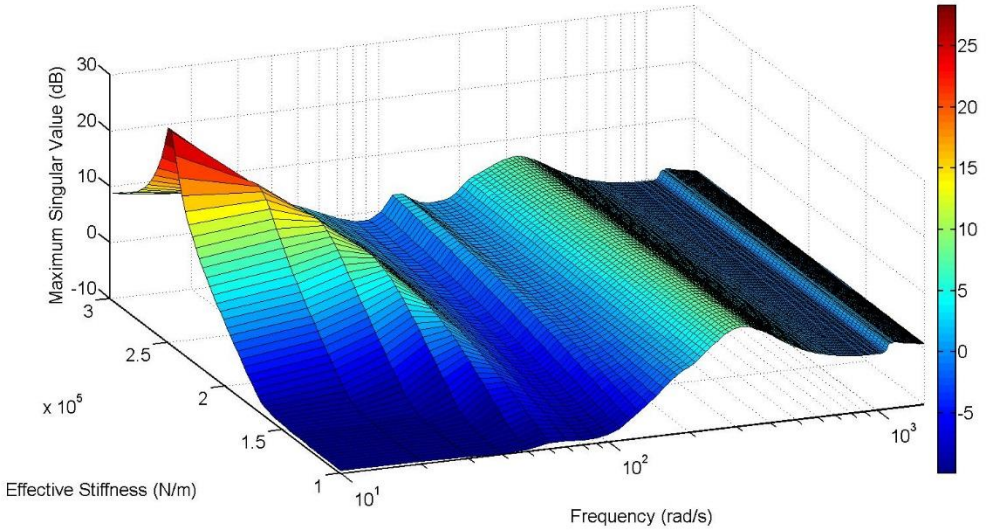

(a) Maximum singular value of closed loop sensitivity

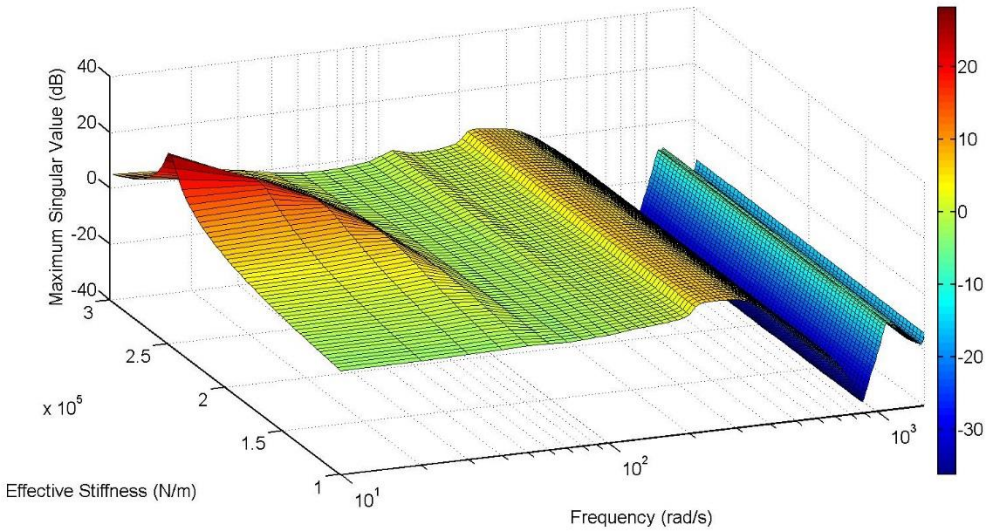

(b) Maximum singular value of closed loop complementary sensitivity

Figure 5.26 Gain-Scheduling control performance estimation with LPV controller saturated at $\overline{\mathbf{K}}_{c,2}$ when effective stiffness varies out of design range as $1 \times 10^5\ \mathrm{N/m} \leq \vec{k}_e \leq 3 \times 10^5\ \mathrm{N/m}$

In such a case of k_e varies out of polytope range, the rotor may be stabilized, and also escaped from contact under control by $\bar{\mathbf{K}}_c(k_e)$. From the small gain theorem as stated in equation (3.31), the robust stability could be guaranteed if the model uncertainties is scaled by the weighting for complementary sensitivity. Model error induced by parameterization is not essential for robust stability. As for time varying contact issues, a sudden out of range effective stiffness feedback may not make the system unstable.

With the three assumptions, this section verifies the contact-dependent controller $\bar{\mathbf{K}}_c(k_e)$ in the frequency domain. However, different static values of k_e may be insufficient to verify the control performance in the time domain, as the contact situation could be transient. A time domain test is therefore examined in the next section, by considering the more stringent robustness against fast parameter variation.

5.5 Simulated Results for Contact-Dependent Controller

In this section, the LMI based H_∞ gain-scheduling controller $\bar{\mathbf{K}}_c(k_e)$ was implemented in simulation (Matlab/Simulink). With several fixed speeds, the controller was tested in different contact modes (rubbing and bouncing). Based on varying effective stiffness, the controller was designed to guarantee stability during contact and reduce the rotor vibration to a designed level. The controller was also tested to recover rotor to contact-free state, during rotor run-up and down operations.

Based on LPV controller implementation shown in equations (4.39)-(4.42), the LMI based gain-scheduling controller $\bar{\mathbf{K}}_c(k_e)$ is implemented in time domain as

$$\bar{\mathbf{K}}_c(k_e) = \bar{\mathbf{K}}_{e,0} + \propto \bar{\mathbf{K}}_{e,k} = \begin{bmatrix} \bar{\mathbf{A}}_K^c(\Pi_{e,1}) + \propto \bar{\mathbf{A}}_K^e & \bar{\mathbf{B}}_K^c \\ \bar{\mathbf{C}}_K^c & \bar{\mathbf{D}}_K^c \end{bmatrix} \tag{5.40}$$

where $\bar{\mathbf{A}}_K^e = \bar{\mathbf{A}}_K^c(\Pi_{e,2}) - \bar{\mathbf{A}}_K^c(\Pi_{e,1})$, the scheduling gain $\propto = \boldsymbol{\Theta}_e/(\Pi_{e,2} - \Pi_{e,1})$ and is saturated at 1 when k_e exceeds the parameter polytope $\boldsymbol{\Theta}_e$.

5.5.1 Simulated Single Speed Contact Test

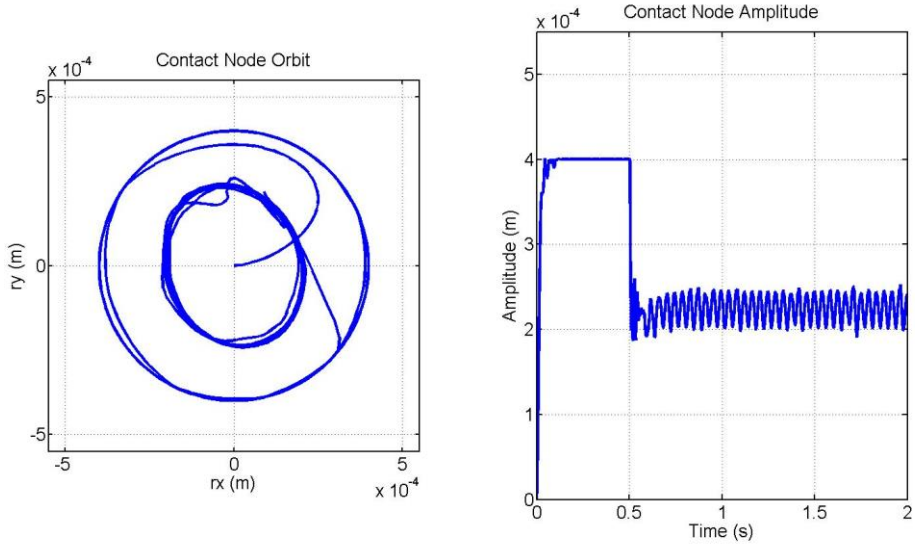

(a) Contact node orbit and amplitude

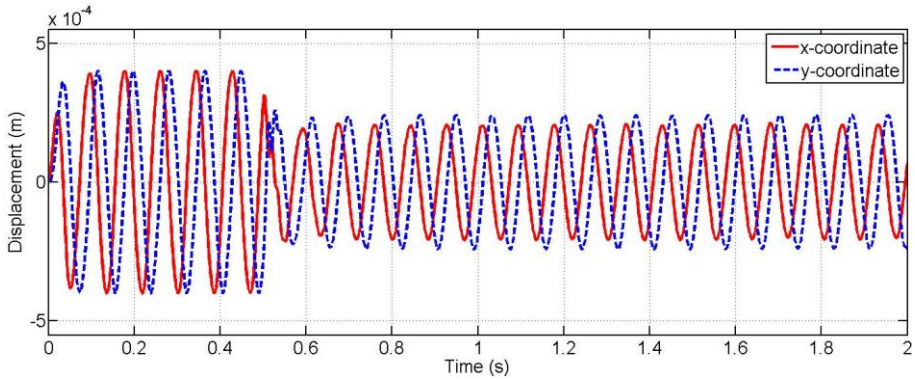

(b) Relative displacement of contacting node

Figure 5.27 Contacting location (node 15) time response during contact recovery control, Ω =75 rad/s with m_e = 850 g.cm when contact occurs at the rotor non-driven end, the controller is activated at 0.5 s

Figure 5.27 shows the rotor response at the contacting node 15 during recovery action by controller $\overline{\mathbf{K}}_c(k_e)$. The control action is activated at 0.5 s, after contact dynamics had settled. From rubbing mode, vibration at the contacting location (node 15 in FEM) is reduced to be within TDB clearance circle, 0.4 mm.

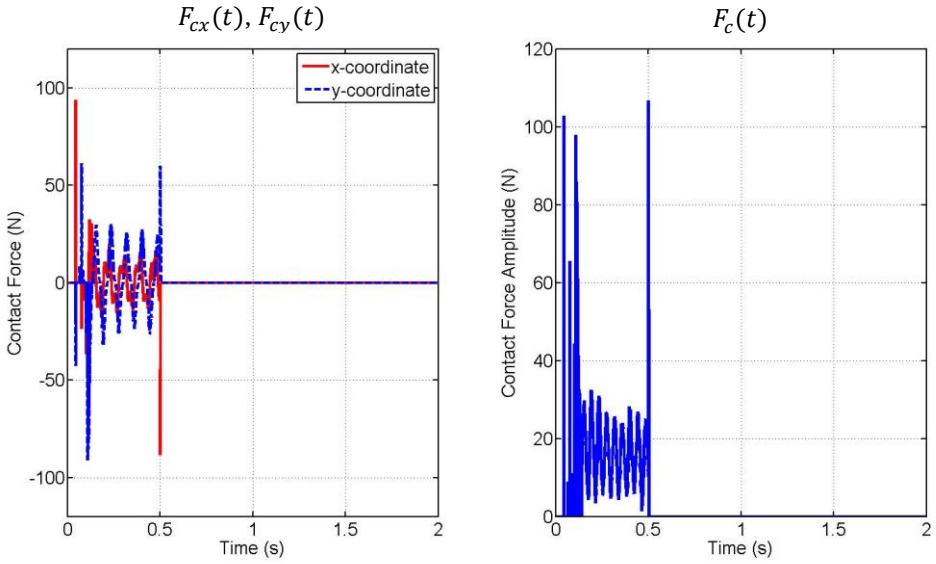

(a) Contact forces and radial amplitude

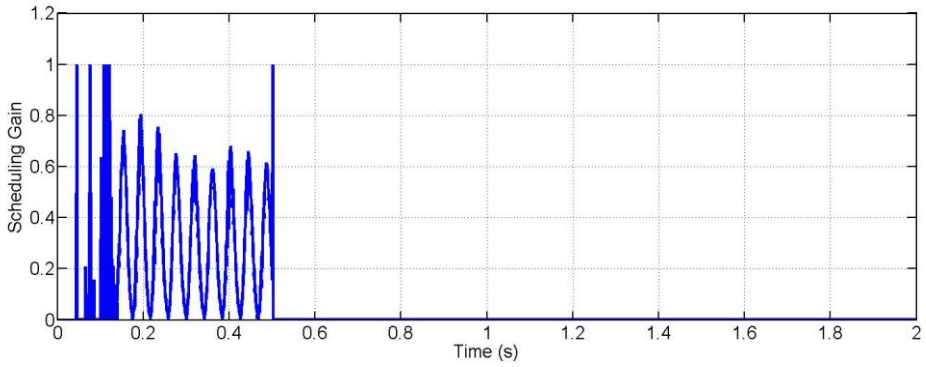

(b) Scheduling gain $\propto (t)$

Figure 5.28 Contact forces occurred at the rotor non-driven end (node 15) and scheduling gain for controller dynamic adaption, Ω =75 rad/s with m_e = 850 g.cm

Figure 5.28 shows the contact forces and scheduling gain fed into the controller. The simulated displacements at sensors locations when control action is activated at 0.5 s are shown in Figure 5.29. As the controller $\bar{\mathbf{K}}_c(k_e)$ only uses feedback from sensors close to rotor ends, vibrations at both ends are well-controlled. Sensors close to the AMBs are under PD control only, which reveals transients induced by the sudden control action from LMI gain-scheduling controller. It then settles down shortly. Figure 5.30 shows the control forces from the PD and from the controller $\bar{\mathbf{K}}_c(k_e)$.

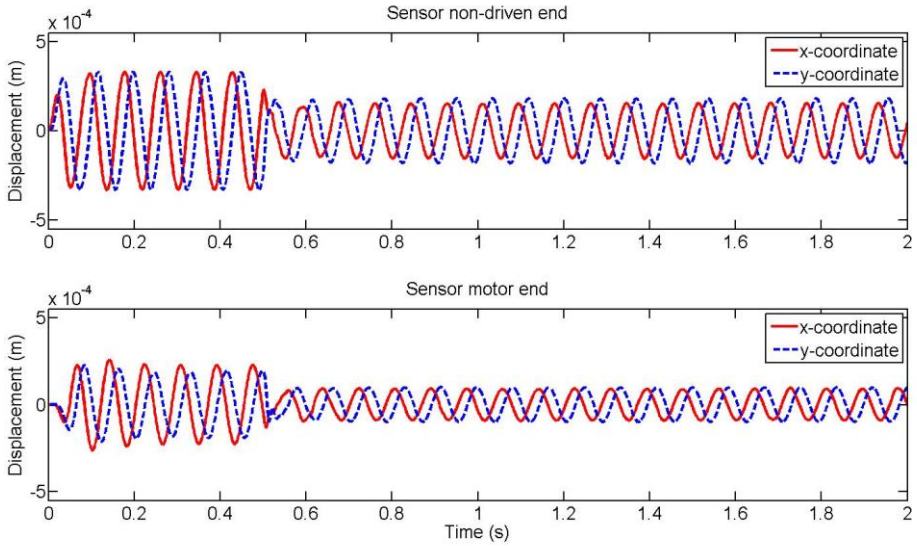

(a) Sensors close to the both rotor ends (node 13 and 3)

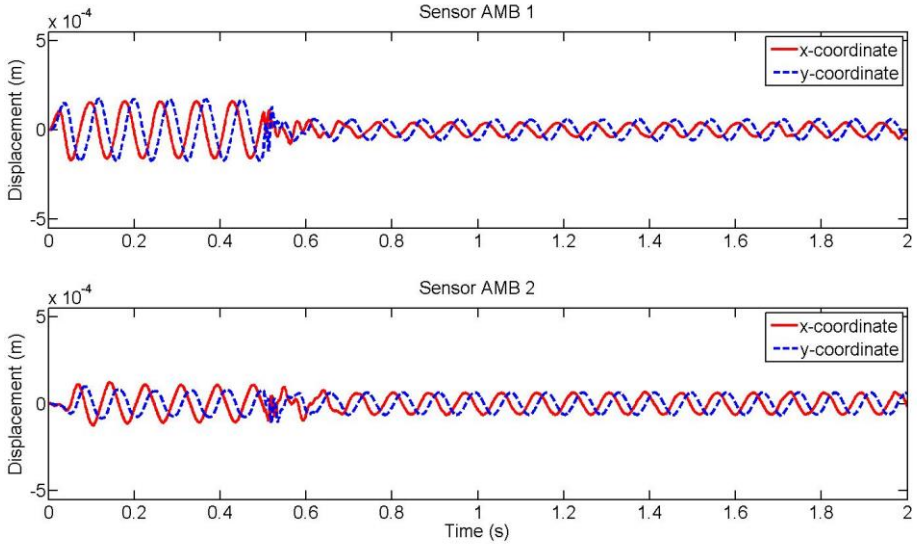

(b) Sensors close to the AMBs (node 11 and 5)

Figure 5.29 Simulated displacements at sensors locations during contact recovery control, Ω =75 rad/s with m_e = 850 g.cm

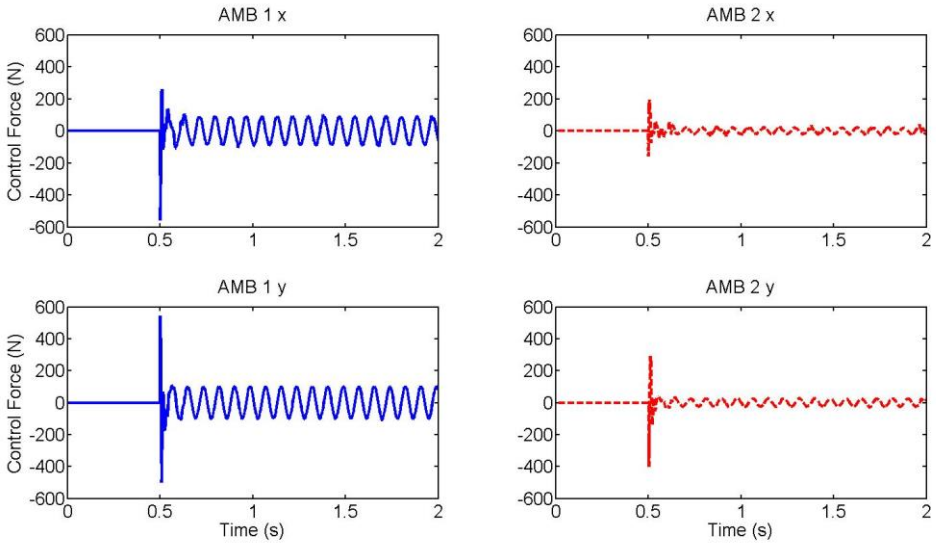

(c) Control forces generated by $\overline{\mathbf{K}}_c(k_e)$

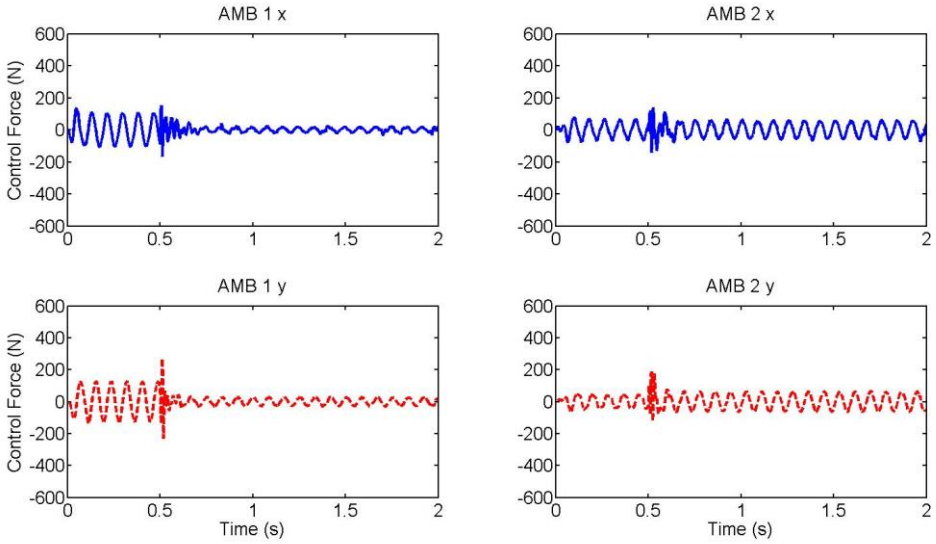

(d) Control force under PD control only

Figure 5.30 Control Forces from AMBs, $\Omega = 75$ rad/s with $m_e = 850$ g.cm

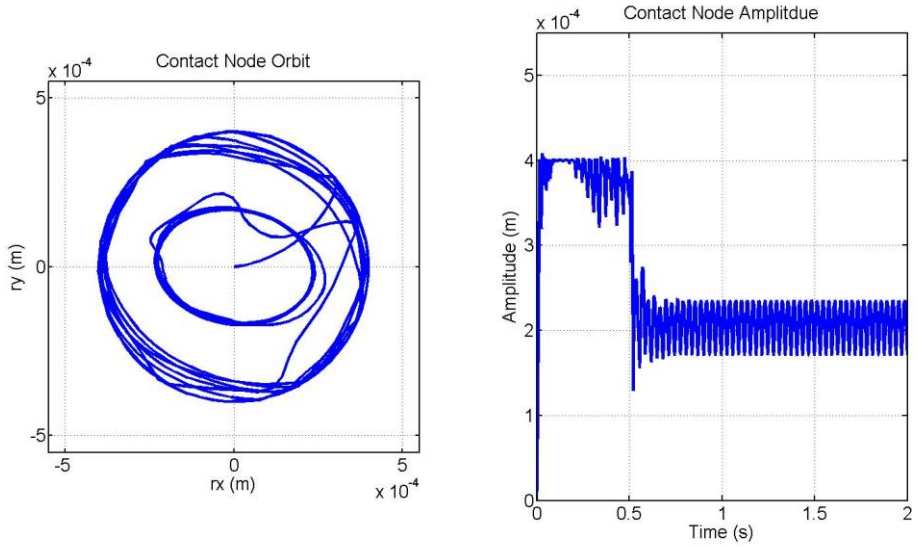

(a) Contact node orbit and amplitude

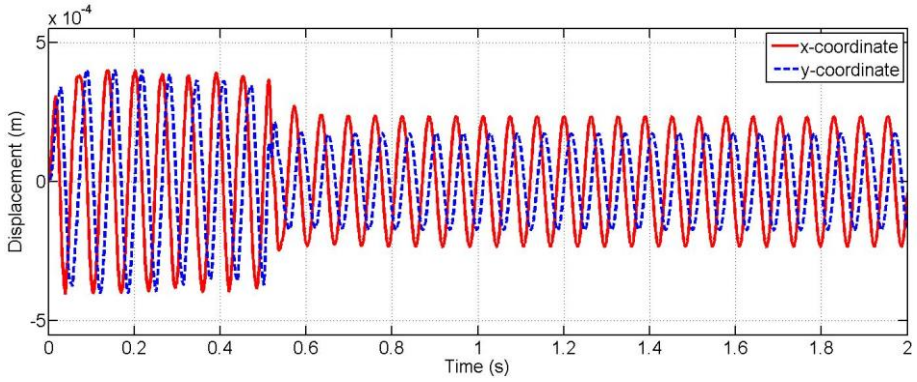

(b) Relative displacement of contact node

Figure 5.31 Contacting location (node 15) time response during contact recovery control, $\Omega = 100$ rad/s with $m_e = 750$ g.cm

Figure 5.31 shows the rotor response at the contacting node 15 during recovery action by controller $\bar{\mathbf{K}}_c(k_e)$. When the rotor is running at 100 rad/s with unbalance 750 g.cm on disk 4 (node 14). The contact mode reveals rubbing and bouncing. After gain-scheduling control action is activated at 0.5 s, the rotor response at the contacting node was centralized to a contact-free state.

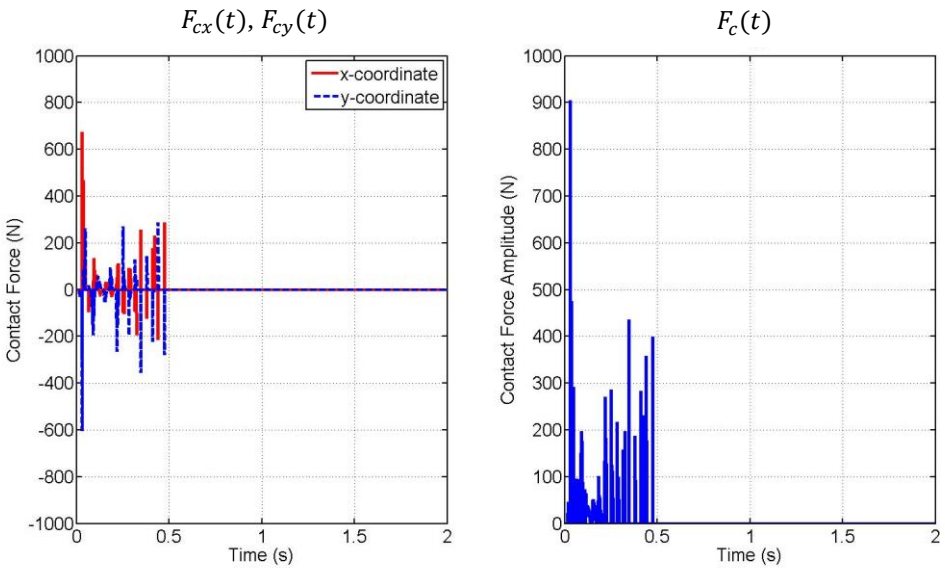

(a) Contact forces and radial amplitude

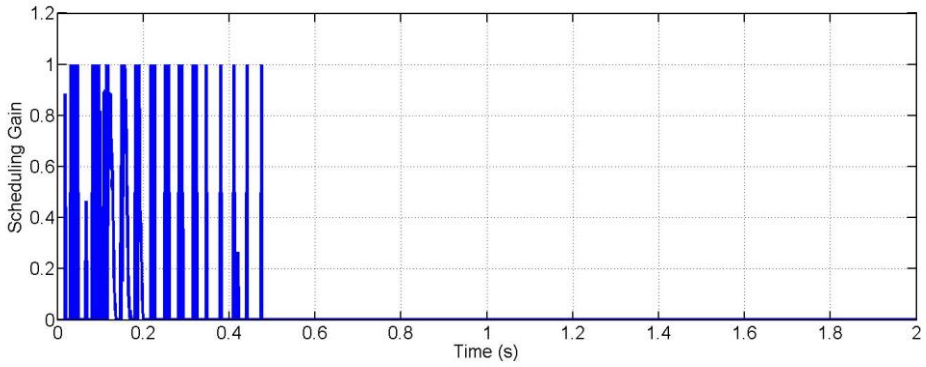

(b) Scheduling gain $\propto (t)$

Figure 5.32 Contact forces occurred at the rotor non-driven end (node 15) and scheduling gain for controller, $\Omega = 100$ rad/s with $m_e = 750$ g.cm

The contact forces and scheduling gain for the controller dynamic adaption are shown in Figure 5.32. Transient impacts induced by rotor bouncing contact mode have large contact force amplitudes. Figure 5.32 (b) shows that the $\propto (t)$ inferred by the contact force amplitude exceeds gain-scheduling design range, and saturates at 1. The rotor was recovered from contact by the gain-scheduling controller $\overline{\mathbf{K}}_c(k_e)$.

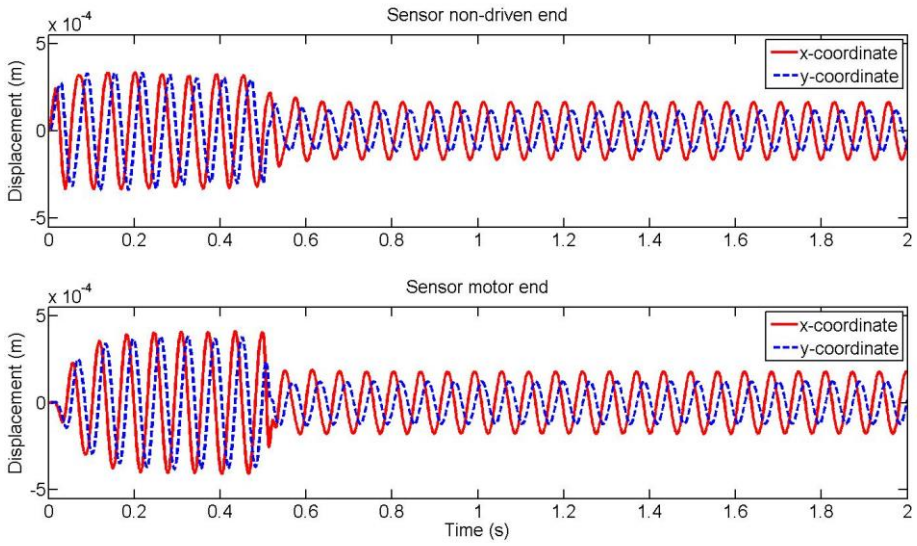

(a) Sensors close to the both rotor ends (node 13 and 3)

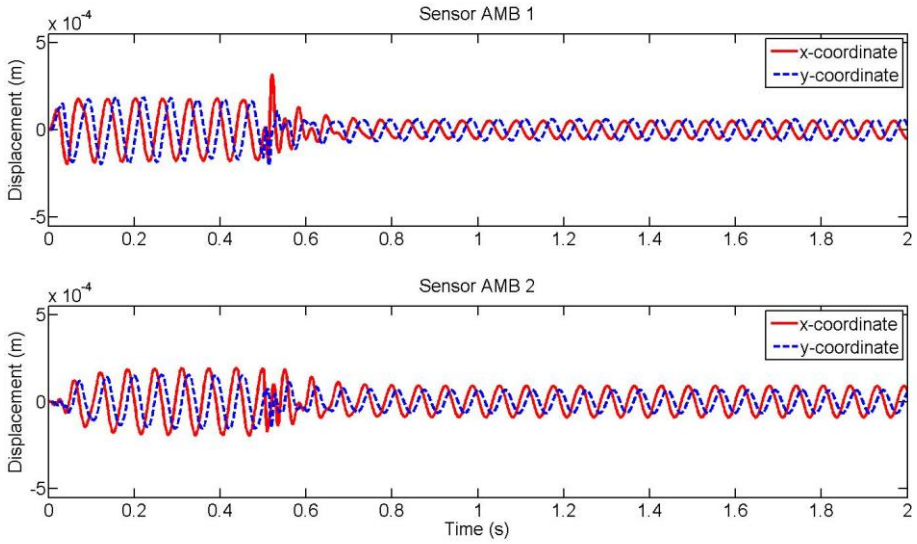

(b) Sensors close to the AMBs (node 11 and 5)

Figure 5.33 Simulated displacements at sensors locations during contact recovery control, Ω =100 rad/s with m_e = 750 g.cm

Figure 5.33 shows the simulated displacements at sensors locations when control action is activated at 0.5 s. At rotational speed Ω =100 rad/s, rotor responses under control by $\bar{\mathbf{K}}_c(k_e)$ are similar to those when running at 75 rad/s shown in Figure 5.29, but more transients are evident at sensor planes close to AMBs as shown in Figure 5.33 (b). Since the rotor flexible mode is not excited at these speeds, rotor responses

remain in rigid domain and they are well-controlled globally. Figure 5.34 shows the control forces from PD control and the controller $\bar{\mathbf{K}}_c(k_e)$.

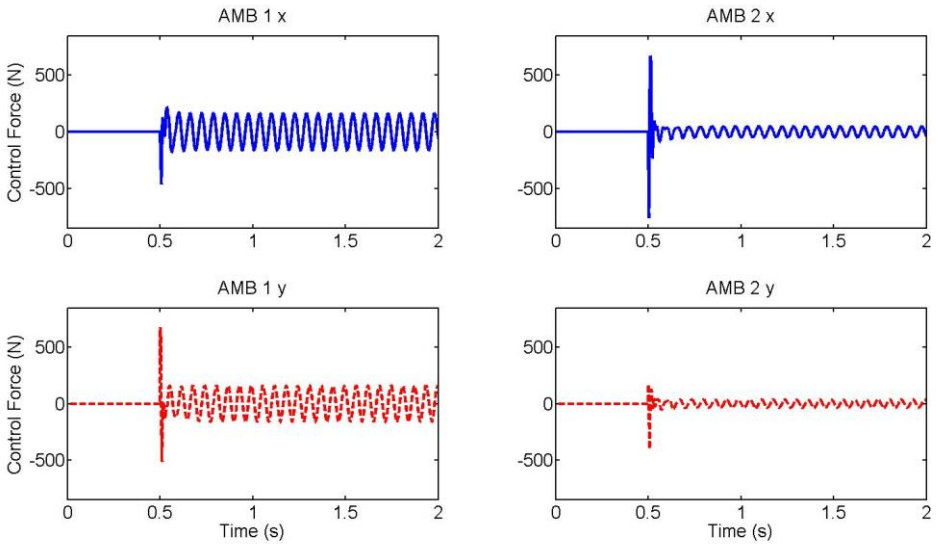

(a) Control force generated by $\bar{\mathbf{K}}_c(k_e)$

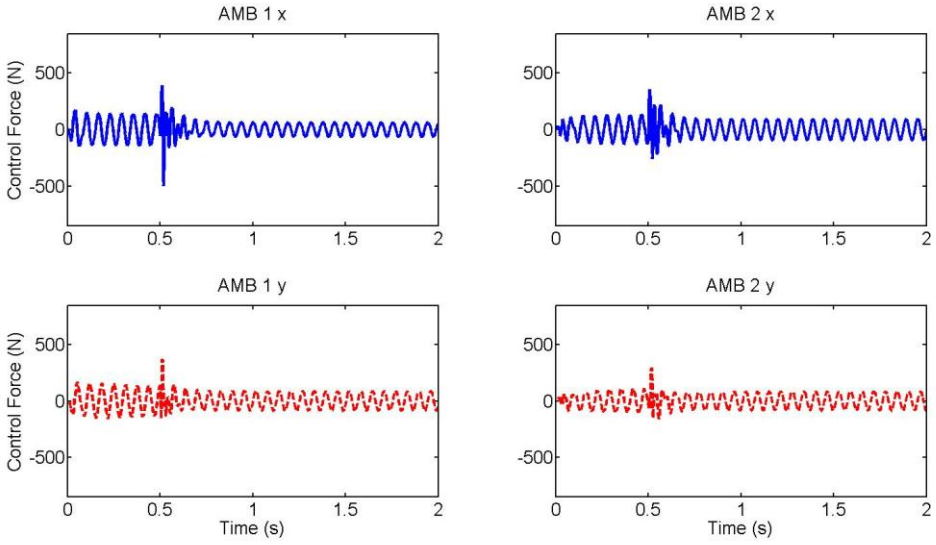

(b) Control force under PD control only

Figure 5.34 Control Force from AMBs, Ω =100 rad/s with m_e =750 g.cm

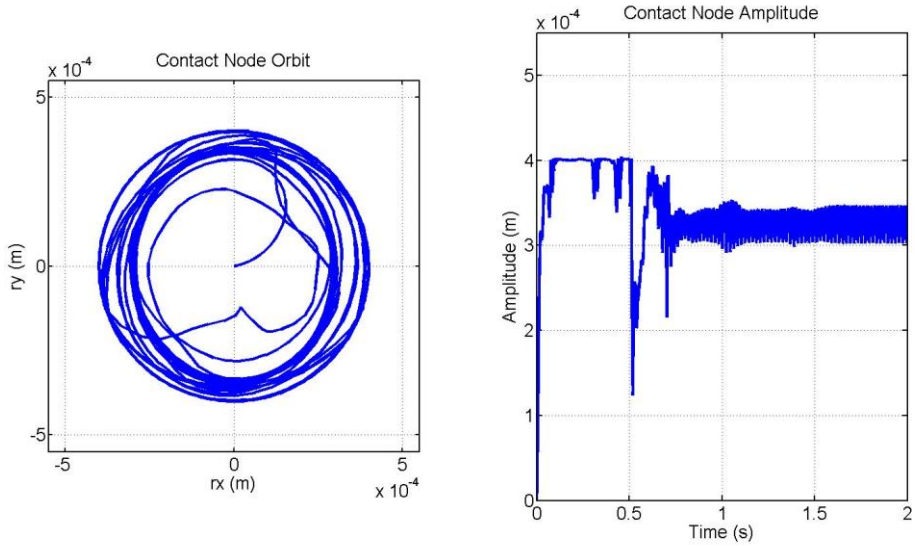

(a) Contact node orbit and amplitude

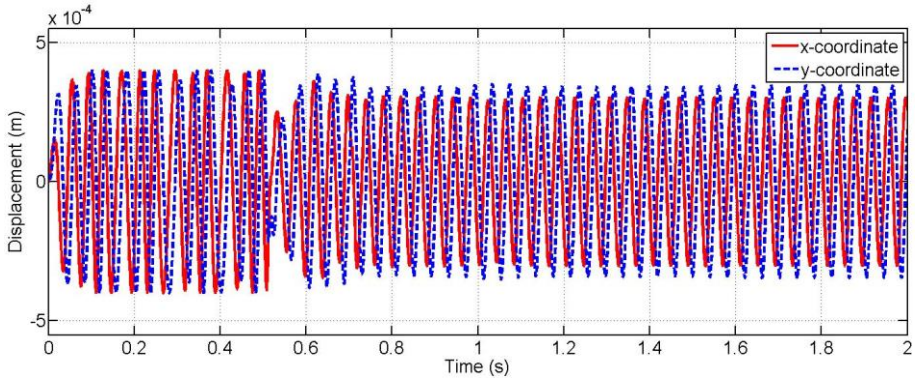

(b) Relative displacement of contact node

Figure 5.35 Contacting location (node 15) time response during contact recovery control, Ω =155 rad/s with m_e = 250 g.cm

Figure 5.35 shows that the controller $\bar{\mathbf{K}}_c(k_e)$ is competitive in the recovery of rotor position from contact at the high speed. When the rotor running at 155 rad/s, control action from $\bar{\mathbf{K}}_c(k_e)$ may not be able to centralize rotor with a small vibration level, which is determined by the weighting designed for sensitivity shown in equations (5.36) and (5.37). However, the control force generated by gain-scheduling control is sufficient enough for contact-free recovery purpose.

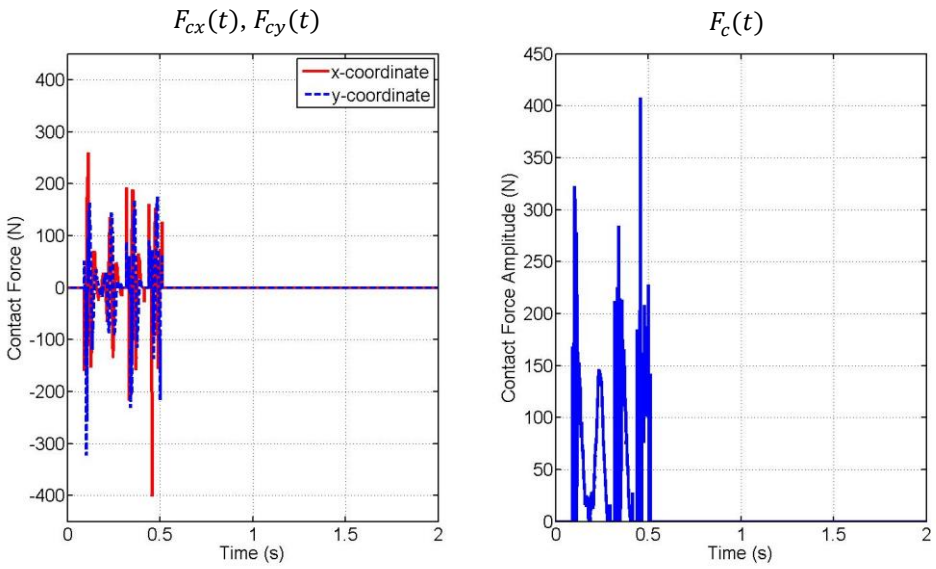

(a) Contact force and amplitude

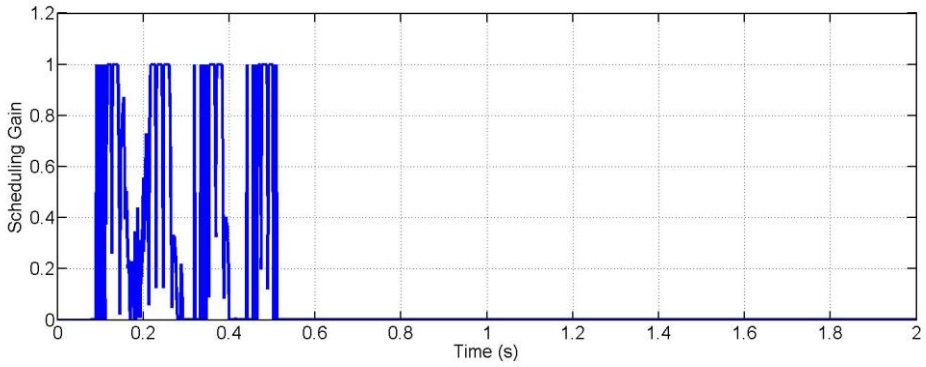

(b) Scheduling gain $\propto (t)$

Figure 5.36 Contact force occurred at the rotor non-driven end (node 15) and scheduling gain for controller, Ω =155 rad/s with m_e = 250 g.cm

The contact forces and scheduling gain for controller dynamic adaption are shown in Figure 5.36. Figure 5.37 shows the rotor responses at sensor planes during contact recovery when running at 155 rad/s. Orbits of the rotor ends are reduced by activating the controller $\overline{\mathbf{K}}_c(k_e)$ at 0.5 s. Vibrations close to the AMBs show some transients, but less compared with these when running at 100 rad/s (as shown in Figure 5.33), due to lower control force at 155 rad/s. Figure 5.38 shows the control forces from PD and the controller $\overline{\mathbf{K}}_c(k_e)$.

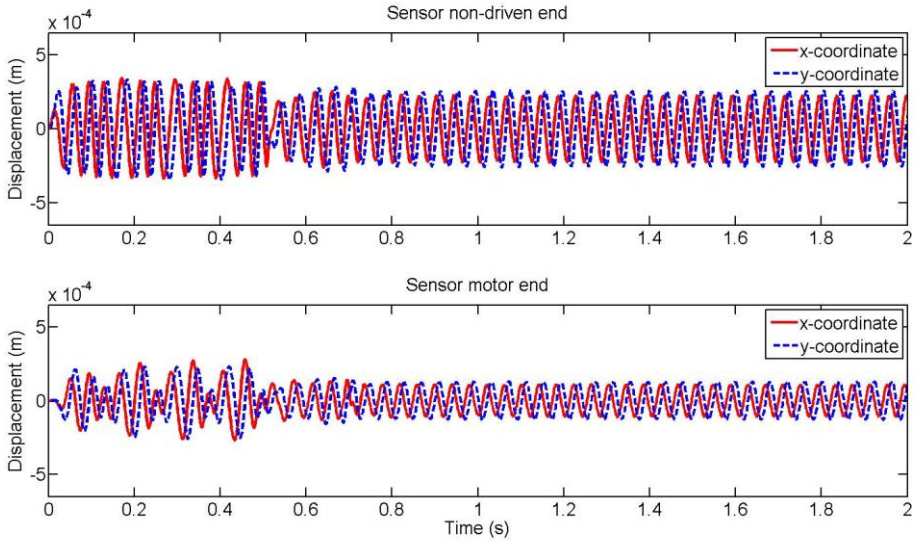

(a) Sensors close to the both rotor ends (node 13 and 3)

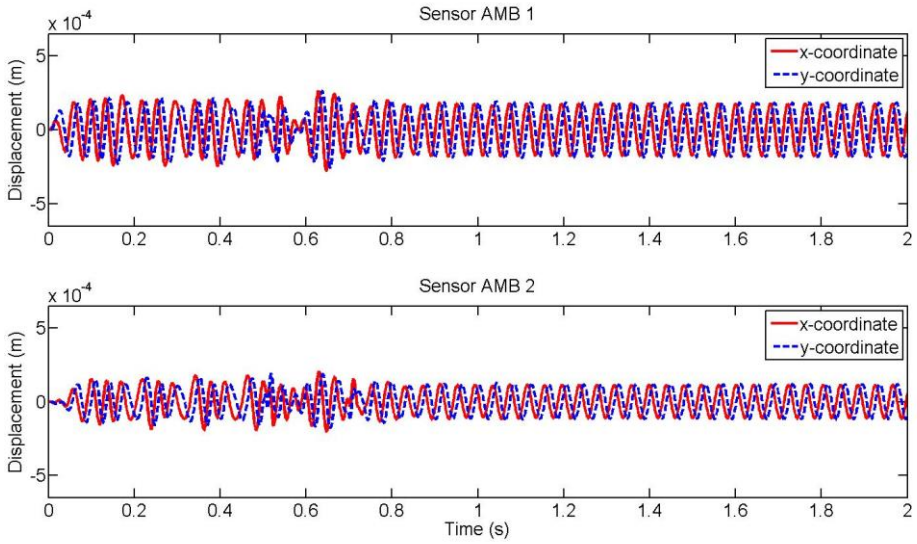

(a) Sensors close to the AMBs (node 11 and 5)

Figure 5.37 Simulated displacements at sensors locations during contact recovery control, Ω =155 rad/s with m_e = 250 g.cm

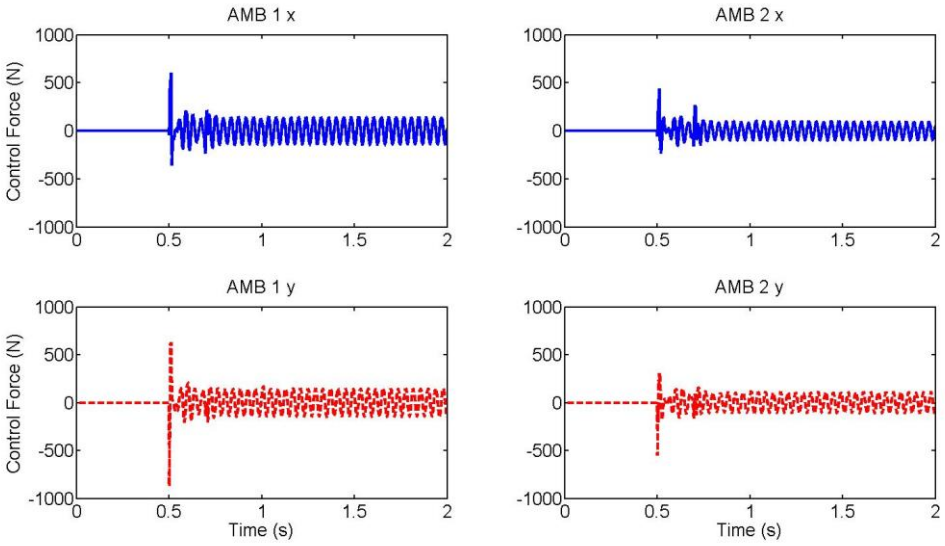

(a) Control forces generated by $\overline{\mathbf{K}}_c(k_e)$

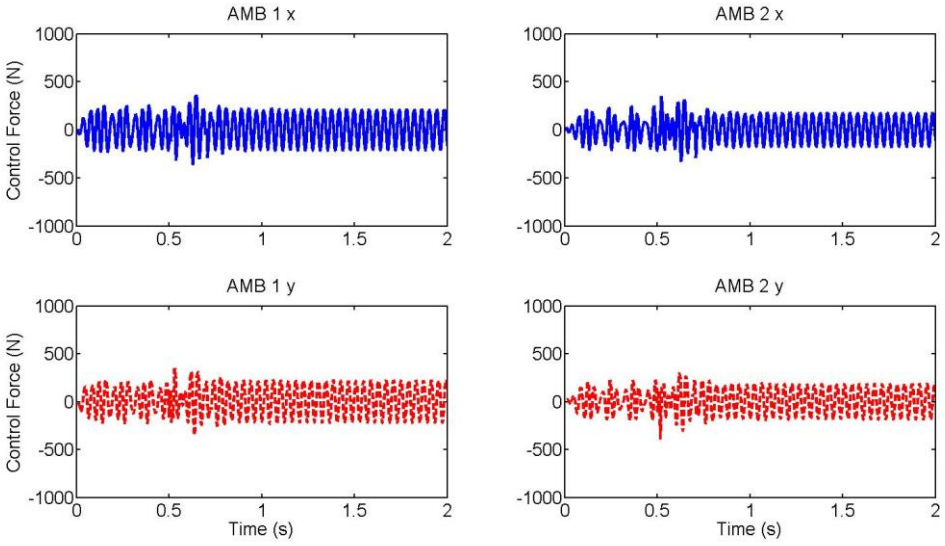

(a) Control forces under PD control only

Figure 5.38 Control forces from AMBs, Ω =155 rad/s with m_e = 250 g.cm

5.5.2 Simulated Contact with Run-up/down

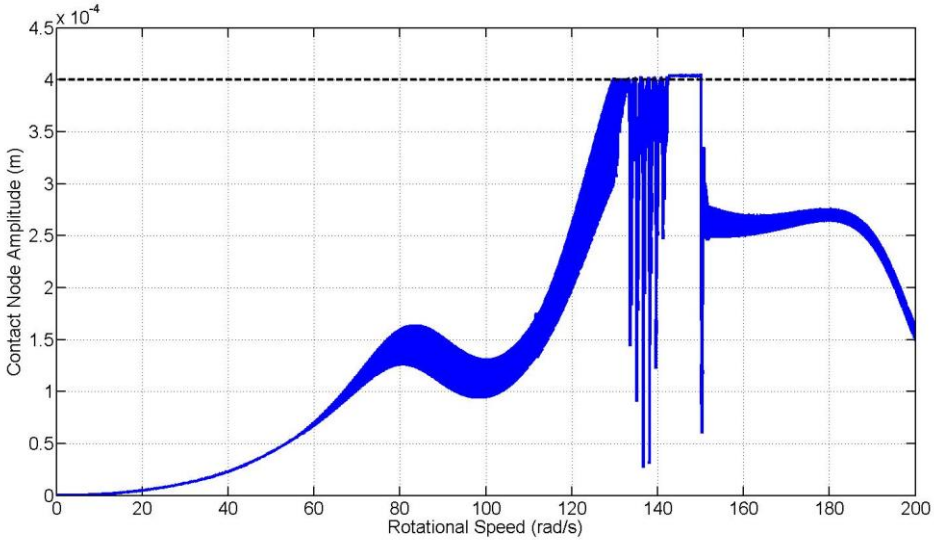

(a) Run-up

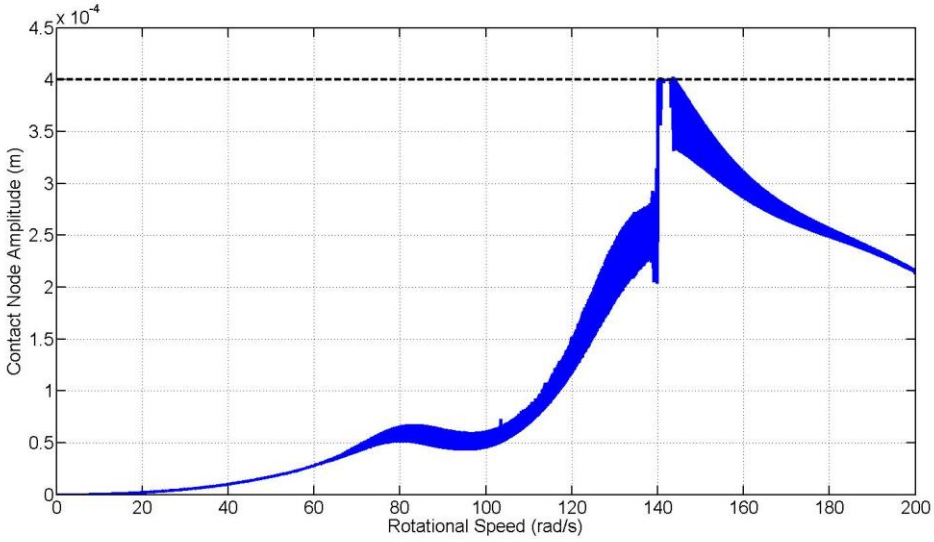

(b) Run-down

Figure 5.39 Simulated bi-stable rotor response at contact location (node 15) with contact recovery under control, with $m_e = 200$ g.cm

Figure 5.39 shows the simulated rotor response during run-up and down operations. In the run-up, the controller $\overline{\mathbf{K}}_c(k_e)$ was activated at 150 rad/s when the rotor contact exhibits a rubbing mode. Figure 5.39 (a) shows the rotor to be recovered successfully

from contact under control action, and it remains in a contact-free state above 150 rad/s.

Controller $\overline{\mathbf{K}}_c(k_e)$ was activated at 140 rad/s when the rotor was under run-down. From bouncing contact, the control action brings the rotor to a contact-free condition. The contact force amplitude and scheduling gain for $\overline{\mathbf{K}}_c(k_e)$ under run-up and down are shown in Figures 5.40 and 5.41. The control forces from PD and the controller $\overline{\mathbf{K}}_c(k_e)$ during speed up and down are shown in Figures 5.42 and 5.43.

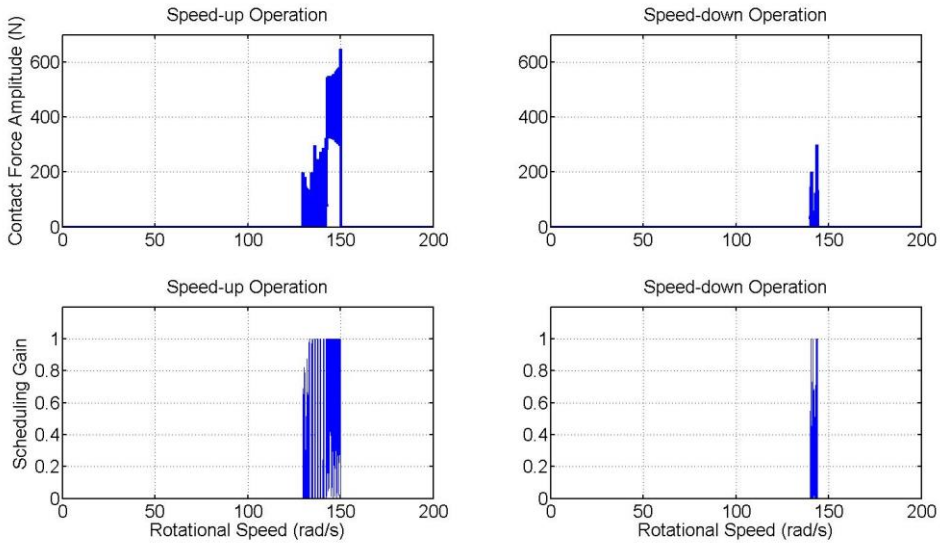

Figure 5.40 Contact force amplitude at the rotor non-driven end (node 15) and Scheduling gain $\propto (t)$, during run-up/down

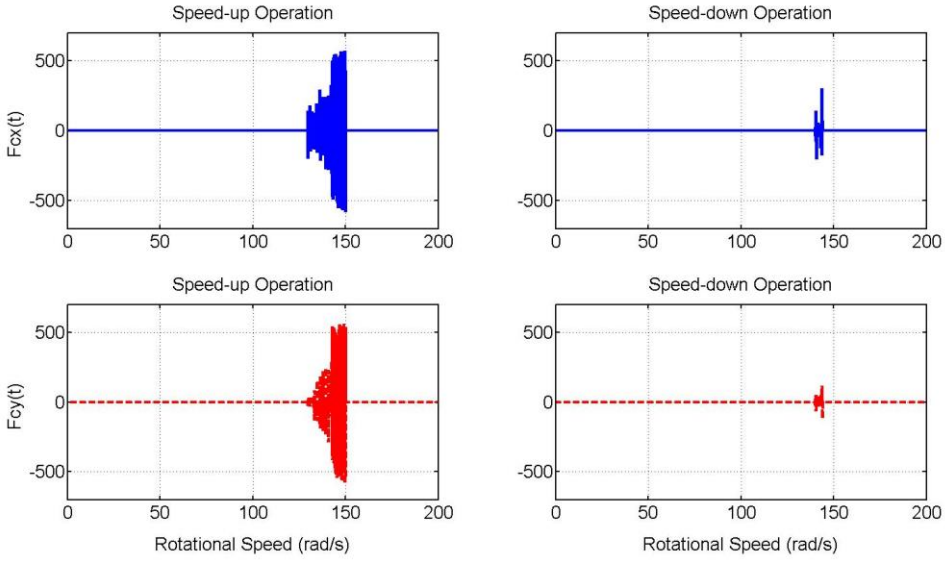

Figure 5.41 Contact forces occurred at the rotor non-driven end (node 15), during run-up/down

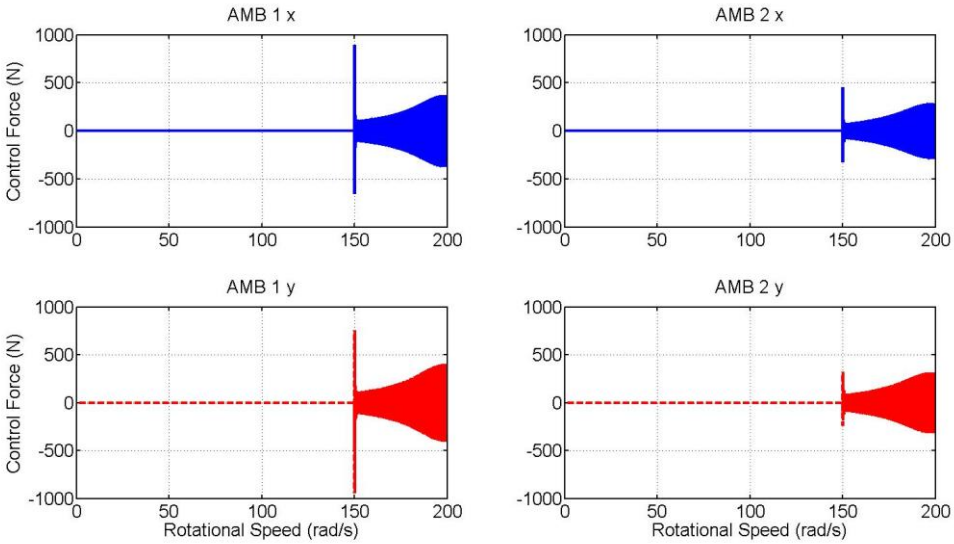

(a) Control forces generated by $\bar{\mathbf{K}}_c(k_e)$

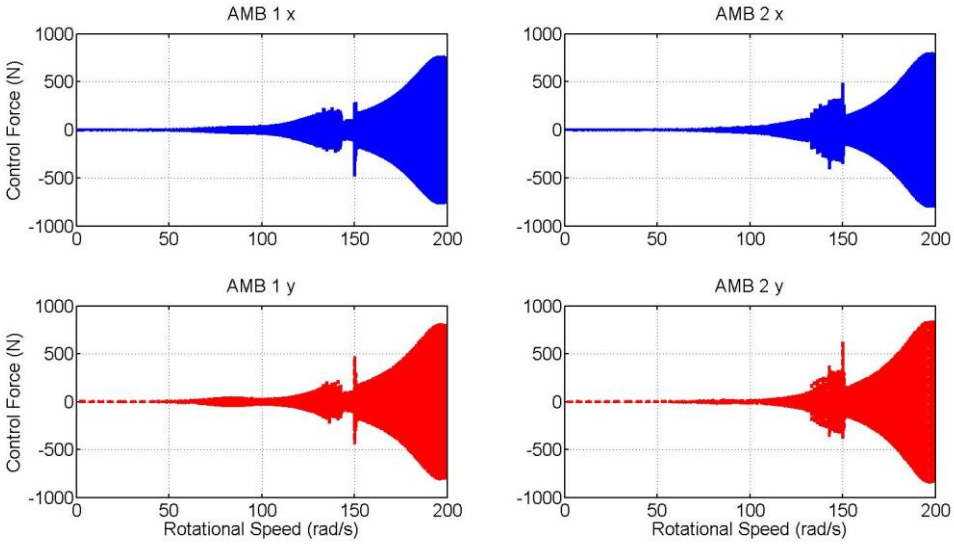

(a) Control forces by PD control only

Figure 5.42 Control forces from AMBs, during run-up

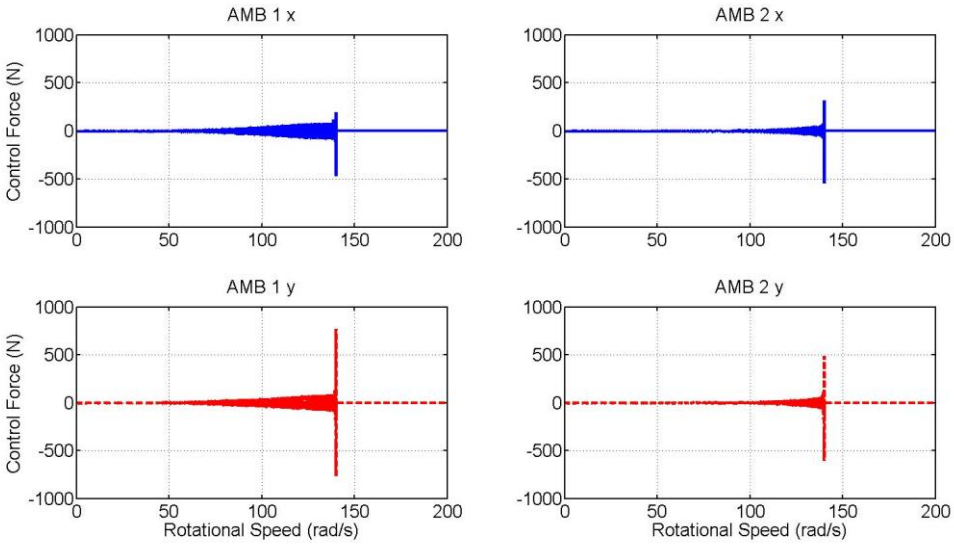

(a) Control forces generated by $\bar{\mathbf{K}}_c(k_e)$

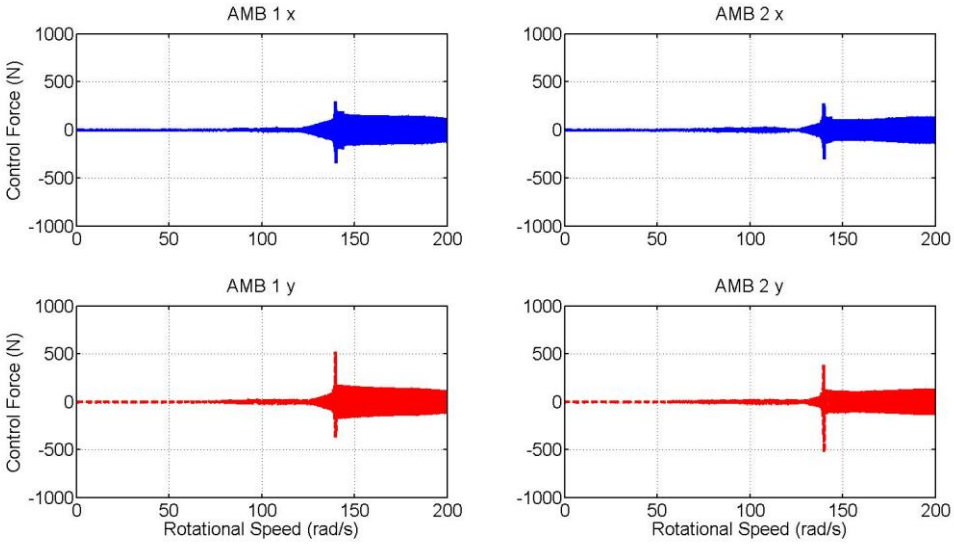

(a) Control forces by PD control only

Figure 5.43 Control forces from AMBs, during run-down

5.6 Closure

By introducing the base model developed in Chapter 2, this Chapter presented rotor/TDB contact dynamics in a rotating frame, including contact modes and bi-stable rotor response under contact. For the contact-dependent LMI based gain-scheduling controller design, a linearization for the complex contact condition is given. With a feedforward observer developed in Section 5.2, rotor/TDB contact condition could be estimated by using accelerometer feedback, and linearized as effective stiffness for the gain-scheduling controller dynamic adaption.

A LPV contact-dependent rotor/base model is introduced in Section 5.3, together with the varying parameter polytope. Through LPV model reduction, a reduced order model is used for contact-dependent controller design. A LMI based gain-scheduling controller having contact-dependency is synthesized in Section 5.4, and verified in the frequency domain. Simulated results in the time domain are presented in section 5.5, with consideration of contact transient characteristics. The results show the potential for the controller to adapt and achieve contact-free rotor operation, with guaranteed robust stability.

Chapter 6 Experiments for LMI Based Gain-Scheduling Controller for Rotor Escape Contact

The LMI based gain-scheduling controller for rotor escape from contact was implemented on the test rig described in Chapter 2. With regard to experiments, rotor/TDB contact events are presented for different unbalance conditions with non-driven end bushing 0% and 50% misaligned. For the real-time implementation, the stability of the controlled system is improved by appropriate weightings in Section 6.1. Then, the improved LMI based gain-scheduling controller is verified experimentally by (1) non-contact robustness stability and control performance assessment, (2) control action for contact-free recovery.

6.1 Controller Improvement for Real-Time Implementation

In contrast with simulation, experimental tests may introduce disturbance noise from the amplifiers, electrical circuits and sensors. LMI gain-scheduling controller for rotor contact recovery designed in Chapter 5 may not able to stabilize the rotor/AMB system experimentally due to such noise and model uncertainties underestimation. Thus, improvement for controller real-time implementation is necessary. Also, the controller may need to be discretized.

6.1.1 Controller Improvement

The controller is improved by appropriate weighting transfer function for the complementary sensitivity. Also, by considering a better controller performance over potential rotor/TDB contact zone, the weighting transfer function is re-designed.

Complementary Sensitivity

By considering model uncertainties including multiplicative model error, the weighting transfer function for complementary sensitivity shown in equation (5.35) may induce zero/pole cancellation in the closed loop system, and underestimate the model uncertainties between the plant shown in equation (5.25) and the rotor/AMB

system. Hence, two weighting transfer functions for robust stability in control were proposed

$$w_{c1}^{e}(s) = 0.3\frac{\frac{s}{2\pi 50}+1}{\frac{s}{2\pi 1000}+1} \tag{6.1}$$

and

$$w_{c2}^{e}(s) = 0.5\frac{\frac{s}{2\pi 30}+1}{\frac{s}{2\pi 1000}+1} \tag{6.2}$$

Both weighting transfer functions shown in equations (6.1) and (6.2) are able to guarantee the stability when the controller is implemented. The weighting transfer function w_{c1}^{e} shown in equation (6.1), has a relative tight boundary for multiplicative model error (0.3) at low frequencies, so that control to reject external disturbances may be achieved. However, the weighting at high frequencies (6) may be too low and may increase controller gain to induce audible noise and possible instability. The weighting function w_{c2}^{e} shown in equation (6.2) approaches (16.7) at high frequencies, and may be sufficient to reduce the controller gain.

Sensitivity

Normally, a less damped second order filter used in sensitivity optimization will introduce a high gain harmonic into controller dynamics, and making it quite sensitive at the notch frequency. However, it may offer good control action, especially in contact-dependent controller design. Thus, based on the weighting transfer function shown in equation (5.37), the weighting transfer functions for sensitivity in control by different damping ratio are given by

$$w_{s1}^{e}(s) = \alpha\left(\frac{{w_n}^2}{s^2 + 2\xi_1 w_n s + {w_n}^2}\right) \tag{6.3}$$

where $w_n = 100\ \mathrm{rad/s}, \alpha = 1$ and $\xi_1 = 0.2$. and

$$w_{s2}^{e}(s) = \alpha\left(\frac{{w_n}^2}{s^2 + 2\xi_2 w_n s + {w_n}^2}\right) \tag{6.4}$$

where $\xi_2 = 0.3$.

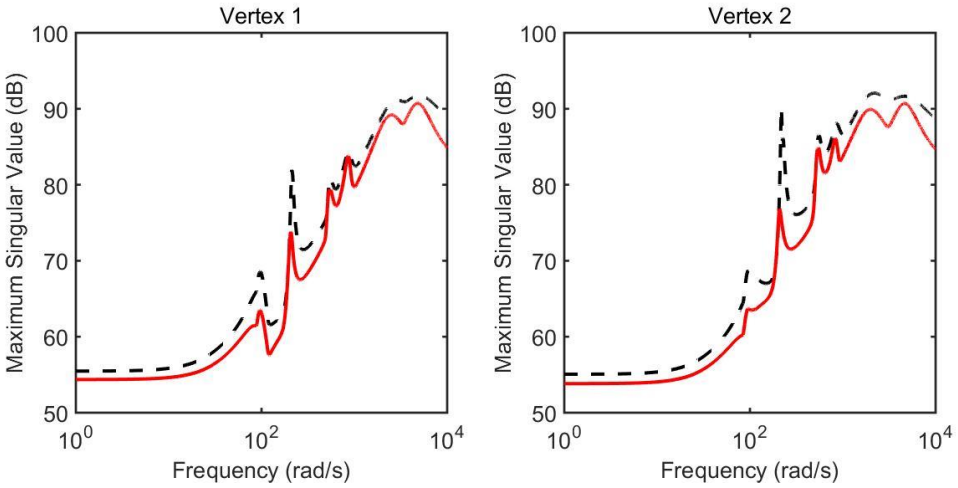

Figure 6.1 Maximum singular values of two proposed controllers dynamics at two vertices, $\bar{\sigma}(\overline{\mathbf{K}}_{c\_1}(s, k_e))$ in dashed line and $\bar{\sigma}(\overline{\mathbf{K}}_{c_2}(s, k_e))$in solid line

Thus, two controllers are synthesized by LMI based gain-scheduling technique stated in the previous chapters. Table 6.1 summarizes the controllers. Figure 6.1 shows in the maximum singular of the two controllers ($\overline{\mathbf{K}}_{c\_1}(k_e)$, $\overline{\mathbf{K}}_{c\_2}(k_e)$). The weightings for controller $\overline{\mathbf{K}}_{c\_1}(k_e)$ introduces a significant harmonic around 210 rad/s. With appropriate weightings design as shown in equation (6.2) and (6.4), the controller $\overline{\mathbf{K}}_{c\_2}(k_e)$ harmonics induced by the second order filter are reduced significantly. Therefore, the potential instability caused by controller natural sensitivity can be avoided in real-time implementation.

Table 6.1 LMI based contact-dependent controllers

Controllers	$\overline{\mathbf{K}}_{c\_1}(k_e)$	$\overline{\mathbf{K}}_{c\_2}(k_e)$
complementary sensitivity	w_{c1}^{e}	w_{c2}^{e}
sensitivity	w_{s1}^{e}	w_{s2}^{e}
γ_s^e	0.66	0.67
States (each vertex)	40	40

6.1.2 Real-Time Implementation

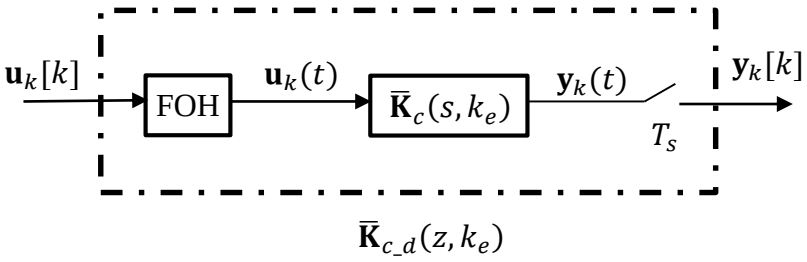

Figure 6.2 First-Order hold method for controller discretion

Due to the A/D converter used in real-time testing, the continuous state-space controller $\bar{\mathbf{K}}_c(s,k_e)$ may need to be discretized with first-order hold (FOH) method shown in Figure 6.2. Due to the dSPACE controller hardware limitation and the complex computations required for LMI based gain-scheduling, the sampling frequency F_s was set at 4000 Hz, Hence the sampling time was $T_s = 0.00025\,\mathrm{s}$. Such high sampling frequency discretizaton retains controller dynamics at low frequencies up to 2000 Hz based on the Nuquist criterion. The controller computing time, including the full order discretised controller $\bar{\mathbf{K}}_{c\_d}(z,k_e)$ having 40 states, is around $0.00018\,\mathrm{s}$, as indicated by the dSPACE ControlDesk software. Such computing time is acceptable, and allows for sufficient turn around in the A/D converting period

Controller Model for Hardware Compliance

With linear interpolation, the gain-scheduling control technique can be complied into dSPACE hardware through SIMULINK model shows in Figure 6.3. Based on the LPV controller implementation shown in equations (4.39)-(4.42), the controller $\bar{\mathbf{K}}_{c\_d}(z,k_e)$ discretized by the FOH method may be expressed as

$$\bar{\mathbf{K}}_{c\_d}(z,k_e)=\begin{bmatrix}\bar{\mathbf{A}}^c_{K\_d}(\Pi_{e,1})+\propto\bar{\mathbf{A}}^e_{K\_d} & \bar{\mathbf{B}}^c_{K\_d}\\ \bar{\mathbf{C}}^c_{K\_d} & \bar{\mathbf{D}}^c_{K\_d}\end{bmatrix} \tag{6.5}$$

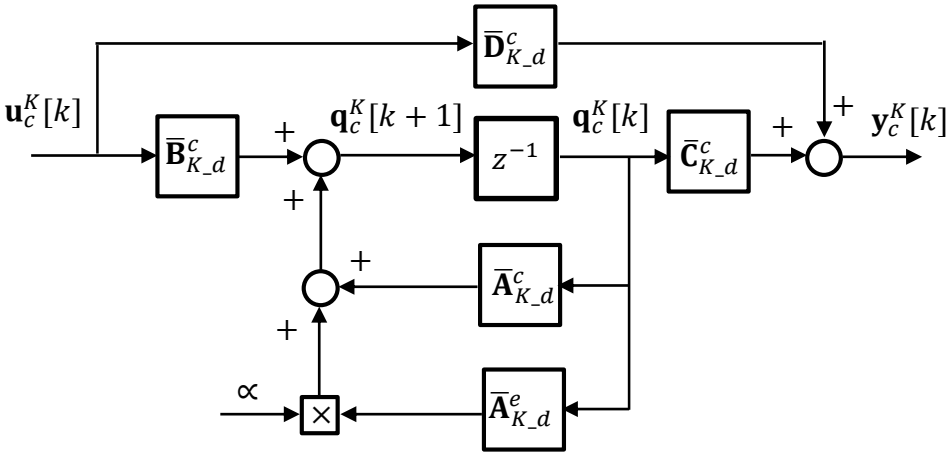

Figure 6.3 Discretized LMI based gain-scheduling controller $\bar{\mathbf{K}}_{c\_d}(z, k_e)$ compiled in dSPACE hardware

6.1.3 Controller Harmonics

Based on the discretization method stated, continuous controllers ($\bar{\mathbf{K}}_{c\_1}(k_e)$, $\bar{\mathbf{K}}_{c\_2}(k_e)$) shown in Table 6.1 were discretized, and implemented in the test rig. Figure 6.4 shows the rotor responses under control by $\bar{\mathbf{K}}_{c\_1}(k_e)$ and $\bar{\mathbf{K}}_{c\_2}(k_e)$. Additionally, controller 1, $\bar{\mathbf{K}}_{c\_1}(k_e)$, gave rise to higher audible noise than controller 2, $\bar{\mathbf{K}}_{c\_2}(k_e)$.

Figure 6.5 shows the frequency content of the sensor signals. High frequency content can be found when rotor is under control from $\bar{\mathbf{K}}_{c\_1}(k_e)$, and those may be induced by the controller inherited harmonic as shown in Figure 6.1. Controller 2, $\bar{\mathbf{K}}_{c\_2}(k_e)$, improved such issues and was chosen to be used in further experimental tests.

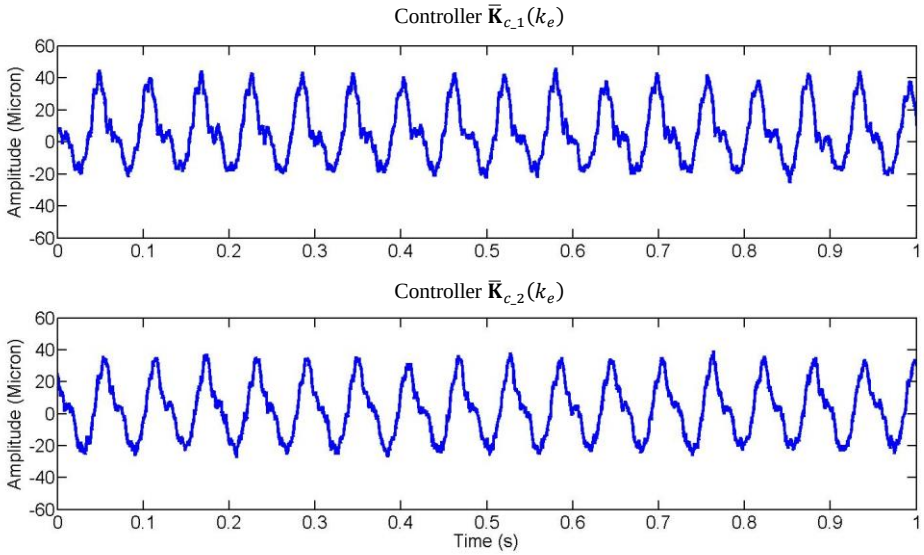

(a) Sensor 3

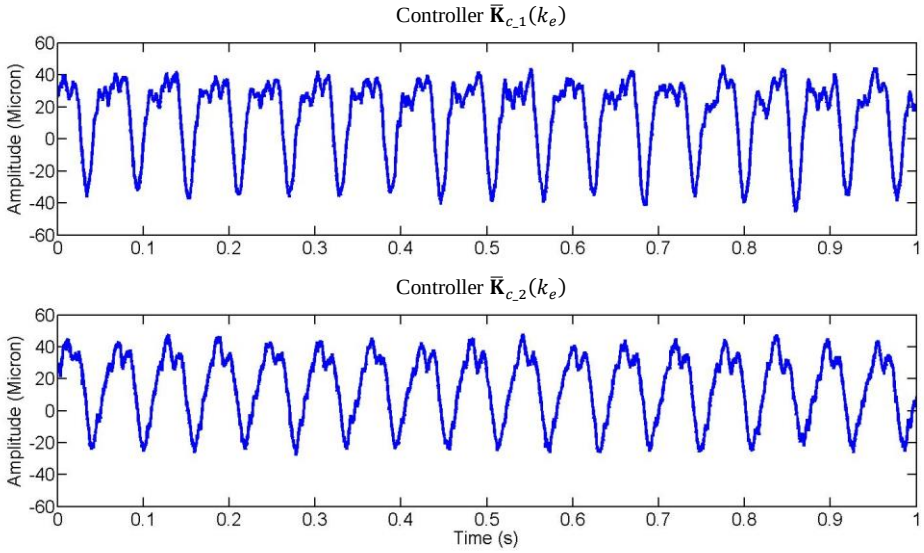

(b) Sensor 4

Figure 6.4 Displacement measurements for sensor planes close to AMB 1 under the controllers $\bar{\mathbf{K}}_{c\_1}(k_e)$ and $\bar{\mathbf{K}}_{c\_2}(k_e)$, when running at 107 rad/s

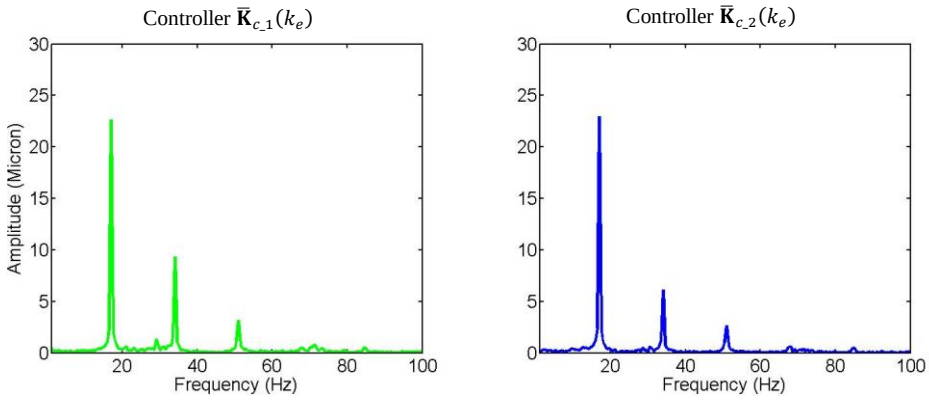

(a) Sensor 3

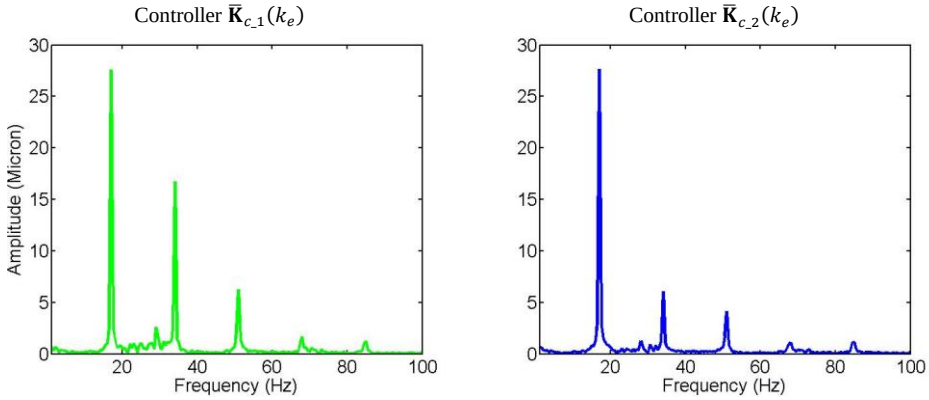

(a) Sensor 4

Figure 6.5 FFT of time domain signal from sensor plane close to AMB 1 running at 107 rad/s

6.2 Unbalance Forcing Contact Issues under PD Control

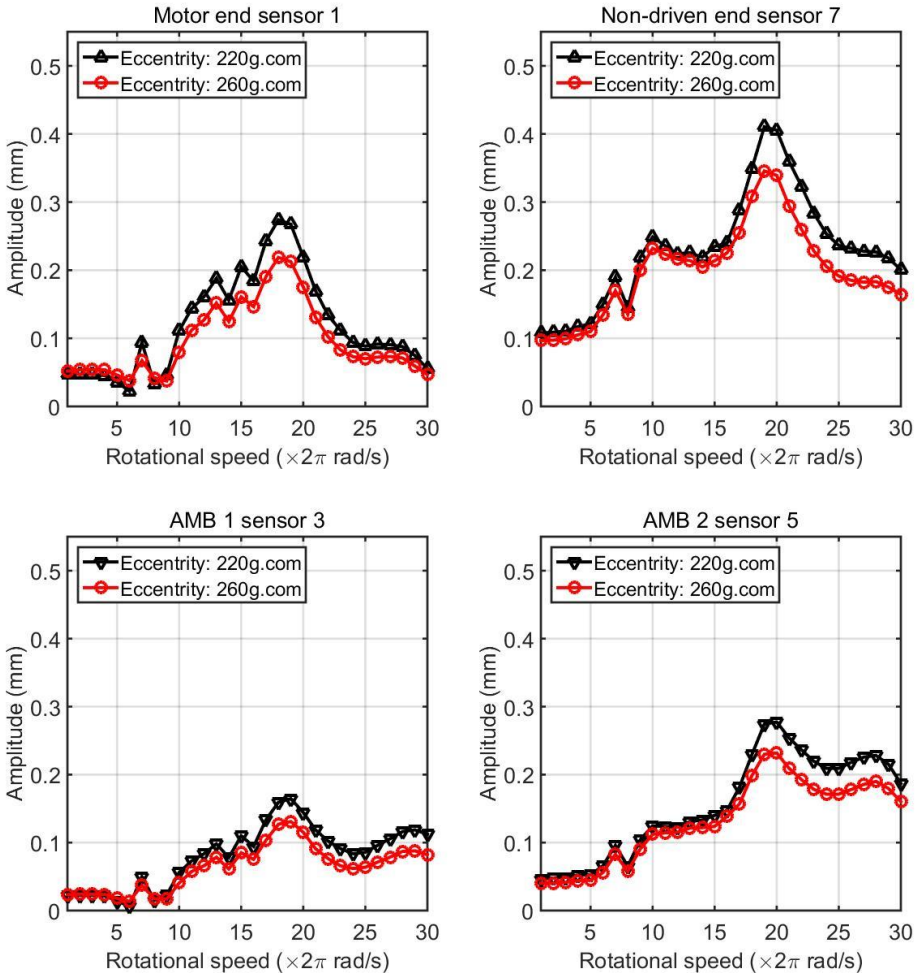

Figure 6.6 Synchronous amplitudes extracted from measured signals with two unbalance cases: 220 g.cm and 260 g.cm added to the non-driven end disk

Depending on the unbalance cases and TDB alignments, rotor responses under contact may differ. Steady rotor responses were measured with different unbalance masses mounted on the disk at the rotor non-driven end. Unbalances (220 g.cm and 260 g.cm) were tested over the full operating speed range from 0 to 188 rad/s, which covers three rotor resonances including translational/conical rigid body modes and the first bending mode. Vibration orbits at the non-driven end were largest around 120 rad/s, which indicates the response of the rotor in the rigid body translational mode. Figure 6.6 shows the synchronous amplitudes extracted from measured

displacement signal under the two unbalance cases. In each case, the rotor was in a contact-free condition.

6.2.1 Rotor Contact with 0% Misalignment of the TDB

After rotor was fully levitated by control under integral action, a non-driven end bush was aligned concentrically (0% misalignment) with the rotor. This arrangement gave a constant 0.4 mm radial clearance around rotor. In run-up/down trials, rotor responses near the non-driven end revealed nonlinear behaviour when contact occurred, as shown in Figure 6.7. Figure 6.7 (a) shows the synchronous amplitudes extracted from the displacement sensor close to the non-driven end (sensor 7). Note that the sensor was slightly offset from the TDB, which is the reason for the apparent contact at 0.35 mm. Under the 260 g.cm unbalance, the rotor response involved contact when speed running above 107 rad/s, which was audible. Contact ceased above 163 rad/s.

Figure 6.7 (b) shows the phase variations of the contact and non-contact conditions. Over 107-163 rad/s the phase difference increased to around 60 deg, otherwise it is small without contact.

After reaching the maximum speed of 188 rad/s, the rotor was run-down with small de-acceleration. Rotor contact then occurred at 150 rad/s and the response was similar to that for run-up. By comparing run-up/down operations under contact, bi-stable responses occurred over 150-163 rad/s.

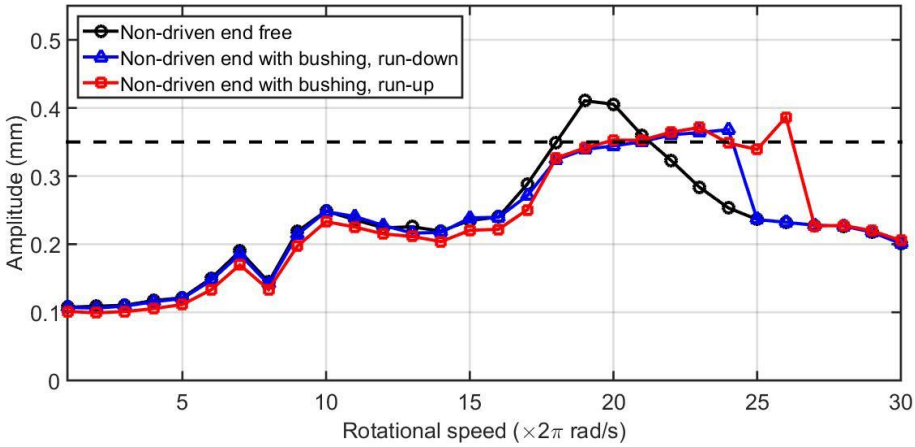

(a) Amplitude

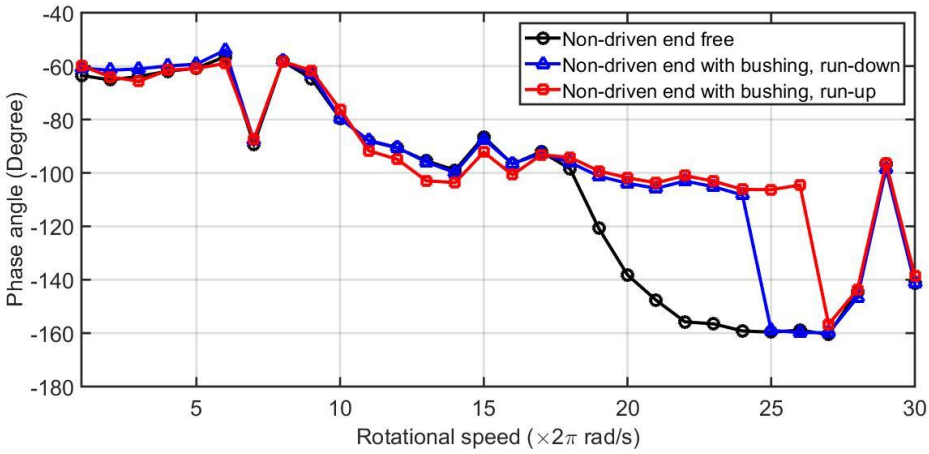

(b) Phase

Figure 6.7 Synchronous amplitude and phase extracted from sensor 7: PID control only with the non-driven end free; PID control only when a non-driven end bush of radial clearance 0.4 mm is included

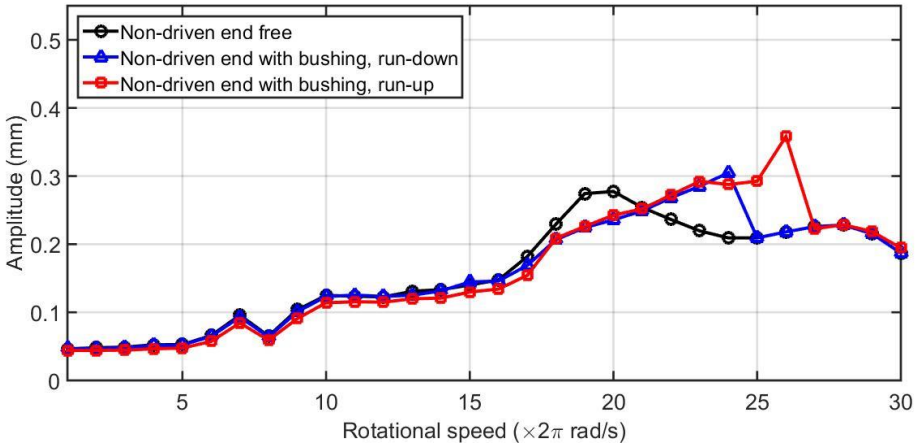

(a) Amplitude

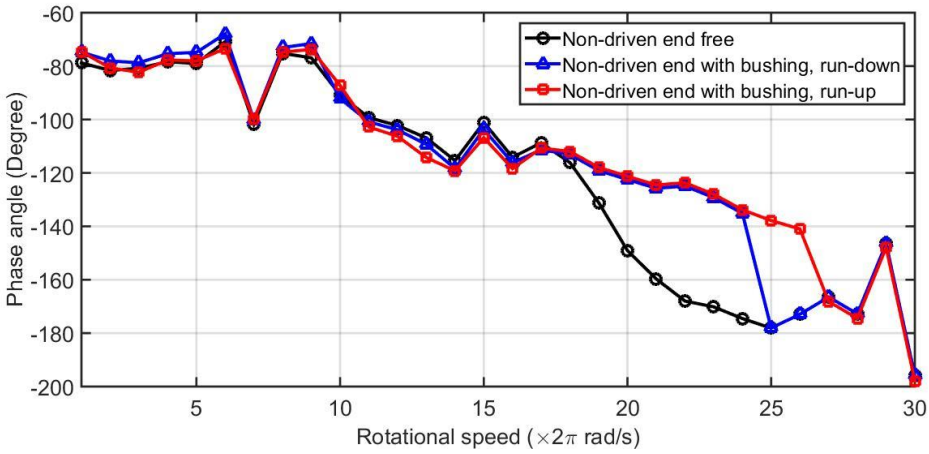

(b) Phase

Figure 6.8 Synchronous amplitude and phase extracted from sensor 5: PID control only with the non-driven end free; PID control only when a non-driven end bush of radial clearance 0.4 mm is included

Figure 6.8 shows the corresponding results for sensor 5, which is close to AMB 1. In contrast with Figure 6.7, rotor flexibility effects are evident.

6.2.2 Rotor Contact with Bush 50% Misalignment of the TDB

In order to consider misalignment influences, the bush was shifted up by 50%. This arrangement offers a non-concentric clearance with a maximum 0.6 mm and minimum 0.2 mm. The unbalance was reduced to 220 g.cm. Bi-stable responses were also found in the 50% misalignment contact test. The results are shown in Figure 6.9, with bi-stable responses over 138-157 rad/s.

Although 50% misalignment provides a minimum clearance of 0.2 mm, contact was not observed by sensor 7 until slight rubbing occurred at 113 rad/s, which is higher than the 0% misalignment case shown in Figure 6.7. In the run-up trial, the rotor became contact-free above 157 rad/s. and phase angle dropped back to that of the contact-free condition from 40 deg. Figure 6.9 shows the amplitude and phase of the response. However, with the 50% misalignment, the rotor contact response was asymmetric. Contact was observed weakly by sensor 8 as shown in Figure 6.10. Figures 6.11 and 6.12 show the synchronous amplitudes and phase angles from sensors 5 and 6 close to AMB 2.

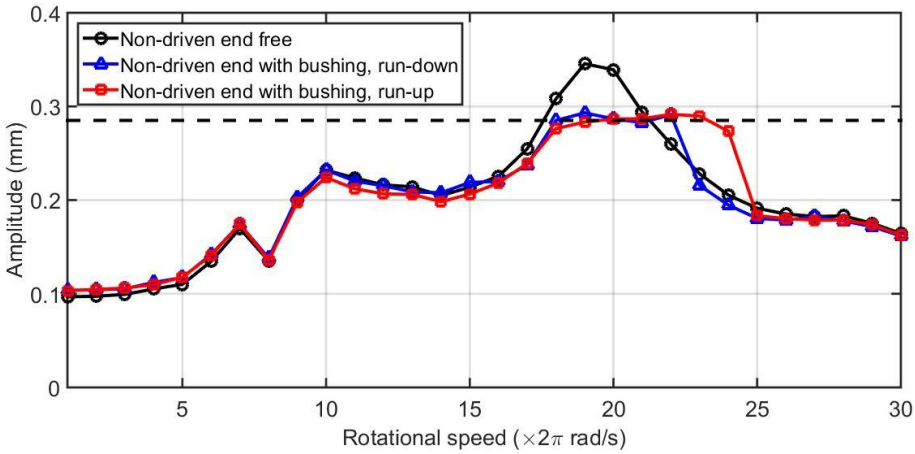

(a) Amplitude

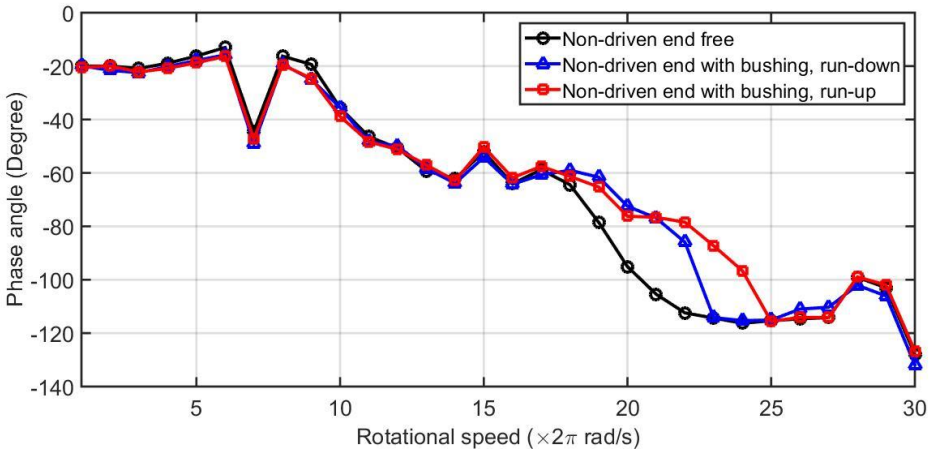

(b) Phase angle

Figure 6.9 Synchronous amplitude and phase extracted from sensor 7: PID control only with the non-driven end free; PID control only when a non-driven end TDB was 50% misaligned

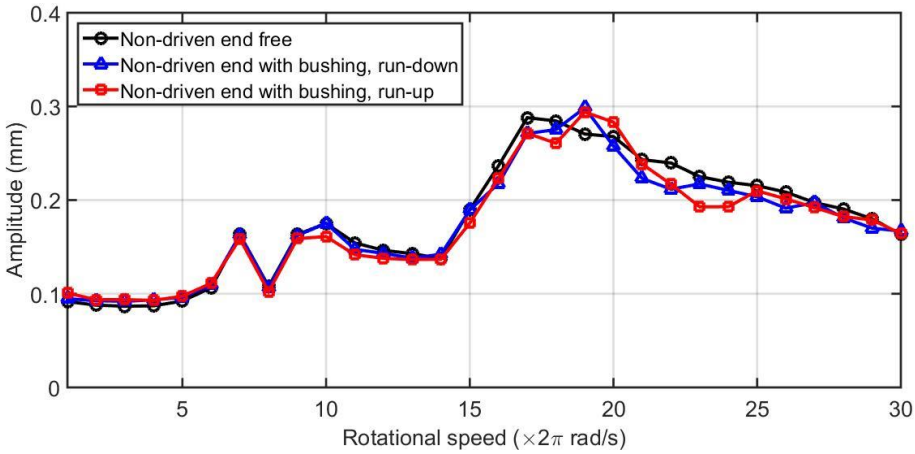

(a) Amplitude

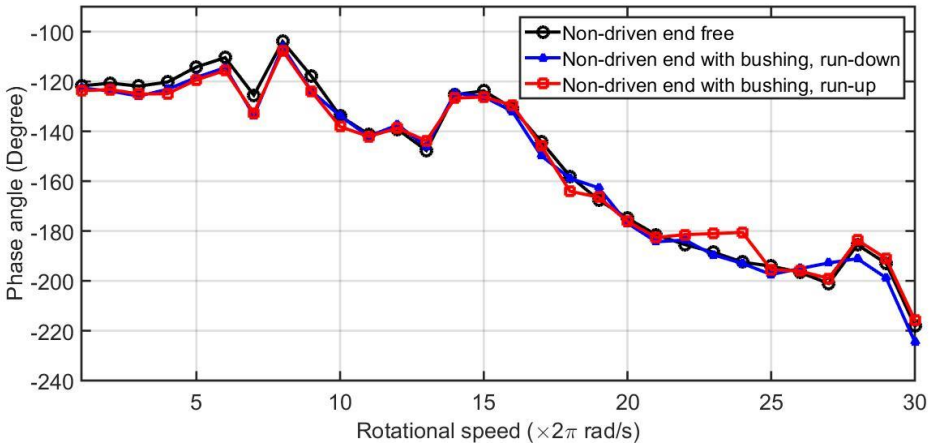

(b) Phase angle

Figure 6.10 Synchronous amplitude and phase extracted from sensor 8: PID control only with the non-driven end free; PID control only when a non-driven end TDB was 50% misaligned

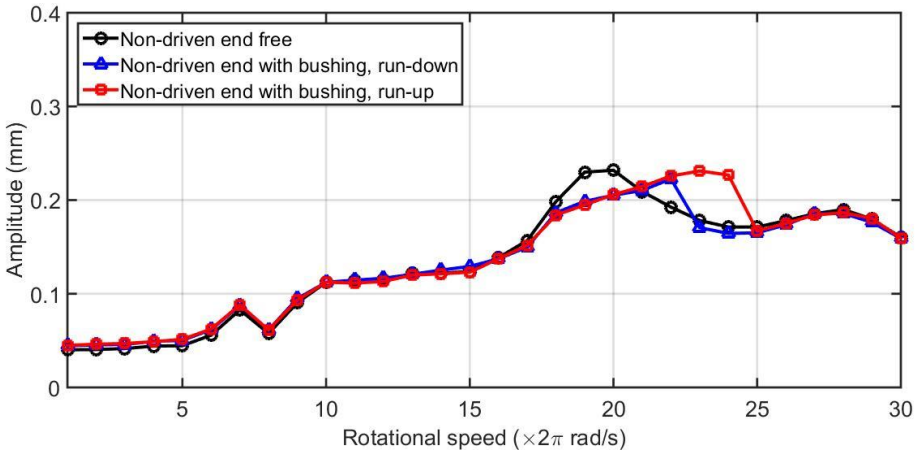

(a) Amplitude

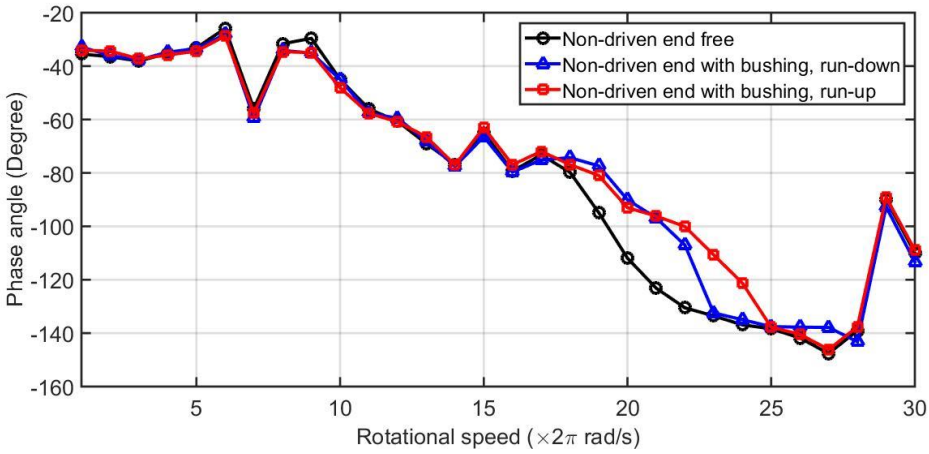

(b) Phase angle

Figure 6.11 Synchronous amplitude and phase extracted from sensor 5: PID control only with the non-driven end free; PID control only when a non-driven end TDB was 50% misaligned

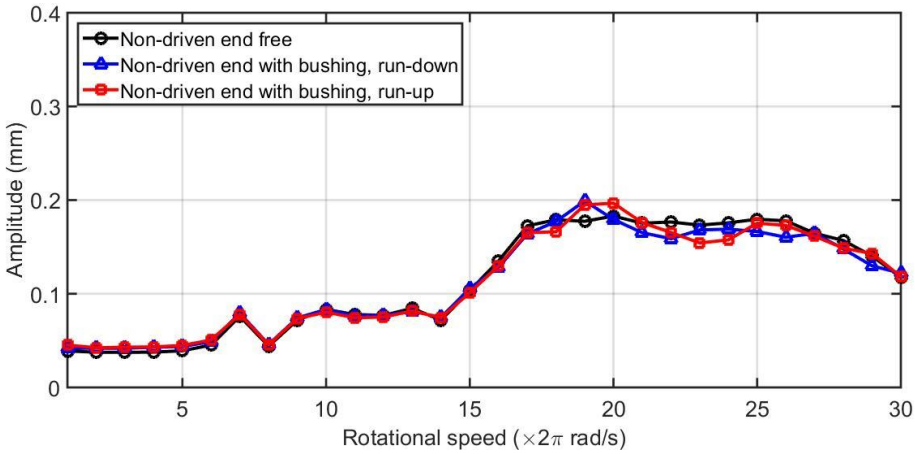

(a) Amplitude

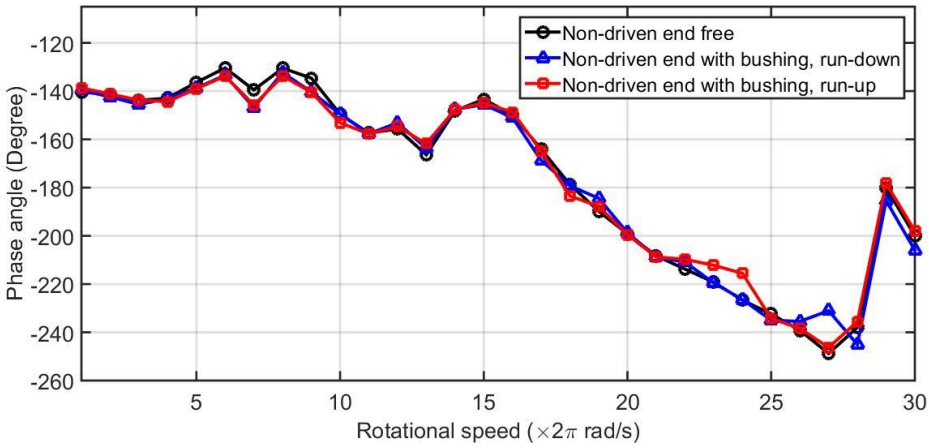

(b) Phase angle

Figure 6.12 Synchronous amplitude and phase extracted from sensor 6: PID control only with the non-driven end free; PID control only when a non-driven end TDB was 50% misaligned

6.3 Contact-Free Recovery by LMI Based Gain-Scheduling Control

A contact-dependent controller was synthesized by the LMI based gain-scheduling technique, in order to enable control action in both contact and non-contact situations. The discrete Controller $\overline{\mathbf{K}}_{c\_2\_d}(k_e)$ having continuous form shown in Table 6.1, was implemented, and tests were undertaken to recover the rotor from contact with both 0% and 50% misalignment of TDB. This section also presents the control performance under a larger unbalance of 400 g.cm with 0% misalignment.

6.3.1 Non-Contact Control Performance Verification

Non-contact control performance provided by the LMI gain-scheduling controller $\overline{\mathbf{K}}_{c\_2\_d}(k_e)$ is necessary to be assessed experimentally. For transients and rotor steady responses under control, controller $\overline{\mathbf{K}}_{c\_2\_d}(0)$ was fixed at the parameter box corner as contact-free ($k_e = 0$ N/m) and implemented in the test rig when the rotor non-driven end had the TDB removed.

Transient Control Performance

The controller $\overline{\mathbf{K}}_{c\_2}(0)$ transient performance due to an impulse force distribution was tested experimentally. An impulse forcing signal (200 N for 1 s) was applied through AMB 1. Figure 6.13 shows the displacement response. The left plots are the transient responses for the rotor under PID control only. The right plots are with controller $\overline{\mathbf{K}}_{c\_2}(0)$ engaged. By comparing the maximum displacement amplitudes, the LMI based H_∞ control capability for disturbance rejection is evident. Moreover, lower overshoots and shorter settling times are good indicators for the benefits of LMI based optimization.

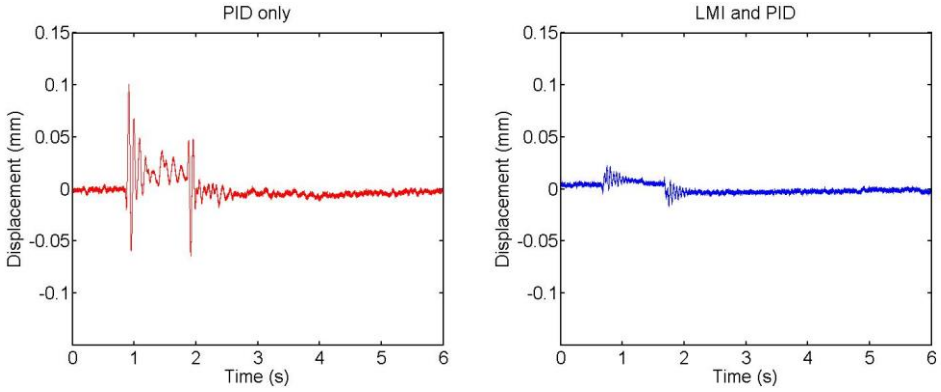

(a) Sensor 1 close to the motor end

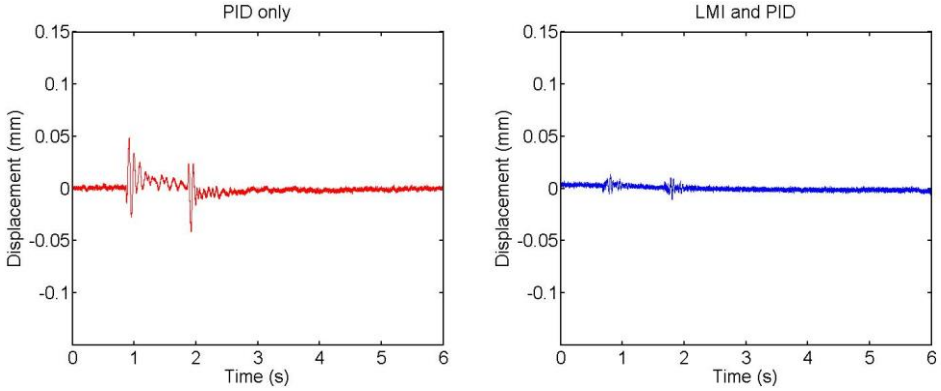

(b) Sensor 3 close to the AMB 1

Figure 6.13 Sensor measured displacement response due to impulse from AMB 1

Steady Controlled Rotor Response

The rotor response controlled by $\overline{\mathbf{K}}_{c\_2\_d}(0)$, was assessed with 260 g.cm and 220 g.cm unbalances. The results are shown in Figures 6.14 and 6.15. At the non-driven end, rotor unbalance forcing responses were well-controlled in the design range. Due to the closed loop sensitivity shaped by the weighting transfer function $w_{s2}^{e}(s)$ as shown in equation (6.4), rotor vibrations were attenuated significantly for rotational speeds from 0-138 rad/s, compared with PID control only. The closed loop response could still benefit from further control action above 138 rad/s.

With the 260 g.cm unbalance, controller $\overline{\mathbf{K}}_{c\_2\_d}(0)$ was insufficient to attenuate vibration at the non-driven end when running at 170 and 176 rad/s. Rotor vibration levels remained similar to those under PID control only, as shown in Figure 6.14.

The rotor could not be recovered from contact due to the insufficient control action at 170 and 176 rad/s.

In addition to the sensors used in the feedback loop of $\overline{\mathbf{K}}_{c\_2\_d}(0)$, rotor vibrations from sensors close to the AMBs, which are used for PID action are also shown in Figures 6.14 and 6.15. Due to the rotor rigid body mode at the critical speed 125 rad/s, vibrations close to the AMBs were attenuated significantly by $\overline{\mathbf{K}}_{c\_2\_d}(0)$ and even benefit from the control action up to 151 rad/s. Then, the rotor exhibited significant response with increasing rotational speed. Rotor orbits under control by LMI and PID became larger than these for PID control only as expected and reached maximum sizes at 176 rad/s close to AMB 2 in both unbalance cases. However, based on these results shown in Figures 6.14 and 6.15, LMI control action would not induce contact with the AMB TDBs since amplitudes are less than the radial clearance of 0.7 mm.

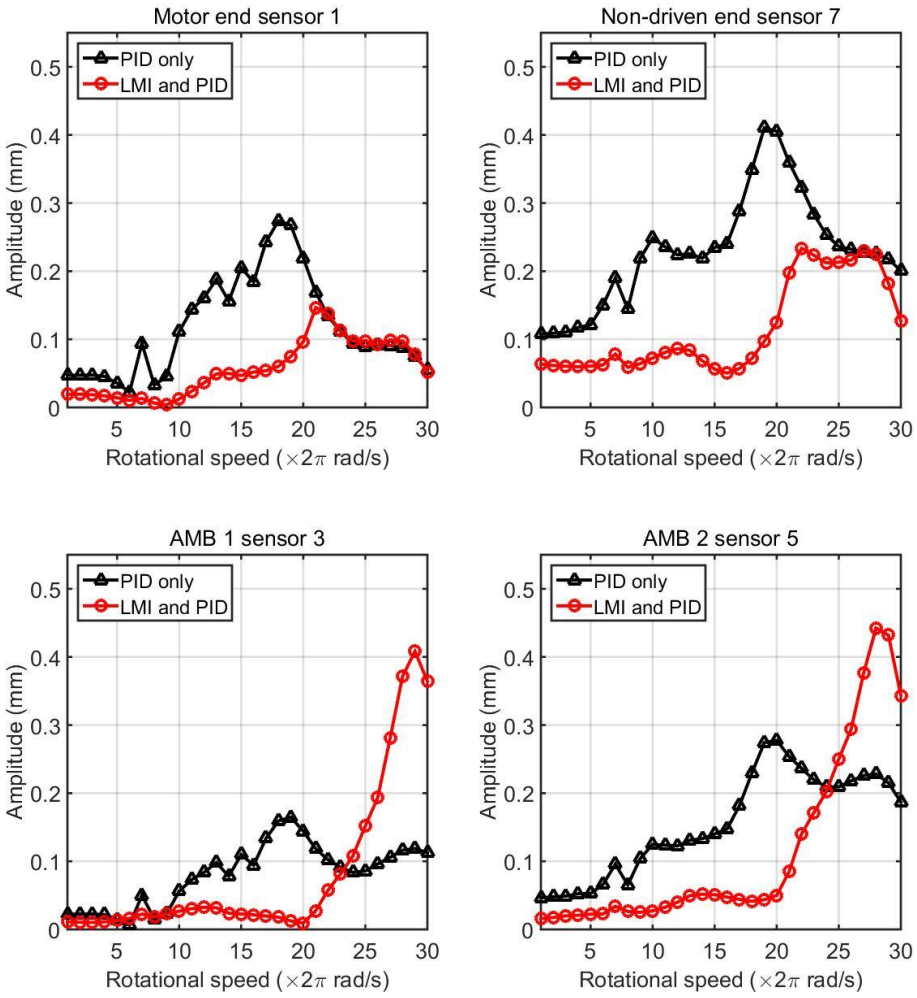

Figure 6.14 Synchronous amplitudes controlled by PID and LMI/PID action, extracted from measured signals when non-driven end is contact-free. The non-driven end disk had a 260 g.cm unbalance

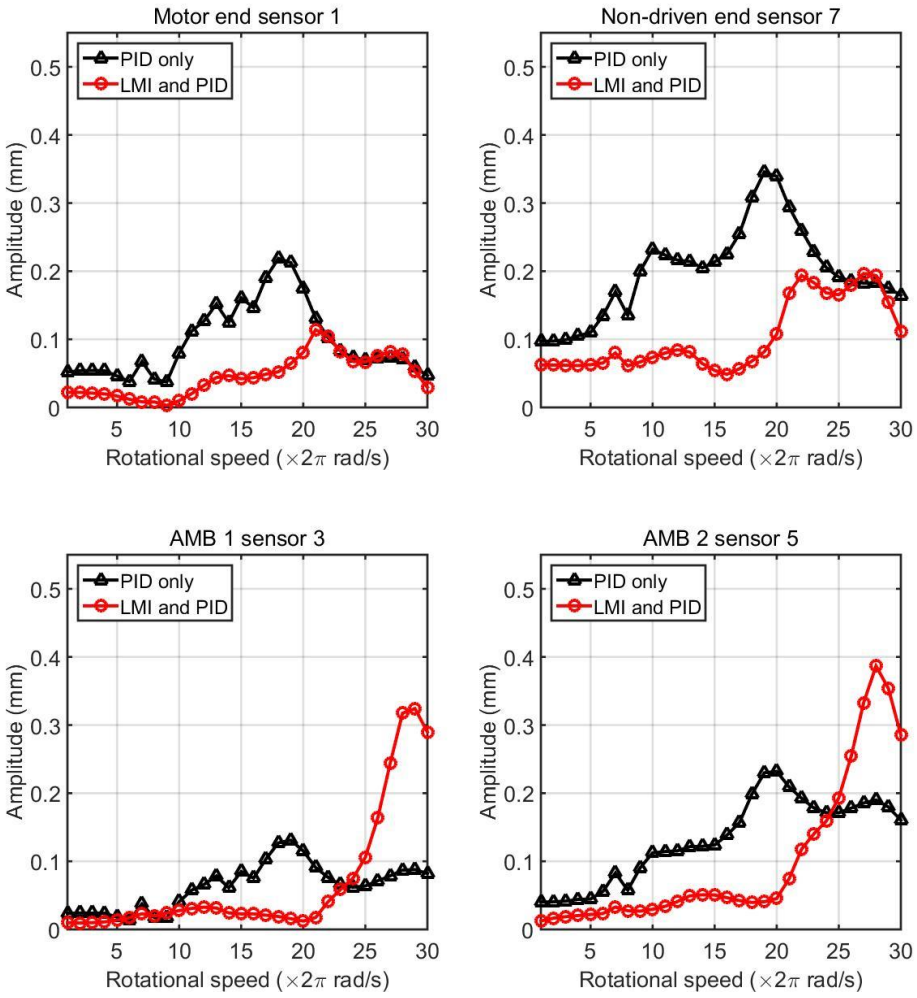

Figure 6.15 Synchronous amplitudes controlled by PID and LMI/PID action, extracted from measured signals when non-driven end is contact-free. The non-driven end disk had a 220 g.cm unbalance

6.3.2 Contact-Free Recovery with 0% Misalignment of TDB under Unbalance 260 g.cm

In 0% TDB misalignment, the contact recovery by controller $\bar{\mathbf{K}}_{c\_2\_d}(k_e)$ was tested experimentally at three speeds (107, 125 and 157 rad/s) under the 260 g.cm unbalance. In order to adapt the varying contact dynamics online, the LMI based gain-scheduling controller $\bar{\mathbf{K}}_{c\_2\_d}(k_e)$ was fed into the observer to infer acceleration arising from contact. The contact recovery procedure was carried out in three steps:

1. The rotor was initially in a contact-free states held in small vibration orbits under LMI control action.
2. The output of controller $\bar{\mathbf{K}}_{c\_2\_d}(k_e)$ was manually disabled, but still computed online. The rotor exhibited contact with the non-driven end bushing, due to insufficient control action under PID feedback.
3. By then enabling $\bar{\mathbf{K}}_{c\_2\_d}(k_e)$, contact recovery action could be assessed.

Figures 6.16-6.18 show the rotor motion during contact and then becoming contact-free due to LMI control action. At a speed of 107 rad/s, the contact event was slight, and only weakly effected rotor vibration orbits. Contact became audible when the rotor was running at 125 rad/s, rotor vibration orbits were constrained by the bushing at the non-driven end as shown in Figure 6.17. More significant contact occurred at the speed of 157 rad/s. Rotor responses in step 2 (controlled by PID action only) were not steady orbits, as shown in Figure 6.18.

LMI control action recovered rotor/TDB contact successfully at those three speeds. The rotor responses controlled by $\bar{\mathbf{K}}_{c\_2\_d}(k_e)$, remained at small vibration levels as shown in Figures 6.17 and 6.18, when running at speeds of 107 and 125 rad/s. At the speed of 157 rad/s, rotor vibrations after successful contact recovery by the control action from $\bar{\mathbf{K}}_{c\_2\_d}(k_e)$**,** was not attenuated significantly as shown in Figure 6.19. Such controlled rotor steady response corresponds with the contact-free control performance estimation shown in Figure 6.14.

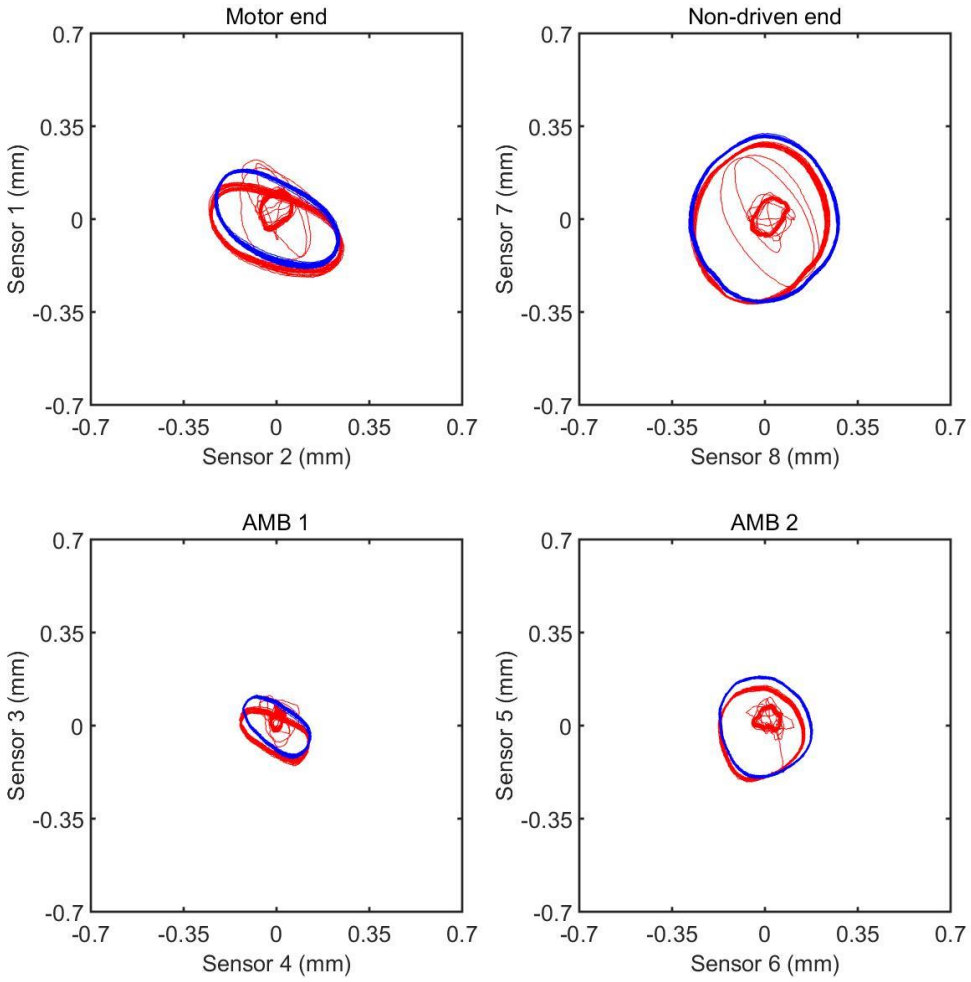

Figure 6.16 Measured orbits running at 107 rad/s: PID control with non-driven end free is shown in blue. LMI/PID control is shown in red.

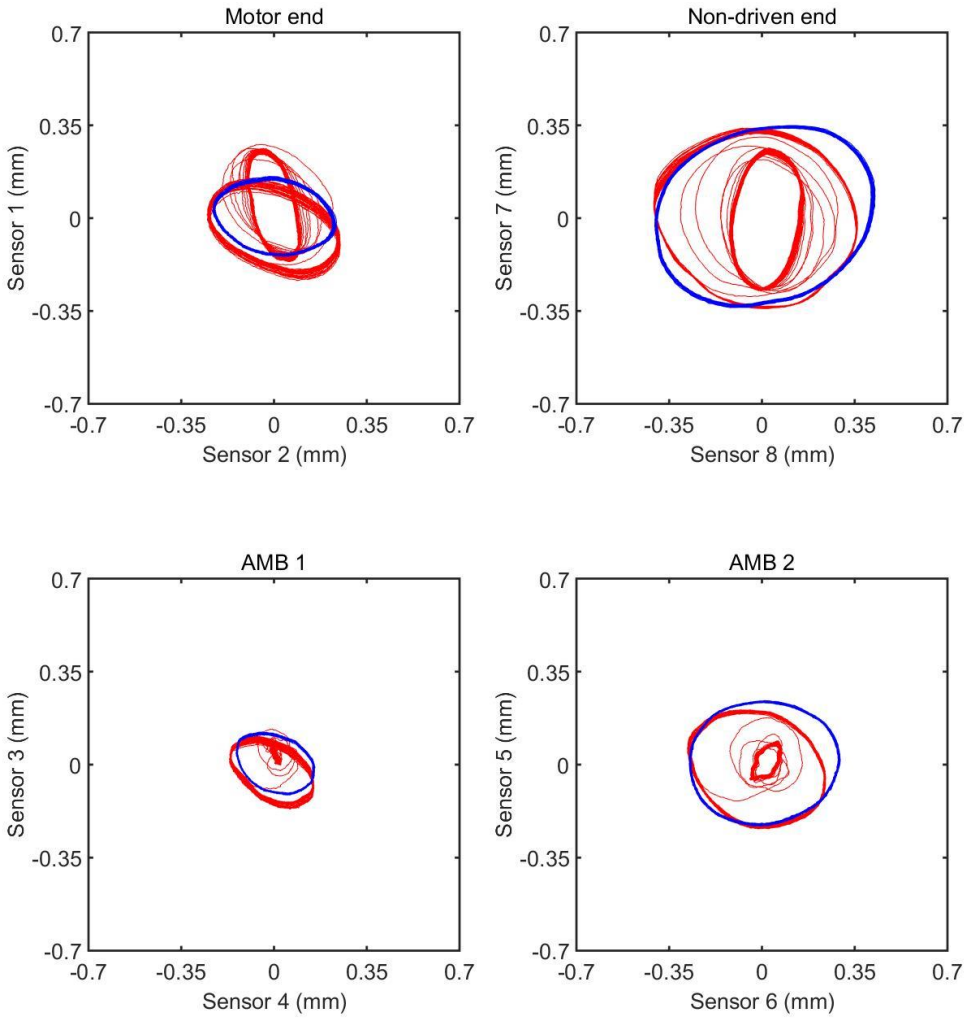

Figure 6.17 Measured orbits running at 125 rad/s: PID control with non-driven end free is shown in blue. LMI/PID control is shown in red.

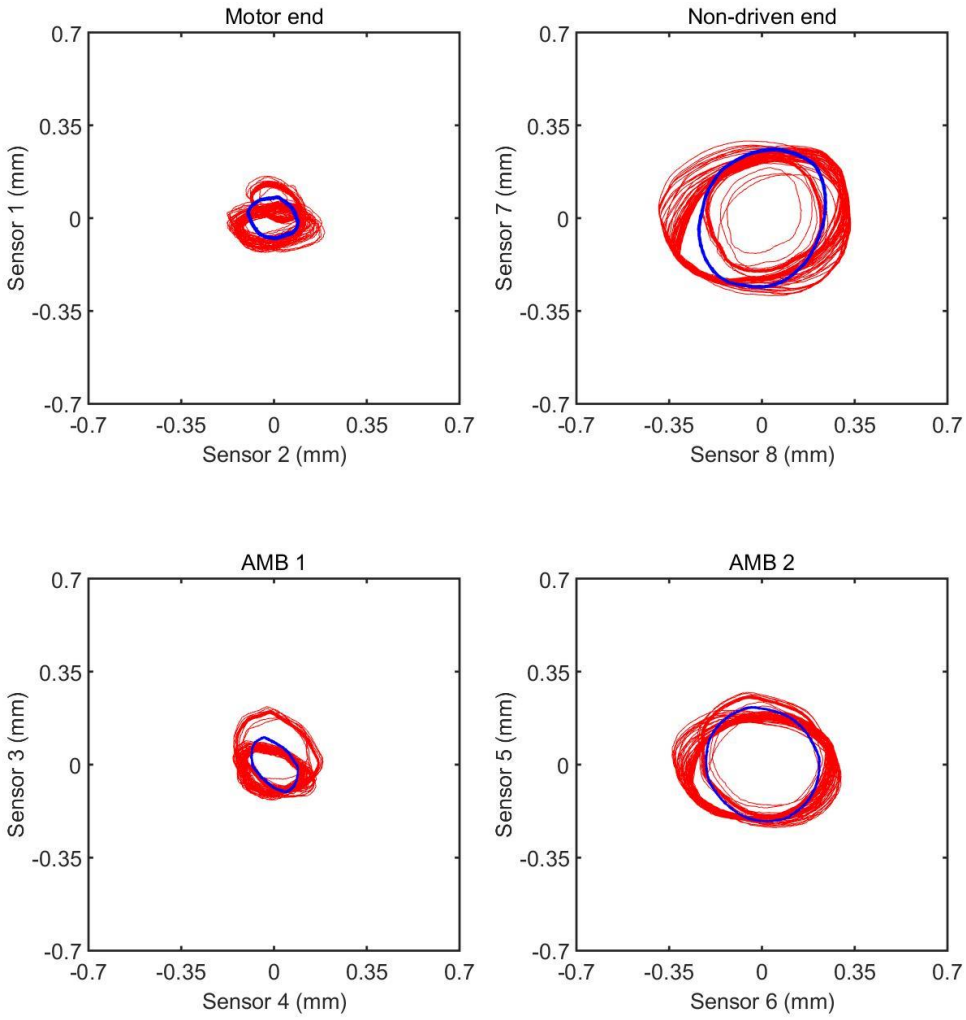

Figure 6.18 Measured orbits running at 157 rad/s: PID control with non-driven end free is shown in blue. LMI/PID control is shown in red.

Based on the feed-forward observer for contact condition estimation stated in Section 5.2, the base motion excited by AMB forcing could be eliminated. The inferred contact induced component of base acceleration was fed into the controller $\overline{\mathbf{K}}_{c\_2\_d}(k_e)$ as a linear varying parameter $k_e(t)$ to adapt control action for rotor/TDB contact events. Figures 6.19-6.21 show the measurements form accelerometer and inferred acceleration induced by contact during the contact recovery at 107, 125 and 157 rad/s. Contact-free states in Steps 1 and 3 are evident as shown 'Inferred acceleration by contact', and indicated the successful contact recovery action by $\overline{\mathbf{K}}_{c\_2\_d}(k_e)$. The amplitudes of the inferred base acceleration induced by contact (indicated as 'PID only') may also describe how significant contact event occurred during step 2. Rubbing mode contact is evident as shown in Figures 6.19 and 6.20, rubbing with sub-harmonic impact contact can be detected when the rotor was running at 157 rad/s as shown in Figure 6.21.

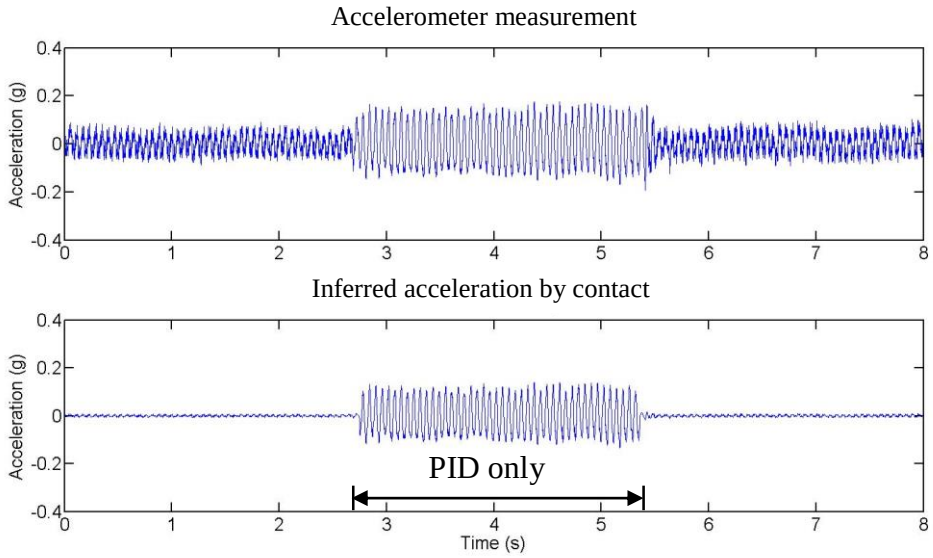

Figure 6.19 Accelerometer measurements and inferred (PID control only) acceleration caused by contact, running at 107 rad/s

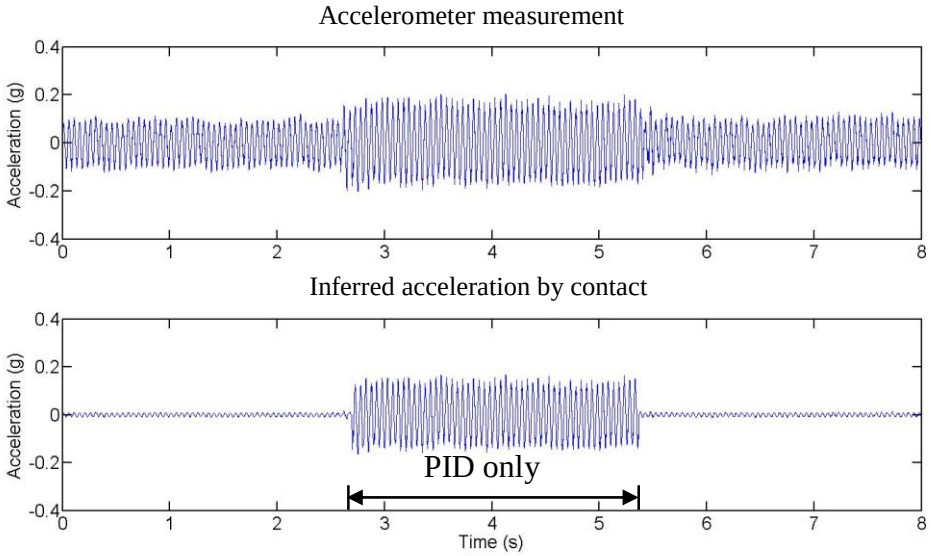

Figure 6.20 Accelerometer measurements and inferred (PID control only) acceleration caused by contact, running at 125 rad/s

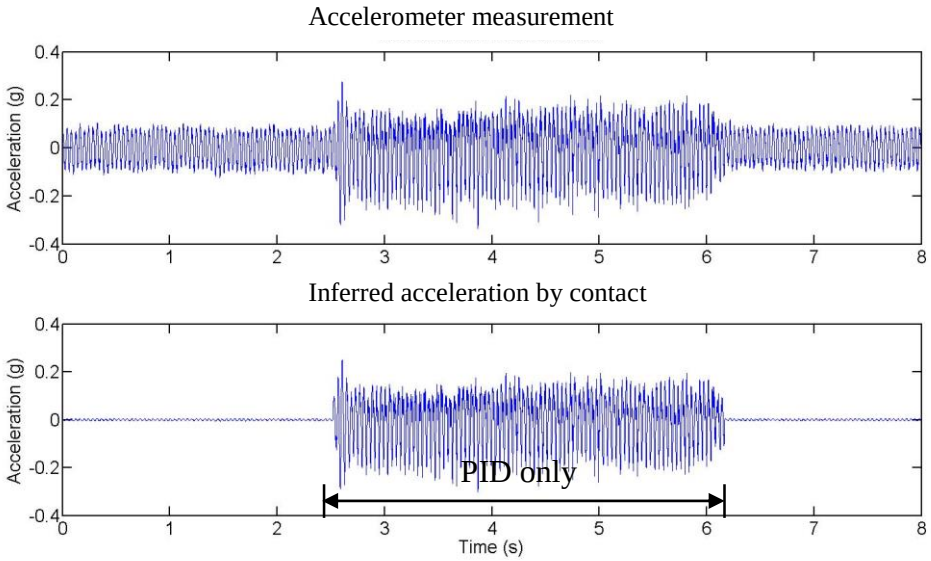

Figure 6.21 Accelerometer measurements and inferred (PID control only) acceleration caused by contact, running at 157 rad/s

LMI control action for contact-free rotor recovery is effective. Figures 6.22-6.24 show the corresponding sensor measurements during the contact recovery, when the rotor was running at 107, 125 and 157 rad/s. Figures 6.25-6.27 show the control forces from $\overline{\mathbf{K}}_{c\_2\_d}(k_e)$ in R/S coordinates as magnetic coils arrangement (each pair is arranged orthogonally at $\pm$45 degs to the vertical) in AMBs, including the contact period as step 2, and contact-free states as Steps 1 and 2.

When running at 125 rad/s, stable rubbing contact is evident from the rotor responses shown in Figure 6.23. Control forces from $\overline{\mathbf{K}}_{c\_2\_d}(k_e)$ were applied at around 5.2 s. Due to the guaranteed stability during contact offered by the gain-scheduling controller, rotor vibration was attenuated shortly, and the rotor became contact-free without significant transients.

Bouncing contact is also shown in the sensor measurements when running at 157 rad/s. The rotor position was recovered to be contact-free shortly after control action was activated round 6 s, as shown in Figure 6.24.

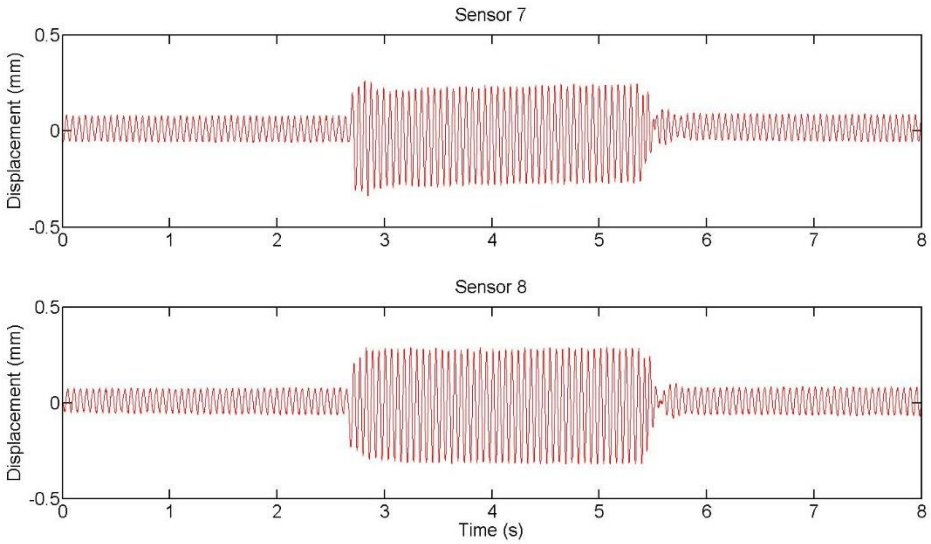

(a) Sensors close to the non-driven end

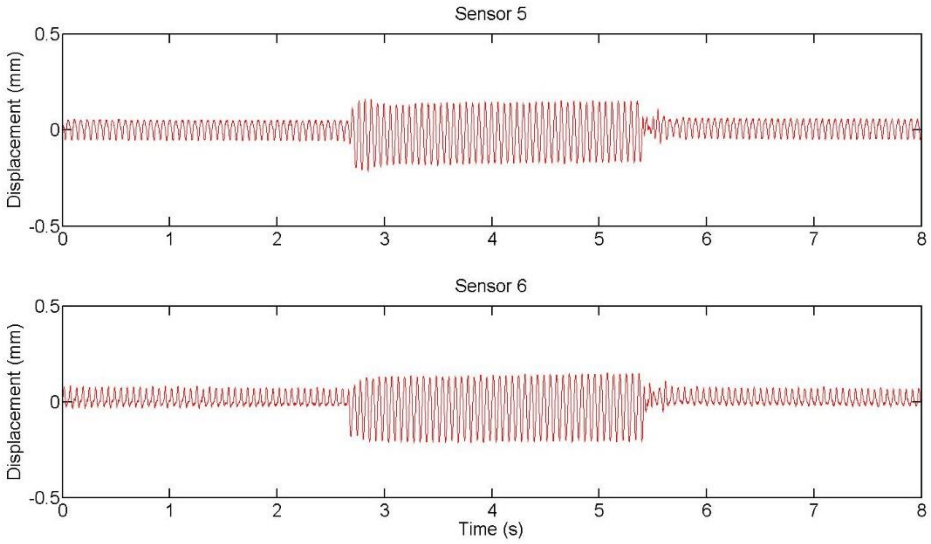

(b) Sensors close to the AMB 2

Figure 6.22 Sensor measurements showing contact recovery when running at 107 rad/s

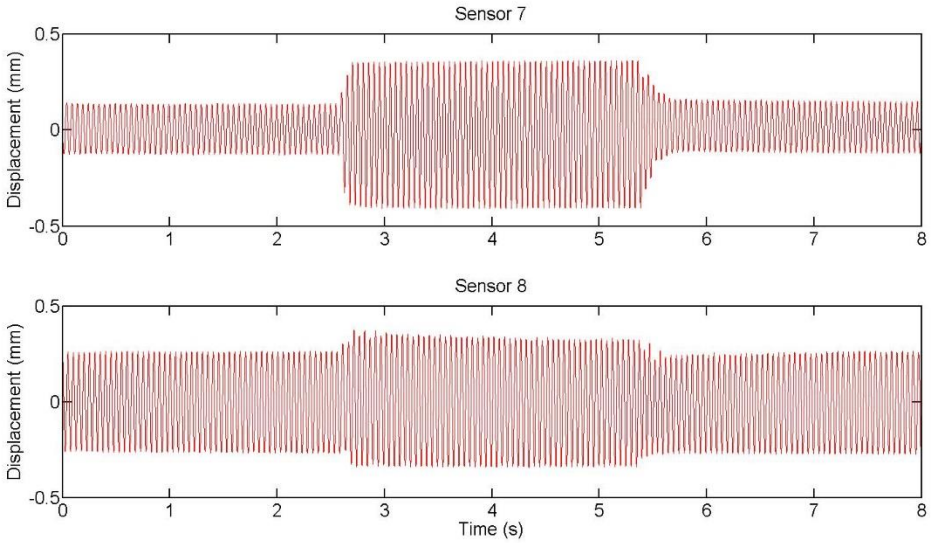

(a) Sensors close to the non-driven end

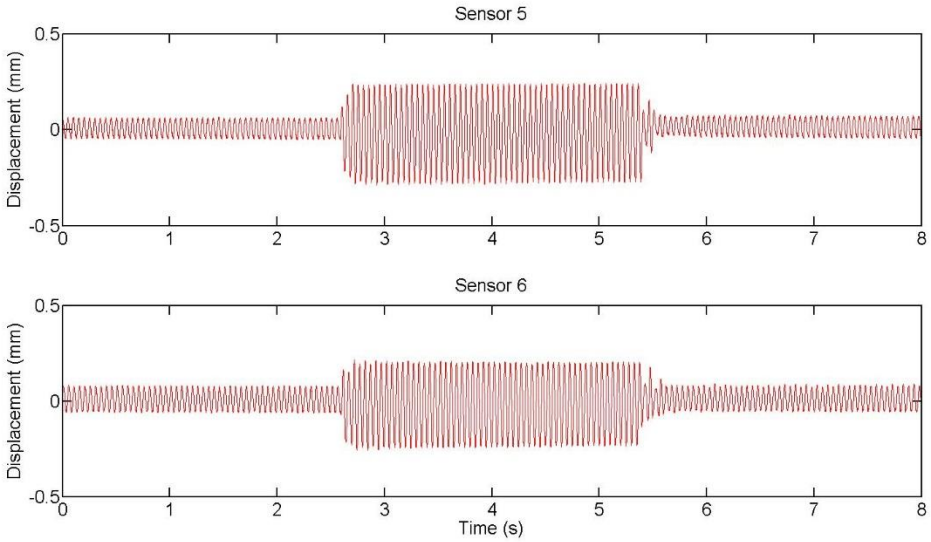

(b) Sensors close to the AMB 2

Figure 6.23 Sensor measurements showing contact recovery when running at 125 rad/s

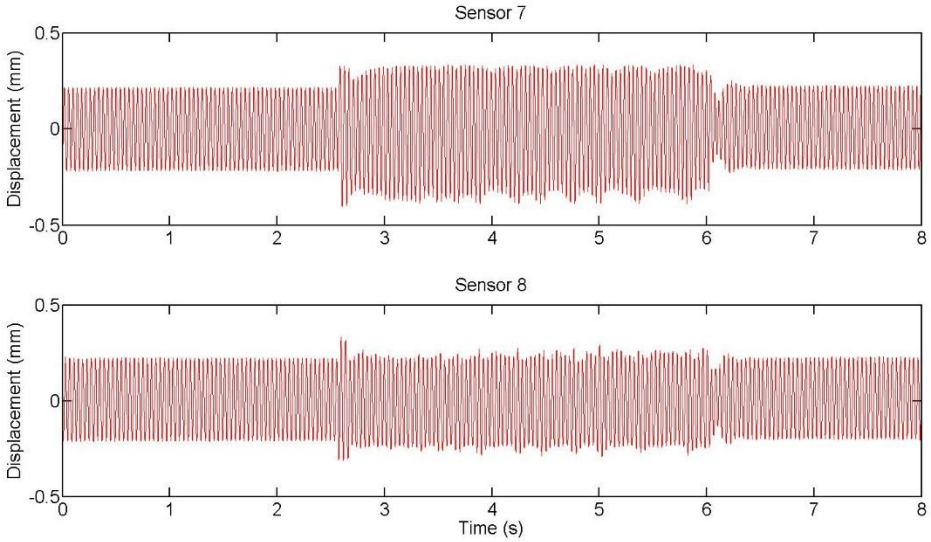

(a) Sensors close to the non-driven end

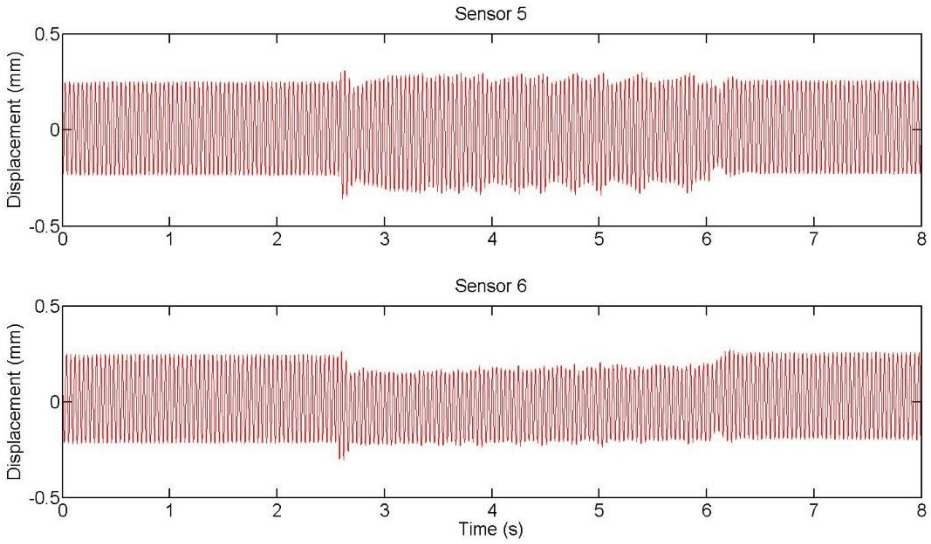

(b) Sensors close to the AMB 2

Figure 6.24 Sensor measurements showing contact recovery when running at 157 rad/s

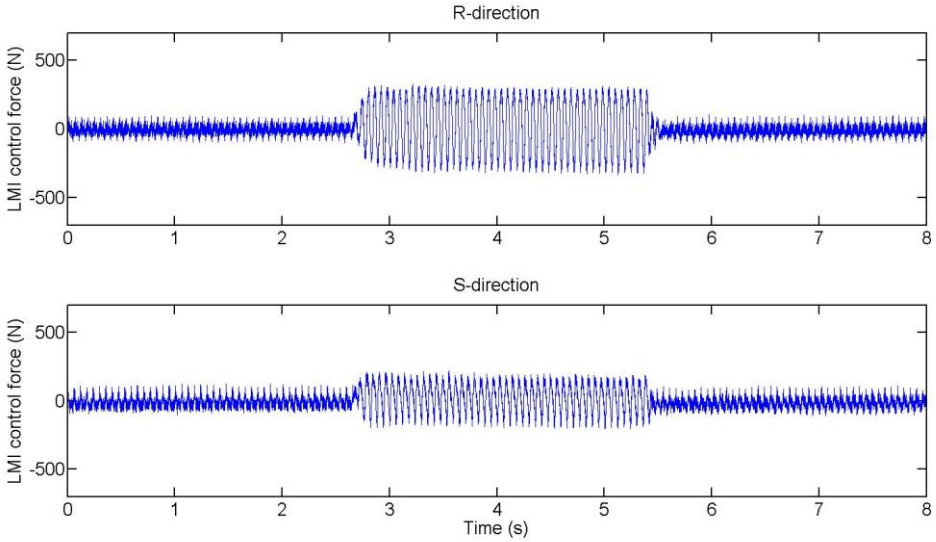

(a) AMB 1

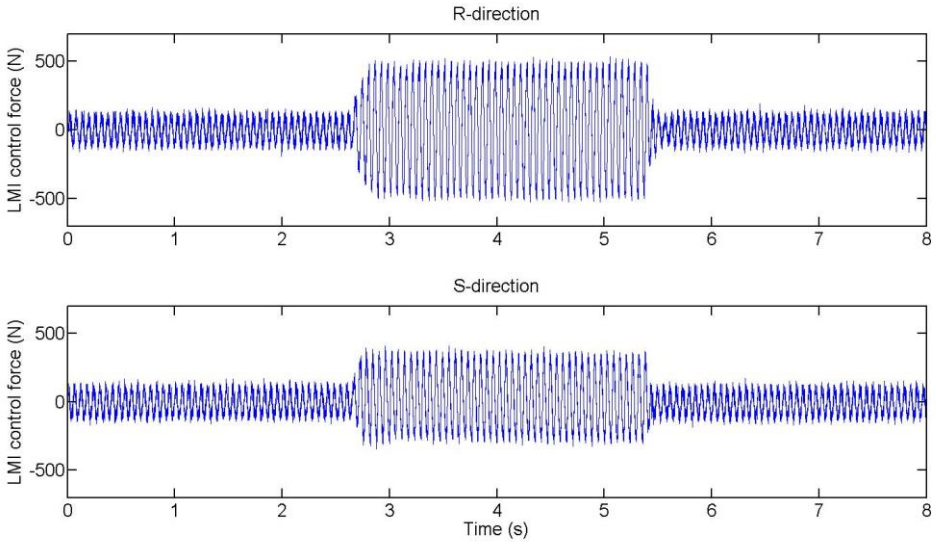

(b) AMB 2

Figure 6.25 Control forces from LMI/PID during contact recovery when running at 107 rad/s

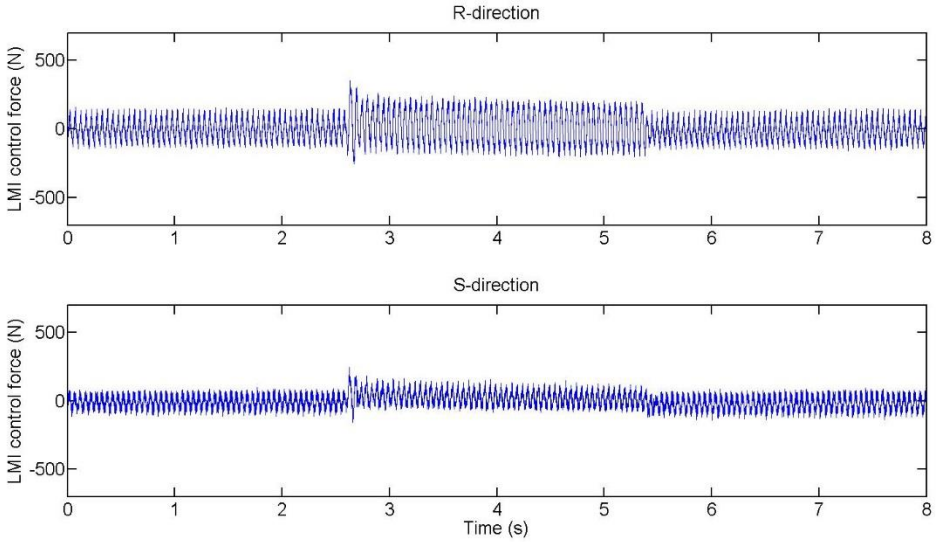

(a) AMB 1

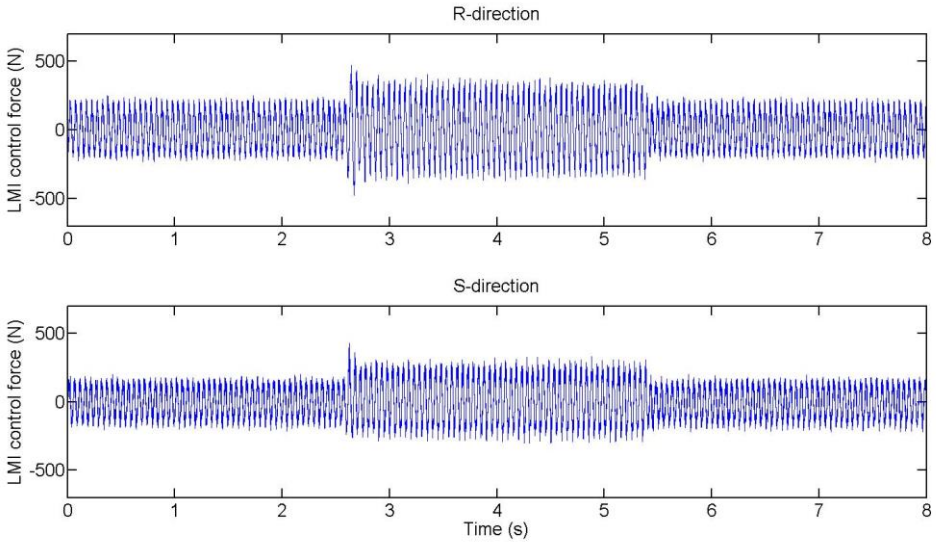

(b) AMB 2

Figure 6.26 Control forces from LMI/PID during contact recovery when running at 125 rad/s

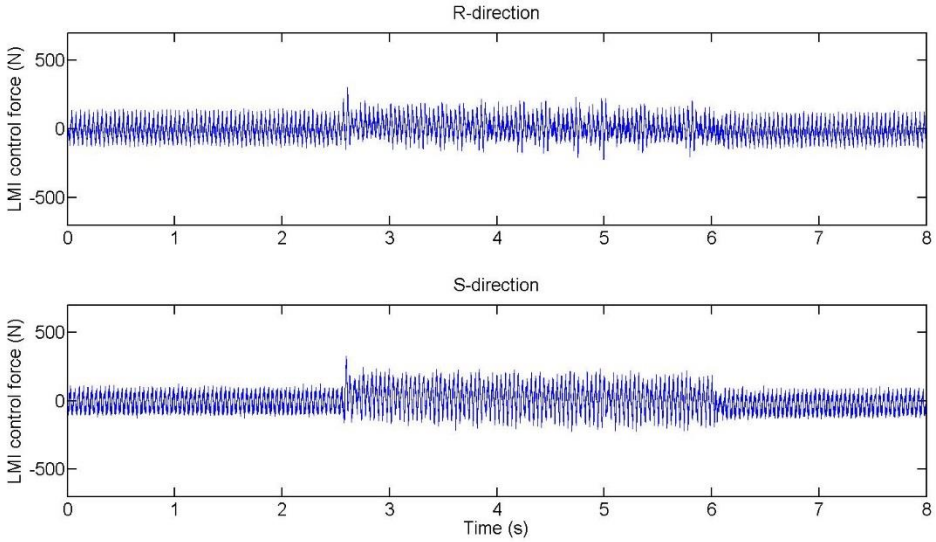

(a) AMB 1

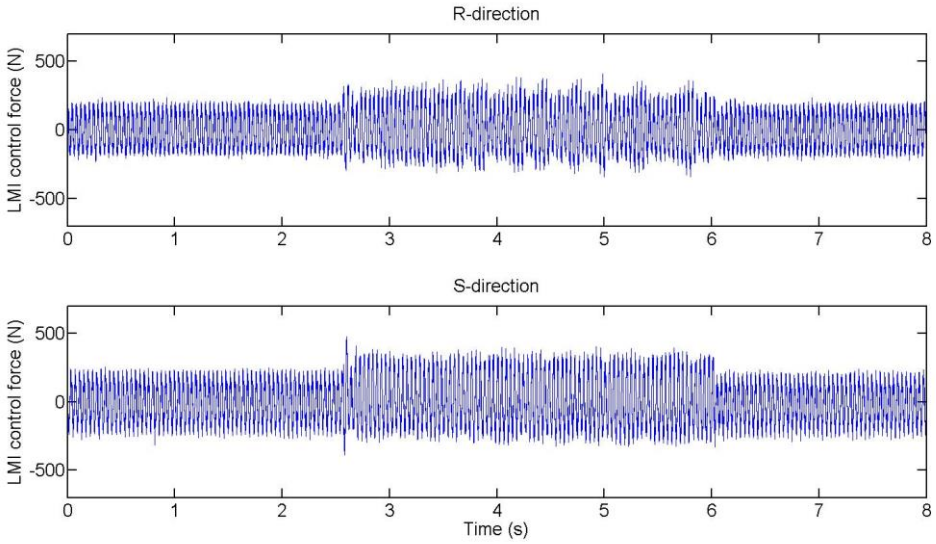

(b) AMB 2

Figure 6.27 Control forces from LMI/PID during contact recovery when running at 157 rad/s

6.3.3 Contact-Free Recovery with 0% Misalignment of TDB under Unbalance 400 g.cm

In order to test the limitation of controller capability, contact recovery was tested when the non-driven end disk unbalance was increased from 260 g.cm to 400 g.cm. In contrast with the unbalance 260 g.cm, the rotor response involved contact issues at lower speeds, and was generally more significant. Contact recovery was tested at three speeds, 100, 113 and 138 rad/s. To reduce the potential for the test rig damage, the contact recovery procedure described in Section 6.3.2 was operated gradually in the rotor releasing action (Step 2); the control action from $\overline{\mathbf{K}}_{c\_2\_d}(k_e)$ was switched off gradually by multiplying a gain (form 1 to 0, with 0.5 decrement).

Figures 6.28-6.29 show the rotor motion plotted in during contact under unbalance 400 g.cm, and then escaping to become contact-free due to LMI control action. Rotor vibration orbits were constrained by non-driven end bushing during contact, compared with those when the non-driven rotor end was free. Contact events were more significant than the unbalance 260 g.cm case. At speeds of 100 and 113 rad/s, controller $\overline{\mathbf{K}}_{c\_2\_d}(k_e)$ centralized the rotor position from contact with TDB, and attenuated rotor vibration effectively (Figures 6.28 and 6.29).

The controller $\overline{\mathbf{K}}_{c\_2\_d}(k_e)$ was insufficient to recover to contact-free operation when rotor running at 138 rad/s. Contact at this speed revealed a bouncing mode with significant impacts, that results in unsteady rotor responses. After activated control action from $\overline{\mathbf{K}}_{c\_2\_d}(k_e)$, significant impacts in contact were eliminated and the rotor entered steady rubbing contact as shown in Figure 6.30.

Figure 6.31 shows the LMI/PID controlled rotor orbits when the non-driven end free as (in blue), and non-driven end bushing (in red). By comparing the red and blue plots, rotor did not recover to a contact-free state since the orbits were still constrained by the non-driven end bushing. Although the contact recovery was unsuccessful at the speed of 138 rad/s, the controller $\overline{\mathbf{K}}_{c\_2\_d}(k_e)$ improved the rotor

response under contact as a steady rubbing mode. That may reduce the potential damage induced by significant impacts involved in bouncing contact.

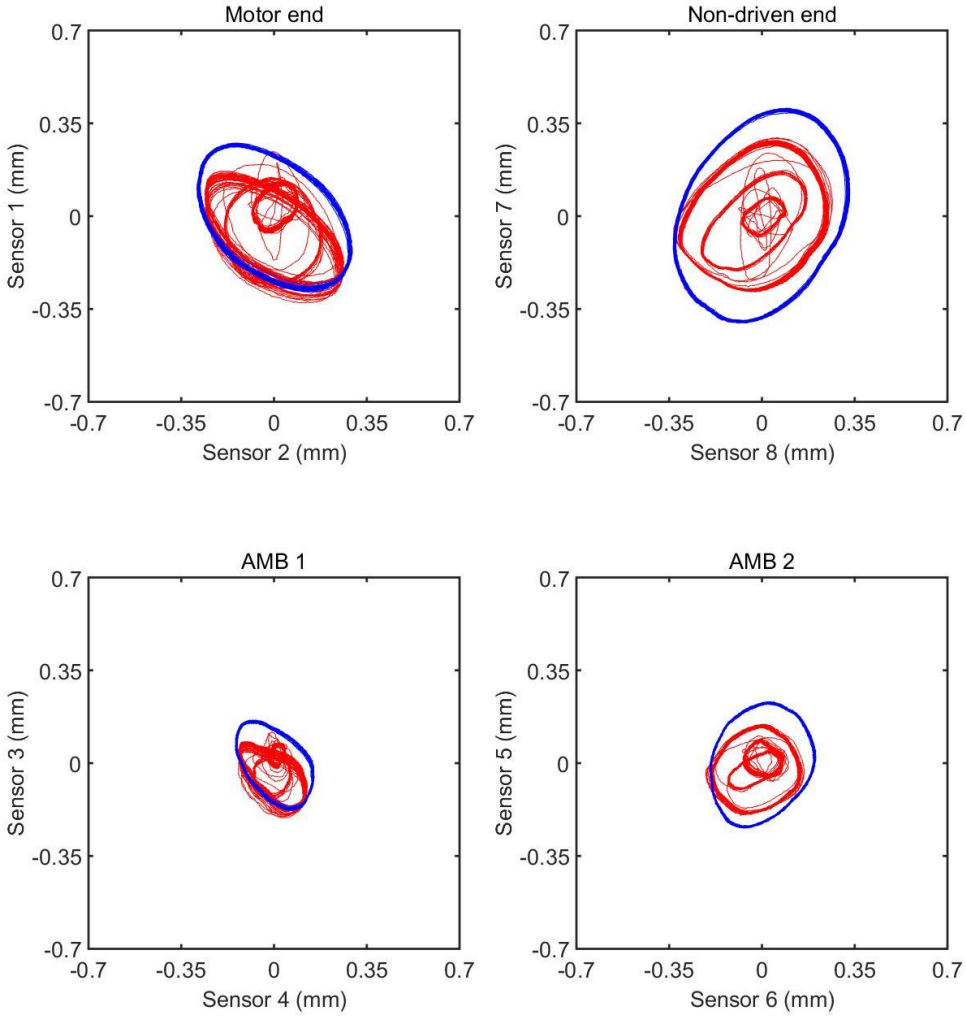

Figure 6.28 Measured orbits running at 100 rad/s: PID control with non-driven end free is shown in blue. LMI/PID control is shown in red.

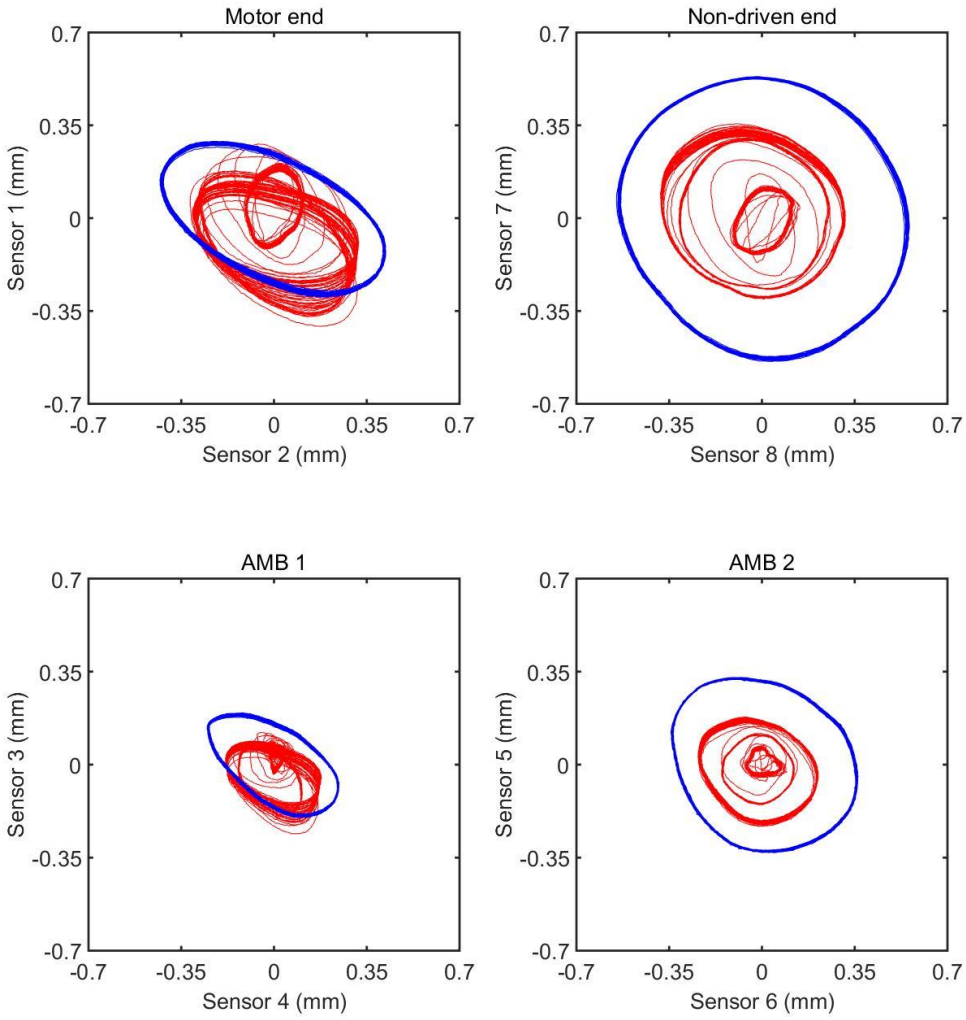

Figure 6.29 Measured orbits running at 113 rad/s: PID control with non-driven end free is shown in blue. LMI/PID control is shown in red.

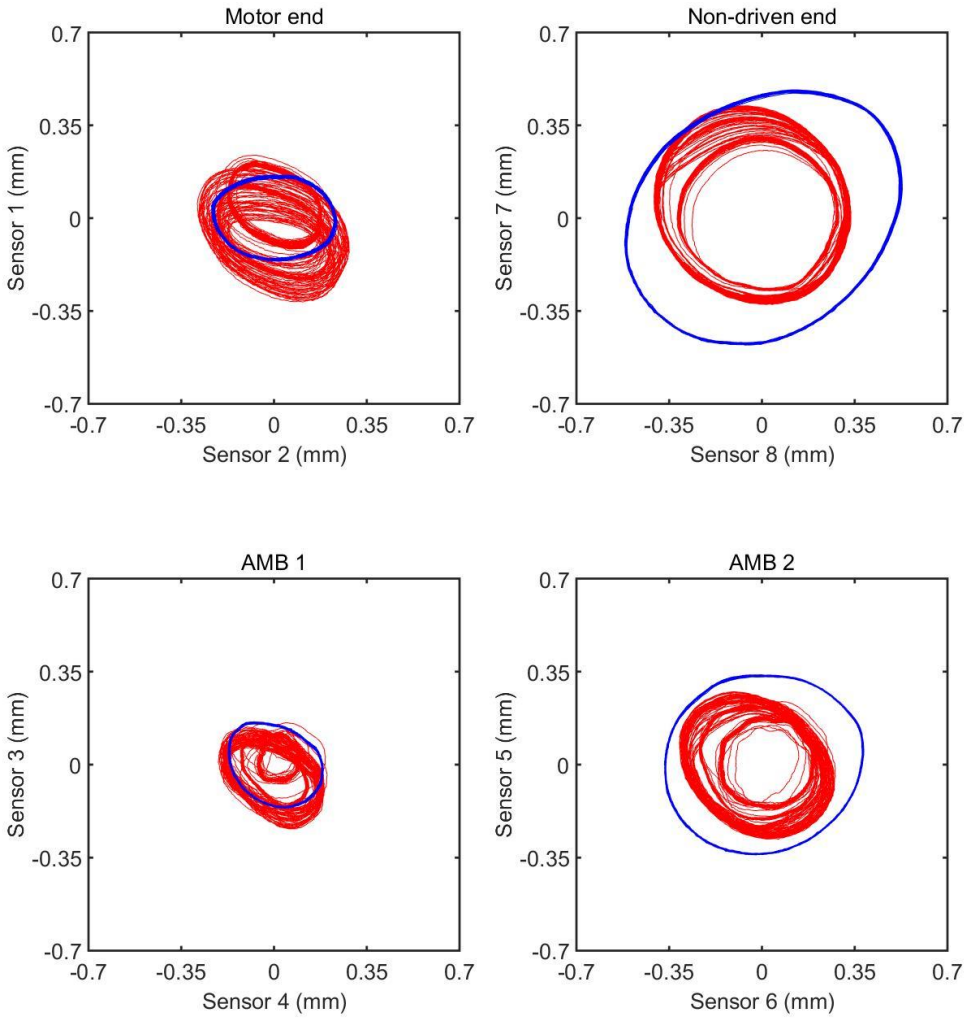

Figure 6.30 Measured orbits running at 138 rad/s: PID control with non-driven end free is in blue. LMI/PID control is shown in red.

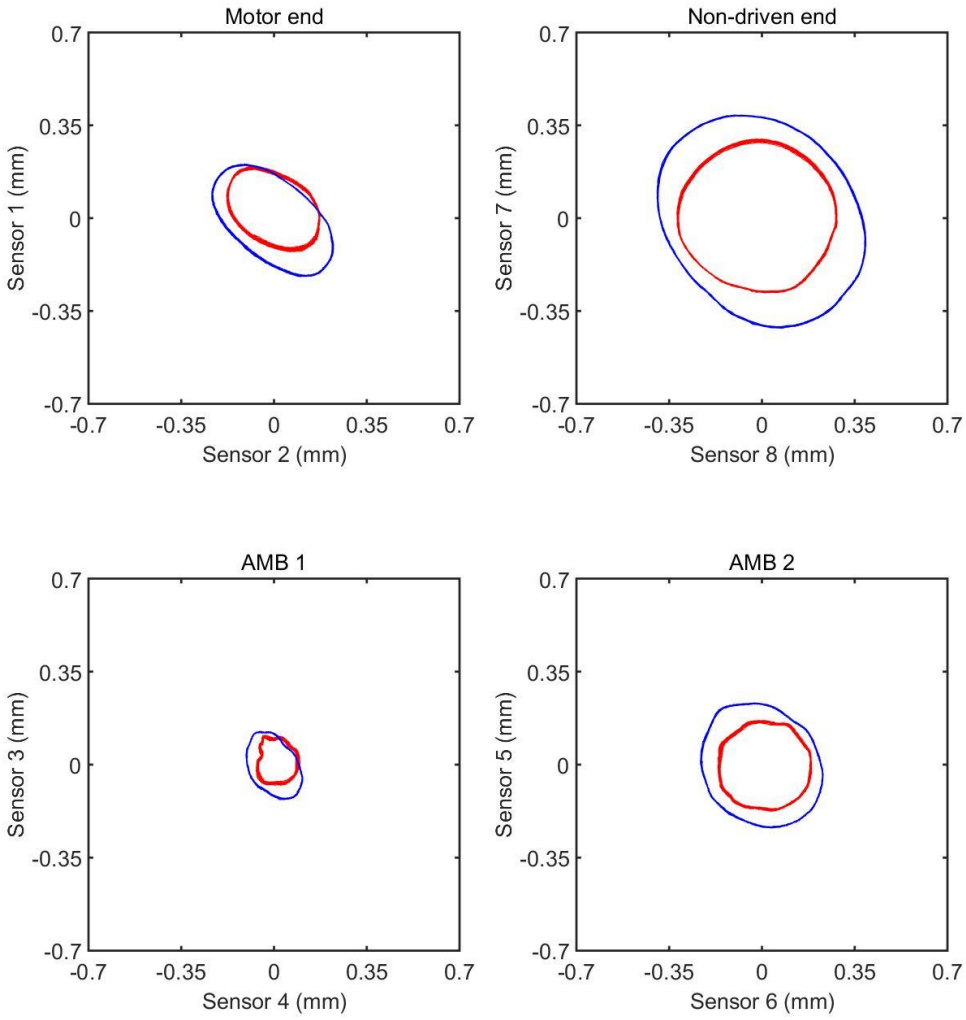

Figure 6.31 Measured orbits running at 138 rad/s: LMI/PID controlled rotor orbit when non-driven end free as shown in blue, LMI/PID controlled rotor orbit when non-driven end bushing as shown in red

The gradual releasing procedure used in case of unbalance 400 g.cm, is shown further in accelerometer measurements and inferred acceleration induced by contact as shown in Figures 6.32-6.34. In contrast with those shown in Figures 6.19-6.20, larger amplitudes of inferred acceleration indicate that contact events were more significant under the unbalance of 400 g.cm. Releasing was operated at 2.5 s and finished around 3.6 s, and no response was seen in predicted contact acceleration during such processing as shown in Figures 6.32 and 6.33. This indicates the contact did not occur until the rotor was fully released (control action from $\overline{\mathbf{K}}_{c\_2\_d}(k_e)$ was full enabled).

The inferred acceleration induced by contact was not eliminated when control action was applied, but became steady response by comparing the 'PID only' period shown in Figure 6.34. That may also demonstrate the contact condition was improved by the controller $\overline{\mathbf{K}}_{c\_2\_d}(k_e)$, even through the rotor was not recovered to a contact-free state.

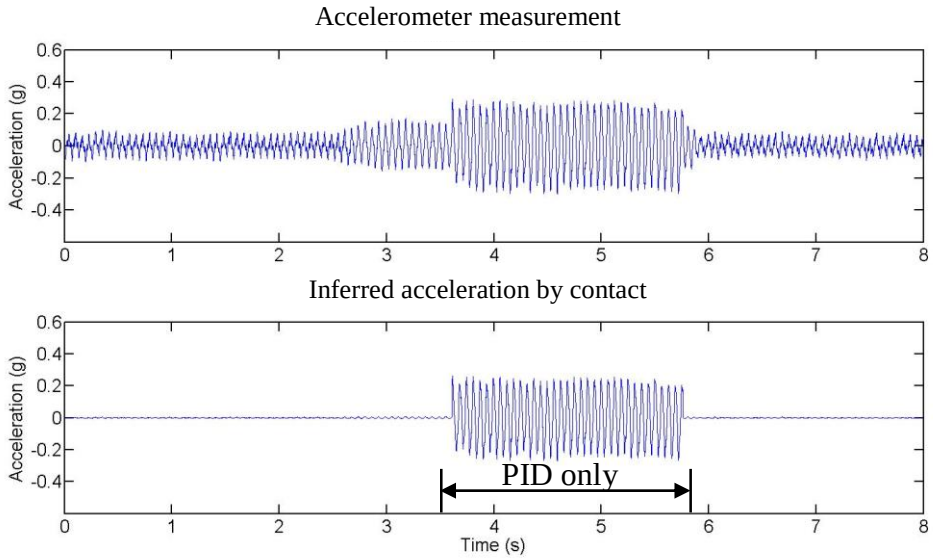

Figure 6.32 Accelerometer measurements and inferred acceleration caused by contact, running at 100 rad/s

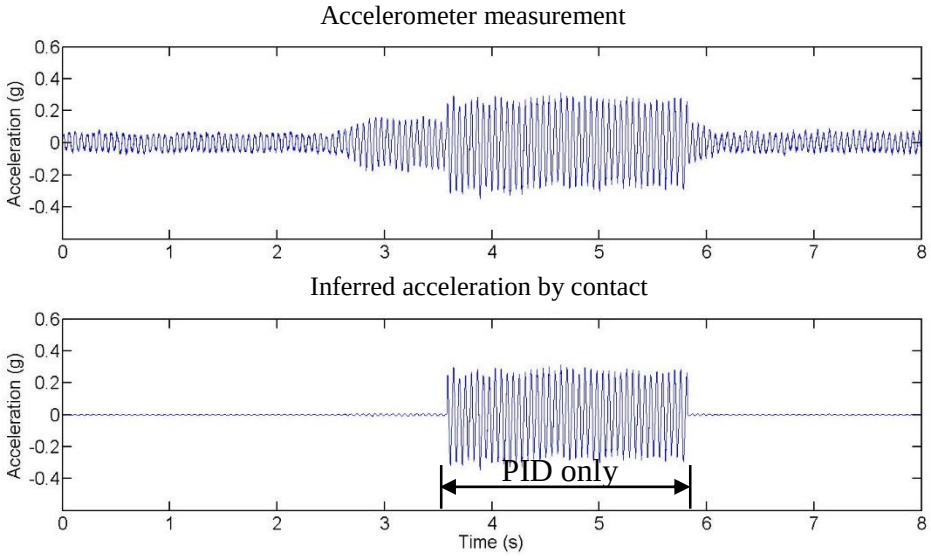

Figure 6.33 Accelerometer measurements and inferred acceleration caused by contact, running at 113 rad/s

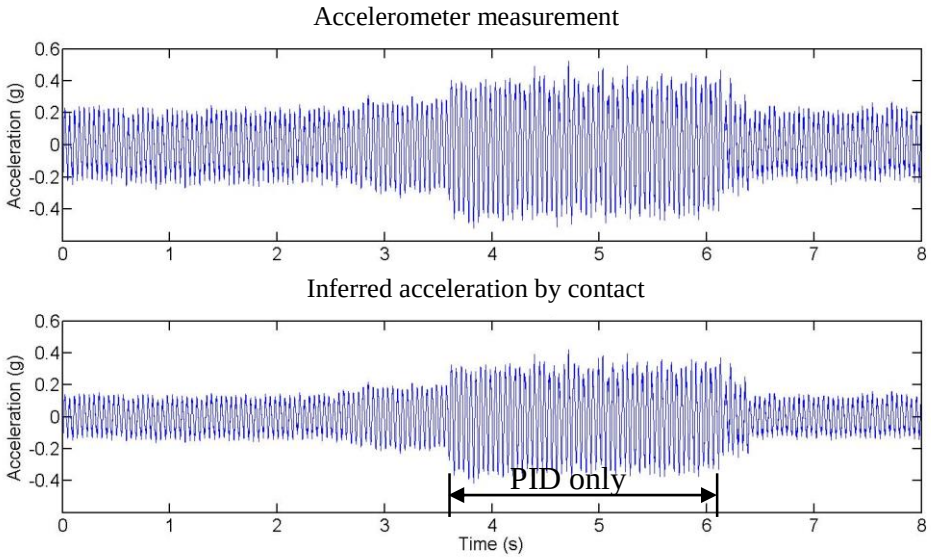

Figure 6.34 Accelerometer measurements and inferred acceleration caused by contact, running at 138 rad/s

Figures 6.35-6.37 show the rotor response in the time domain during the whole contact recovery procedure. Figures 6.38-6.40 show corresponding control forces from the LMI gain-scheduling controller $\overline{\mathbf{K}}_{c\_2\_d}(k_e)$ in R/S coordinates.

Similar as the case with the unbalance of 260 g.cm, the LMI controller enabled the rotor to escape from contact effectively with good transient performance as shown in Figures 6.35-6.37. From sensor measurements shown in Figure 6.37, bouncing during contact is evident, which may have a directional bias, and it was eliminated when LMI control action was activated again.

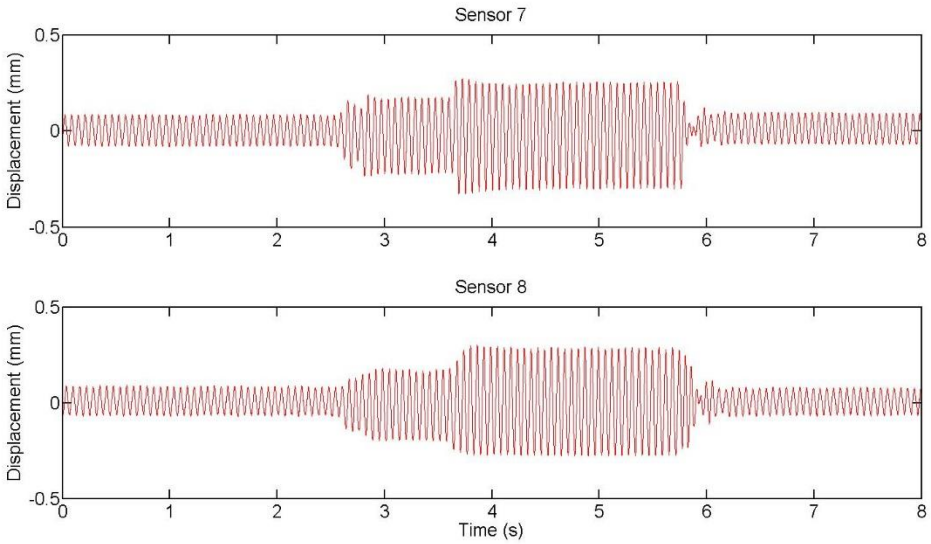

(a) Sensors closed to the non-driven end

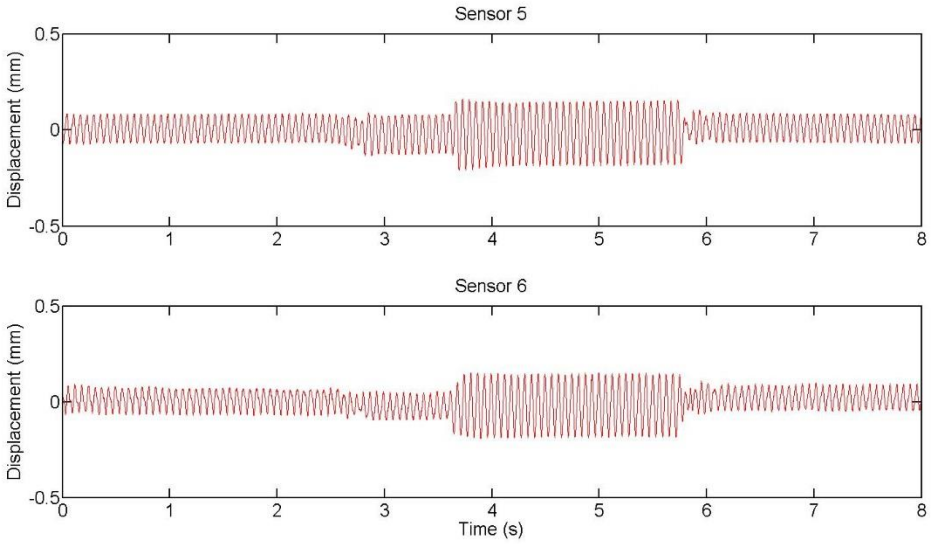

(b) Sensors close to AMB 2

Figure 6.35 Sensors measurements when running at 100 rad/s

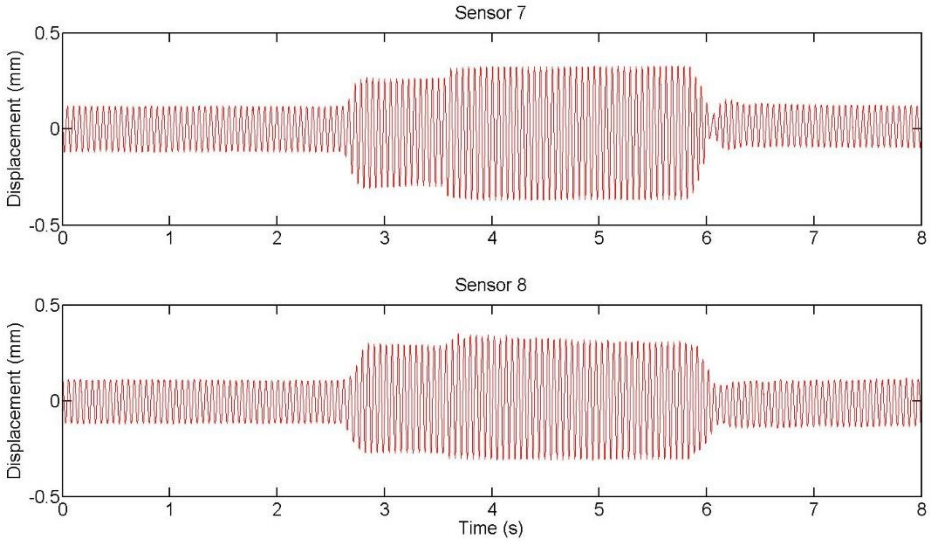

(a) Sensors close to the non-driven end

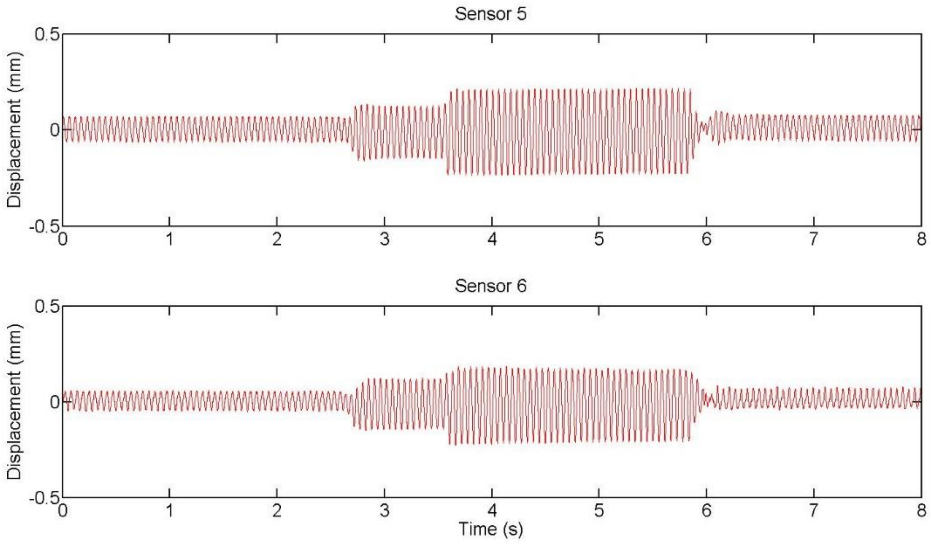

(b) Sensors close to AMB 2

Figure 6.36 Sensors measurements when running at 113 rad/s

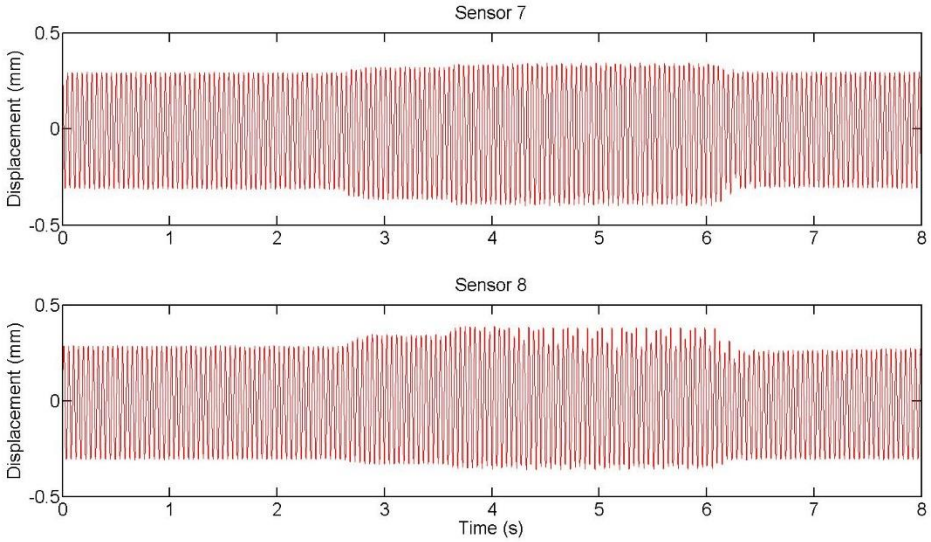

(a) Sensors close to the non-driven end

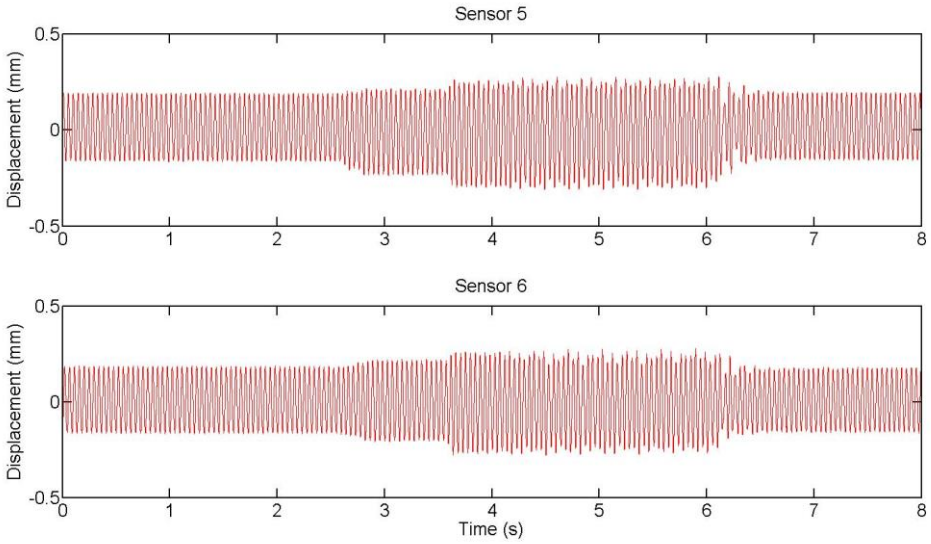

(b) Sensors close to the AMB 2

Figure 6.37 Sensors measurements when running at 138 rad/s

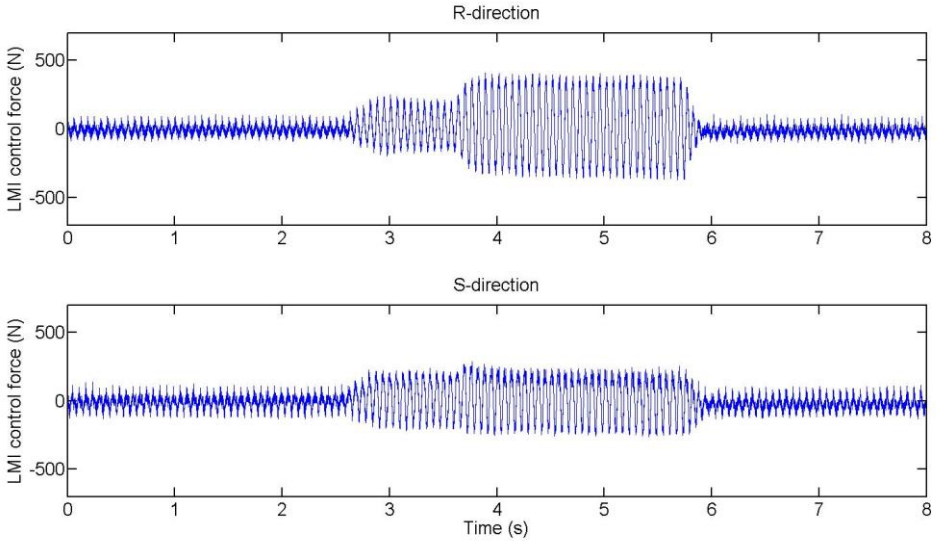

(a) AMB 1

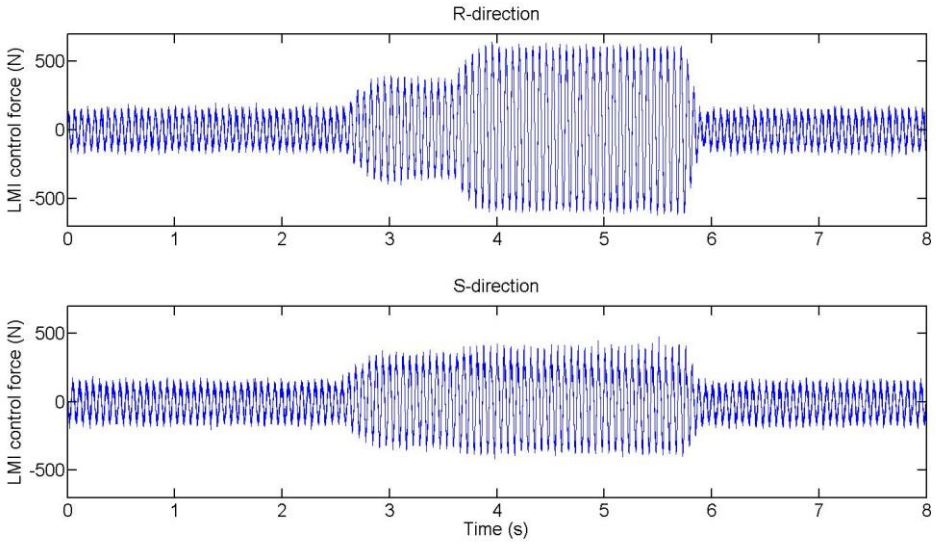

(b) AMB 2

Figure 6.38 Control forces from LMI/PID when running at 100 rad/s

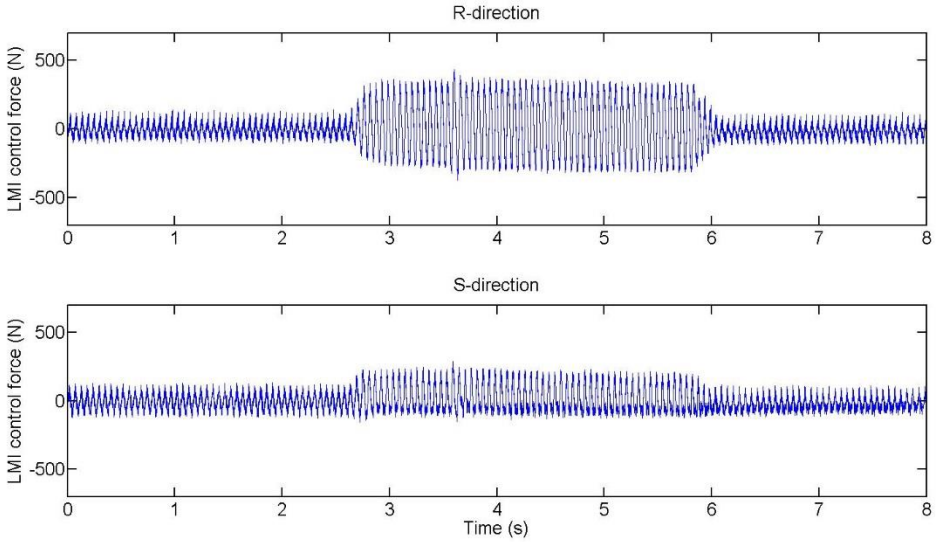

(a) AMB 1

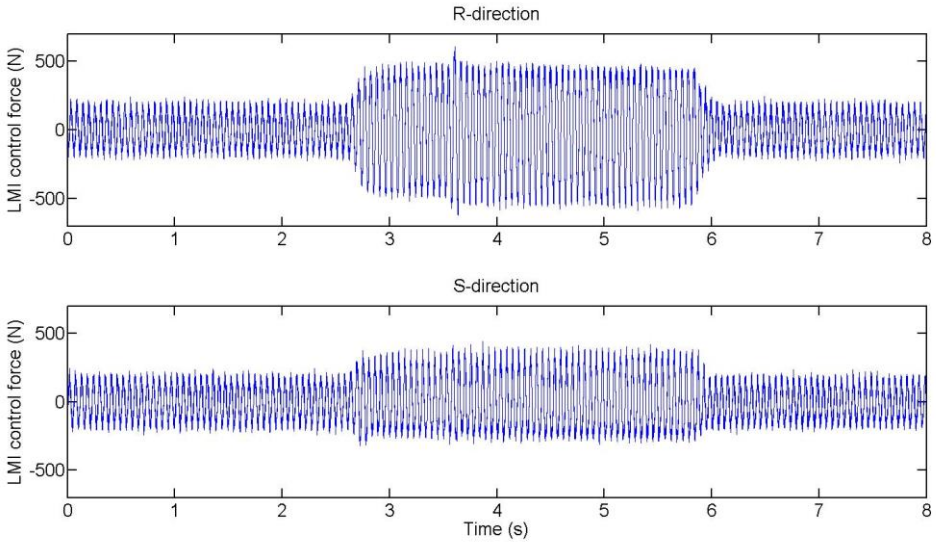

(b) AMB 2

Figure 6.39 Control forces from LMI/PID when running at 113 rad/s

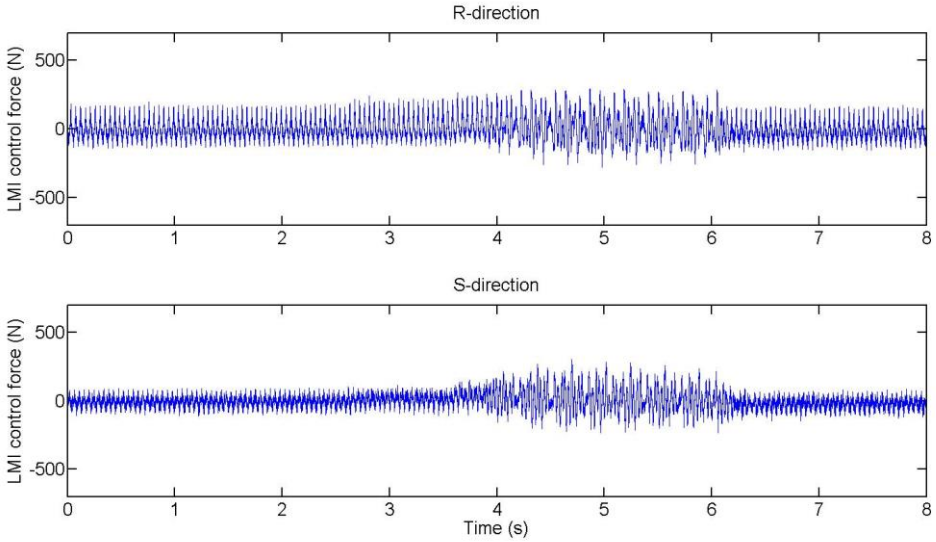

(a) AMB 1

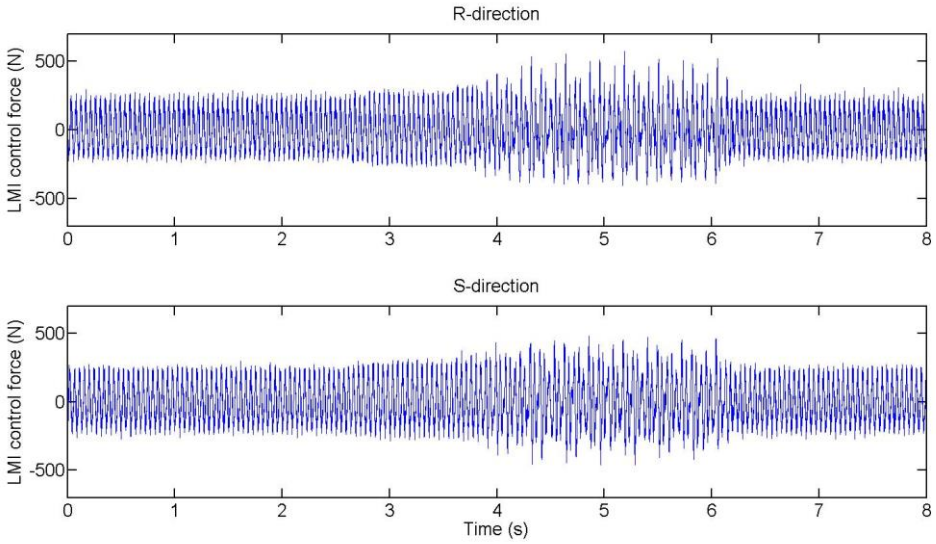

(b) AMB 2

Figure 6.40 Control forces from LMI/PID when running at 138 rad/s

6.3.4 Contact-Free Recovery with 50% Misalignment of Touchdown Bushing under Unbalance 220 g.cm

In this section, the rotor was run with the non-driven end disk unbalance of 220 g.cm. The controller's capability to recover contact-free operation was assessed for speeds 113, 132 and 145 rad/s, when the non-driven end TDB had 50% vertical misalignment. Due to reduced clearance (minimum 0.2 mm), the contact-free recovery procedure relies on control action. The contact recovery procedure is operated in steps as same as in the case shown in Section 6.3.2.

Figures 6.41-6.43 show the rotor motion (in red) during contact with 50% non-driven end bushing misaligned and then escaping to become contact free due to LMI control action. PID controlled rotor responses when the rotor non-driven end free, are shown in blue. The results shown in Figure 6.9 indicate that the contact occurred above 113 rad/s rotational speed. Due to the TDB misalignment, there was slight contact at the rotor non-driven end, with significant vibrations transmitted to the motor end (Figures 6.41-6.43). The contact is observed in the elliptical orbits shapes. This asymmetric rotor displacement under contact, became much more obvious with increased running speed as can be seen in Figures 6.42 and 6.43 at 132 rad/s and 145 rad/s, respectively.

Controller $\overline{\mathbf{K}}_{c\_2\_d}(k_e)$ enabled recovery to a contact-free state in each of these typical speeds. At 113 rad/s, rotor position was centralized when LMI control force was implemented after the release used to initiate contact in speed 113 rad/s. The controller $\overline{\mathbf{K}}_{c\_2\_d}(k_e)$ tended to reshape rotor orbits to become circular, by reducing the larger displacements.

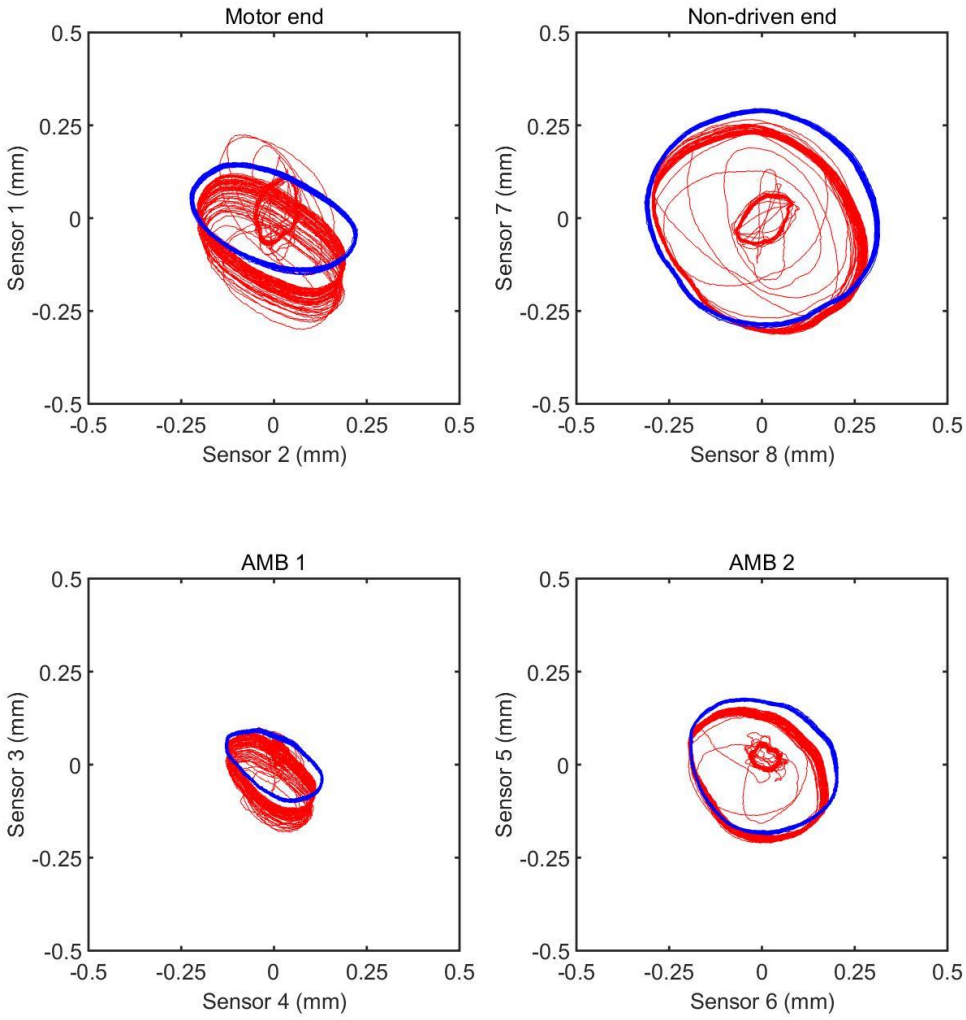

Figure 6.41 Measured orbits with 50% misalignment running at 113 rad/s: PID control with non-driven end free (blue), LMI/PID control is indicated in red.

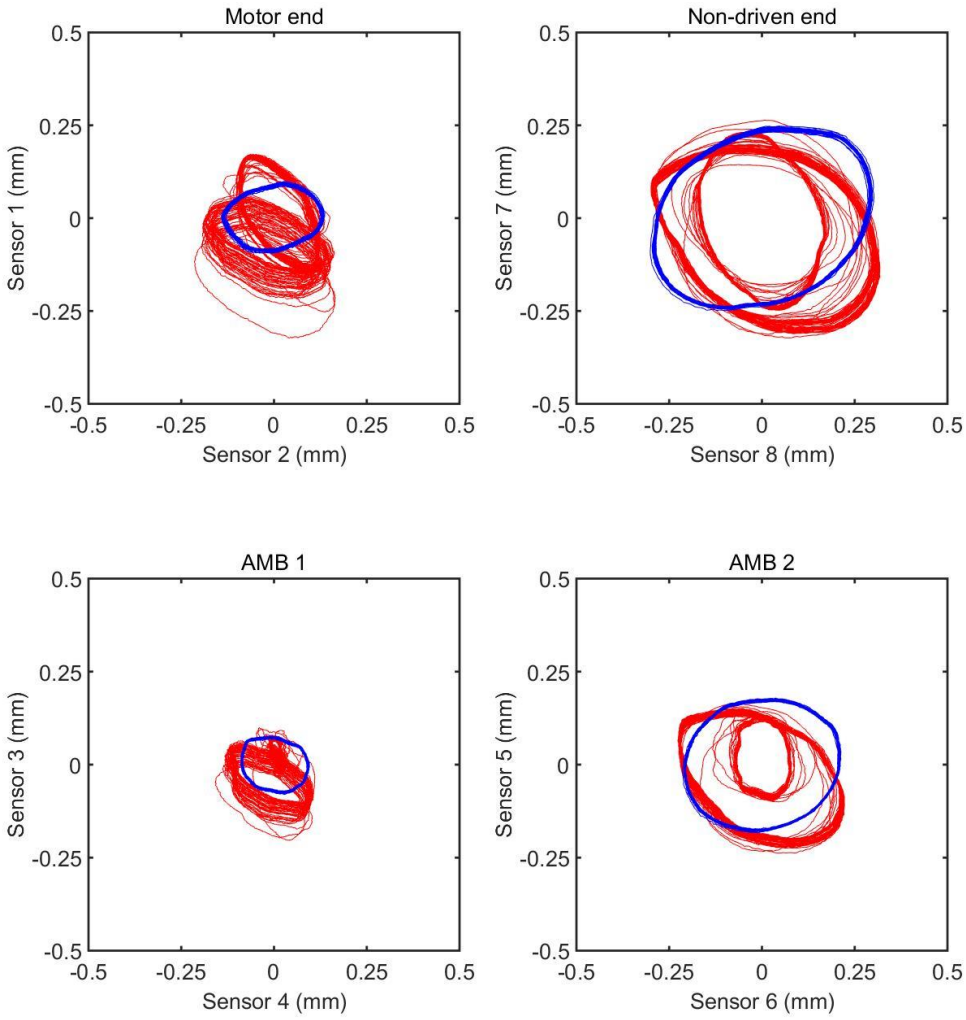

Figure 6.42 Measured orbits with 50% misalignment running at 132 rad/s: PID control with non-driven end free (blue), LMI/PID control is indicated in red.

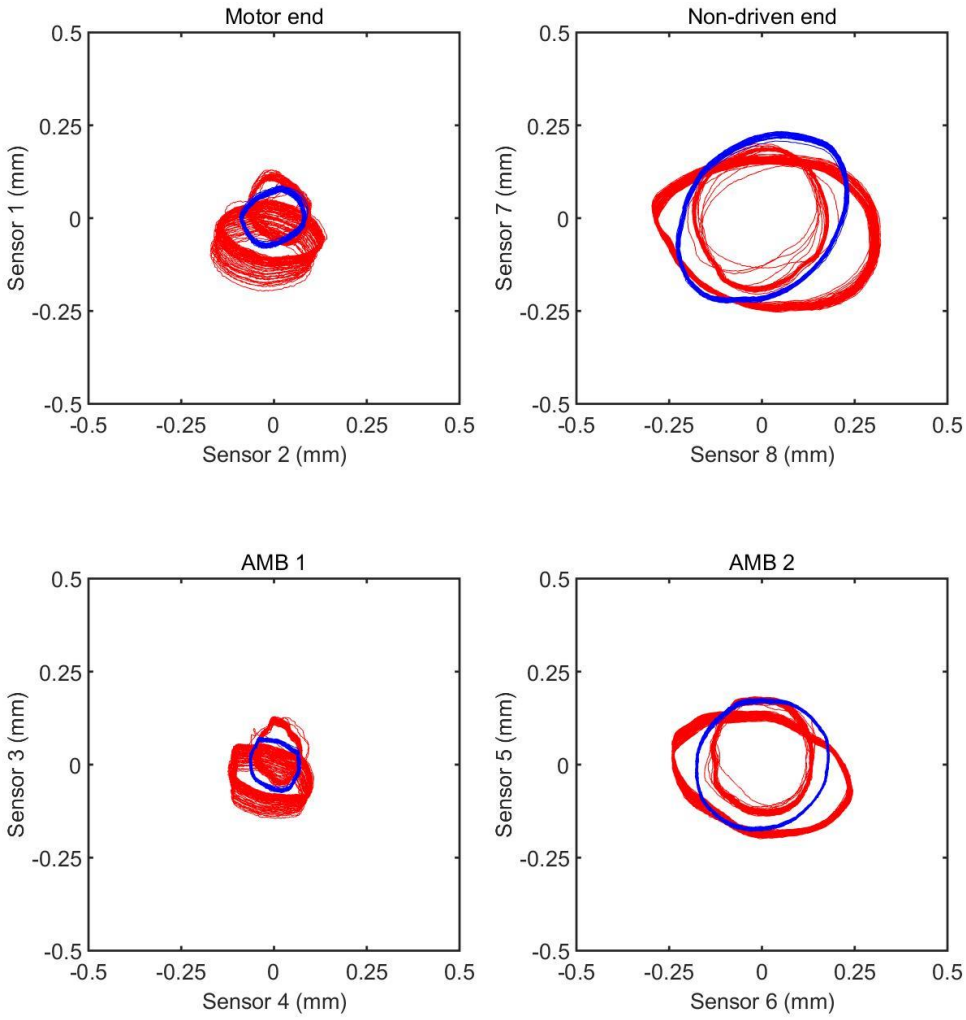

Figure 6.43 Measured orbits with 50% misalignment running at 145 rad/s: PID control with non-driven end free (blue), LMI/PID control is indicated in red.

The accelerometer measurements and inferred acceleration induced by contact at the three speeds are shown in Figures 6.44-6.46. From the inferred acceleration induced by contact, the rotor came into contact with the bushing more smoothly at 113 rad/s as shown in Figure 6.44. However, transient overshoot is evident at 132 rad/s and 145 rad/s. Some bouncing is observed at 132 rad/s and 145 rad/s. Successful contact-free recovery by the LMI gain-scheduling control is also demonstrated by the elimination in the inferred acceleration signal.

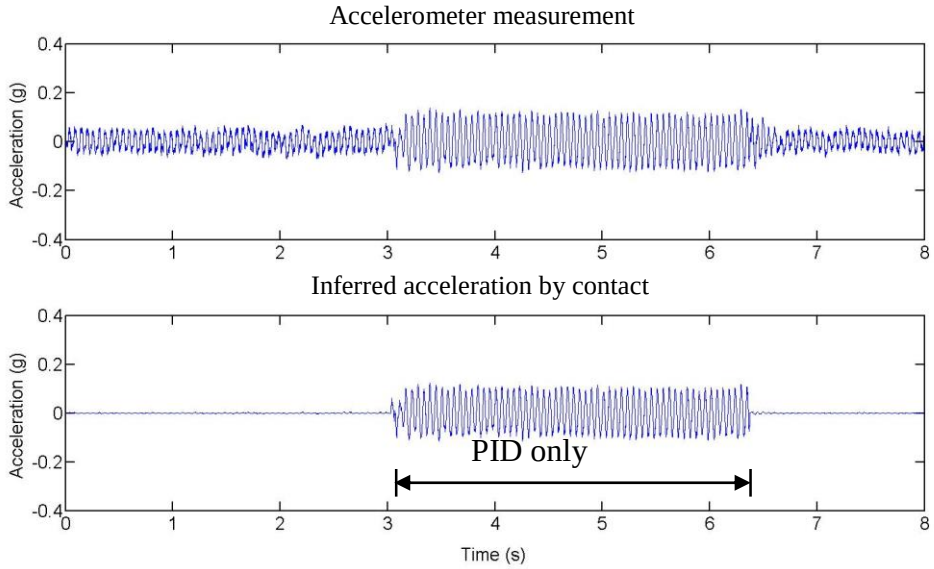

Figure 6.44 Accelerometer measurements and inferred acceleration caused by contact, running at 113 rad/s

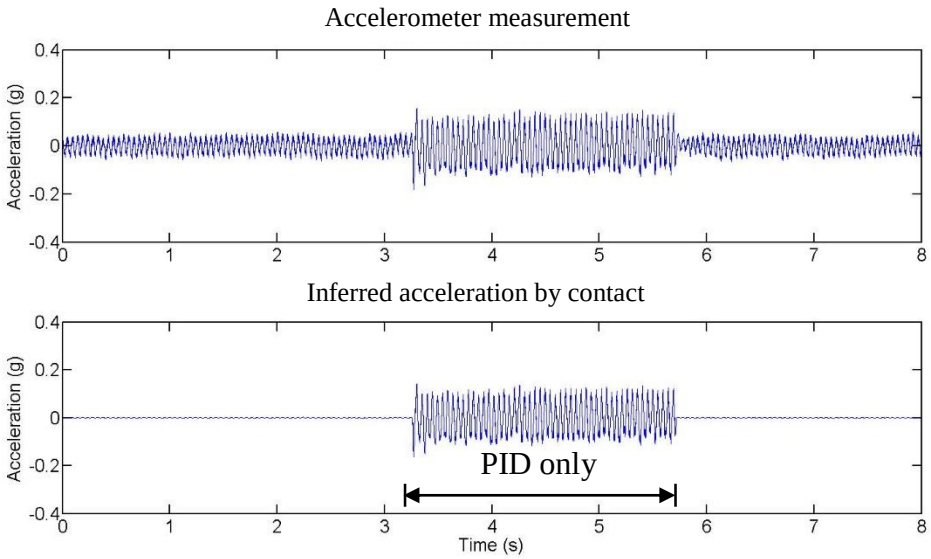

Figure 6.45 Accelerometer measurements and inferred acceleration caused by contact, running at 132 rad/s

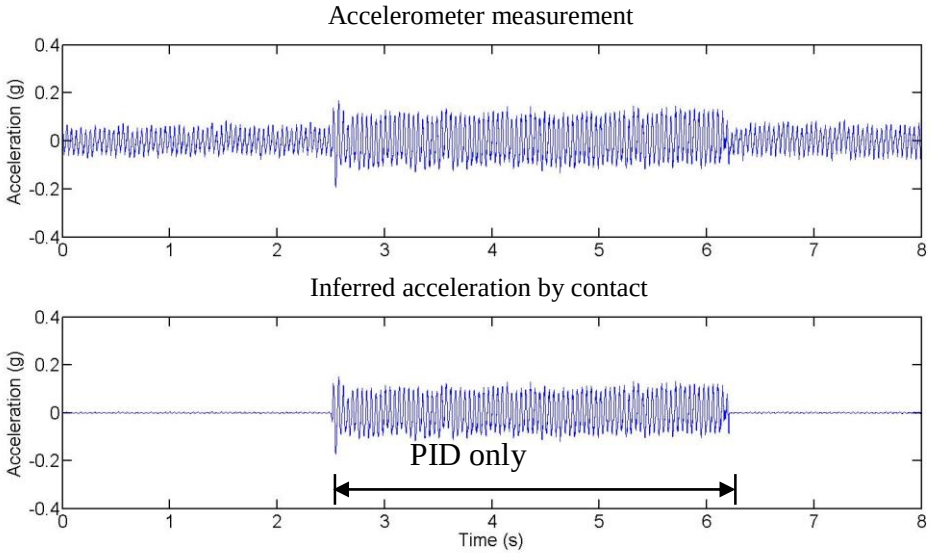

Figure 6.46 Accelerometer measurements and inferred acceleration caused by contact, running at 145 rad/s

Figures 6.47-6.49 show the displacement sensor measurements during contact-free recovery at different speeds. The LMI controller is effective with low transients in restoring contact-free operation. The asymmetric displacements due to bushing misalignment, have been corrected into more central orbits by the LMI control action. The control forces in R/S coordinates shown in Figure 6.50-6.52 also demonstrate that the model based LMI gain-scheduling controller actuated the rotor with asymmetric control forces to enable the rotor to escape from trapped contact.

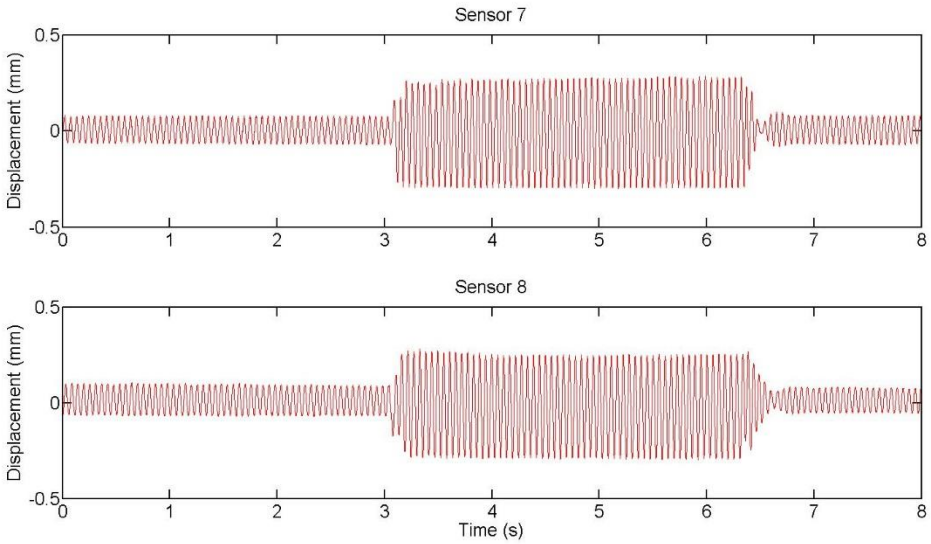

(a) Sensors located close to the non-driven end

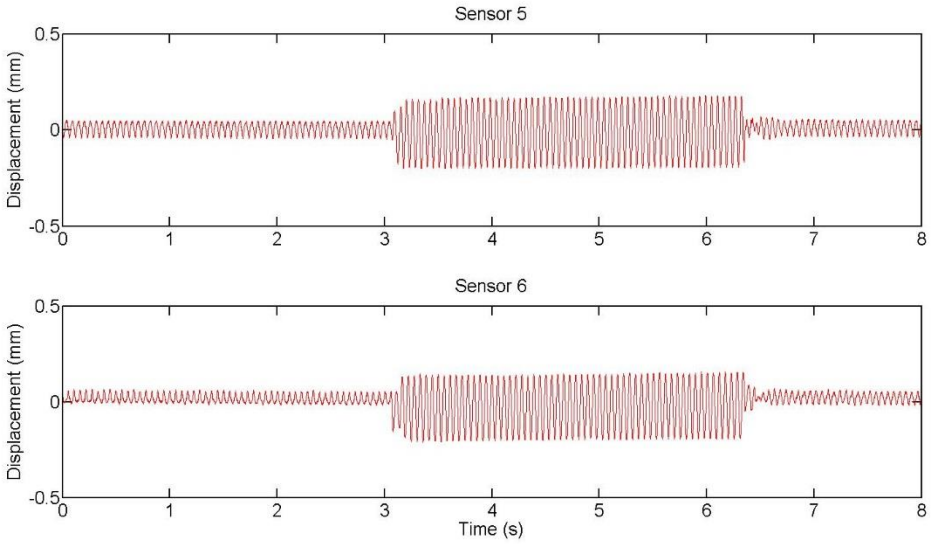

(b) Sensors located close to AMB 2

Figure 6.47 Sensors measurements when running at 113 rad/s

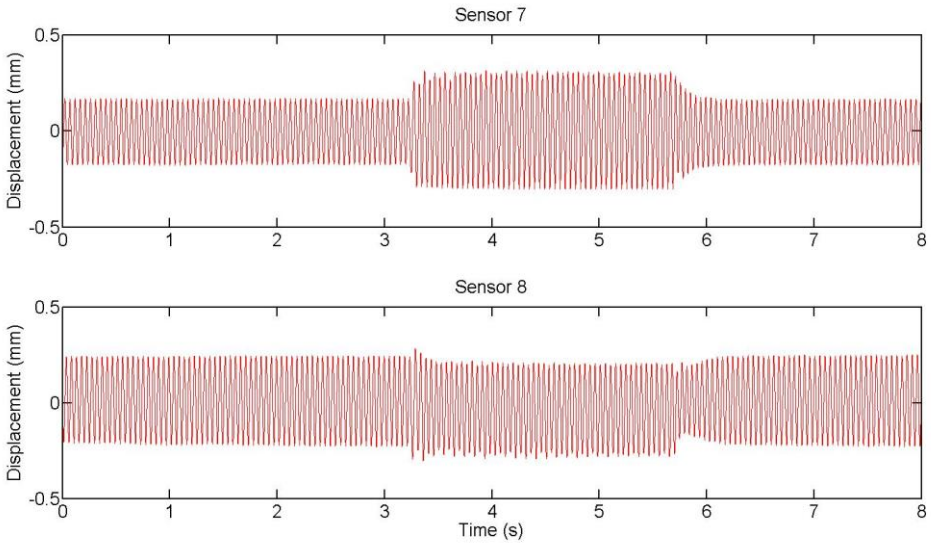

(a) Sensors located close to the non-driven end

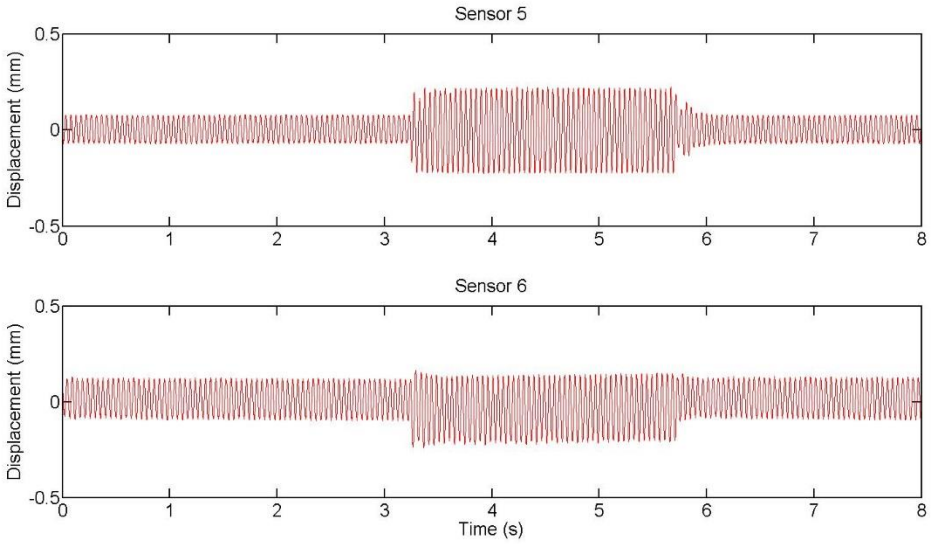

(b) Sensors located close to AMB 2

Figure 6.48 Sensors measurements when running at 132 rad/s

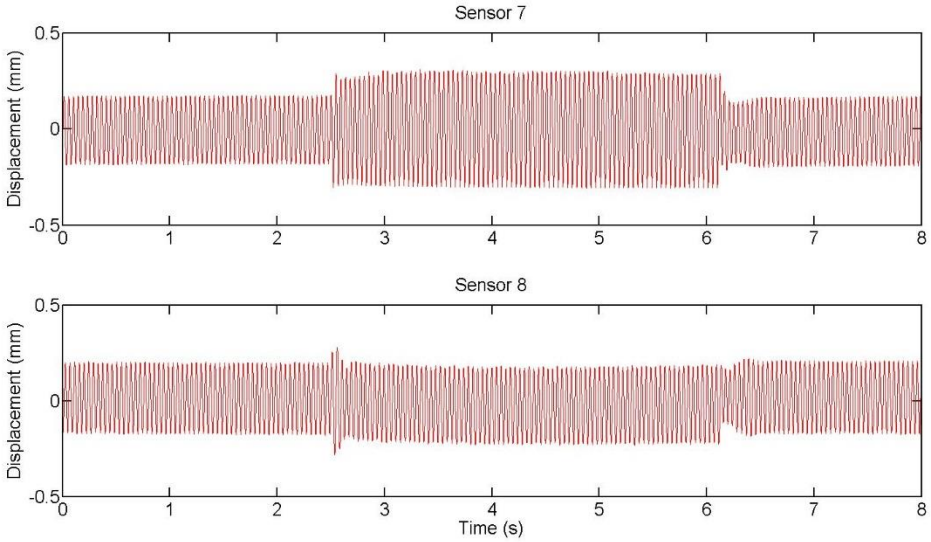

(a) Sensors located close to the non-driven end

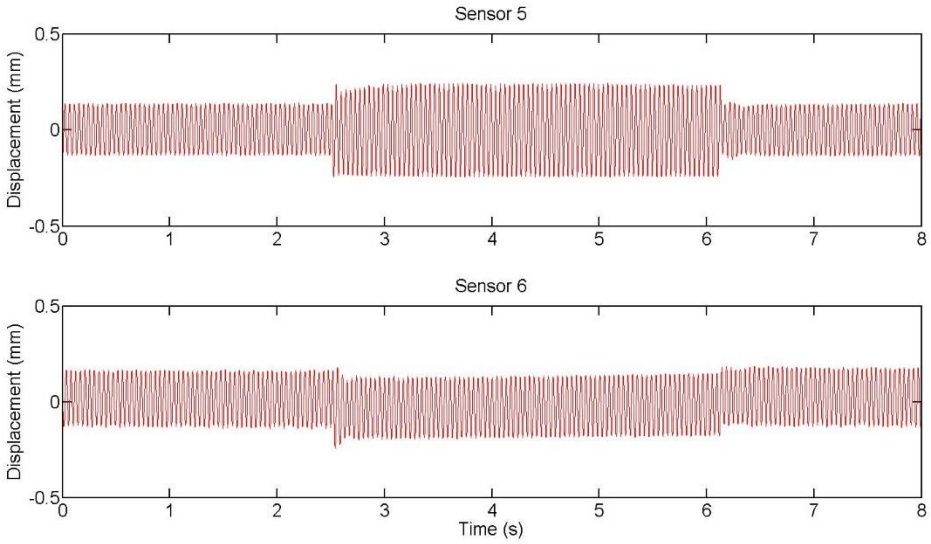

(b) Sensors located close to AMB 2

Figure 6.49 Sensors measurements when running at 145 rad/s

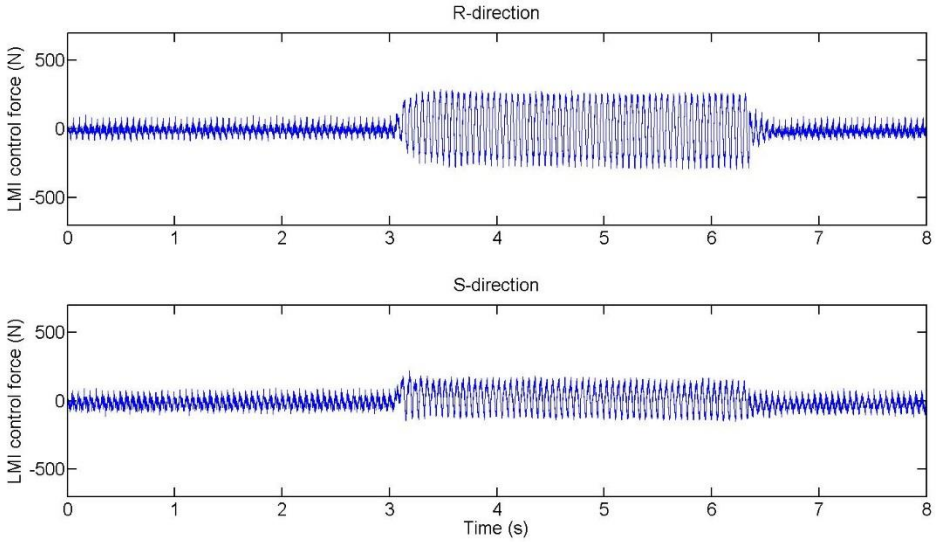

(a) AMB 1

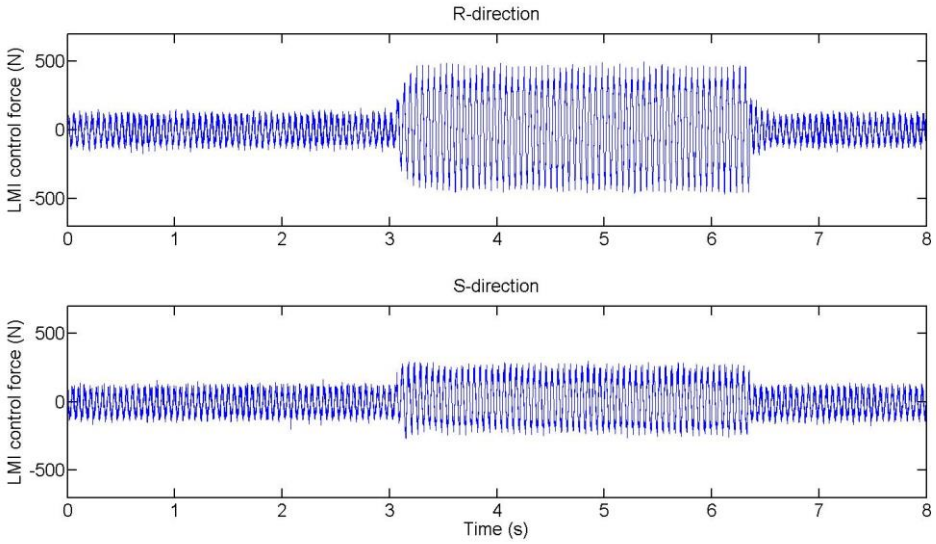

(b) AMB 2

Figure 6.50 Control forces from LMI /PID when running at 113 rad/s

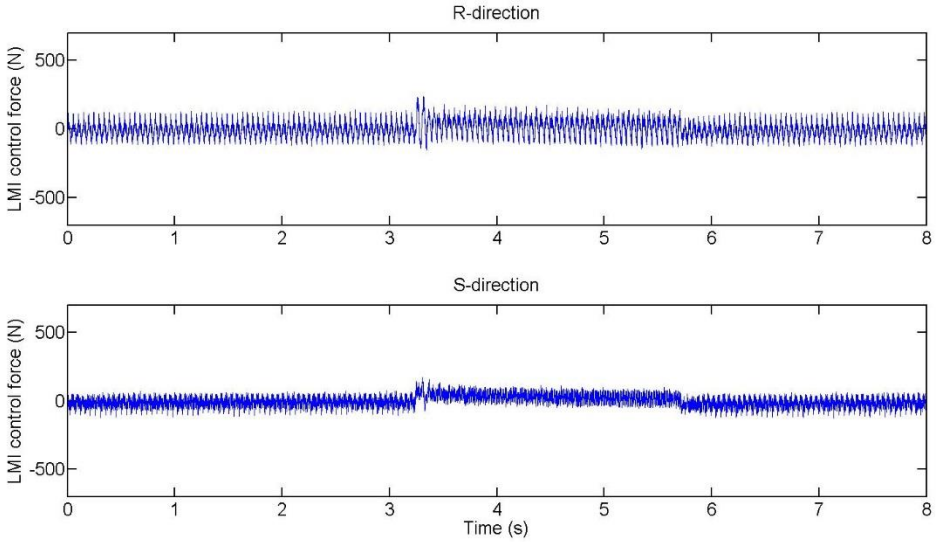

(a) AMB 1

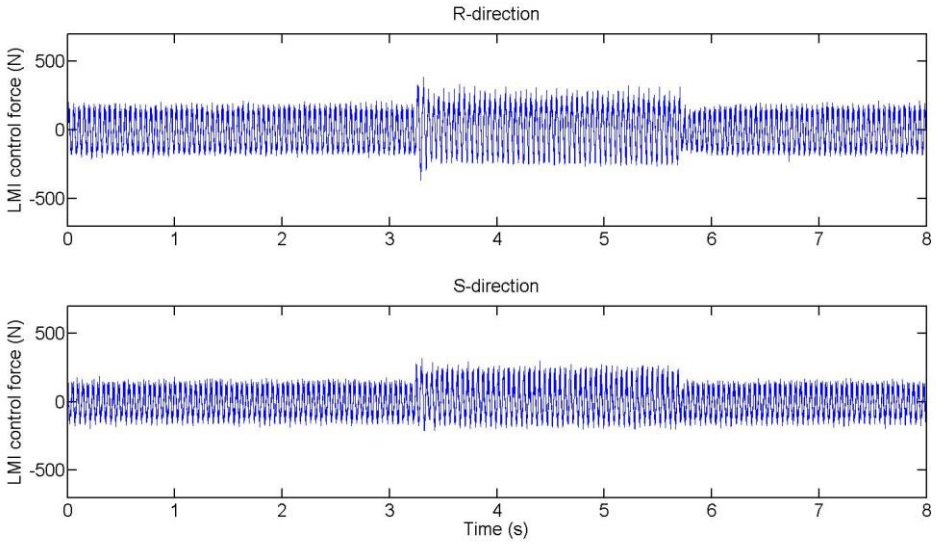

(b) AMB 2

Figure 6.51 Control forces from LMI/PID when running at 132 rad/s

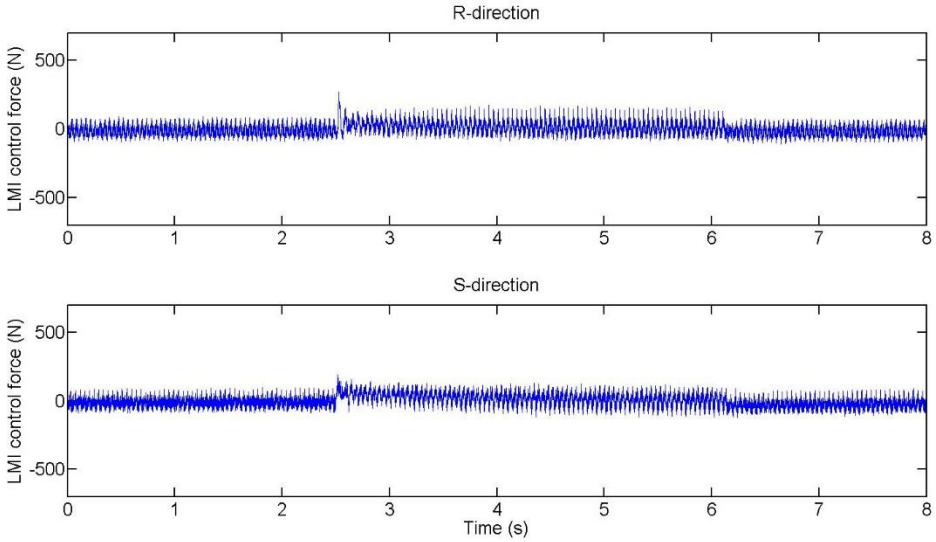

(a) AMB 1

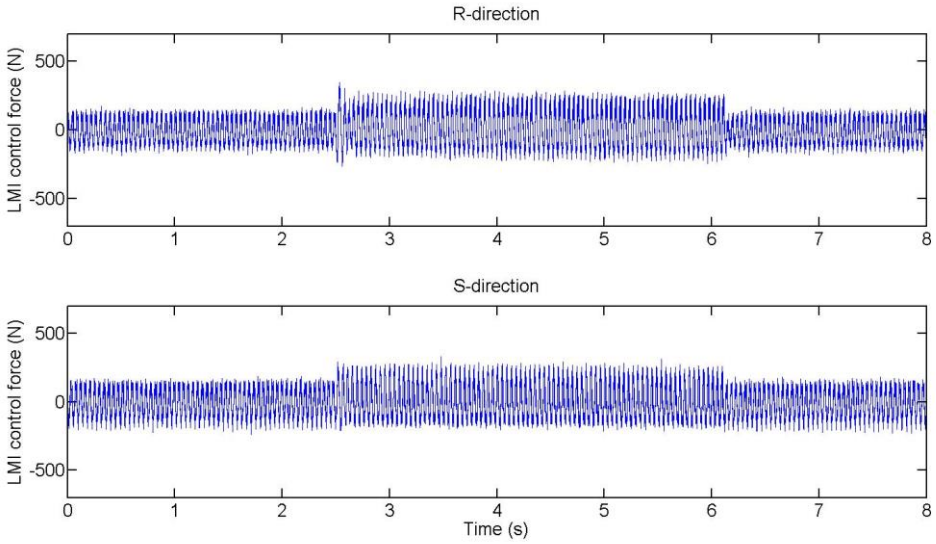

(b) AMB 2

Figure 6.52 Control forces from LMI/PID when running at 145 rad/s

6.4 Coast Down Experiment for LMI Based Gain-Scheduling Contact-Free Recovery

In order to test contact recovery when rotational speed is varying in a transient manner, coast down experimental tests were undertaken in both bushing misalignments (0% and 50%). With the non-driven end bushing, the rotor was run up to the maximum speed of 188 rad/s in a state of no contact. Then the motor was switched off and allowed to coast down.

6.4.1 Coast Down Test with 0% Misalignment of Non-Driven End Bushing under Unbalance of 260 g.cm

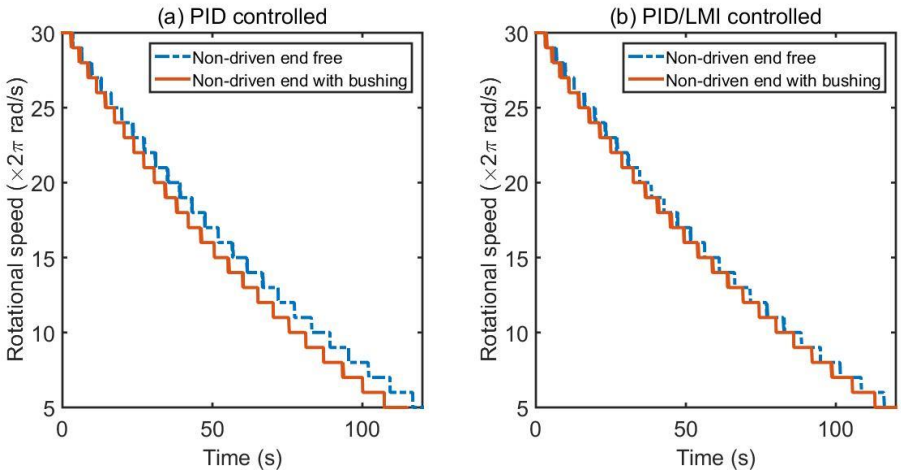

Figure 6.53 Rotational speed recorded by encoder during coast down tests

Figure 6.53 shows the rotational speed recorded by the encoder during coast down tests, with/without the non-driven end bushing. Figure 6.53 (a) shows the speed condition when rotor was controlled by PD action only, while (b) shows the case under LMI control action. Due to different contact conditions, such as frictional rub and multi-contact bouncing, speeds did not decrease at the same rate. Such differences are more evident as shown in Figure 6.53 (a). That may indicate that more frictional rub occurred in contact events when rotor was controlled by PID only.

Figures 6.54-6.57 show the corresponding displacement sensor measurements during the coast down. Initially, the rotor was contact-free, then during coast down it came

into contact with the non-driven end TDB. The unsteady rotor response induced by bouncing contact events are evident under control by PID feedback only, which then progress to rubbing. In contrast with the non-driven end free case, the constrained rotor vibrations are evident as shown in Figures 6.54 (a) and 6.55 (a). The PID control action recovered the rotor to a contact-free state after 45 s.

Under the LMI based gain-scheduling controller $\bar{\mathbf{K}}_{c\_2\_d}(k_e)$, the rotor was initially centralized to a contact-free position. When the motor was switched off, coast down test involved rotor/TDB contact around 5 s (rotor was running at around 176 rad/s as shown in Figure 6.53). The control action was insufficient to recover the rotor from contact as the synchronous unbalance was out of the designed disturbance rejection range, which was also demonstrated in the control performance under non-contact condition (Figure 6.14). Contact events also happened in AMB TDBs, as evident in the measurements from sensor 5 and 6 as shown in Figures 6.56 (b) and 6.57 (b). After 10 s (rotor was running at around 157 rad/s shown in Figure 5.53), the LMI controller recovered the rotor from trapped contact, and centralized the rotor to a position with smaller vibration compared with PID control only (Figure 6.54 (b)-6.57 (b)).

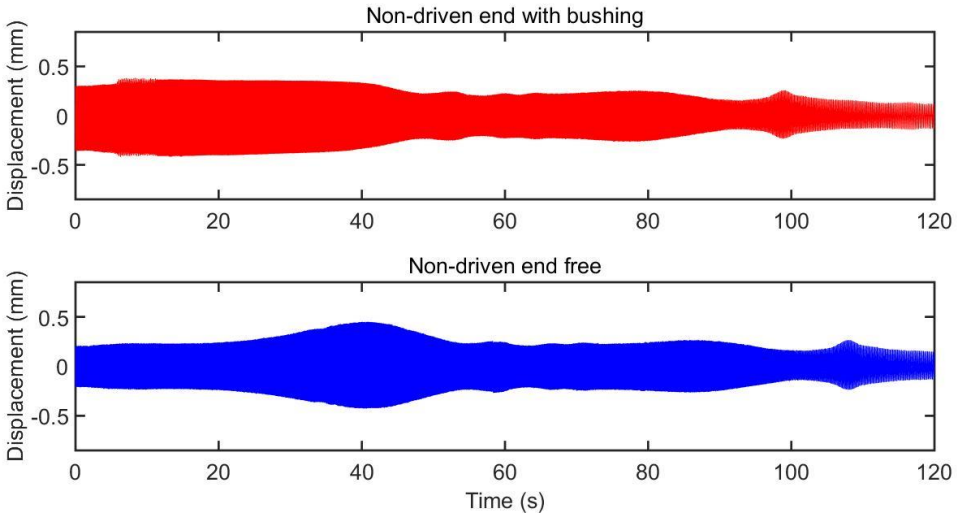

(a) PID controlled

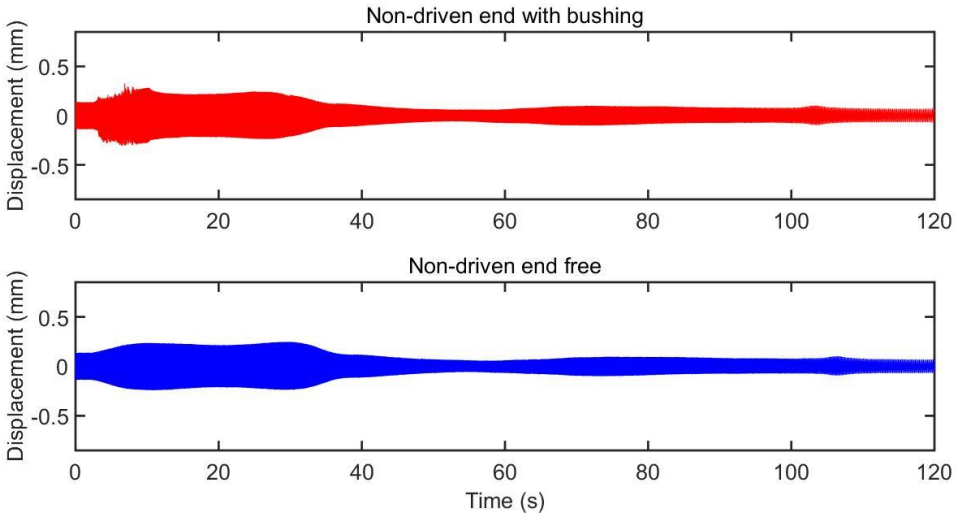

(b) LMI/PID controlled

Figure 6.54 Measurements from sensor 7 under coast down, with 0% non-driven end bushing misaligned under unbalance of 260 g.cm

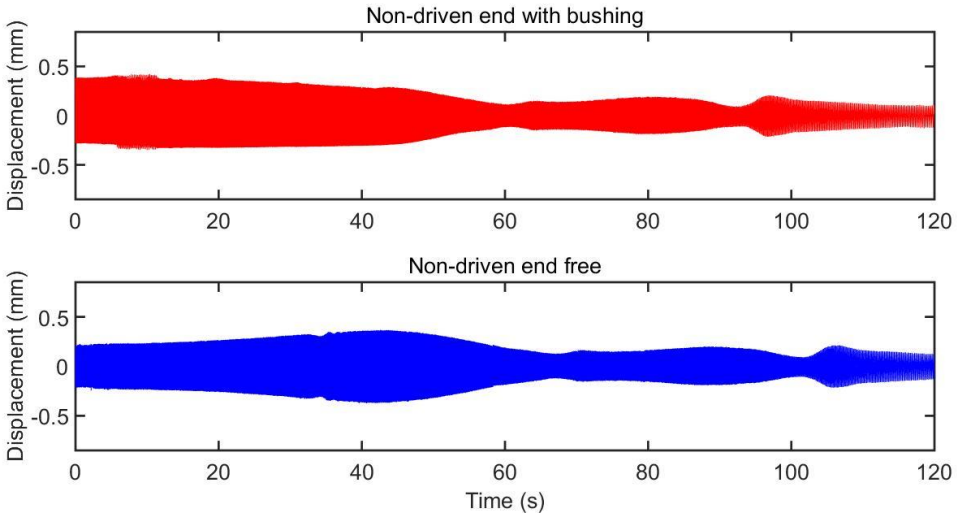

(a) PID controlled

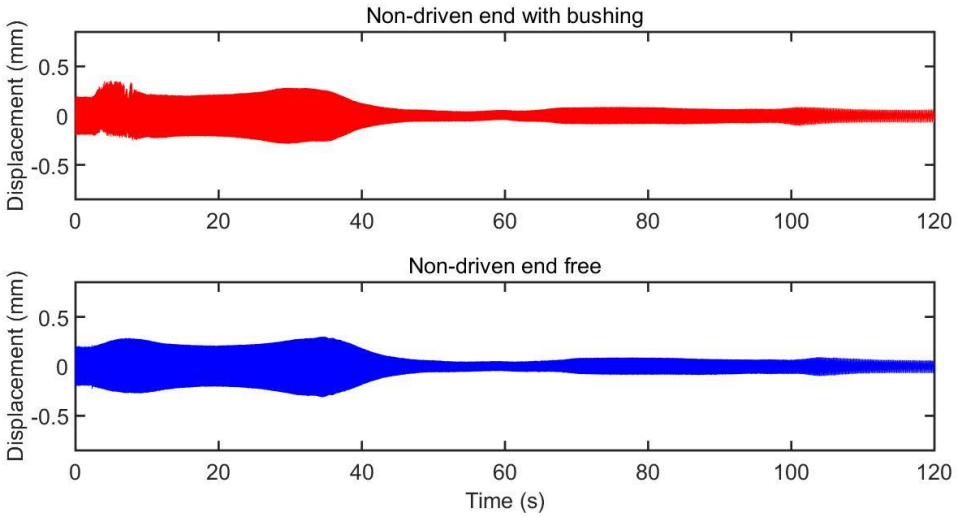

(b) LMI/PID controlled

Figure 6.55 Measurements from sensor 8 under coast down, with 0% non-driven end bushing misaligned under unbalance of 260 g.cm

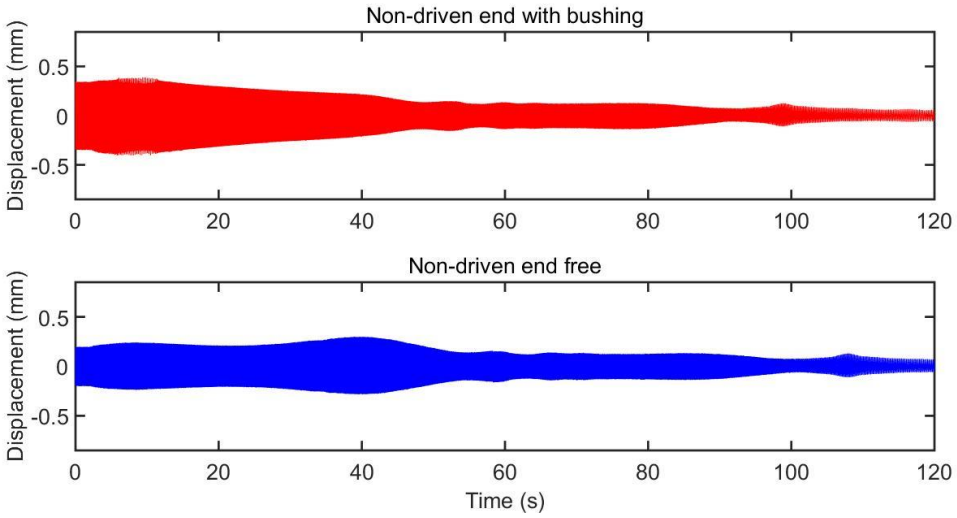

(a) PID controlled

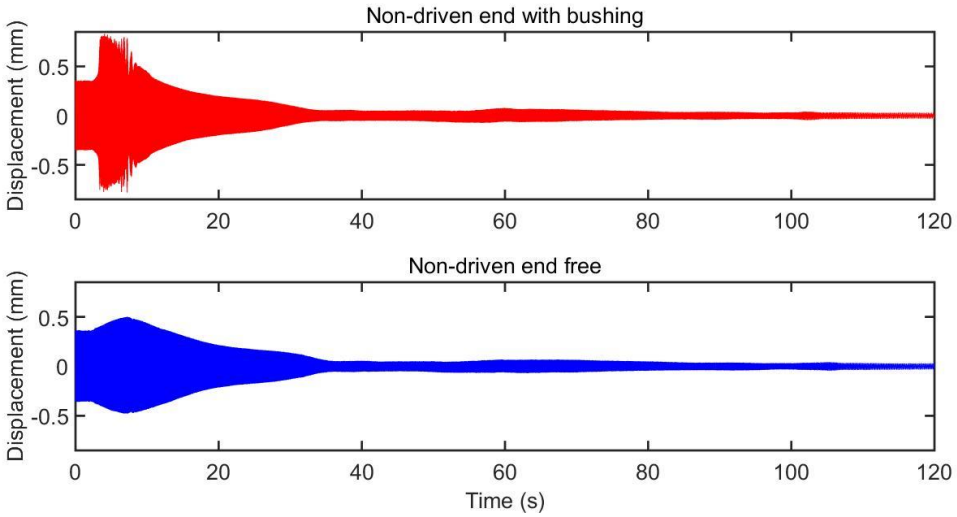

(b) LMI/PID controlled

Figure 6.56 Measurements from sensor 5 under coast down, with 0% non-driven end bushing misaligned under unbalance of 260 g.cm

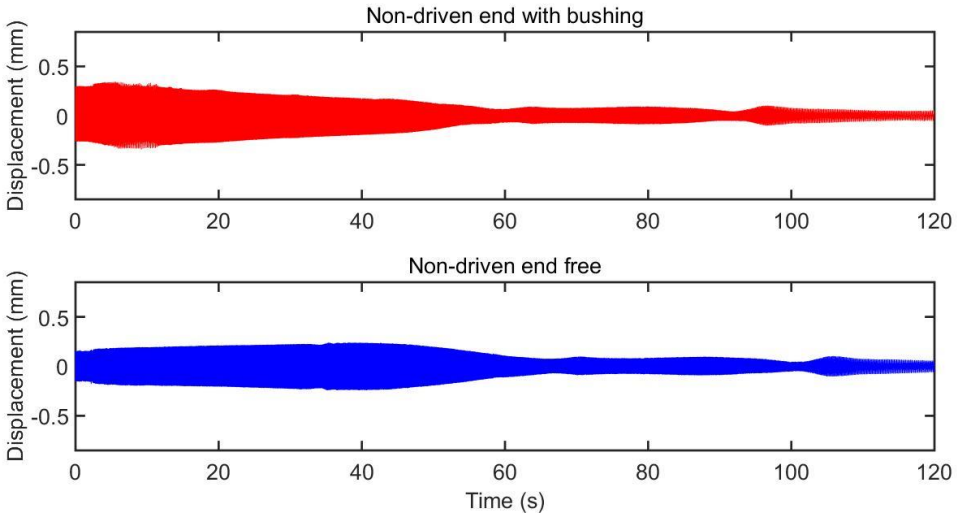

(a) PID controlled

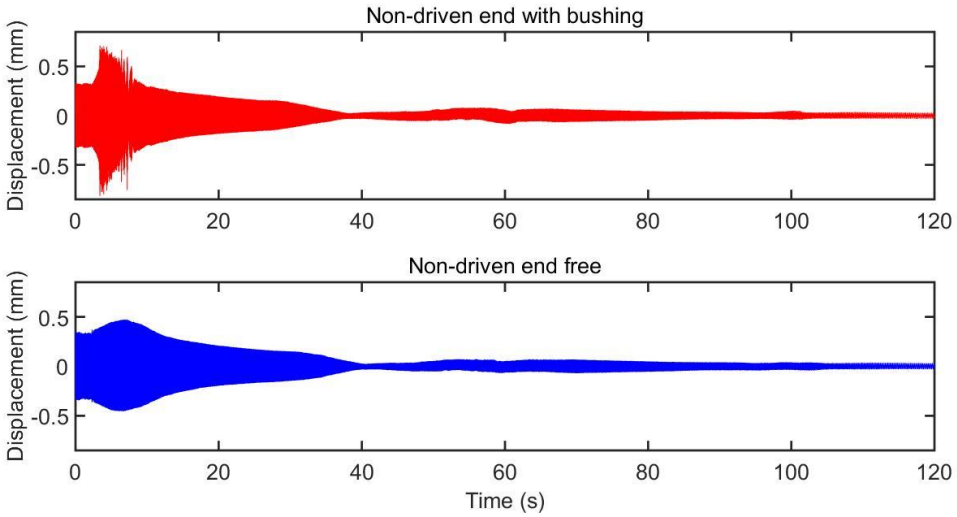

(b) LMI/PID controlled

Figure 6.57 Measurements from sensor 6 under coast down, with 0% non-driven end bushing misaligned under unbalance of 260 g.cm

6.4.2 Coast Down Test with 50% Misalignment of Non-driven End Bushing under Unbalance of 220 g.cm

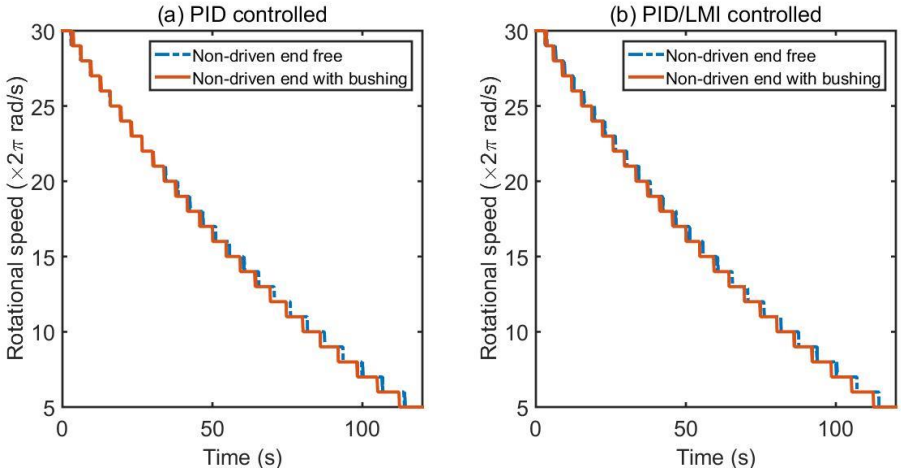

Figure 6.58 Rotational speed recorded by encoder during coast down tests

Figure 6.58 shows in rotational speed recorded by the encoder during coast down tests with the non-driven end bushing 50% misaligned and with 220 g.cm unbalance.

Figures 6.59-6.62 show the corresponding displacement sensor measurements during the coast down with 50% misalignment of non-driven end bushing under unbalance of 220 g.cm. Compared with the results shown in Figures 6.59 (a) and 6.60 (a), the rotor under PID control action involved contact event around 25 s with revealed asymmetric responses due to misaligned non-driven end bushing. After contact events lasting around 30 s, the rotor under control by PID was recovered to a contact-free state for the remainder of the coast down test (6.59 (a)-6.62 (a)).

During the coast down test controlled by $\overline{\mathbf{K}}_{c\_2\_d}(k_e)$, rotor/TDB contact occurred around 5 s (rotor was running at around 176 rad/s as shown in Figure 6.58), are evident from sensors 7 and 8 shown in Figures 6.59 (b) and 6.60 (b). It also results in the rotor entering a multi-contact state. Contact was also detected at TDBs inside AMBs according to the measurements from sensors 5 and 6 as shown in Figures 6.61 (b) and 6.62 (b). However, the contact event occurred at such speeds was expected as the synchronous unbalance was out of the vibration attenuation range, which could

also be demonstrated as the steady LMI controlled rotor response shown in Figure 6.15. After short contact event lasting for 5 *s* (rotor speed range from 176 rad/s to 170 rad/s as shown in Figure 6.58), rotor was recovered to a contact-free state for the remainder of the coast down test and with significant vibration attenuation provided by the controller $\overline{\mathbf{K}}_{c\_2\_d}(k_e)$. The coast down results could prove the robust stability offered by the LMI gain-scheduling controller for contact-free recovery.

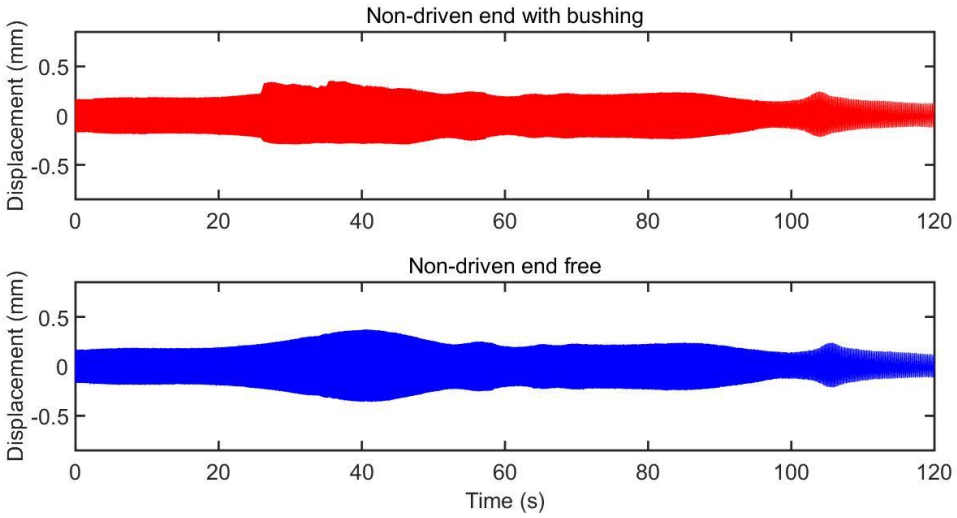

(a) PID controlled

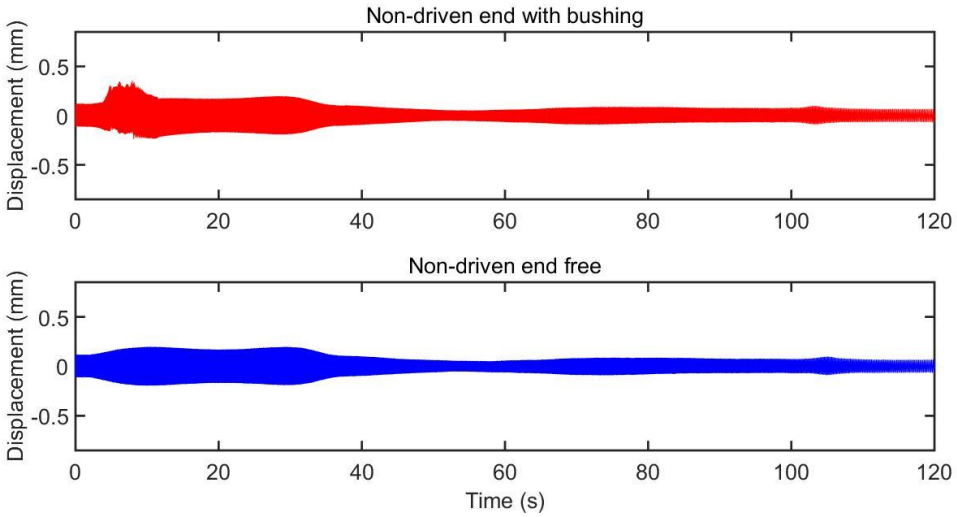

(b) LMI/PID controlled

Figure 6.59 Measurements from sensor 7 under coast down, with 50% non-driven end bushing misaligned under unbalance of 220 g.cm

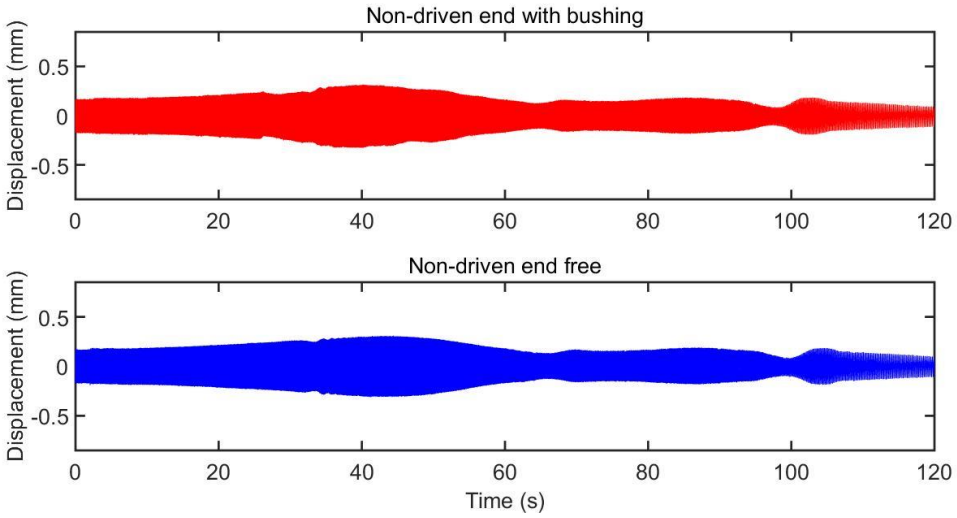

(a) PID controlled

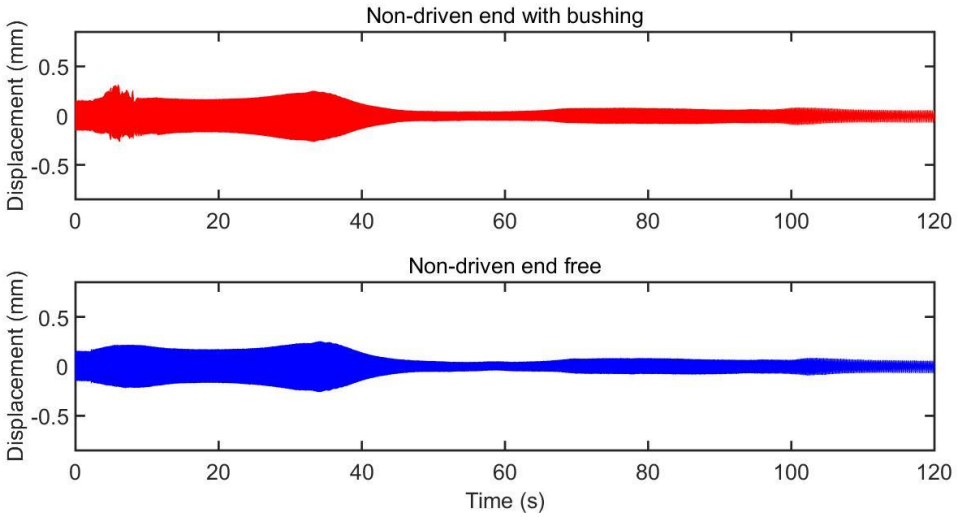

(b) LMI/PID controlled

Figure 6.60 Measurements from sensor 8 under coast down, with 50% non-driven end bushing misaligned under unbalance of 220 g.cm

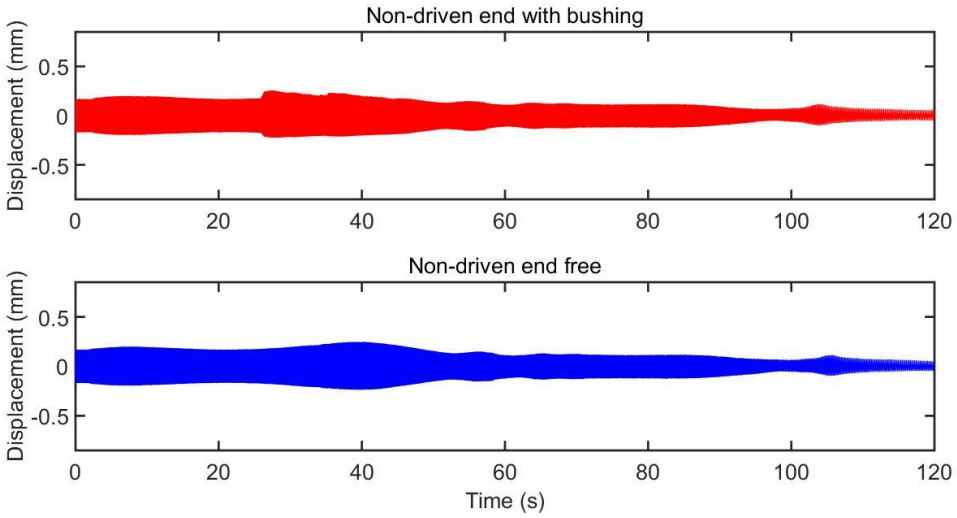

(a) PID controlled

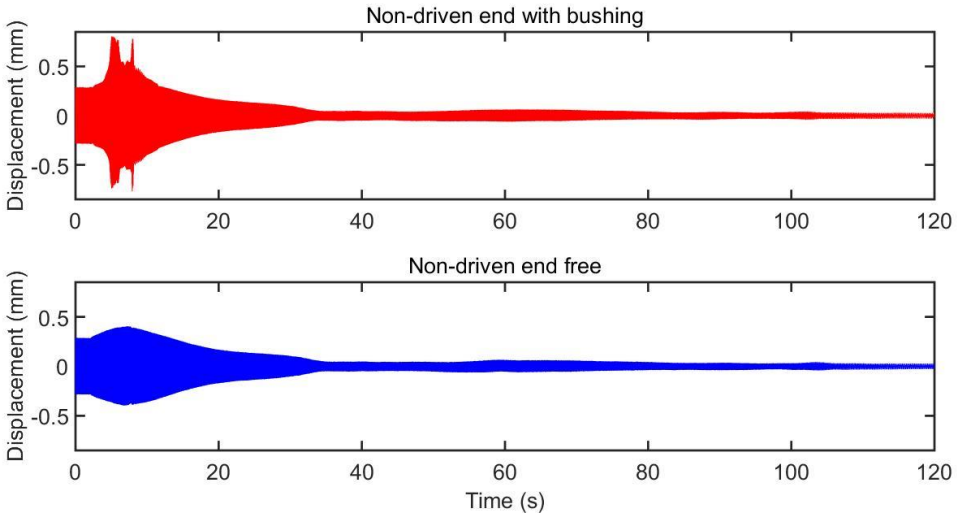

(b) LMI/PID controlled

Figure 6.61 Measurements from sensor 5 under coast down, with 50% non-driven end bushing misaligned under unbalance of 220 g.cm

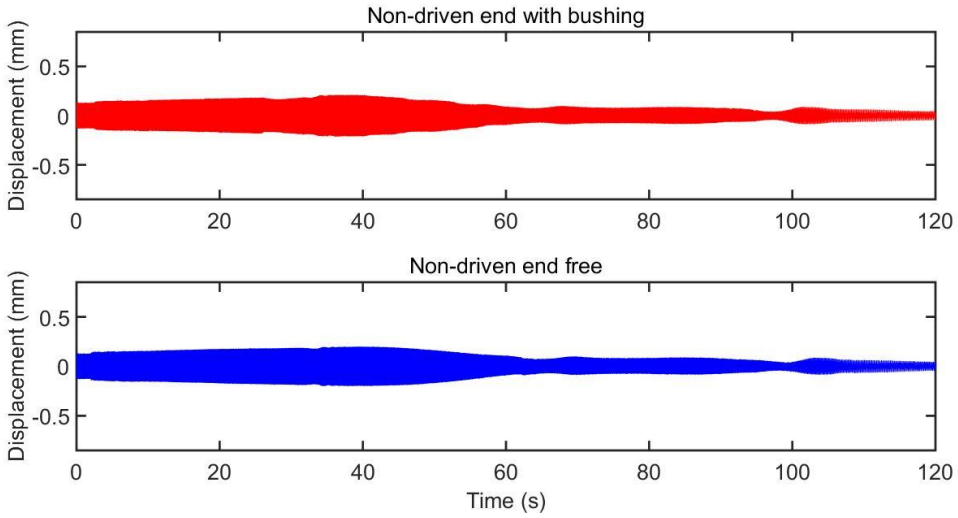

(a) PID controlled

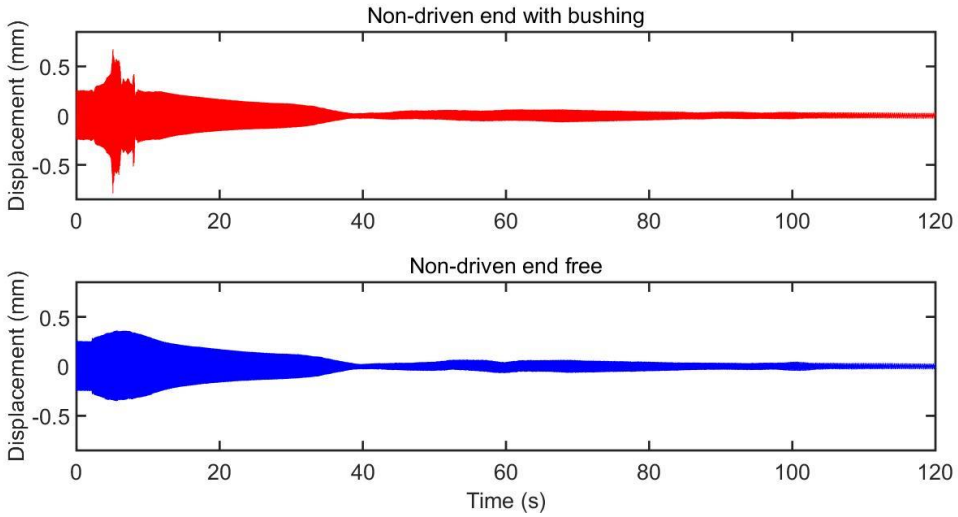

(b) LMI/PID controlled

Figure 6.62 Measurements from sensor 6 under coast down, with 50% non-driven end bushing misaligned under unbalance of 220 g.cm

6.5 Closure

Using appropriate transfer functions for mixed sensitivity, a LMI based gain-scheduling controller for rotor contact-free recovery was implemented for real-time operation. This was verified in terms of stability and control performance. With various unbalances levels, rotor bi-stable responses under contact with the non-driven end touchdown bushing in different misalignments (0% and 50%) was presented.

Based on different conditions (unbalance, TDB misalignment), the controller's capability to recover the rotor to a contact-free was state verified experimentally. Rotor position was centralized and escaped from contact effectively. Also, the potential limitation for contact-free recovery was also presented when the unbalance was large.

Coast down experimental tests under PID and PID/LMI control were also undertaken. The robust stability offered by the LMI gain-scheduling controller for contact-free recovery was assessed when rotational speed varies in a transient manner. When the rotor was running out of controller disturbance rejection range, contact events occurred in a short period. Then, the controller stabilized and recovered rotor to a contact-free state for the remainder of the coast down tests.

Chapter 7. Conclusions

7.1 Importance of the Study

Appropriate control strategies are essential for rotor/AMB system operation. Due to their simple implementation, PID controllers are popular in most applications, but they may be deficient in certain operating conditions. H_∞ optimization offers a powerful solution through the mixed sensitivity problem in robustness MIMO control design. A linear time invariant (LTI) H_∞ controller designed after consideration of the control action from PID action, could enable rotor/AMB system vibrations to be attenuated significantly with guaranteed robust stability.

In addition to LTI aspect, a rotor/AMB system has parameter-dependent variation during operation, such as speed dependency induced by the gyroscopic effects and dynamics varying when rotor/touchdown bearing contact events occur. Potential instability may arise in the parameter-dependent system operating under standard LTI control action. A novel linear matrix inequality (LMI) based gain-scheduling controller synthesis technique could enable H_∞ optimization to be achieved when system dynamics vary. This was used in the control of a speed-dependent rotor/AMB system in contact-free conditions.

Due to the complexity of contact events, open-loop control strategies with explicit synchronous forces have been implemented by other researchers for rotor/touchdown bearing contact-free recovery. However, the LMI technique offers the potential to synthesize an intelligent controller to solve the contact problem in a closed loop format. This thesis proposes a LMI based gain-scheduling H_∞ controller to facilitate rotor contact-free recovery. It is able to detect contact through an estimated effective stiffness for use as a linear parameter varying (LPV), hence enabling recovery of the rotor from trapped contact.

7.2 Main Results and Contributions

Based on the objectives of the thesis, a H_∞ optimal control solution was proposed in three parts:

1. According to the Riccati based solution to H_∞ optimization for the rotor/AMB system, several LTI controllers were designed to attenuate vibrations when the rotor is running under contact-free conditions;
2. Introducing LMI gain-scheduling control to implement parameter dependency within the rotor/AMB system. When the rotor was running with variable speed, a controller was synthesized to guarantee stability and achieve disturbance rejection for low vibration responses;
3. Based on the LMIs, a contact-dependent controller having gain-scheduling dynamic adaption was synthesized to achieve recovery of the rotor to a contact-free condition. Simulated/experimental results for control performance were presented to demonstrate the benefits.

As a mathematical model of an experimental facility, a finite element framework was introduced to describe a flexible rotor. Under the actuation from radial AMBs controlled by PD action, rotor dynamics were investigated. A state-space description of the rotor/AMB system was developed and augmented for contact-free robust controller design. In contrast to the experimental measurements, the mathematical model was obtained with sufficient accuracy for robust controller design purposes. The dynamic parameters of the base structure were estimated from measured natural frequencies and software-based estimation of the mass centre and inertias. A rigid body base model was developed and transformed into a MIMO system as a preparation for a contact-dependent plant modelling in a rotating frame of reference. The base structure system was also included in the rotor dynamic model. From the frequency response, the rotor/base interaction was weak when rotor was in a contact-free state.

A mathematical model reduction technique was introduced for an LTI system. This method could effectively keep the multiplicative model error at a small level (-30 dB) over the designed frequency range. For the mixed sensitivity optimization, an augmented plant including eight sensor feedback signals and four actuation axes for LTI H_∞ controller design was presented. An LTI controller was synthesized with a second order sensitivity weighting filter. In contrast with PD control action only, the LTI H_∞ controller could stabilize the rotor/AMB with less sensitivity to external disturbances, especially at rotor resonances (83 rad/s and 125 rad/s). However, singular value issues induced by non-full column rank were experiences. That resulted in a sub-optimized H_∞ control solution with insufficient disturbance rejection. In order to achieve better LTI control performance, a solution to that problem was developed by scaling the output dimension. A 'square' plant having the same number of inputs and outputs was derived. It enabled a fully optimized H_∞ control solution for the mixed sensitivity problem. The benefits from 'square' control were verified numerically. From the simulated results, 'square' control action offered a better control performance at rotor resonances (83 rad/s and 125 rad/s) and even out of the design range (110 rad/s and 140 rad/s). Switching control involving two 'square' LTI H_∞ controllers was also proposed. The stability when the LTI independent controllers were working in tandem was examined numerically. Step switching action excited closed loop system high frequency modes and induced significant overshoot at 102 rad/s. A ramp switching signal reduced the transients.

The speed-dependent rotor/AMB system was described through LPVs (formed in polytope). With a linear fractional transformation, system uncertainties induced by the varying parameter could be structured through linear interpolation. A model reduction of the LPV system was derived for efficient controller design. The speed-dependent multiplicative model error was estimated and remained at a small level. By considering controller states, the speed-dependent controller used sensor feedback from both ends of the rotor. The control performance was estimated in the frequency domain at various rotational speeds. The control action enlarged rotor vibration amplitudes at the middle when the first flexible mode was excited (running

above 160 rad/s). However, this action avoided rotor/TDB contact events. Simulated results were presented in single speed tests with the scheduling gain fixed. Rotor vibrations were well-controlled. Then run-up tests, with the scheduling gain varied, were undertaken in simulation. When the rotational speed was varied in a transient manner, the control performance was also sufficient to avoid rotor/TDB contact.

Rotor/touchdown bearing contact dynamics were investigated numerically for the bi-stable rotor responses. Two typical contact modes (rubbing and bouncing) were presented. A linearized effective stiffness was defined to identify the occurrence of complex rotor/touchdown bearing contact events. Also, a feedforward observer was derived from the base model, and verified numerically to estimate an effective contact stiffness parameter from accelerometer feedback. Rotor/TDB contact was estimated by the observer and inputted to the LMI based gain-scheduling controller. A contact-dependent model with a movable base was presented. This was used in an augmented plant for contact-free recovery robust controller design. By analysing the contact-dependent model characteristics, a linear varying parameter (effective stiffness) polytope range was defined. A LMI based gain-scheduling controller having contact-dependency was then synthesized. The stability and control performance were estimated in the frequency domain. With a finite parameter box, the LMI gain-scheduling control was able to recover the rotor from contact events when the effective stiffness varied over the designed range. Additionally, the stability during parameter variation out of the designed range, was also evident when significant contact occurred. Simulated results showed that the contact-free recovery offered by the LMI gain-scheduling controller was successful over the bandwidth of sensitivity weighting filter (0-150 rad/s).

For real-time implementation, the LMI based gain-scheduling controller for contact-free recovery was improved by appropriate weighting filters. In contrast with different weighting designs, a controller with less inherited harmonics achieved contact-free recovery during experimental testing. Also, the control performance was estimated under contact-free conditions. Based on the rotor bi-stable responses under

contact events, the contact zones were found. The contact-free recovery experimental tests were undertaken with different non-driven end touchdown bushing misalignment (0% and 50%), under different unbalances (220 g.cm, 260 g.cm and 400 g.cm). The contact-dependent controller recovered the rotor from contact successfully over the sensitivity filter bandwidth, and with non-driven end bushing misalignments (0% and 50%), under unbalances (220 g.cm and 260 g.cm). In the case of contact-free recovery with 0% misalignment of touchdown bushing under the higher unbalance (400 g.cm), the LMI gain-scheduling controller was not able to recover complete contact-free conditions when rotor was running at 138 rad/s. However, the control action reduced significant the severity of the contact conditions, reducing bouncing contact to a rubbing response. In order to assess control performance when rotor speed was varying, run-down experimental tests were also undertaken. In contrast to PID control only, a contact-dependent controller provided a better rotor operation during run-down tests. Under LMI gain-scheduling contact-free recovery control, the rotor came into contact with a TDB when running at 176 rad/s. Then, the control action recovered the contact events effectively with coast down speed, and centralized rotor position in the remainder of the run-down test.

7.3 Future Research

A LTI H_∞ controller synthesized for the plant having eight outputs and four inputs, could obtain good control performance. However, improved augmentation through the inclusion of an inverse plant could be beneficial. It would be interesting in future work to examine whether an inverse plant model could be developed to overcome the non-full column rank problem.

The contact-dependent controller presented in this thesis relies on the feedforward observer to estimate the contact condition using base mounted accelerometer signal for feedback. A contact force sensor could be introduced into the test rig, to enable contact estimation more directly. That would enhance the efficiency of the contact-dependent controller. A more efficient contact-dependent model and model uncertainties estimation during contact, are still desired. Moreover, the contact-

dependent controller may also be enhanced to be more universal by taking the rotational speed into account. The parameter polytope may be defined by two dimensions, through effective stiffness and rotational speed, which would advance the potential for more complete performance.

References

[1] ISO 14839-2:2004 Standard, Mechanical Vibration – Vibration of Rotating Machinery Equipped with Active Magnetic Bearings – Part 2: Evaluation of Vibration, 2004.

[2] American Petroleum Institute (API) Standard 684, Tutorial on the API Standard Paragraphs Covering Rotor Dynamics and Balance (An Introduction to Lateral Critical and Train Torsional Analysis and Rotor Balancing), 1996.

[3] Christopher, D., and Beach, R. (1998). Flywheel technology development program for aerospace applications. Aerospace and Electronic Systems Magazine, IEEE, 13(6), 9-14.

[4] Schweitzer, G., Maslen, E.H. (eds): (Contributors: Bleuler, H., Cole, M., Keogh, P., Larsonneur, R.,Maslen, E.H., Nordmann, R., Okada, Y., Schweitzer, G., Traxler, A.), Magnetic Bearings–Theory, Design and Application to Rotating Machinery. Springer, Berlin Heidelberg , 2009.

[5] European Research Project. Magnetic bearings for smart aero engines. Technical report, EC GROWTH, Project G4RD-CT-2001-00625, 2001–2005.

[6] Earnshaw, S. (1842). On the nature of the molecular forces which regulate the constitution of the luminiferous ether, Trans. Camb. Phil. Soc, 7, 97-112.

[7] Budig, P. and Werner, R. Stiffness of magnetic bearings, Proceedings of the Fourth International Symposium on Magnetic Bearings, 251–256, August 1994.

[8] Sahinkaya, M. N., Cole, M. O. T., and Burrows, C. R. (2001). Fault detection and tolerance in synchronous vibration control of rotor—magnetic bearing systems.

Proceedings of the Institution of Mechanical Engineers, Part C: Journal of Mechanical Engineering Science, 215(12), 1401-1416.

[9] Keogh, P., Cole, M., Sahinkaya, N., and Burrows, C. (2002, January). On the control of synchronous vibration in rotor/magnetic bearing systems involving auxiliary bearing contact. In ASME Turbo Expo 2002: Power for Land, Sea, and Air (pp. 599-606). American Society of Mechanical Engineers

[10] Schweitzer, G. (2005). Safety and reliability aspects for active magnetic bearing applications-a survey. Proceedings of the Institution of Mechanical Engineers, Part I: Journal of Systems and Control Engineering, 219(6), 383-392.

[11] Schroeder, M. (1970). Synthesis of low-peak-factor signals and binary sequences with low autocorrelation (corresp.). Information Theory, IEEE Transactions on, 16(1), 85-89.

[12] Cole, M. O. T., Keogh, P. S., and Burrows, C. R. (1998). Vibration control of a flexible rotor/magnetic bearing system subject to direct forcing and base motion disturbances. Proceedings of the Institution of Mechanical Engineers, Part C: Journal of Mechanical Engineering Science, 212(7), 535-546.

[13] Keogh, P. S. (2012). Contact dynamic phenomena in rotating machines: active/passive considerations. Mechanical Systems and Signal Processing, 29, 19-33.

[14] Keogh, P. S., and Morton, P. G. (1993, June). Journal bearing differential heating evaluation with influence on rotor dynamic behaviour. In Proceedings of the Royal Society of London A: Mathematical, Physical and Engineering Sciences (441, 527-548, No. 1913).

[15] Keogh, P. S., and Morton, P. G. (1994, May). The dynamic nature of rotor thermal bending due to unsteady lubricant shearing within a bearing. In Proceedings

of the Royal Society of London A: Mathematical, Physical and Engineering Sciences (445, 273-290, No. 1924).

[16] Schmied, J., and Pradetto, J. C. (1992, July). Behavior of a one ton rotor being dropped into auxiliary bearings. In Third International Symposium on Magnetic Bearings, Alexandria, VA, July (29-31).

[17] Kirk, R. G., and Ishii, T. (1993). Transient rotor drop analysis of rotors following magnetic bearing power outage. In MAG'93- Magnetic Bearings, Magnetic Drives and Dry Gas Seals Conference & Exhibition, Alexandria, VA (53-61).

[18] Ecker, H. (1999). Nonlinear stability analysis of a single mass rotor contacting a rigid backup bearing (79-88). Springer Berlin Heidelberg.

[19] Popprath, S., and Ecker, H. (2007). Nonlinear dynamics of a rotor contacting an elastically suspended stator. Journal of Sound and Vibration, 308(3), 767-784.

[20] Keogh, P. S., and Cole, M. O. T. (2003). Rotor vibration with auxiliary bearing contact in magnetic bearing systems Part 1: Synchronous dynamics. Proceedings of the Institution of Mechanical Engineers, Part C: Journal of Mechanical Engineering Science, 217(4), 377-392.

[21] Cade, I. S., Keogh, P. S., Sahinkaya, M. N., and Burrows, C. R. (2007, January). Wavelet coefficient characteristics during rotor/auxiliary bearing contact in active magnetic bearing systems. In ASME 2007 International Design Engineering Technical Conferences and Computers and Information in Engineering Conference (1327-1334).

[22] Muszynska, A., and Goldman, P. (1995). Chaotic responses of unbalanced rotor/bearing/stator systems with looseness or rubs. Chaos, Solitons & Fractals, 5(9), 1683-1704.

[23] Choy, F. K., Padovan, J., and Yu, J. C. (1990). Full rubs, bouncing and quasi chaotic orbits in rotating equipment. Journal of the Franklin Institute, 327(1), 25-47.

[24] Ehrich, F. F. (1965). Bi-stable Vibration of Rotors in Bearing Clearance. ASME paper 65-WA/MD -1.

[25] Black, H. F. (1968). Interaction of a whirling rotor with a vibrating stator across a clearance annulus. Proceedings of the Institution of Mechanical Engineers, Part C: Journal of Mechanical Engineering Science, 10(1), 1-12.

[26] Xie Hu, Flowers GT, Feng L, and Lawrence CH. (1999). Steady-state dynamic behavior of a flexible rotor with auxiliary support from a clearance bearing. ASME Journal of Vibration and Acoustics, 121(1), 78-83.

[27] Childs, D. W. (1979). Rub-induced parametric excitation in rotors. ASME Journal of Mechanical Design, 101(4), 640-644.

[28] Muszynska, A. (1984). Partial lateral rotor to stator rubs. In International Conference on Vibrations in Rotating Machinery, 3rd, Heslington, England (327-335).

[29] Hori, Y., and Kato, T. (1990). Earthquake-induced instability of a rotor supported by oil film bearings. ASME Journal of Vibration and Acoustics, 112(2), 160-165.

[30] Keogh, P. S., and Cole, M. O. (2006). Contact dynamic response with misalignment in a flexible rotor/magnetic bearing system. ASME Journal of Engineering for Gas Turbines and Power, 128(2), 362-369.

[31] Childs, D. W. (1982). Fractional-frequency rotor motion due to non-symmetric clearance effects. ASME Journal of Engineering for Gas Turbines and Power, 104(3), 533-541.

[32] Muszynska, A. (2002, February). Rotor-to-stationary part full annular contact modeling. In Proceedings of the 9th International Symposium on Transport Phenomena and Dynamics of Rotating Machinery (1–8).

[33] Ehrich, F. F. (1988). High order subharmonic response of high speed rotors in bearing clearance. ASME Journal of Vibration and Acoustics, 110(1), 9-16.

[34] Cole, M. O. T., and Keogh, P. S. (2003). Asynchronous periodic contact modes for rotor vibration within an annular clearance. Proceedings of the Institution of Mechanical Engineers, Part C: Journal of Mechanical Engineering Science, 217(10), 1101-1115.

[35] Bartha, A. R. (1998, September). Dry friction induced backward whirl: theory and experiment. In 5th IFToMM Conference on Rotor Dynamics, Darmstadt, Germany, September (7-10).

[36] Burrows, C. R., Keogh, P. S., and Tasaltin, R. (1993). Closed loop vibration control of flexible rotors—an experimental study. Proceedings of the Institution of Mechanical Engineers, Part C: Journal of Mechanical Engineering Science, 207(1), 1-17.

[37] Burrows, C. R., and Sahinkaya, M. N. (1983, March). Vibration control of multi-mode rotor-bearing systems. In Proceedings of the Royal Society of London A: Mathematical, Physical and Engineering Sciences (386, 77-94, No. 1790).

[38] Knospe, C. R., Hope, R. W., Fedigan, S. J., and Williams, R. D. (1995). Experiments in the control of unbalance response using magnetic bearings. Mechatronics, 5(4), 385-400.

[39] C. Knospe and E. G. Collins. (1996, Sept). Introduction to the special issue on magnetic bearing control, IEEE Tans. on Control Systems Technology, 4, 481–482.

[40] Schweitzer, G., Traxler, A., and Bleuler, H. (2013). Magnetlager: Grundlagen, Eigenschaften und Anwendungen berührungsfreier, elektromagnetischer Lager. Springer-Verlag.

[41] Burrows, C. R., Sahinkaya, N., Traxler, A., and Schweitzer, G. (1989). Design and application of a magnetic bearing for vibration control and stabilization of a flexible rotor. In Magnetic Bearings (159-168). Springer Berlin Heidelberg.

[42] Nonami, K., and Ito, T. (1996). μ synthesis of flexible rotor-magnetic bearing systems. Control Systems Technology, IEEE Transactions on, 4(5), 503-512.

[43] Ehmann, C., Kytka, P., and Nordmann, R. (2004). Comparison of PID-, LQR- and Mu-Synthesis Control for the Electromagnetic Suspension of a Flexible Rotor. In 7th International Conference on Motion and Vibration Control MOVIC (Vol. 4).

[44] Yu, S. S., Wu, S. J., and Lee, T. T. (2003, July). Optimal fuzzy control of radial active magnetic bearing systems. In Computational Intelligence in Robotics and Automation, 2003. Proceedings. 2003 IEEE International Symposium on(Vol. 3, 1393-1398).

[45] Hong, S. K., and Langari, R. (2000). Robust fuzzy control of a magnetic bearing system subject to harmonic disturbances. Control Systems Technology, IEEE Transactions on, 8(2), 366-371.

[46] Sahinkaya, M. N., Hartavi, A. E., Burrows, C. R., and Tuncay, R. N. (2004, August). Bias current optimization and fuzzy controllers for magnetic bearings in turbo molecular pumps. In 9th International Symposium on Magnetic Bearings (ISMB9), Lexington, KY.

[47] Salm, J., and Schweitzer, G. (1984). Modelling and control of a flexible rotor with magnetic bearings. In International Conference on Vibrations in Rotating Machinery, 3rd, Heslington, England (553-561).

[48] Keogh, P. S., Burrows, C. R., and Berry, T. (1996). On-line controller implementation for attenuation of synchronous and transient rotor vibration. ASME Journal of Dynamic Systems, Measurement, and Control, 118(2), 315-321.

[49] Maciejowski, J. M. (1989). Multivariable feedback design. Electronic Systems Engineering Series, Wokingham, England: Addison-Wesley, 1989, 1.

[50] Glover, K., and Doyle, J. C. (1988). State-space formulae for all stabilizing controllers that satisfy an H∞-norm bound and relations to relations to risk sensitivity. Systems & Control Letters, 11(3), 167-172.

[51] Ortega, M. G., and Rubio, F. R. (2004). Systematic design of weighting matrices for the H_∞ mixed sensitivity problem. Journal of Process Control, 14(1), 89-98.

[52] Keogh, P. S., Mu, C., and Burrows, C. R. (1995). Optimized design of vibration controllers for steady and transient excitation of flexible rotors. Proceedings of the Institution of Mechanical Engineers, Part C: Journal of Mechanical Engineering Science, 209(3), 155-168.

[53] Doyle, J. C., Glover, K., Khargonekar, P. P., and Francis, B. (1989). State-space solutions to standard H_2 and H_∞ control problems. Automatic Control, IEEE Transactions on, 34(8), 831-847.

[54] Chen, Y., and Zhu, C. (2008). Active vibration control based on linear matrix inequality for rotor system under seismic excitation. Journal of Sound and Vibration, 314(1), 53-69.

[55] Fan, Y., Cliff, E. M., Lutze, F. H., and Anderson, M. R. (1996). Mixed H_2 / H_∞ optimal control for an elastic aircraft. Journal of Guidance, Control, and Dynamics, 19(3), 650-655.

[56] Keogh, P. S., Sahinkaya, M. N., Burrows, C. R., and Prabhakar, S. (2006). Wavelet based adaptation of H-infinity control in flexible rotor/magnetic bearing system. In Proceedings of the IFTOMM 7th International Conference on Rotor dynamics, Vienna, Austria.

[57] Keogh, P. S., Cade, I. S., and Sahinkaya, M. N. (2006). The use of Wavelet analysis for the closed loop control of vibration in magnetic bearing systems. In The tenth International Symposium on Magnetic Bearings (ISMB10).

[58] Cade, I. S., Keogh, P. S., and Sahinkaya, M. N. (2007). Transient rotor/active magnetic bearing control using sampled wavelet coefficients. ASME Journal of Engineering for Gas Turbines and Power, 129(2), 549-555.

[59] Cole, M. O. T., Keogh, P. S., Burrows, C. R., and Sahinkaya, M. N. (2006). Wavelet domain control of rotor vibration. Proceedings of the Institution of Mechanical Engineers, Part C: Journal of Mechanical Engineering Science, 220(2), 167-184.

[60] Wang, M., Sahinkaya, M. N., and Keogh, P. S. (2013, June). Switching Action in Rotor-AMB Systems for Smooth Vibration Control. In ASME Turbo Expo 2013: Turbine Technical Conference and Exposition (pp. V07AT29A020-V07AT29A020).

[61] Gahinet, P., and Apkarian, P. (1994). A linear matrix inequality approach to H_∞ control. International Journal of Robust and Nonlinear Control, 4(4), 421-448.

[62] Iwasaki, T., and Skelton, R. E. (1994). All controllers for the general H_∞ control problem: LMI existence conditions and state-space formulas. Automatica, 30(8), 1307-1317.

[63] El Ghaoui, L., Feron, E., and Balakrishnan, V. (1994). Linear matrix inequalities in system and control theory (Vol. 15, p. 1). Philadelphia: Society for Industrial and Applied Mathematics.

[64] Gahinet, P. (1996). Explicit controller formulas for LMI-based H_∞ synthesis. Automatica, 32(7), 1007-1014.

[65] Scherer, C., Gahinet, P., and Chilali, M. (1997). Multiobjective output-feedback control via LMI optimization. Automatic Control, IEEE Transactions on, 42(7), 896-911.

[66] Packard, A. (1994). Gain scheduling via linear fractional transformations. Systems & Control Letters, 22(2), 79-92.

[67] Apkarian, P., and Gahinet, P. (1995). A convex characterization of gain-scheduled H_∞ ontrollers. Automatic Control, IEEE Transactions on, 40(5), 853-864.

[68] Apkarian, P., and Gahinet, P. (1993, December). A Convex Characterization of Parameter-dependent $H\infty$ controllers. In Decision and Control, 1993, Proceedings of the 32nd IEEE Conference on (1654-1659).

[69] Sivrioglu, S., and Nonami, K. (1996, December). LMI approach to gain scheduled H∞ control beyond PID control for gyroscopic rotor-magnetic bearing system. InDecision and Control, 1996., Proceedings of the 35th IEEE Conference on (4, 3694-3699).

[70] Tsiotras, P., and Mason, S. (1996, November). Self-scheduled H∞ controllers for magnetic bearings. In International Mechanical Engineering Congress and Exposition, Atlanta, GA (151-158).

[71] Cole, M. O. T, Wongratanaphisan, T., and Keogh, P. S. (2006). On LMI-based optimization of vibration and stability in rotor system design. ASME Journal of Engineering for Gas Turbines and Power, 128(3), 677-684.

[72] Schlotter, M., and Keogh, P. S. (2008). The vibration control of speed-dependent flexible rotor/magnetic bearing systems using linear matrix inequality gain-scheduled H∞ design. Proceedings of the Institution of Mechanical Engineers, Part I: Journal of Systems and Control Engineering, 222(2), 97-107.

[73] Keogh, P., Cole, M., Sahinkaya, N., and Burrows, C. (2002, January). On the control of synchronous vibration in rotor/magnetic bearing systems involving auxiliary bearing contact. In ASME Turbo Expo 2002: Power for Land, Sea, and Air (599-606).

[74] Cole, M. O. T., and Keogh, P. S. (2003). Rotor vibration with auxiliary bearing contact in magnetic bearing systems Part 2: robust synchronous control for rotor position recovery. Proceedings of the Institution of Mechanical Engineers, Part C: Journal of Mechanical Engineering Science, 217(4), 393-409.

[75] Schlotter, M., and Keogh, P. S. (2007). Synchronous position recovery control for flexible rotors in contact with auxiliary bearings. ASME Journal of Vibration and Acoustics, 129(5), 550-558.

[76] Nelson, H. D. and McVaugh, J. M. (1976). The dynamics of rotor-bearing systems using finite elements. Transactions of the ASME, Journal of Engineering for Industry, 98(2), 593-600.

Appendix

A. Simulated Results

Some corresponding simulated results in Chapter 3 are listed here.

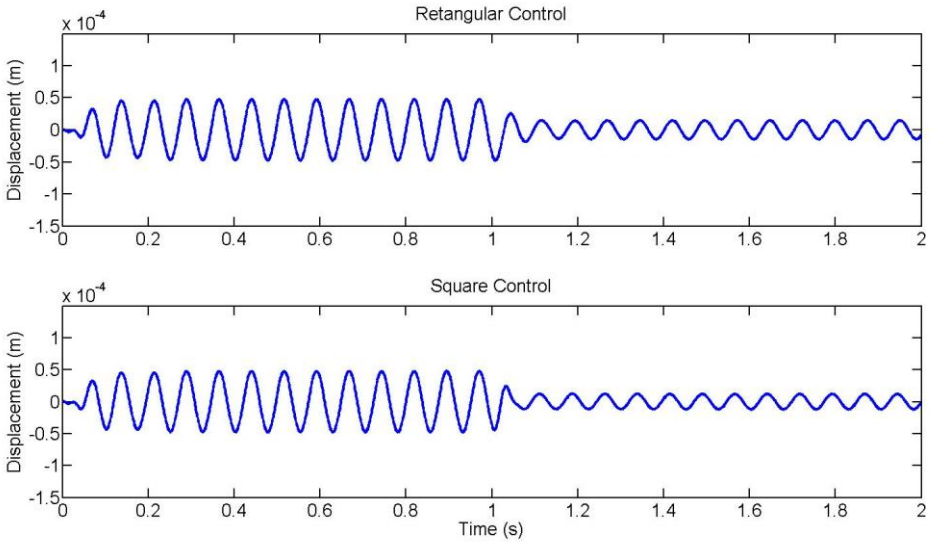

Figure 1 Rotor displacement in *x*-direction at sensor plane close to AMB 1 (node 5) when $\Omega = 83$ rad/s

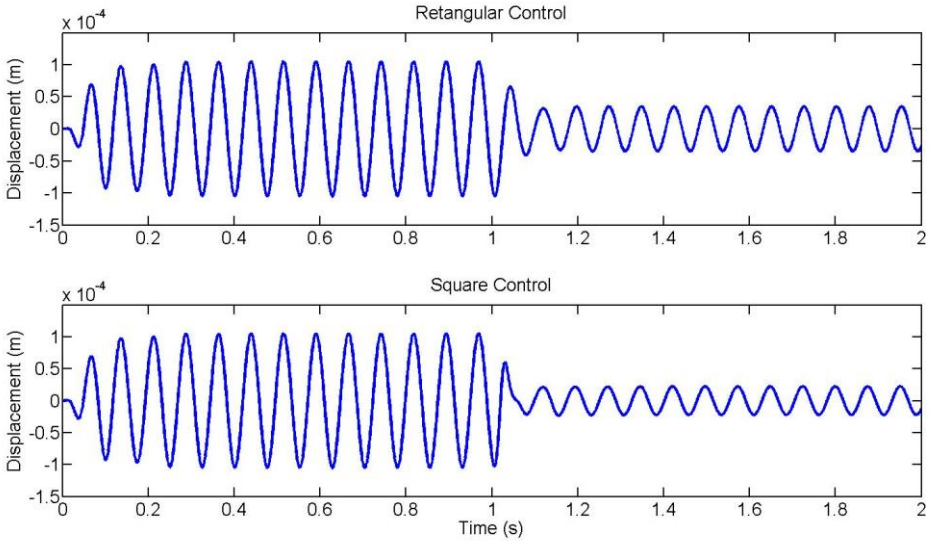

Figure 2 Rotor displacement in x-direction at sensor plane close to the motor end (node 3) when $\Omega = 83$ rad/s

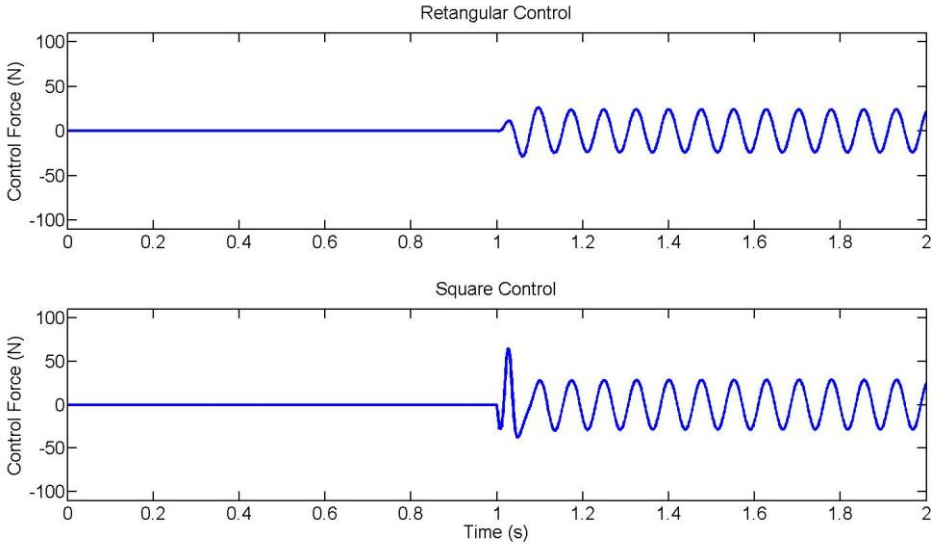

Figure 3 Control forces applied on AMB 2 in x-direction when $\Omega = 83$ rad/s

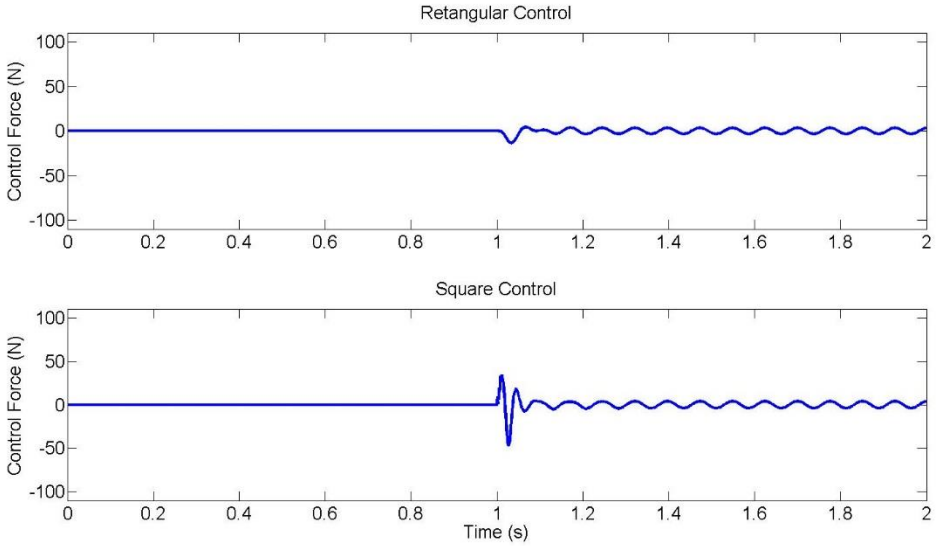

Figure 4 Control forces applied on AMB 1 in x-direction when $\Omega = 83$ rad/s

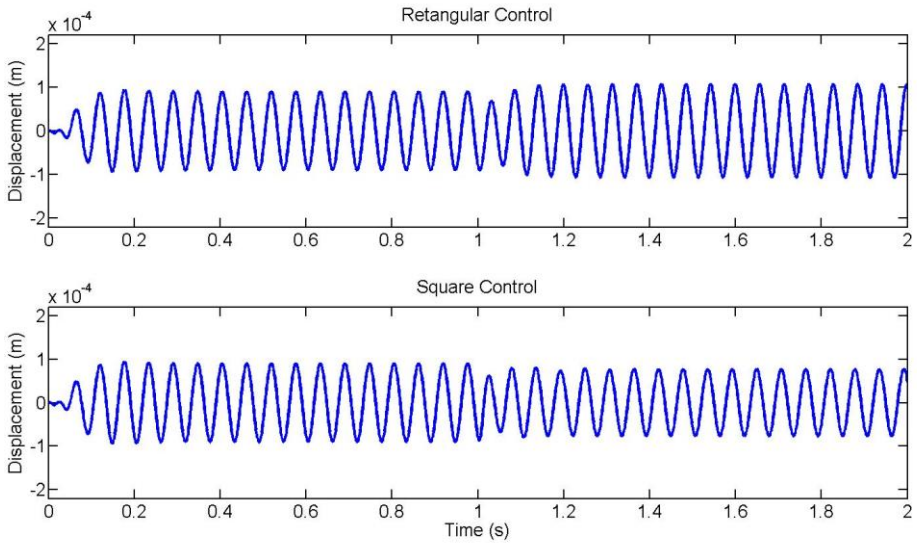

Figure 5 Rotor displacement in x-direction at sensor plane close to AMB 1 (node 5) when $\Omega = 110$ rad/s

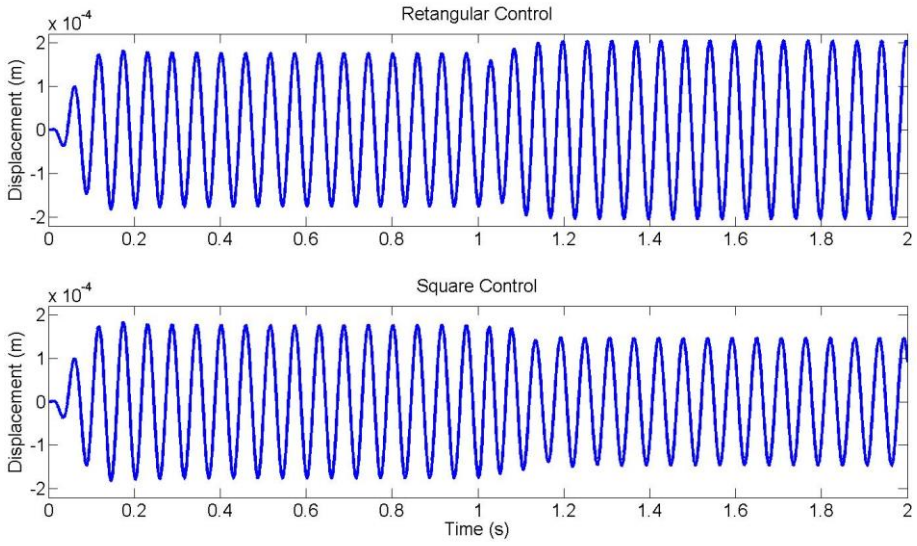

Figure 6 Rotor displacement in x-direction at sensor plane close to the motor end (node 3) when $\Omega = 110$ rad/s

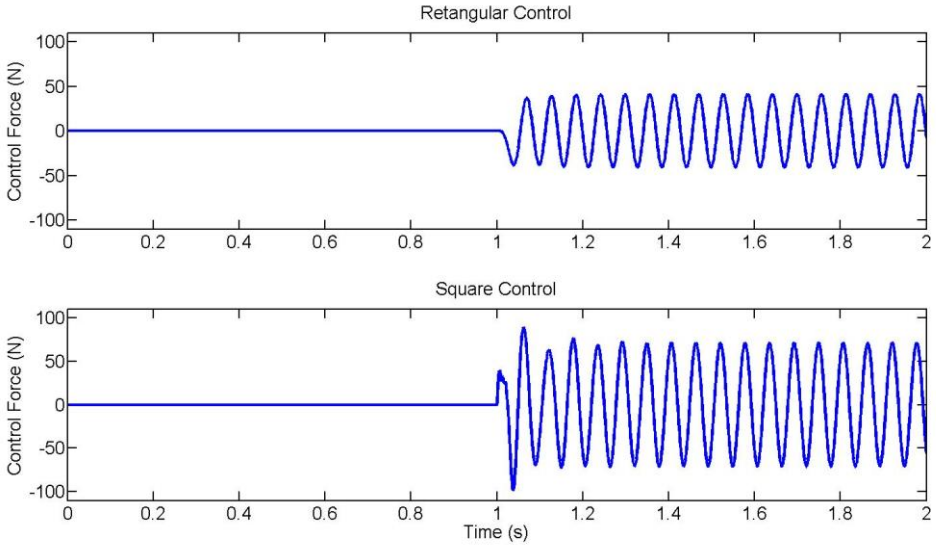

Figure 7 Control forces applied on AMB 2 in x-direction when $\Omega = 110$ rad/s

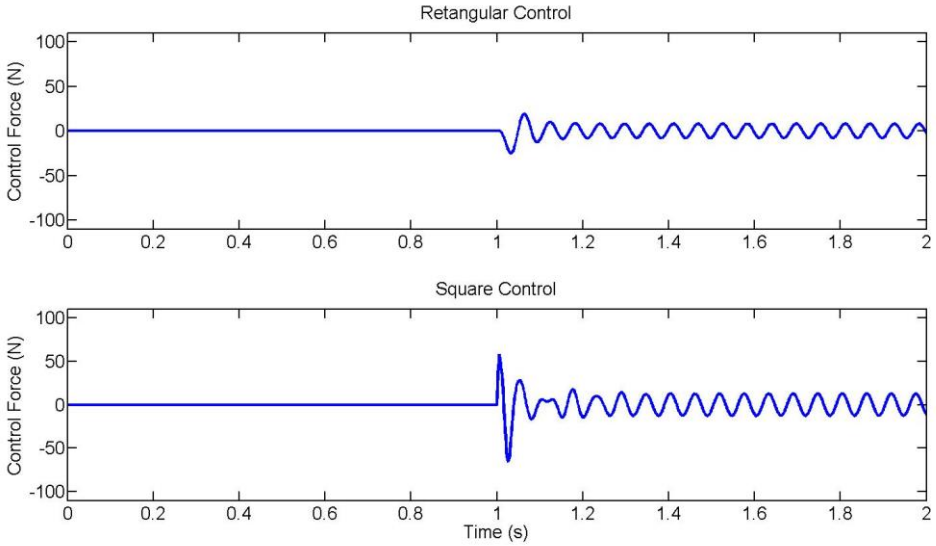

Figure 8 Control forces applied on AMB 1 in x-direction when $\Omega = 110$ rad/s

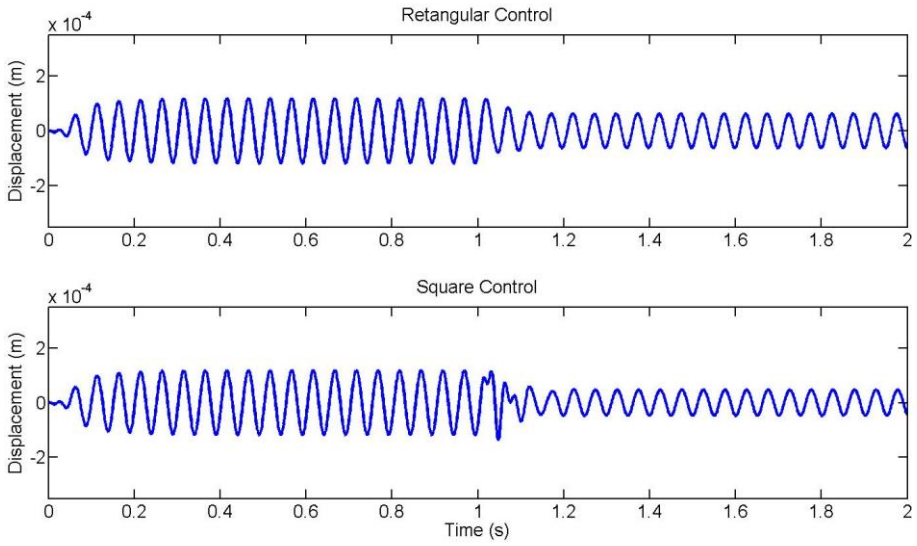

Figure 9 Rotor displacement in x-direction at sensor plane close to AMB 1 (node 5) when $\Omega = 125$ rad/s

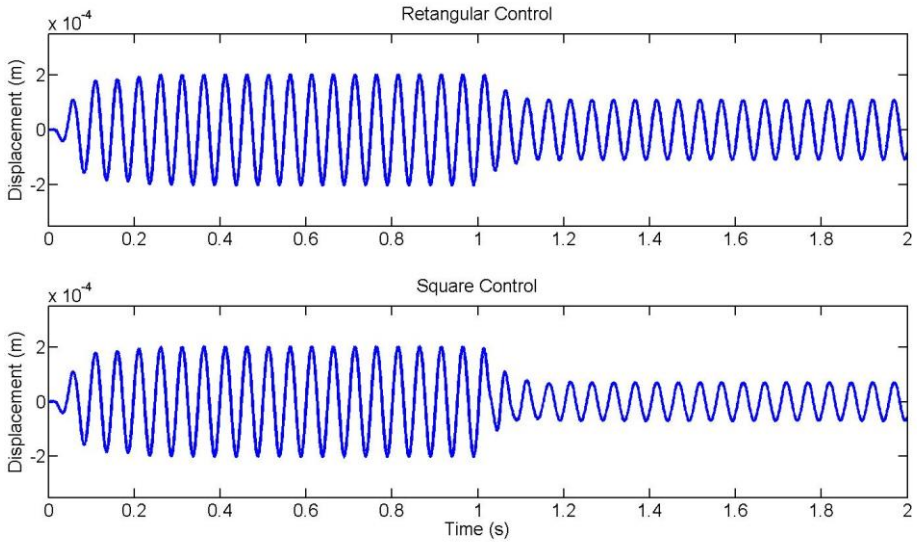

Figure 10 Rotor displacement in x-direction at sensor plane close to the motor end (node 3) when $\Omega = 125$ rad/s

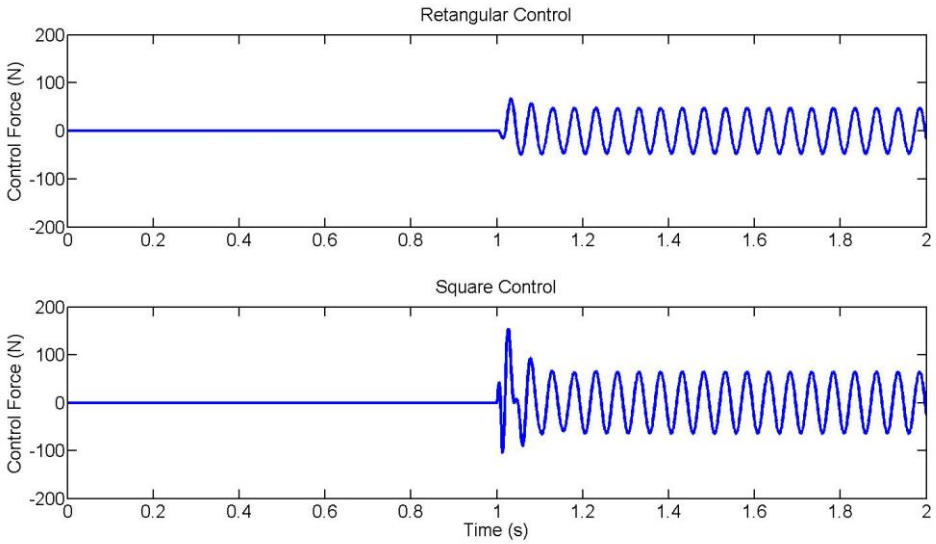

Figure 11 Control forces applied on AMB 2 in x-direction when $\Omega = 125$ rad/s

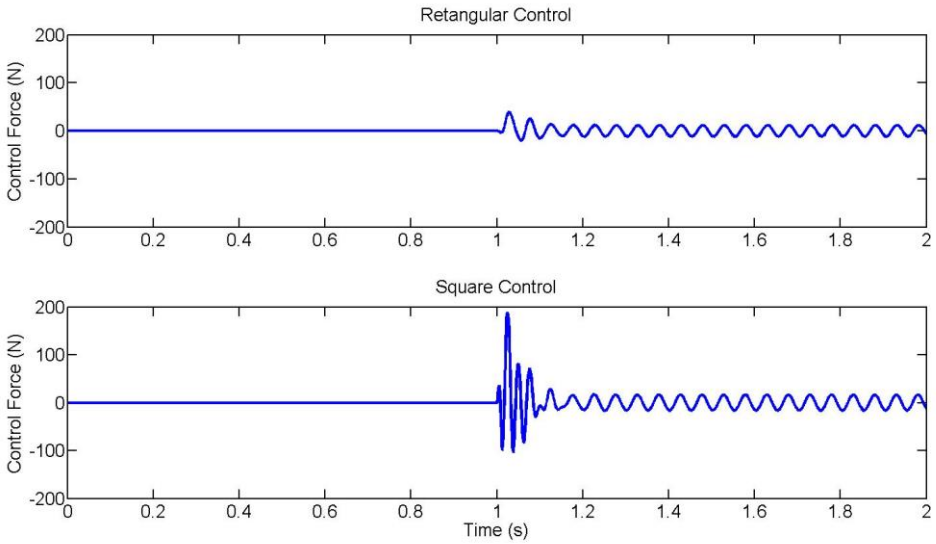

Figure 12 Control forces applied on AMB 1 in x-direction when $\Omega = 125$ rad/s

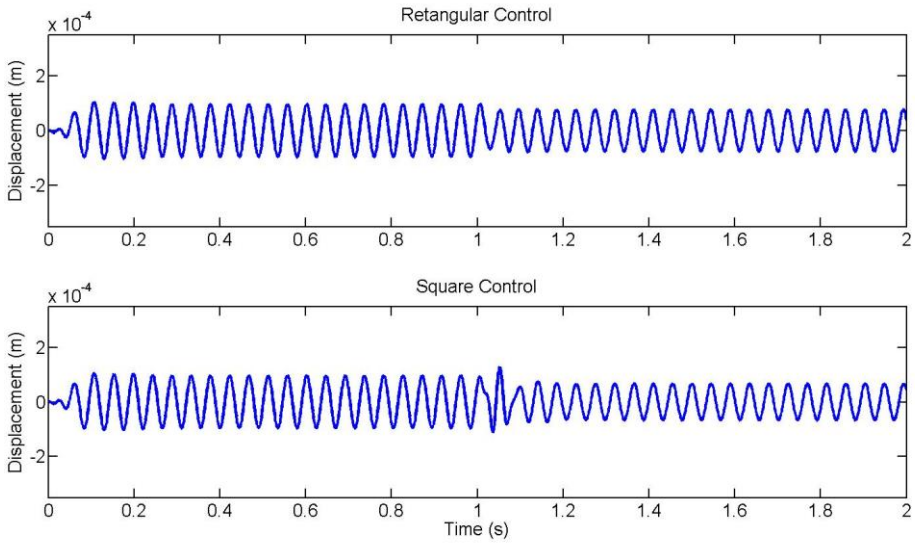

Figure 13 Rotor displacement in x-direction at sensor plane close to AMB 1 (node 5) when $\Omega = 140$ rad/s

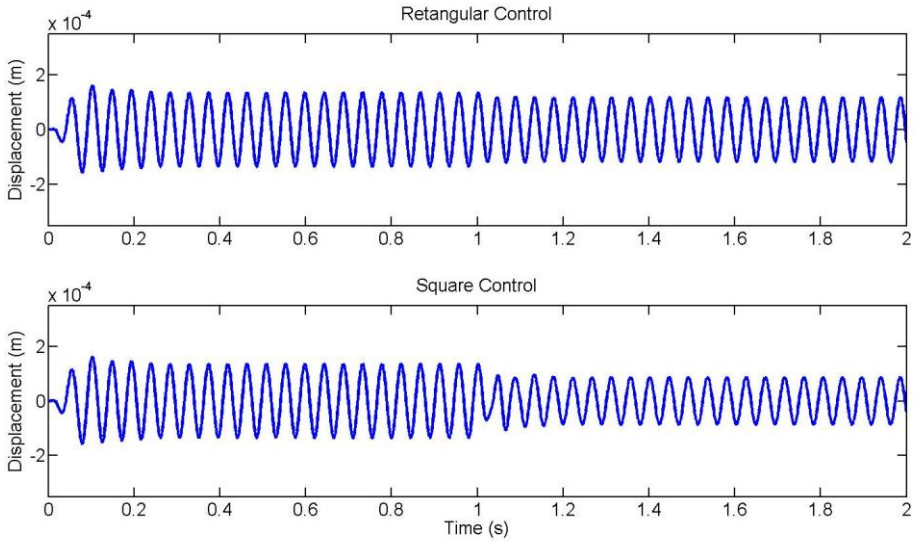

Figure 14 Rotor displacement in x-direction at sensor plane close to the motor end (node 3) when $\Omega = 140$ rad/s

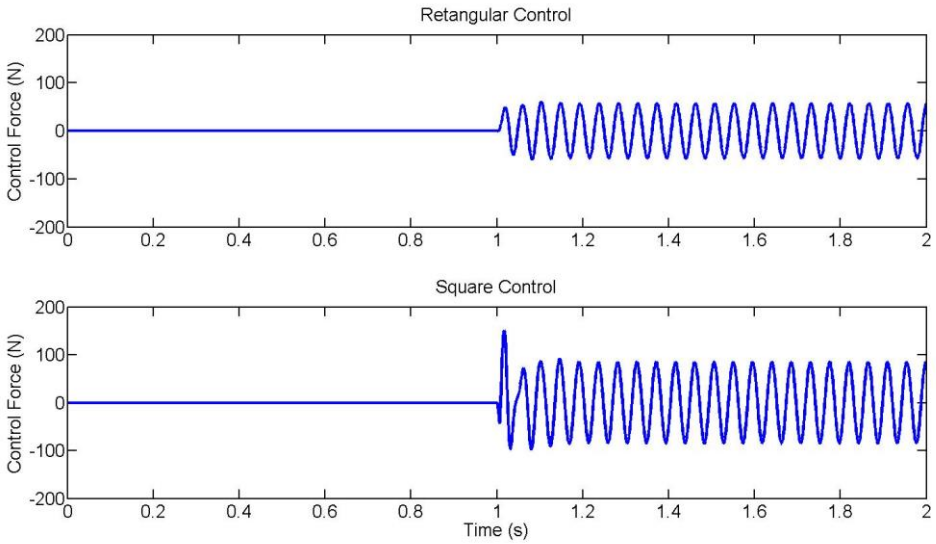

Figure 15 Control forces applied on AMB 2 in x-direction when $\Omega = 140$ rad/s

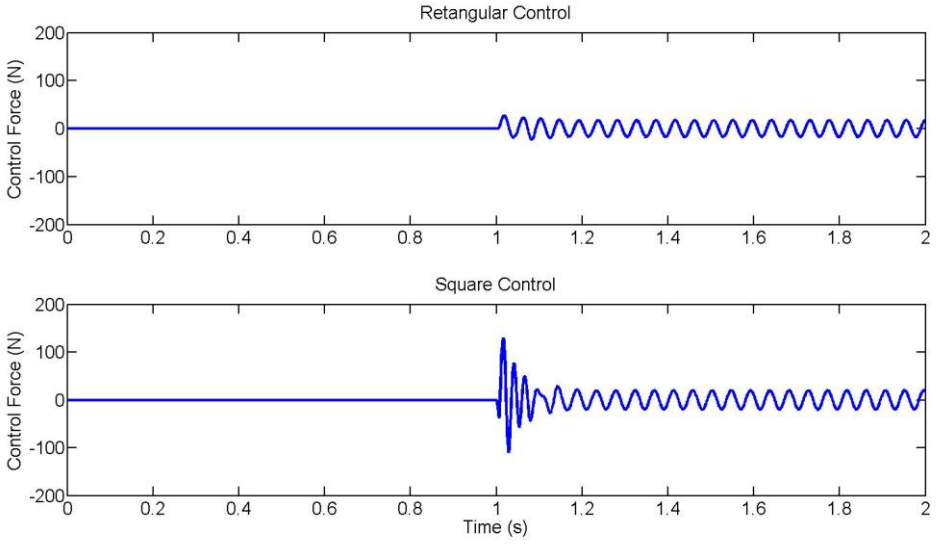

Figure 16 Control forces applied on AMB 1 in x-direction when when $\Omega = 140$ rad/s

B. Notation

B.1 Symbols

α_p	Angle between pole pairs
A_p, A_a	pole cross-section area, effective cross-section area
A_b, ρ	beam element cross-section area, beam density
c_r c_s	TDB radial clearance, sensor postion clearance
D_M	magnetic flux density
d_b, d_d, d_c	beam diameter, disk diameter, core diameter
d_x, d_y	part distance from base mass centre
E_b, G, κ	Young's modulus, shear modulus, shear form factor
E_{AMB}	energy generated AMB pole
F_{AMB}^{S}	AMB saturation force
F_{Bx} F_{By}, m_e	unbalance force components, eccentricity
F_{cr}, F_{ct}, θ_c	contact radial force, tangential force, impact angle
i_B, i_m	bias current, maximum current
i_l, i_{0i}	levitation current, current for each core
k_i, k_s	current gain, negative stiffness
k_P, k_D, k_I,	proportional, derivative, integral gain in PID
L_b	element length
l_f, l_a	length of core, effective length of core
m_b, m_d m_c	beam mass, disc mass, core mass
n_p, n_t	number of poles, Coil turns per pole
τ	cut-off freqeuncy

s_a, V_M	average radial gap, air gap volume during
μ_f, μ_a	permeability of free space, effective permeability
Θ_d^a, Θ_d^p, Θ_c^a, Θ_c^p	moment inertial in axial polar for disck and core
v	RMS based unbalance forcing response
$\alpha(t)$	switching signal
γ	H_∞ cost
ω, Ω	circular frequency, rotational speed
δ	contact penetration
ω_n, ξ	natural frequency, dynamic damping
ϱ	system numerical balancing scalar
k_e	effective stiffness
T_s, F_s	sampling time, sampling frequency
M, **G**, **K**	mass matrix, damping matrix, stiffness matrix
A, **B**, **C**, **D**	state-space matrix
q, **s**	system states, states vector
d e n r	disturbance, error, noise, demand
y, **u**	system output/input vector
f	force vector
P	plant in state space form
$\mathbf{G}_p$	MIMO transfer function for PD control action
$\mathbf{T}_u$, $\mathbf{T}_y$	Location matrices for MIMO base model
V Λ	matrix for eigen-values/vectors
$\mathbf{\Delta}_r$, $\mathbf{\Delta}_m$	model uncertainties, multiplicative model errors
T, **S**	closed loop complementary sensitivity and sensitivity
$\mathbf{W}_t$, $\mathbf{W}_s$, w_t, w_s	weighting matrices and transfer functions

$\mathbf{\Sigma}$, Σ	singular values diagonal matrix, singular value
$\mathbf{\Theta}$, $\theta(t)$	parameter polytope, time varying parameter
$\propto$	scheduling gain
$\mathbf{R}$, $\mathbf{S}$,$\mathbf{M}$, $\mathbf{N}$	temporary matrices in LMIs
$\mathbf{X}$	positive definite solution to LMI
$\boldsymbol{N}_R$, $\boldsymbol{N}_S$	orthonormal bases of the null spaces
$\mathbf{\Psi}$, Π	vertex system, polytope vertex
$\mathbf{K}_{rec}$, $\mathbf{K}_{sqr}$	LTI 'rectangular' controller, LTI 'square' controller
$\mathbf{F}_l$, $\mathbf{F}_u$, $\mathbf{F}_{cl}$	lower, upper, closed loop LFT

B.2 Subscripts

aug	augmentation
R,p	rotor model, , PD control
b,B	rigid body base model, MIMO base model
l,h	low frequencies, high frequencies
r	reduced order model
rec,sqr	'rectangular', 'square'
x,y,z	*x*-, *y*-, *z*- direction
$+,-$	positive, negative direction
$switch$	switching action
$0,\theta$	parameter independent, parameter dependent
K	control action

G,e	gyroscopic, effective stiffness dependency
Δ	multiplicative model error
u,v	rotating frame coordinates
acc,AMB	accelerometer, AMB
R,I	real, imaginary parts
i,k,m,n	general numbering indices

B.3 Accents

$\breve{}$	eigen-transformation
$\bar{}$	largest
$\tilde{}$	normalized
$\hat{}$	dimension scaling
$\vec{}$	parameter varies out of polytope
$\acute{}$	numerical balancing

B.4 Operators

$\|.\|_\infty$	infinity norm
$\mathrm{Re}(.), \mathrm{Im}(.)$	real, imaginary part
$\mathbf{F}(.,.)$	linear fractional transformation
$\mathbf{Co}\{.\}$	convex hull
$\sigma(.)$	singular value
$\mathcal{H}$	the negative definite Hessian

B.5 Constants

e	Euler's number $e \approx 2.71$
g	gravity $g \approx 9.81\ \mathrm{m/s^2}$
j	imaginary unit; $j = \sqrt{-1}$
π	area of a circle of radius 1: $\pi \approx 3.14$
$\mathbf{I}$	identity matrix: $\mathbf{I} = \mathrm{diag}(1,1,\ldots,1)$

C System Matrix

C.1 Timenshenko Beam Element Solution in FEM

The Timoshenko finite element matrices for homogeneous beam elements, defined in equations (2.15), (2.18) and (2.20) are listed here. By assuming with thin element, the diametral moment of inertia $\Theta_d = \rho A_b R^2/4$ and polar moment of inertia $\Theta_d = \rho A_b R^2/2$.

Translational mass matrix

$$\mathbf{M}_{b0}^{t} = \frac{\rho A_b L_b}{420(1+\emptyset)^2}\begin{bmatrix} 156 & 0 & 0 & 22L_b & 54 & 0 & 0 & -13L_b \\ 0 & 156 & -22L_b & 0 & 0 & 54 & 13L_b & 0 \\ 0 & -22L_b & 4L_b^2 & 0 & 0 & -13L_b & -3L_b^2 & 0 \\ 22L_b & 0 & 0 & 4L_b^2 & 13L_b & 0 & 0 & -3L_b^2 \\ 54 & 0 & 0 & 13L_b & 156 & 0 & 0 & -22L_b \\ 0 & 54 & -13L_b & 0 & 0 & 156 & 22L_b & 0 \\ 0 & 13L_b & -3L_b^2 & 0 & 0 & 22L_b & 4L_b^2 & 0 \\ -13L_b & 0 & 0 & -3L_b^2 & -22L_b & 0 & 0 & 4L_b^2 \end{bmatrix}$$

$$\mathbf{M}_{b1}^{t} = \frac{\rho A_b L_b}{420(1+\emptyset)^2}\begin{bmatrix} 294 & 0 & 0 & 38.5L_b & 126 & 0 & 0 & -31.5L_b \\ 0 & 294 & -38.5L_b & 0 & 0 & 126 & 31.5L_b & 0 \\ 0 & -38.5L_b & 7L_b^2 & 0 & 0 & -31.5L_b & -7L_b^2 & 0 \\ 38.5L_b & 0 & 0 & 7L_b^2 & 31.5L_b & 0 & 0 & -7L_b^2 \\ 126 & 0 & 0 & 31.5L_b & 294 & 0 & 0 & -38.5L_b \\ 0 & 126 & -31.5L_b & 0 & 0 & 294 & 38.5L_b & 0 \\ 0 & 31.5L_b & -7L_b^2 & 0 & 0 & 38.5L_b & 7L_b^2 & 0 \\ -31.5L_b & 0 & 0 & -7L_b^2 & -38.5L_b & 0 & 0 & 7L_b^2 \end{bmatrix}$$

$$\mathbf{M}_{b2}^{t} =$$

$$\frac{\rho A_b L_b}{420(1+\emptyset)^2}\begin{bmatrix} 140 & 0 & 0 & 17.5L_b & 70 & 0 & 0 & -17.5L_b \\ 0 & 140 & -17.5L_b & 0 & 0 & 70 & 17.5L_b & 0 \\ 0 & -17.5L_b & 3.5L_b^2 & 0 & 0 & -17.5L_b & -3.5L_b^2 & 0 \\ 17.5L_b & 0 & 0 & 3.5L_b^2 & 17.5L_b & 0 & 0 & -3.5L_b^2 \\ 70 & 0 & 0 & 17.5L_b & 140 & 0 & 0 & -17.5L_b \\ 0 & 70 & -17.5L_b & 0 & 0 & 140 & 17.5L_b & 0 \\ 0 & 17.5L_b & -3.5L_b^2 & 0 & 0 & 17.5L_b & 3.5L_b^2 & 0 \\ -17.5L_b & 0 & 0 & -3.5L_b^2 & -17.5L_b & 0 & 0 & 3.5L_b^2 \end{bmatrix}$$

Rotational mass matrix

$$\mathbf{M}_{b0}^{r} =$$

$$\frac{\Theta_d}{30L_b(1+\emptyset)^2}\begin{bmatrix} 36 & 0 & 0 & 3L_b & -36 & 0 & 0 & 3L_b \\ 0 & 36 & -3L_b & 0 & 0 & -36 & -3L_b & 0 \\ 0 & -3L_b & 4L_b^2 & 0 & 0 & 3L_b & -L_b^2 & 0 \\ 3L_b & 0 & 0 & 4L_b^2 & -3L_b & 0 & 0 & -L_b^2 \\ -36 & 0 & 0 & -3L_b & 36 & 0 & 0 & -3L_b \\ 0 & -36 & 3L_b & 0 & 0 & 36 & 3L_b & 0 \\ 0 & -3L_b & -L_b^2 & 0 & 0 & 3L_b & 4L_b^2 & 0 \\ 3L_b & 0 & 0 & -L_b^2 & -3L_b & 0 & 0 & 4L_b^2 \end{bmatrix}$$

$$\mathbf{M}_{b1}^{r} =$$

$$\frac{\Theta_d}{30L_b(1+\emptyset)^2}\begin{bmatrix} 0 & 0 & 0 & -15L_b & 0 & 0 & 0 & -15L_b \\ 0 & 0 & 15L_b & 0 & 0 & 0 & 15L_b & 0 \\ 0 & 15L_b & 5L_b^2 & 0 & 0 & -15L_b & -5L_b^2 & 0 \\ -15L_b & 0 & 0 & 5L_b^2 & 15L_b & 0 & 0 & -5L_b^2 \\ 0 & 0 & 0 & 15L_b & 0 & 0 & 0 & -15L_b \\ 0 & 0 & -15L_b & 0 & 0 & 0 & -15L_b & 0 \\ 0 & 15L_b & -5L_b^2 & 0 & 0 & -15L_b & 5L_b^2 & 0 \\ -15L_b & 0 & 0 & -5L_b^2 & -15L_b & 0 & 0 & 5L_b^2 \end{bmatrix}$$

$$\mathbf{M}_{b2}^{r} =$$

$$\frac{\Theta_d}{30L_b(1+\emptyset)^2}\begin{bmatrix} 0 & 0 & 0 & 0 & 0 & 0 & 0 & 0 \\ 0 & 0 & 0 & 0 & 0 & 0 & 0 & 0 \\ 0 & 0 & 10L_b^2 & 0 & 0 & 0 & 5L_b^2 & 0 \\ 0 & 0 & 0 & 10L_b^2 & 0 & 0 & 0 & 5L_b^2 \\ 0 & 0 & 0 & 0 & 0 & 0 & 0 & 0 \\ 0 & 0 & 0 & 0 & 0 & 0 & 0 & 0 \\ 0 & 0 & 5L_b^2 & 0 & 0 & 0 & 10L_b^2 & 0 \\ 0 & 0 & 0 & 5L_b^2 & 0 & 0 & 0 & 10L_b^2 \end{bmatrix}$$

Gyroscopic matrix

$\mathbf{G}_{b0} =$

$$\frac{\Theta_p}{30L_b}\begin{bmatrix} 0 & -36 & 3L_b & 0 & 0 & 36 & 3L_b & 0 \\ 36 & 0 & 0 & 3L_b & -36 & 0 & 0 & 3L_b \\ -3L_b & 0 & 0 & -4L_b^2 & 3L_b & 0 & 0 & L_b^2 \\ 0 & -3L_b & 4L_b^2 & 0 & 0 & 3L_b & -L_b^2 & 0 \\ 0 & 36 & -3L_b & 0 & 0 & -36 & -3L_b & 0 \\ -36 & 0 & 0 & -3L_b & 36 & 0 & 0 & 3L_b \\ -3L_b & 0 & 0 & L_b^2 & 3L_b & 0 & 0 & -4L_b^2 \\ 0 & -3L_b & -L_b^2 & 0 & 0 & 3L_b & 4L_b^2 & 0 \end{bmatrix}$$

$\mathbf{G}_{b1} =$

$$\frac{\Theta_p}{30L_b}\begin{bmatrix} 0 & 0 & -15L_b & 0 & 0 & 0 & -15L_b & 0 \\ 0 & 0 & 0 & -15L_b & 0 & 0 & 0 & -15L_b \\ 15L_b & 0 & 0 & -5L_b^2 & -15L_b & 0 & 0 & 5L_b^2 \\ 0 & 15L_b & 5L_b^2 & 0 & 0 & -15L_b & -5L_b^2 & 0 \\ 0 & 0 & 15L_b & 0 & 0 & 0 & 15L_b & 0 \\ 0 & 0 & 0 & 15L_b & 0 & 0 & 0 & 15L_b \\ 15L_b & 0 & 0 & 5L_b^2 & -15L_b & 0 & 0 & -5L_b^2 \\ 0 & 15L_b & -5L_b^2 & 0 & 0 & -15L_b & 5L_b^2 & 0 \end{bmatrix}$$

$\mathbf{G}_{b2} =$

$$\frac{\Theta_p}{30L_b}\begin{bmatrix} 0 & 0 & 0 & 0 & 0 & 0 & 0 & 0 \\ 0 & 0 & 0 & 0 & 0 & 0 & 0 & 0 \\ 0 & 0 & 0 & 10L_b^2 & 0 & 0 & 0 & -5L_b^2 \\ 0 & 0 & 10L_b^2 & 0 & 0 & 5L_b & 5L_b^2 & 0 \\ 0 & 0 & 0 & 0 & 0 & 0 & 0 & 0 \\ 0 & 0 & 0 & -5L_b & 0 & 0 & 0 & 0 \\ 0 & 0 & 0 & -5L_b^2 & 0 & 0 & 0 & -10L_b^2 \\ 0 & 0 & 5L_b^2 & 0 & 0 & 0 & 10L_b^2 & 0 \end{bmatrix}$$

Stiffness matrix

$\mathbf{K}_{b0}=$

$$\frac{E_b I_b}{L_b^3(1+\emptyset)}\begin{bmatrix} 12 & 0 & 0 & 6L_b & -12 & 0 & 0 & 6L_b \\ 0 & 12 & -6L_b & 0 & 0 & -12 & -6L_b & 0 \\ 0 & -6L_b & 4L_b^2 & 0 & 0 & 6L_b & 2L_b^2 & 0 \\ 6L_b & 0 & 0 & 4L_b^2 & -6L_b & 0 & 0 & 2L_b^2 \\ -12 & 0 & 0 & -6L_b & 12 & 0 & 0 & -6L_b \\ 0 & -12 & 6L_b & 0 & 0 & 12 & 6L_b & 0 \\ 0 & -6L_b & 2L_b^2 & 0 & 0 & 6L_b & 4L_b^2 & 0 \\ 6L_b & 0 & 0 & 2L_b^2 & -6L_b & 0 & 0 & 4L_b^2 \end{bmatrix}$$

$\mathbf{K}_{b1}$=

$$\frac{E_b I_b}{L_b^3(1+\emptyset)}\begin{bmatrix} 0 & 0 & 0 & 0 & 0 & 0 & 0 & 0 \\ 0 & 0 & 0 & 0 & 0 & 0 & 0 & 0 \\ 0 & 0 & L_b^2 & 0 & 0 & 0 & -L_b^2 & 0 \\ 0 & 0 & 0 & L_b^2 & 0 & 0 & 0 & -L_b^2 \\ 0 & 0 & 0 & 0 & 0 & 0 & 0 & 0 \\ 0 & 0 & 0 & 0 & 0 & 0 & 0 & 0 \\ 0 & 0 & -L_b^2 & 0 & 0 & 0 & L_b^2 & 0 \\ 0 & 0 & 0 & -L_b^2 & 0 & 0 & 0 & L_b^2 \end{bmatrix}$$

C.2 Rigid body base

The mass, stiffness and damping matrices defined in equation (2.48), are listed here.

$$\mathbf{M}_b = \begin{bmatrix} M_b & 0 & 0 & 0 \\ 0 & M_b & 0 & 0 \\ 0 & 0 & I_x & 0 \\ 0 & 0 & 0 & I_y \end{bmatrix}$$

$$\mathbf{K}_b = \begin{bmatrix} 4k_x & 0 & 2k_x(d_2-d_1) & 0 \\ 0 & 4k_y & 0 & 2k_y(d_2-d_1) \\ 2k_x(d_2-d_1) & 0 & 2k_x({d_1}^2+{d_2}^2)+4k_z{d_w}^2 & 0 \\ 0 & 2k_y(d_2-d_1) & 0 & 2k_y({d_1}^2+{d_2}^2) \end{bmatrix}$$

$$\mathbf{G}_b = \begin{bmatrix} 4c_b & 0 & 2c_b(d_2-d_1) & 0 \\ 0 & 4c_b & 0 & 2c_b(d_2-d_1) \\ 2c_b(d_2-d_1) & 0 & 2c_b({d_1}^2+{d_2}^2) & 0 \\ 0 & 2c_b(d_2-d_1) & 0 & 2c_b({d_1}^2+{d_2}^2) \end{bmatrix}$$